The University Of Sheffield.

Soft Magnetostrictive and Mechanical Properties of thin Fe-Co-Cr films

by

Saturi Baco

A thesis submitted in partial fulfillment of the requirements for the degree of
Doctor of Philoshopy

in the

Department of Materials Science and Engineering
Faculty of Engineering

December 2020

Abstract

Soft amorphous magnetic materials with small coercivity, H_c and anisotropy fields, H_k high saturation magnetostriction constant, λ_s and excellent mechanical properties are desirable for magnetic microelectromechanical (MagMEMs) sensors. Apart from these properties, materials with low magnetic damping, α are sought-after materials in spintronic applications to minimize the power consumption. To develop a fundamental understanding on the soft amorphous magnetostrictive properties of FeCoCr thin films, studies on the magnetostrictive, structural, magnetic damping and mechanical properties of FeCo and FeCoCr thin films at varied growth conditions are presented in this thesis. The primary aim of this study is to achieve soft amorphous magnetostrictive FeCoCr films with lower H_c (< 10 kAm^{-1}), lower H_k (< 15 kAm^{-1}), but higher saturation magnetostriction, λ_s (> 20 ppm) and smaller α (≤ 0.01) compared to the other soft magnetic thin films. The findings showed that FeCoCr films with soft amorphous properties were achieved when sputtered at power 75 W and pressure 4.8 x 10^{-3} Torr. Nevertheless, the structure changed to polycrystalline as the sputtering power increased to 125 W and 150 W. For the films grown at 75 W, the effective magnetostriction constant, $\lambda_s = 28$ ppm was determined to be a factor of five higher compared to the polycrystalline films at 150 W. While the sputtering power demonstrated a substantial effect on tailoring the structure and the magnetostrictive properties, the film thickness however does not significantly impact on those properties. The H_c of the FeCoCr films obtained decreased with Cr compositions, similar to the H_k which also found reduced to as low as 3 kAm^{-1} with increasing the Cr concentrations up to at. 7.2% Cr. The measured H_k determined by MOKE measurement showed a similar trend with the H_k measured by VNA-FMR technique. The α increased with increasing the Cr content to at.7.2%, but at a lower Cr at 2.6% film it was found to be smaller. The damping constant of FeCoCr films arose from the inhomogeneity of the samples. From mechanical testing by nanoindentation, it was found that the yield strength, σ_y of FeCoCr films was determined at a maximum of 1014 MPa. In summary, it was feasible to achieve soft amorphous FeCoCr magnetostrictive films by careful control of the growth sputtering. Fabrication of soft amorphous magnetic FeCoCr thin films with a lower concentration of at.2.6% Cr at optimised sputtering power 75 W, a lower $H_c < 0.2$ kAm^{-1} and H_k < 3 kAm^{-1} and the α as low as 0.0065 were successfully achieved while sustaining a higher saturation magnetostriction constant, $\lambda_s \approx 39$ ppm. The Cr substitutions into FeCo films also play a role to hinder the dislocation movement of atoms, hence improve mechanical strength of FeCo films.

Acknowledgements

In the name of Allah, the Most Beneficent, the Most Merciful..

My PhD journey has taught me about the meaning of "with every difficulties, there is an ease". It would not have been possible for me to went through my days in Sheffield without supportive people around me. Therefore, I would like to express my deepest gratitude to:

Ministry of Higher Education Malaysia (MOHE) and Universiti Malaysia Sabah (UMS) for the golden opportunity in supporting my finances throughout my studies.

My supervisor, Prof. Nicola Morley. It reminds me four years ago when I was looking for a supervisor, and I have crossed your profile. I thanked God that I have made a right decision emailed you. Thank you for giving me a chance to be one of your students and always make me believe that I can do things. I would never forget all your understanding, kindness, and encouragement.

My second supervisor, Dr. Tom Hayward. Thank you for always keep me motivated. I'm indebted your guidance until I have learned a lot about VNA-FMR, which is definitely new knowledge for me.

Prof. Dan Alwood and **the members of Functional Magnetic Materials Group**, thank you for lend me your hands with the lab stuffs and constructive discussions during the group meetings. To **Ms. Joanne Sharp** I truly appreciated your assistance on TEM experiment. To **Mrs. Dawn Bussey**, I owed your kind help on the AFM and Nanoindentation training during my last stage of experimental works.

My beloved parents, Mr. Baco and Mrs. Sadi . Your constant prayers are my strength for me to keep standing when I feel down. As a daughter I could not thank you enough, but always praying that May Allah grants you both Syurga Firdausi.

My siblings; Abil, Umiek, Aman, Ima, Basri, Aishah and **Aby**, your terrific supports are momentum for me to keep moving.

The one and only my husband, Soeffeyan. It reminds me back in 2003, you flew to Sheffield to chase your dreams. And never we expected that after more a decade, I got the chance to pursue my dreams also in Sheffield. Sheffield has created "sweet love-long distance relationship story" in our life! Your unconditional love, indeed, the greatest gift for me to complete this journey, despite we are thousands miles apart. *Terima kasih Sayang. Semoga kasih sayang kita sampai ke Syurga. Amin..*

Conferences and Publications

Poster Presentation:

Magnetism 2017 3rd – 4th April 2017. University of York, United Kingdom.

Magnetism 2018. 2nd April – 3rd April 2018. University of Manchester, United Kingdom.

INTERMAG Conference 2018. 23rd April – 27th April 2018. Marina Bay Sands Convention Centre, Singapore.

Publications as co-author:

E.Miskevich, F. K. Alshammari, W.G. Yang, J.Sharp, **S. Baco**, Z. Leong, Q.A.Abbas, and N. A. Morley. Artificial multiferroic structures using soft magnetostrictive bilayers on $Pb(Mg_{1/3}Nb_{2/3})$–$PbTiO_3$ J. Phys. D: Appl. Phys. 51 (2018) 085001.

Q.A. Abbas, M.Rodrigues, **S. Baco**, S. Guan, N.A Morley. Influence of annealing temperature on the structural and magnetic properties of FeGaSiB thin films. Thin Solid Films 701 (2020) 137955.

Manuscript In-preparation:

S. Baco, Qayes A. Abbas, T.J. Hayward and N. A. Morley. An investigation on Mechanical Properties of Soft Magnetic of FeCoCr films by Nanoindentation.

Contents

Abstract i

Acknowledgements ii

Conferences and Publications iii

List of Figures vii

List of Tables xiii

Symbols xiv

Abbreviations xvii

1 Introduction 1

1.1 Soft Magnetostrictive Materials 1
1.2 Thesis Outline 3

2 Theoretical Background 6

2.1 Classification of Magnetic Materials 6
2.1.1 Temperature Dependence of Magnetic Materials 7
2.2 Magnetization Process and Magnetic Energies 8
2.2.1 Magnetostatic Energy 10
2.2.2 Magnetocrystalline Energy 11
2.2.3 Exchange Energy 12
2.2.4 Magnetoelastic Energy 13
2.2.5 Zeeman Energy 13
2.3 Magnetization Damping 14
2.4 Magnetic Anisotropy for Amorphous Materials 16
2.5 Induced Anisotropy 18
2.5.1 Magnetic Annealing 18
2.5.2 Roll Anisotropy 19
2.5.3 Stress Annealing 19
2.6 Magnetostriction Principle 19
2.6.1 Magnetostriction for Different Materials 20
2.6.2 Surface Magnetostriction 22
2.7 Theory on Nanoidentation for Measuring the Mechanical Properties . . . 22

3 Literature Review 28
3.1 Structural, Magnetic and Magnetostrictive of FeCo 28
3.1.1 Effect of Fe and Co Compositions 29
3.1.2 Effect of Annealing 32
3.1.3 Effect of underlayer/multilayers films 36
3.1.4 Effect of Additives 39
3.2 Magnetostrictive materials of Fe-X based (X=Tb,Dy,Ga) 41
3.3 Measurement Techniques of Magnetostriction 44
3.3.1 Direct Measurement 45
3.3.1.1 Strain Gauge Technique 45
3.3.1.2 Capacitance Method 46
3.3.2 Indirect Measurement 47
3.3.2.1 Cantilever Deflection Method 47
3.3.2.2 Strain-Modulated Ferromagnetic Resonance (SMFMR) . 49
3.4 Ferromagnetic Resonance studies on FeCo-based thin films 49
3.5 Mechanical Properties of FeCo-based Films 53

4 Experimental Techniques 57
4.1 Film Fabrication 57
4.1.1 Sputtering Principle 57
4.2 Thin Film Growth and Film Stress 60
4.2.1 Modes of Film Growth and Microstructure 60
4.2.2 Stress in Thin Film 63
4.2.3 Deposition of Films by Nordiko Sputter System 65
4.2.4 Substrate Preparation and Thin Film Deposition 67
4.2.5 Thickness Calibration 69
4.3 Atomic Force Microscopy (AFM) 70
4.4 Scanning Electron Microscope and Energy Dispersive X-Ray (SEM-EDX) 72
4.5 X-Ray Diffraction (XRD) 73
4.6 Transmission Electron Microscope (TEM) 77
4.7 Magneto-Optical Kerr Effect (MOKE) 78
4.8 Measurement of Magnetostriction by the Villari Effect 81
4.9 Measurement of Damping Properties by Vector Network Analyzer and Ferromagnetic Resonance (VNA-FMR) 86
4.10 Measurement of Saturation Magnetisation by SQUID-VSM Technique . . 88
4.11 Measurement of Mechanical properties by Nanoidentation 90
4.11.1 System Calibration 90
4.11.2 Sample Mounting 92

5 Characterisation of FeCo and FeCoCr films under different sputtering conditions 93
5.1 Introduction 93
5.2 Structural Properties of FeCo 94
5.3 Structural Properties of FeCoCr 96
5.4 Compositional and Structural Studies by SEM- EDX and TEM 99
5.5 Morphology Studies of FeCoCr by AFM 100
5.6 Studies on Magnetic Properties 102

5.6.1 Magnetic Properties of FeCo 104
5.6.2 Magnetic Properties of FeCoCr films 105
5.7 Magnetostriction Studies on FeCo and FeCoCr 115
5.7.1 Summary 117

6 Structural, Magnetostrictive and Magnetic Damping Properties of Soft FeCoCr Thin Films 119
6.1 Introduction 119
6.2 Sample Fabrication 121
6.3 Compositions Analysis by EDX 121
6.4 Structural Analysis by XRD 122
6.5 Magnetic Properties of FeCoCr films 123
6.5.1 Magnetic Properties by MOKE 123
6.5.2 Magnetic Properties by SQUID-VSM 127
6.6 Magnetostriction Analysis 131
6.7 Ferromagnetic Resonance Analysis by VNA-FMR 132
6.8 Comparison between FeCoCr and other Soft Magnetic Materials 139
6.9 Summary 141

7 The Mechanical Properties of FeCo and FeCoCr thin films using the Nanoindentation Technique 143
7.1 Introduction 143
7.2 Sample Preparation of Thick Films 145
7.3 Nanoindentation Measurement 145
7.4 Mechanical properties of Si substrate 146
7.5 Mechanical properties of FeCo thin films 147
7.6 Mechanical properties of FeCoCr thin films 150
7.7 Elastic recovery of FeCo and FeCoCr films 156
7.8 Analysis of the Material Effect 158
7.9 Yield Strength of FeCo and FeCoCr films 161
7.10 Summary 165

8 Conclusion and Future Work 166
8.1 Conclusions 166
8.2 Future Works 170

Bibliography 172

List of Figures

2.1 The arrangement of magnetic moments in (a) paramagnet (b) antiferromagnet (c) ferromagnet (d) ferrimagnet. Figure adapted from 7

2.2 The initial curve of hysteresis and the growth of domains in ferromagnetic material when magnetic field is applied. Figure adapted from 9

2.3 The existence of magnetic dipole on the surface (a) and (b). The magnetostatic energy, E_{ms} is minimised when the closure domain is formed (c) as disappearance of magnetic dipole on the surface. Figure adapted from 10

2.4 Magnetization of Fe in easy $< 100 >$ and hard axes $< 111 >$ 11

2.5 Magnetization of Co in easy $< 0001 >$ and hard axes $< 1010 >$ 12

2.6 (a) The precession motion of magnetization based on Landau-Lifshitz (b) The additional term of damping proposed by Gilbert showing the magnetization in the direction of external magnetic field. Figure adapted from 15

2.7 The random anisotropy model for amorphous showing that the correlation length, D is much smaller compare to the exchange length, L_{ex} 18

2.8 Magnetostriction due to the spin orbit coupling. Taken from 21

2.9 The load-displacement curve. Figure taken from 24

2.10 The schematic diagram of unloading and loading process of indenter tip into sample. Figure taken from [63]. 24

2.11 Process of nanoindentation involves measurement of some parameters in obtaining the hardness, reduced elastic modulus and Young's modulus. . . 26

2.12 Geometry of (a) Knoop indenter (b) spherical indenter and SEM images of (c) Knoop indenter (d) spherical indenter. Figure taken from 27

3.1 The saturation magnetisation of FeCo at varied composition (a) and (b)the lattice parameter in disordered and ordered structure. Figure taken from 29

3.2 The plot of magnetostriction of FeCo with percentages Co (a) as-deposited films and (b) samples at different heat treatment. Figure taken from . . . 33

3.3 XRD pattern for $Fe_{32}Co_{68}$ at different annealing temperature showing the existence of FCC phases at higher temperature. Figure taken from . . 34

3.4 XRD pattern for FeCoCr grown at varied power. Figure taken from . . . 42

3.5 Set-up of strain gauge technique. Figure taken from 46

3.6 Schematic diagram of capacitance cell. Figure taken from 47

3.7 Cantilever deflection method. Figure taken from 48

3.8 Compositional dependence of $Fe_{1-x}Co_x$ on the damping parameters in the regions of phases structures (bcc, fcc and mixed). It presenting damping from radiative, α_{rad} (green); spin-pump, α_{sp} (grey) and calculated intrinsic, α_{int} (black). The total of damping,α_{tot} contributed by α_{rad}, α_{sp} and α_{int} shown by red-line. Also shown the α_b for bulk value (open-circle). Figure taken from . . . 50
3.9 The plot showing linewidth dependence on the FMR frequency of CoFeB film thickness 75nm that fitted to Kittle's formula. Figure taken from . . 52
3.10 The average of hardness and modulus of different substrates. The values determined by standard method of Oliver and Pharr. Figure taken from . 54
3.11 The schematic diagram of indenter pressing the film surface, showing the existence of internal stresses based on Sneddon's analysis. Figure taken from [134]. . . . 55

4.1 Three categories of thin film growth modes (a) Volmer - Weber (b) Frank - van der Merwe and (c) Stranski - Krastanov. Figure adapted from . . . 61
4.2 Model of Zone Structure for sputtered materials. Taken from . . . 62
4.3 The sputter system operation for obtaining low vacuum down to 10^{-2} Torr by mechanical pump through roughing valve. . . . 66
4.4 The sputter system operation for obtaining higher vacuum down to 10^{-5} to 10^{-8} Torr by diffusion pump through high vacuum and foreline valve. . 67
4.5 An image on difference in stepheight between FeCoCr film and substrate to determine the film thickness. . . . 71
4.6 Graph of thickness calibration of FeCoCr with varied deposition time . . . 71
4.7 Schematic operation of AFM in tapping mode. Figure adapted from . . . 72
4.8 Interaction processes of electron with sample. Figure adapted from 74
4.9 Braggs Law on X-Ray diffraction. Figure adapted from . . . 76
4.10 The FWHM curve fitting for the experimental data of FeCo (100nm) using the Gaussian function, whereby w = FWHM; y_0 = base; x_c = center; A = area. . . . 76
4.11 (a) Directed beam is used to image bright-field and (b) Diffracted beam which is away from optic axis is selected to form the dark-field image. Figure taken from [163]. . . . 78
4.12 Three different of MOKE configurations. Figure taken from . . . 79
4.13 Schematic of polar MOKE showing the reflected light being rotated at angle, θ_K and elliptically polarised characterised by η_K. Figure taken from 80
4.14 Schematic diagram of Low Field MOKE magnetometer. . . . 82
4.15 Magnetostriction measurement using different bending tools. . . . 84
4.16 Magnetisation curves of the representative FeCoCr film after bent using three different radii tools. . . . 84
4.17 Magnetization curves upon the stress application using three different bending tools. It showing the determination of H_k at the positive part of magnetization switching. . . . 85
4.18 The fitted linear graph of anisotropy field, H_k as a function of inverse bending radii,$1/R$. H_k^+ and H_k^- are anisotropy measured at upper part and lower part of hysteresis loop, respectively. . . . 86
4.19 Scattering parameters for VNA with two-ports. . . . 87
4.20 Experimental data which fitted to (a) Kittle equation and (b) FMR linewidth in obtaining the M_s, H_k and α. . . . 88

4.21 The components of SQUID MPMS 3 system. Figure taken from 89
4.22 Sample position on the mounting station. 90
4.23 Figure showing the position of the sample mounted on the stage along with the polycarbonate sample on the TI 950 TriboIndenter Hysitron. The nanoindentation was firstly performed onto the polycarbonate before the nanoindentation is conducted on the thin film. 92

5.1 XRD profiles of FeCo with and without magnetic field during deposition for different film thicknesses. 95
5.2 XRD profiles of FeCoCr as function of thickness at the same Cr concentration at.% 14 grown in magnetic field. Shown in plot also is the FeCo at 100nm grown with magnetic field, for a structure comparison. 97
5.3 XRD profiles of FeCoCr as function of sputtering power grown at thickness 100nm deposited with magnetic field. 98
5.4 Bright field images of FeCoCr films deposited at sputtering power (a) 75 W (b) 150 W (c) dark field image of FeCoCr film at 150 W showing columnar structure. 101
5.5 SAED images of FeCoCr films sputtered at power (a) 75 W (b) 150 W. . 102
5.6 Surface roughness of FeCoCr (a) as a function of film thicknesses (fixed sputtering power 75 W) and (b) as a function of sputtering power (constant thickness 100 nm). 103
5.7 AFM micrographs of 100 nm thick FeCoCr films grown with sputtering power (a) 75 W (b) 100 W (c) 125 W and (d) 150 W in the presence of magnetic field. Data scale: 10nm; Scan size $2\mu m \times 2\mu m$. 103
5.8 Roughness analysis with scan size $2\mu m \times 2\mu m$ of 100 nm thick at 125 W sputtering power. The image also shows the presence of particles due to contamination on the film surface. 104
5.9 Normalised magnetization measured at easy axis of FeCo films sputtered with applied field (120 kAm^{-1}) at different thicknesses. 106
5.10 Normalised magnetization measured at easy axis of FeCo films sputtered without applied field at different thicknesses. 106
5.11 The average of coercive field of FeCo sputtered under magnetic field and no field with the shown error bars represent the standard error calculated from three different samples for each film thickness. 107
5.12 The average of saturation field of FeCo sputtered under magnetic field and no field with the shown error bars indicate the standard error calculated from three different samples for each film thickness. 107
5.13 Angular dependence of remanence ratio, M_r/M_s of two different set of FeCo films grown with no magnetic field (a) 70 nm (b) 100 nm (c) 120 nm and with magnetic field (d) 70 nm (e) 100 nm (f) 120 nm. 108
5.14 The average of coercive field and anisotropy field of FeCoCr as function of thickness (sputtering power 75 W). The error bars represent the standard errors calculated from three different samples. 109
5.15 The average coercive field of FeCoCr films as a function of sputtering power. Also shown the anisotropy field of films sputtered from 75 W to 125 W (grown under magnetic field at the same film thickness of 100 nm). The error bars indicate the standard error calculated from three different samples. 110

5.16 Comparison of normalised magnetization between FeCo and FeCoCr (t= 100nm) grown at similar sputtering conditions. 111
5.17 Normalised magnetization on easy and hard axes for series of thickness FeCoCr (a) 56 nm (b) 80 nm (c) 100 nm (d) 125 nm and (e) 165 nm grown at sputtering power 75 W. 112
5.18 Plots of easy and hard axes for FeCoCr at different sputtering power (a) 75 Watt, (b) 100 Watt (c) 125 Watt (d) 150 Watt at fixed thickness 100 nm. 113
5.19 Angular dependence of FeCoCr at varied thickness (a) 56 nm (b) 80 nm (c) 100 nm (d) 125 nm and (e) 165 nm. 114
5.20 Comparison of angular dependence of M_r/M_s between films grown at sputtering power of (a) 75 W and (b) 150 W. 114
5.21 Comparison of magnetostriction constant, λ_s between FeCo and FeCoCr as function of film thickness at fixed sputtering power 75 W. The data point and error bars represent the average of λ_s from a number of measurements on the same sample, respectively. 116
5.22 Magnetostriction constant, λ_s of FeCoCr against sputtering power with each film has thickness 100 nm. The data point and error bars represent the average of λ_s and the standard error of a number of measurements on the same sample, respectively. 117

6.1 Plot of element concentrations determined in fabricated sample based on number of Cr target used. 122
6.2 The XRD diffraction pattern of films at varied Cr percentages with thickness of samples, $t = 65$ nm. 124
6.3 Normalised magnetization at easy and hard axes for representative FeCoCr film at varied Cr compositions. 125
6.4 Angular dependence of remanence ratio, M_r/M_s of FeCoCr varying Cr concentrations showing a strong uniaxial anisotropy. 126
6.5 The dependence of the average of coercive and saturation fields of FeCoCr against Cr compositions with the error bars represent the standard error of three different samples. 128
6.6 The average of anisotropy field, H_k of FeCoCr films as a function of Cr concentration determined from hard axis loops measured on the MOKE magnetometer with the error bars indicate measurement of three different samples. 129
6.7 The magnetisation (M-H) curves of FeCoCr at varied composition measured at room temperature. 130
6.8 The average saturation magnetisation of FeCoCr measured by the SQUID-VSM and error bars indicate the standard error of three different samples. Also shown in the graph the calculated value of the anisotropy constant, K_u and the error bars as a function of Cr concentrations. 130
6.9 The dependence of the average magnetostriction constant, λ_s on the Cr percentages with the error bars represent a different number of measurements on the same samples. 132
6.10 Ferromagnetic spectra from reflection data, S_{11} of the representative sample of the FeCo at.2.6% Cr. The raw data with the fits to (a) real part of response and (b) imaginary part of response. The data then fitted to extract the resonant frequency and the linewidth. 133

6.11 The curves of FMR frequency (S_{11}) fitted by Kittel's formula in obtaining the H_k and M_s at varied Cr concentration (a) 2.6% (b) 5.6% (c) 7.2% (d) 9.6% Cr compositions. 134
6.12 The average of anisotropy field, H_k determined from VNA-FMR fitting line as a function of Cr concentrations. The error bars shows standard error determined from three different samples. 135
6.13 Saturation magnetization of FeCoCr films as a function of Cr concentration measured by two different techniques; VNA-FMR (blue) and SQUID-VSM (red).The error bars represent the standard errors measured from three different samples. 135
6.14 The fitted FMR linewidth for samples at varies Cr concentration showing the dependencies on the frequency (a) 2.6%, (b) 5.6%, (c) 7.2% and (d) 9.6%. 137
6.15 The repeatable measurement of FMR linewidth fitting allowing the extraction of the damping constant, α of C1 = 2.6%, C2 = 5.6%, C3 = 7.2% and C4 = 9.6%. The point represent a single measurement and the error bars indicate the standard error from each fitting. 138
6.16 The dependence of the average damping constant, α_{ave} on the Cr concentrations of films with a similar thicknesses, 65 nm with the data point and the error bars represent the average value of damping and standard errors from three different samples, respectively. 139
6.17 Damping parameter, α as a function of $Fe_{41}Co_{45}Cr_{14}$ film thickness grown with magnetic field at sputtering power of 75 W. The error bars shows the standard error determined from the fitting. 140
6.18 Ranges of soft magnetic thin films reported in the literature with the saturation induction, $\mu_0 M_s$ and the coercivity, H_c. The plot also presenting the magnitude of saturation magnetisation of Permendur (FeCo), Permalloy (NiFe) and $Fe_{49}Co_{49}V_2$ in bulk (shown by ** symbols) and the measured FeCoCr thin films with varied Cr concentration presented in this study [29,71,89,91,186,204-209]. 141

7.1 Graph of force versus displacement on the FeCo films at different thickness that involved 25 cycles of indenter with maximum of force, 13000μN was applied. 146
7.2 Graph of the average hardness, H_r as a function of displacement for the Si substrate with thickness 360 μm with the error bars are the standard errors from a series of nanoindentation. An abrupt increase in hardness at low penetration depth is observed. 148
7.3 Graph of the average reduced modulus of elasticity, E_r of Si substrate as a function of contact depth with the error bars are the standard errors from a series of nanoindentation. 148
7.4 The average hardness, H_r against the displacement, h_c of FeCo at thickness 431 nm, 603 nm and 758 nm. The graph also presenting the average hardness for Si substrate at thickness 360 μm.The error bars in each plot represent the standard errors from a series of nanoindentation. 150
7.5 Plot of the average reduced modulus of elasticity, E_r of the different thicknesses of FeCo and the average reduced modulus of Si substrate as a function of displacement.The error bars in each plot represent the standard errors from a series of nanoindentation. 151

7.6 Plot of Young's modulus, E_Y calculated from the measured of reduced modulus showing that the magnitude of E_Y have less influenced on film thickness. 151
7.7 The average hardness, H_r as function of displacement for FeCoCr at varies Cr concentrations at.2.6% (604 nm), at.5.6% (590 nm), at.7.2% (600 nm),and at.9.6% (601 nm) from a series of nanoindentation. 152
7.8 The average reduced modulus of elasticity, E_r as function of displacement for FeCoCr at varies Cr concentrations at.2.6% (604 nm), at.5.6% (590 nm), at.7.2% (600 nm),and at.9.6% (601 nm) from a series of nanoindentation. 153
7.9 Young's modulus, E_Y of FeCoCr films at varied Cr concentrations as a function of tip displacement. 153
7.10 AFM images on the surface roughness demonstrating different microstructure between FeCo and FeCoCr films. Scan size 5μm x 5μm. 155
7.11 XRD profiles showing different structure between selected thick of FeCo and FeCoCr films. 155
7.12 The average of elastic recovery, h_e of FeCoCr films as a function of Cr concentration 157
7.13 Comparison of a load-displacement curves between the FeCo (603 nm) and FeCoCr at.%9.6 (601 nm) films presenting that the elastic recovery, h_e of FeCoCr is slightly higher than the FeCo film. The h_e is calculated from the difference between the maximum displacement, h_{max} and the final depth, h_f. 157
7.14 The images of a cross-section analysis (on the bottom) and 3D view (on the top-right) showing a small pile-up has occurred on FeCo film thickness 758 nm after indentation with load of 13 mN. Data scale is 200 nm with the scan size of 19 μm x 19 μm. 159
7.15 The images of a cross-section analysis (on the bottom) and 3D view (on the top-right) showing a significant pile-up has occurred on FeCoCr film at.% 2.6 Cr after indentation with load of 13 mN. Data scale is 200 nm with the scan size of 19 μm x 19 μm. 160
7.16 The images of a cross-section analysis (on the bottom) and 3D view (on the top-right) showing a significant pile-up has occurred on FeCoCr film at.% 9.6 Cr after indentation with load of 13 mN. Data scale is 200 nm with the scan size of 19 μm x 19 μm. 161
7.17 The plot of strain-stress curves of FeCo and FeCoCr determined from a representative of indentation. 162
7.18 The representative of stress-strain curve of FeCoCr film at.% 9.6 Cr from microindentation using spherical tip (19 μm) with load applied of 100 mN. In the plot showing an estimation of a yield point by a linear fit of elastic region as shown in inserted graph. 163
7.19 The graph of average yield strength, σ_y measured from strain-stress curves. 164

List of Tables

3.1 Magnetostriction constants of some materials from previous studies. . . . 45
3.2 Magnetic damping constant, α of ranges of thin film materials. 52

5.1 Lattice parameters and FWHM values with respect to BCC peaks in FeCo and FeCoCr films. 96
5.2 The atomic percentages of Fe, Co and Cr for various sputtering power. . . 100

6.1 Concentrations level of Fe, Co and Cr in atomic percentage (at.%) determined by EDX Spectroscopy. 122
6.2 The magnetic parameters of FeCoCr at varied compositions determined by MOKE and SQUID-VSM. 129

7.1 The mechanical parameters of FeCo and Si at different thickness determined from the nanoidentation with E_r: reduced modulus of elasticity; H_r: hardness; E_Y: Young's modulus. 154
7.2 The calculated of elastic recovery, h_e from the difference between the parameter of the contact depth at the maximum load, h_{max} and the final contact depth, h_f taken from the part of an unloading curve. 156

Symbols

Roman

a	Lattice constant
a_0	Bulk lattice constant
A	Exchange stiffness
d	atomic distance
d_{hkl}	Crystallograhic plane
D	Grain size
E_a	Magnetocrystalline energy
E_c	Thermal energy
E_{el}	Magnetoelastic energy
E_{ex}	Exchange energy
E_f	Young's modulus of film
E_{ms}	Magnetostatic energy
E_r	Reduced modulus of eleasticity
E_s	Young's modulus of substrate
E_Y	Young's modulus of film
E_Z	Zeeman energy
f_{FMR}	FMR resonance frequency
H_r	Hardness
H_{app}	Applied field
H_c	Coercive field
H_d	Demagnetizing field
H_{eff}	Effective field
H_k	Anisotropy field
H_0	Inhomogeneity broadening

H_s	Saturation field
H_W	Molecular field
I_0	Incident of light intensity
k_B	Boltzmann constant
K	Anisotropy constant
K_u	Uniaxial anisotropy constant
K_σ	Stress anisotropy constant
$K_{\alpha 1}$	X-Ray wavelength
L_{ex}	Exchange length
M_{eff}	Effective magnetisation
M_r	Remanence magnetisation
M_s	Saturation magnetisation
N_d	Demagnetizing factor
Pd	Target-substrate distance
R	Bending radius
R_a	Surface roughness
R_{ms}	Root-mean square
S	Stiffness
t_f	Thickness of film
t_s	Thickness of Substrate
T_C	Curie temperature
T_d	Deposition temperature
T_m	Melting temperature
T_N	Néel's temperature
T_s	Substrate temperature

Greek

α	Damping constant
α_{int}	Intrinsic damping constant
α_{rad}	Radiative damping constant
α_{sp}	Spin-pump damping constant
$\alpha_{T,f}$	Thermal expansion coefficient of film
$\alpha_{T,s}$	Thermal expansion coefficient of substrate

Symbol	Description
$\alpha_1, \alpha_2, \alpha_3$	Direction cosines of magnetization
$\beta_1, \beta_2, \beta_3$	Direction cosines of magnetostriction is measured
χ	magnetic susceptibility
ε	Strain
γ_G	Gyromagnetic ratio
γ	Molecular field constant
λ	X-Ray wavelength
λ_{eff}	Effective magnetostriction
λ_s	Saturation magnetostriction
$\lambda_{s/i}$	Surface magnetostriction
λ_v	Volume magnetostriction
λ_{100}	Saturation magnetostriction along $< 100 >$ direction
λ_{111}	Saturation magnetostriction along $< 111 >$ direction
μ	Absorption coefficient
μ_0	permeability of free space
μ_B	Bohr magnetron
ν_f	Poisson's ratio of film
ν_s	Poisson's ratio of substrate
σ_i	internal stress
σ_y	Yield strength
ω	glancing angle

Abbreviations

AFM	Atomic Force Microscopy
AG	Auger Electron
BCC	Body-Centered Cubic
BF	Bright-Field
BSE	Back Scattered Electron
CVD	Chemical Vapour Deposition
DC	Direct Current
DF	Dark-Field
DUT	Device Under Test
EDX	Energy Dipersive X-Ray
FCC	Face-Centered Cubic
FIB	Focused-Ion Beam
FMR	Ferromagnetic Resonance
FWHM	Full Width Half Maximum
GA-XRD	Glancing Angle X-Ray Diffraction
HRTEM	High Resolution Transmission Electron Microscopy
LPCVD	Low-Pressure Chemical Vapour Deposition
MagMEMS	Magnetic Microelectromechanical Sensor
MOCVD	Metalorganic Chemical Vapour Deposition
MOKE	Magneto-Optical Kerr Effect
MRAM	Magnetic Random Access Memory
PECVD	Plasma-enhanced Chemical Vapour Deposition
PVD	Physical Vapour Deposition
RAM	Random Anisotropy Model
RF	Radio Frequency

SE	Secondary Electron
SEM	Scanning Electron Microscopy
SMFMR	Strain-Modulated Ferromagnetic Resonance
SPM	Scanning Probe Microscopy
SQUID	Superconducting Quantum Interference Device
TEM	Transmission Electron Microscopy
VNA	Vector Network Analyzer
VSM	Vibrating Sample Magnetometer
XRD	X-Ray Diffraction

Chapter 1

Introduction

1.1 Soft Magnetostrictive Materials

Numerous studies on different magnetostrictive materials have been reported up to the present [1–6] as they have shown outstanding properties for applications, for instance, they have been used for magnetic microelectromechanical (MagMEMs) sensor and actuators applications, such as magnetic field sensor [7, 8], SONAR transducer [9], energy harvester [10] and health monitoring [11] . It has also been reported that magnetostrictive materials with high magnetostriction, low damping and narrow resonance linewidth are suitable candidates for microwave and spinwave device applications as well as magnetic random access memory (MRAM) [12]. The first magnetostriction study was conducted by Joule in 1840 who had found that iron (Fe) changed its length when subjected to a magnetic field [13]. In the early 1960's Clark and his co-workers [14] worked on the rare-earth elements terbium (Tb) and dysprosium (Dy) at low temperature (78 K) exhibited giant magnetostriction more than $\lambda = 1000$ ppm. As the high magnetostriction of these single elements was not possible to be achieved at room temperature in particular for devices application, these two elements were mixed with other elements such as Ni, Co or Fe to form alloy with high magnetostriction at 300K. It has been shown that the magnetostriction of a single crystal Terfenol-D (Tb-Dy-Fe) can be as high as 2000 ppm [15]. Due to the cost production of Tb and Dy are very expensive, researchers started working on finding new materials which are more cost effective but still have large magnetostriction. Galfenol (Fe-Ga) has received great interest as an alternative to Terfenol-D because it is more ductile and has better mechanical properties at low

fields. It has been reported that the magnetostriction of Fe-Ga at room temperature was ten fold (λ = 300 ppm) than that of Fe when a compressive stress up to 120 MPa was applied [16].

To date, soft amorphous magnetic materials have drawn wide attention among material scientist as they show promising properties notably for high frequency applications [17]. Compared to soft crystalline materials, soft amorphous materials have higher resistivity, which reduces eddy current losses [18]. In addition, these materials not only exhibit low energy losses but also low coercivity, large saturation magnetisation and high permeability, so become excellent candidates that can be used in data storage [19] as well as in MagMEMs devices [20, 21]. Soft magnetic materials with these properties include, SiFe, Metglas (FeSiB), Permalloy ($Ni_{80}Fe_{20}$) and Permendur ($Fe_{50}Co_{50}$). Many studies have focused on FeCo-based materials (Fe-Co-Nb, Fe-Co-Tb, Fe-Co-Ga) either in bulk or thin films [3, 22] due to their remarkable properties (higher saturation magnetization, high Curie temperature and larger magnetostriction) compared to other soft materials. A study reported that the magnetostriction of bulk at equiatomic Fe–Co ($Fe_{50}Co_{50}$) had a magnetostriction of 60 ppm [23], while it has been reported that increasing Co content up to 75 at.%, a magnetostriction as high as 108 ppm was achieved [24] for the bulk FeCo alloyed. Soft amorphous properties in thin films however, offers more advantages over the bulk materials [25] as they are economical and easy to design so are compatible to the processing technologies for miniaturization of MEMs devices [26]. Despite its advantages, these materials have drawbacks particularly for the as-deposited films which are associated with a large coercive field; more than H_c=10 kAm^{-1} [27]. The ideal soft magnetostrictive material for MagMEMs actuators devices with high performance under low magnetic fields needs not only a high magnetostriction constant ($\lambda > 20$ ppm) but also a lower coercive ($H_c < 10$ kAm^{-1}) and anisotropy fields ($H_c < 15$ kAm^{-1}).

The main goal of this research is to investigate a new FeCo-based soft amorphous magnetostrictive material. Although many researchers have studied the magnetostriction of FeCo, research on soft magnetostrictive properties of Fe-Co-Cr thin films has not been studied comprehensively to date. Studies have been reported that adding an antiferromagnet element such as Cr can result in higher magnetostriction i.e at 61 ppm for 30 wt.% Cr and 15 wt.% Co in a bulk sample. However, the coercivity of this sample was not reported and therefore it was unclear whether the required soft magnetic properties were present in the optimised films [28]. Further work also found that soft magnetic

properties were achieved in FeCo films with coercivity as low as 748 Am^{-1} by adding 20 at.% Cr, nevertheless no magnetostriction data were given [29]. Similarly the magnetostrictive properties of $(\mathrm{Fe}_{54}\mathrm{Co}_{46})_{1-x}\mathrm{Cr}_x$ thin films were not included in the reported literature [30]. Thus alloying the FeCo with the non-magnetic element of Chromium (Cr), along with controlling the fabrication growth conditions it is expected that soft amorphous magnetostrictive properties can be achieved that are suitable for MagMEMs at low field sensing and high frequency applications. In addition to the magnetic studies, the mechanical properties of Fe-Co-Cr films will be also investigated using the nanoindentation method, to determine whether the mechanical strength of FeCo can be improved by adding Cr. Moreover, Young's Modulus of FeCoCr film itself can be used to calculate the magnetostriction constant more precisely. To achieve those objectives, several questions have arisen and need answers:

(a) Do the growth conditions, for instance, the application of a magnetic field during fabrication, sputtering power, film thickness, have a significant effect on the structural properties and magnetostriction constant of the FeCo and FeCoCr films?

(b) Can Cr reduce the coercive and anisotropy fields, hence improve the soft magnetostrictive properties of the FeCo films?

(c) How much percentages of Cr that can be added into FeCo to achieve the ideal soft magnetic properties; $H_c < 10$ kAm^{-1}, $H_k < 15$ kAm^{-1}, $\lambda_s > 20$ ppm and magnetic damping constant $\alpha \leq 0.0100$ of FeCoCr films?

(d) Does the addition of Cr improve the mechanical properties such as the hardness, Young's Modulus and the yield strength, σ_y of the FeCo films?

1.2 Thesis Outline

This thesis is organized into eight chapters as follows:

Chapter 2 begins with the theoretical background on magnetic materials and the magnetic energies associated in ferromagnetic materials. The cornerstone of these energies are crucial in order to understand what contributes to the existence of domains in ferromagnetic materials. This PhD study also needs to determine the damping constant for soft FeCoCr films, thus a description of Gilbert damping from Landau-Lifshitz-Gilbert

(LLG) equation and the mechanisms of damping are given as well. The last section of this chapter will outline the origins of magnetostriction and its equation related to the different types of materials.

Chapter 3 presents a literature review on magnetostriction focusing on FeCo-based materials. It reviews the structural, magnetic properties and magnetostriction studies carried out and it is split into sub-sections highlight to different factors which influence these properties, such as composition, heat treatment, multilayer films, combination of a third element as well as the growth conditions. Magnetostriction studies on the rare-earth elements and other materials have also been reviewed in this chapter. The mechanical studies on FeCo and other magnetic materials also have been reviewed at the end of this chapter.

The experimental techniques both film fabrication (RF Magnetron Sputtering) and sample characterizations (Atomic Force Microscopy, Scanning Electron Microscopy with Energy Dispersive X-Ray, X-Ray Diffraction, Magneto-Optical Kerr Effect, Vector Network Analyzer-Ferromagnetic Resonance, Transmission Electron Microscope and Nanoidentation) along with the fundamentals behind each techniques are explained in detail in Chapter 4.

The main parts which contributes to the most of the thesis is the results chapters, which provide the answers to the questions mentioned above. These are structured into three chapters: Chapter 5 demonstrates the characterization of FeCo films fabricated with varied thickness and the effect of magnetic field and no magnetic field during sample deposition. Results on the structural, magnetic and magnetostriction studies of FeCoCr films under different thickness and sputtering power are discussed in this chapter.

Chapter 6 is devoted to the results of the role of Cr on the structural, morphology and magnetostrictive properties in various composition of FeCoCr. This chapter aims to determined whether the magnetic and structural properties of the film have dependencies on the Cr compositions. Magnetic studies by means of Ferromagnetic Resonance (FMR) to define the damping constant and the magnetization are given in this chapter. At the end of this chapter, a comparison between various types of soft magnetic materials which have been studied by other researchers and the soft FeCoCr are presented, in terms of their saturation induction, $\mu_0 M_s$ and the coercive field, H_c.

Chapter 7 presents a study of mechanical properties of FeCo and FeCoCr films for different thicknesses (more than 400nm) by nanoidentation. This chapter provides the information on the hardness, Young's Modulus and the Yield strength of the FeCo and FeCoCr films since there is a lack of the information on the mechanical strength specifically for these materials.

The summary of this research is drawn in the final Chapter 8 accompanied by proposed future work.

Chapter 2

Theoretical Background

This chapter describes an overview of different magnetic materials and magnetization process in ferromagnetic materials which are associated with different magnetic energies (magnetocrystalline, magnetostatic, magnetoelastic, exchange and Zeeman). The factors which influence the magnetic anisotropy in crystalline and amorphous magnetic materials also presented in this chapter. It is then followed by the principles of magnetostriction and magnetization dynamics which are related to the extraction of magnetic damping.

2.1 Classification of Magnetic Materials

Susceptibility, χ is property of material, referred to as the ratio of magnetization to applied field which for ferromagnetic material has a temperature dependence based on the Curie- Weiss Law (described in the later subsection). In general, diamagnetic materials have χ = - 10^{-6} to -10^{-5} and their magnetic response to the applied field is in the opposite direction. For both paramagnetic and antiferomagnetic materials, $\chi = 10^{-5}$ to 10^{-3}. While the ferromagnetic and ferrimagnetic have similar magnitude; $\chi = 10^{1}$ to 10^{3} [31, 32]. Magnetic materials can be distinguished by their magnetic moments and their arrangements as depicted in Figure 2.1. In paramagnetic materials (Figure 2.1a), moments are disordered which results in zero magnetization. For antiferromagnetic materials, the individual magnetic moments are aligned anti-parallel, thus cancelling each other, so the total magnetization is also zero. The magnetic moments in ferromagnetic

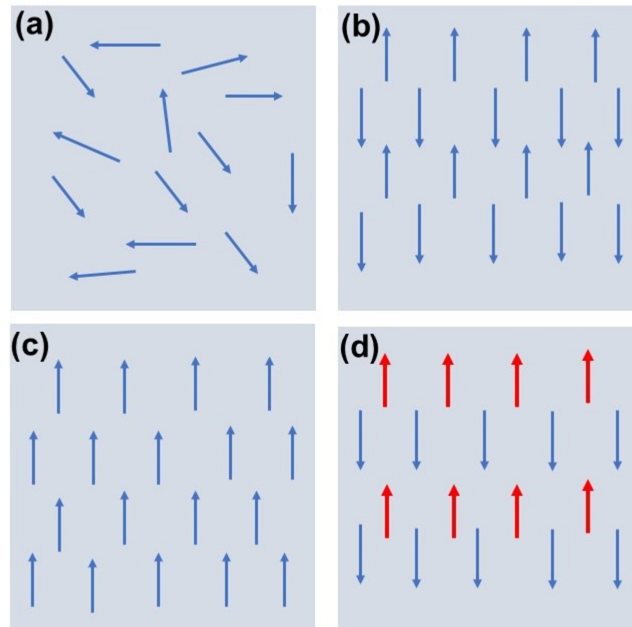

Figure 2.1: The arrangement of magnetic moments in (a) paramagnet (b) anti-ferromagnet (c) ferromagnet (d) ferrimagnet. Figure adapted from [33].

substances shown in Figure 2.1c have a large net magnetization as result of the magnetic moments aligned parallel to each other. Meanwhile in a ferrimagnetic material, there are two sub-lattices of magnetic moments, with different size moments indicated by two different arrow lengths, but in opposite directions as given in Figure 2.1d. This group of material also have net magnetization with large positive susceptibility, but not as strong as ferromagnetic materials.

2.1.1 Temperature Dependence of Magnetic Materials

Susceptibility, χ of ferromagnetic material has a temperature dependence, when the temperature is changed, the thermal energy of the magnetic moment changes. The susceptibility is defined as the ratio of magnetization (M) to the applied field, (H_{app}). Temperature variation of susceptibility, χ for paramagnetic material is given by the Curie's Law [32]:

$$\chi = \frac{M}{H_{app}} = \frac{C}{T} \tag{2.1}$$

In ferromagnetic materials, Weiss postulated that there is an internal interaction between the localized moments, called a "molecular field", H_W. He suggested that the H_W

is a mutual interaction between the electrons which makes the magnetic moments in the same directions to each other. It is assumed that, H_W is linearly proportional to magnetization, M:

$$H_W = \gamma M \tag{2.2}$$

where γ is molecular field constant. Thus, the total field is from both applied field, H_{app} and molecular field, H_W ($H_{tot} = H_{app} + H_W$).

By substituting H_{tot} into Equation 2.1, the χ can be written as:

$$\chi = \frac{M}{H_{app} + \gamma M} = \frac{C}{T} \tag{2.3}$$

or by rearranging the above equation, it becomes:

$$M = \frac{CH_{app} + C\gamma M}{T} \tag{2.4}$$

therefore, the susceptibility of ferromagnetic material can be expressed by:

$$\chi = \frac{M}{H_{app}} = \frac{C}{T - \gamma C} = \frac{C}{T - T_c} \tag{2.5}$$

where γC called as Curie point or Curie temperature, T_C. The Equation 2.5 is well known as Curie-Weiss Law. When temperature is increased beyond T_C, ferromagnetic behaviour will disappear and change to paramagnetic behaviour. For antiferromagnetic materials, the Curie-Weiss on temperature dependence of χ can be shown by Néel's temperature, T_N where the two sub-lattices arrange anti-parallel to each other:

$$\chi = \frac{C}{T + T_N} \tag{2.6}$$

2.2 Magnetization Process and Magnetic Energies

The initial magnetization process of a ferromagnetic material and the domain theory was postulated by Weiss in 1907 [34]. The magnetization of a ferromagnetic material varies from zero to the saturation value and this phenomena can be explained by the existence of small regions called domains. Domains are the regions in ferromagnetic substance in

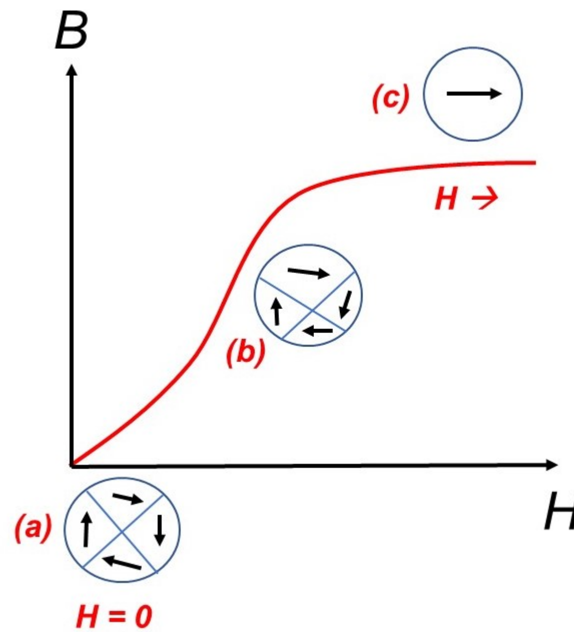

Figure 2.2: The initial curve of hysteresis and the growth of domains in ferromagnetic material when magnetic field is applied. Figure adapted from [33].

which magnetic moments are uniform. In demagnetized state of ferromagnetic materials, domains have different orientations hence the total of magnetization is zero. When a sample magnetized, all domains are aligned parallel to each other. The variation of domain directions when no external field and a small magnetic field is applied until the saturation point is achieved can influence the hysteresis curve of ferromagnetic material. The initial curve of hysteresis and the growth of domain in response with applied field is illustrated in Figure 2.2. When no external field is applied at point (a) (undemagnetized state), domains are randomly oriented, and the overall magnetization is zero. When the magnetic field is gradually increased at point (b), the domains start to grow. The domains closest to the direction of magnetic field will expand more than the other domains. The expansion of domains is accompanied by the domain wall movement. As the magnetic field increases, all the domains walls are removed, leaving a single domain as shown at point (c). At this point, the saturation magnetization has been achieved whereby the domain pointing in the same direction as the external applied field [33]. In ferromagnetic materials, the magnetisation process involves the minimisation of the total energy in magnetic system. The contributions to the total energy are from magnetocrystalline anisotropy, magnetostatic energy, Zeeman energy, exchange energy and magnetoelastic energy [35]. These energies will be described in the following subsections.

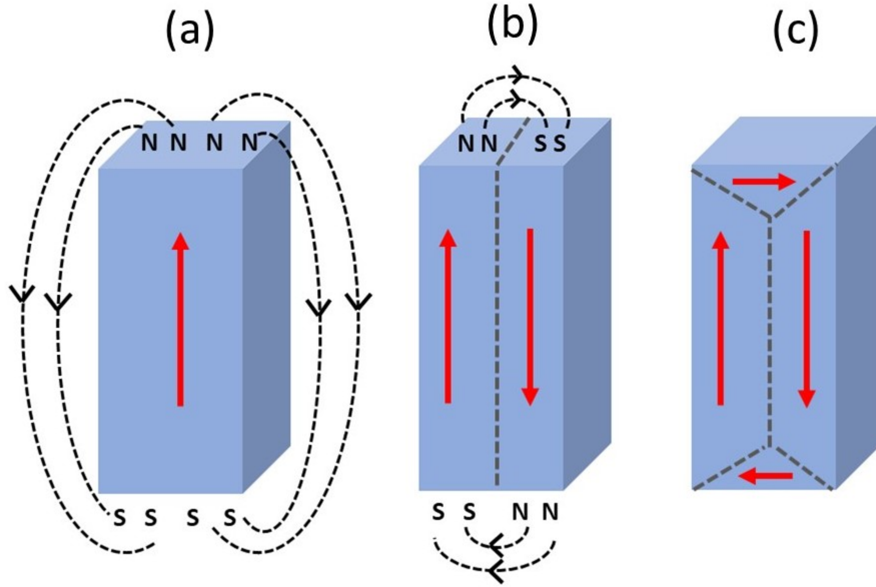

Figure 2.3: The existence of magnetic dipole on the surface (a) and (b). The magnetostatic energy, E_{ms} is minimised when the closure domain is formed (c) as disappearance of magnetic dipole on the surface. Figure adapted from [33].

2.2.1 Magnetostatic Energy

The energy of system which associated with its own demagnetizing field, H_d is called magnetostatic energy, E_{ms}. This field acts in opposite direction to the sample's magnetization, M. It depends on the shape and geometry of the specimen and can be described as H_d = - N_d M, where N_d is the demagnetizing factor [33]. The magnetostatic energy of ferromagnetic material with known shape and geometry can be written by:

$$E_{ms} = \mu_0 N_d \int M.dM = \frac{\mu_0}{2} N_d M^2 \tag{2.7}$$

Figure 2.3 shows how the magnetostatic energy can be reduced by formation of domain. Consider a ferromagnetic material with an external field and its own demagnetizing field, H_d shown in Figure 2.3a. In this case, the magnetostatic energy is larger. The magnetostatic energy for this material can be reduced with two domains shown in Figure 2.3b, hence, its demagnetizing field reduced. In order to reduce the magnetostatic energy to zero, a closure domain with no magnetic poles at the surface is formed as shown in Figure 2.3c [33].

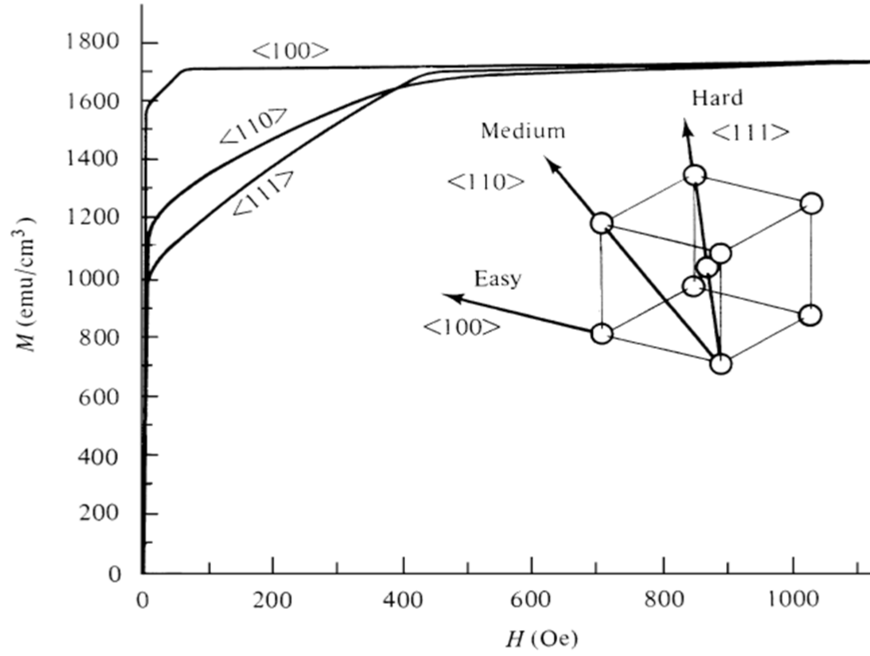

Figure 2.4: Magnetization of Fe in easy $< 100 >$ and hard axes $< 111 >$ [36].

2.2.2 Magnetocrystalline Energy

Another energy which contributes to the total energy in a ferromagnetic material is the magnetocrystalline anisotropy E_a. The magnetisation of a magnetic material depends on the crystal structure, due to the magnetic moments oriented to a certain crystal direction called the easy axis. This energy exists due to the interaction of the magnetisation with the crystal lattice, which occurs via the orbital overlap of electrons called spin-orbit coupling. In the case of iron (Fe) which has a cubic crystal structure as presented in Figure 2.4 the magnetization is favourable along $< 100 >$ direction.

The magneto-crystalline anisotropy energy of the cubic anisotropy as a series expansion of the direction cosines (α_1,α_2, α_3,etc) can be expressed by the following equation [36]:

$$E_a = K_1(\alpha_1^2\alpha_2^2 + \alpha_2^2\alpha_3^2 + \alpha_1^2\alpha_3^2) + K_2(\alpha_1^2\alpha_2^2\alpha_3^2) + ... \tag{2.8}$$

Where K_1 and K_2 for Iron at room temperature are K_1 = 4.8 x 10^4 J/m^3 and K_2 = -1.0 x 10^4 J/m^3. While, for Cobalt which has uniaxial anisotropy, the easy axis lies along the hexagonal $< 0001 >$ c axis (Figure 2.5) and the anisotropy energy is depends on the

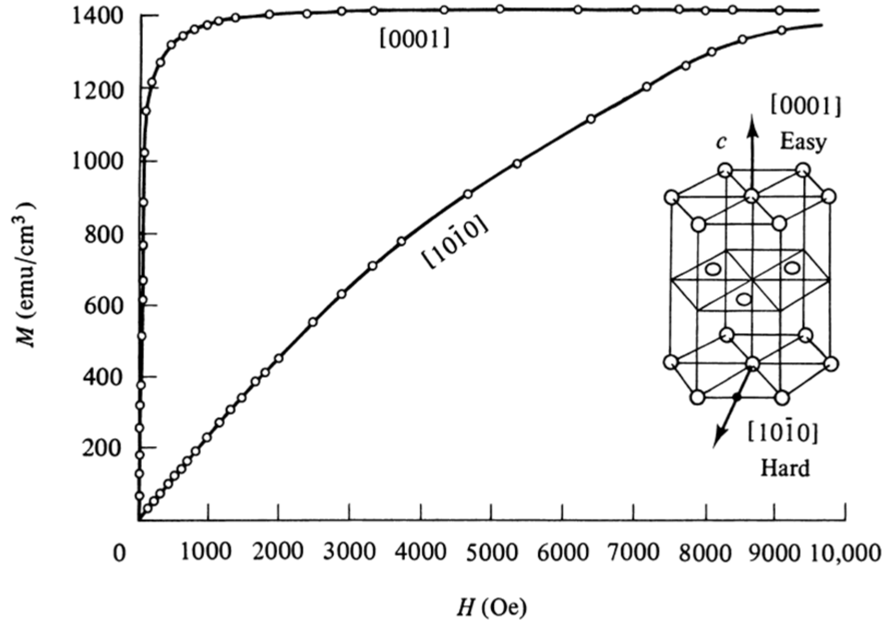

Figure 2.5: Magnetization of Co in easy $< 0001 >$ and hard axes $< 1010 >$ [31].

angle, θ between magnetization vector and easy direction. The expression of uniaxial anisotropy in this case is given by :

$$E_a = K_1 \sin^2\theta + K_2 \sin^4\theta + ... \tag{2.9}$$

with the uniaxial anisotropy constants of Co at 15^0C are $K_1 = 4.53$ x 10^5 J/m^3 and K_2 = 1.44 x 10^4 J/m^3 [37].

2.2.3 Exchange Energy

Exchange energy E_{ex} can be described as a result of interaction between two neighbouring spins and this energy tends to keep these adjacent spins parallel to each other. The exchange energy, E_{ex} between two spins S_i and S_j can be expressed by the following equation [33]:

$$E_{ex} = -2J_{ex}\vec{S_i}.\vec{S_j} = -2J_{ex}S_iS_j\cos\theta_{ij} \tag{2.10}$$

where J_{ex} is the exchange integral and θ_{ij} is the angle between two spins. J_{ex} can be positive or negative whether the spins align parallel (ferromagnetic) or anti-parallel (antiferromagnetic).

This energy can be related directly to the Curie temperature, T_C based on the thermal energy per moment, $3k_BT$. The alignment of magnetic moment is destroyed when the thermal energy per moment is equal or above the exchange energy per magnetic moment. This is reflected by the transition from ferromagnetic to paramagnetic state . From this relationship, one can estimate the exchange energy per moment for given material with known T_C. For instance, Iron at T_C = 1043 K the E_{ex} = 4.3 x 10^{-20} J ; while Cobalt at T_C = 1404 K thus E_{ex} = 5.8 x 10^{-20} J [31].

2.2.4 Magnetoelastic Energy

In the absence of stress, the magnetocrystalline anisotropy is dominant, but when the material is subjected to stress, the magnetization directions is depends on both the anisotropy, K and the stress, σ. For isotropic materials have a saturation magnetostriction, λ_s the magnetoelastic energy can be written as [36]:

$$E_{me} = \frac{3}{2}\lambda_s \sigma \sin^2 \phi \tag{2.11}$$

where ϕ is represents the angle between the magnetization and the stress, σ. The equation 2.11 can be related by stress anisotropy energy, which is also magnetoelastic energy:

$$E_{me} = K_\sigma \sin^2 \phi \tag{2.12}$$

where K_σ is anisotropy constant and equal to $\frac{3}{2}\lambda_s\sigma$.

2.2.5 Zeeman Energy

Another contribution to total energy comes from the Zeeman energy, E_z which is the interaction between magnetization and the external field. This energy can be minimized when the magnetization is in the direction of the applied field. By applying an external field parallel to magnetization, M, the domain wall will move and increasing the size

of domain. Then eventually the domain, which opposed the field will disappear. This energy in the presence of external field, H_{ext} for a volume of sample, V is given by:

$$E_Z = -\mu_0 \int_V M.H_{ext} dV \tag{2.13}$$

2.3 Magnetization Damping

Magnetisation damping in ferromagnetic materials involves dissipation of energy via the transformation of energy from the macroscopic motion of the local magnetisation field into microscopic thermal motion [38]. The energy dissipation can be intrinsic (spin-orbit interaction) or extrinsic which associated to the defects and non-uniformity within a ferromagnetic system [39].

To describe magnetic damping, consider when a magnetic field, H is applied to ferromagnetic material, the magnetic moment experiences a torque, τ and magnetic moment tends to align with the magnetic field. The torque exerted on the magnetic moment by a magnetic field is:

$$\tau = M \times H \tag{2.14}$$

Under strong damped conditions which magnetic moment strongly coupled with other moment, they will slowly rotate into the field direction. This precession process to align the magnetic moment parallel to the magnetic field is defined as magnetic damping or Gilbert damping, α which was successfully formulated by Gilbert [38]. The equation of precession motion for undamped magnetization was firstly introduced by Landau and Lifshitz [40] known as LL equation:

$$\frac{dM}{dt} = -\gamma M \times H_{eff} \tag{2.15}$$

Here H_{eff} is effective field contributions of external field, demagnetization, exchange, anisotropy and magnetoelastic ; γ_G is refer to gyromagnetic ratio of electron ($\gamma < 0$). Gilbert then came up with the solution on the LL equation by adding the terms for

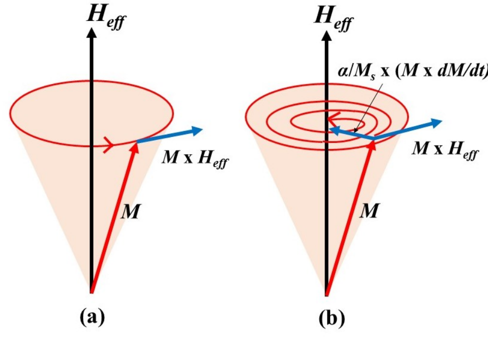

Figure 2.6: (a) The precession motion of magnetization based on Landau-Lifshitz (b) The additional term of damping proposed by Gilbert showing the magnetization in the direction of external magnetic field. Figure adapted from [41].

damped motion and later the equation known as Landau-Lifshitz-Gilbert (LLG equation) as given below:

$$\frac{dM}{dt} = -\gamma M \times H_{eff} + \frac{\alpha}{M_s}\left(M \times \frac{dM}{dt}\right) \tag{2.16}$$

where α is dimensionless which describes how fast the precession motion dampens. The LL and LLG equation due to the damping are described in Figure 2.6. This parameter can be used depending on how large or small it is for switching application for instance, in spin-transfer switching devices a low damping constant is required [42]. The intrinsic Gilbert damping originates from spin-orbit coupling [43] and also can arise from the extrinsic contributions. These include two magnon scattering and inhomogeneity broadening in magnetic structure. In two magnon (quantized spin waves) scattering, the damping increases when the ferromagnetic resonance (FMR) linewidth is increases. Such scattering occurs when the magnons having wavevector of $\kappa = 0$ are excited to degenerate states, $\kappa \neq 0$ [44]. This mechanism depends on crystal defects as the crystal symmetry near the defects is broken leading to the two magnon scattering [45, 46]. Another contribution to the magnetic damping is the inhomogeneity, which is independent to frequency. This is can be shown by the expression below :

$$\Delta H = \Delta H_0 + \frac{4\pi\alpha f}{\gamma} \tag{2.17}$$

where ΔH_0 is the inhomegeneity contribution to the linewidth. It is believed that, the inhomogeneity is associated with the variation in anisotropy [47] and the surface and

interface roughness [48]. The second term in above equation is presents the intrinsic Gilbert damping constant which is dependent on the resonance frequency, f. The determination of damping constants in this present study by means of Vector Network Analyzer and Ferromagnetic Resonance will be explained further in the experimental technique section.

2.4 Magnetic Anisotropy for Amorphous Materials

Magnetic anisotropy from long-range order does not exist in the amorphous material as the atoms are randomly arranged. The magnetic anisotropy within the material however is related to the local random anisotropy which is averaged out as it varies with direction. The explanation of magnetic anisotropy for amorphous has been successfully addressed in the model called Random Anisotropy Model (RAM)[49], then later Herzer [18, 50, 51] adopted and extended that model for nanocrystalline materials as well. This model starts by characterizing the interaction between the local magnetic anisotropy oriented over the grain size, D and the exchange coupling by the free energy density :

$$\phi = A \sum_{i=x,y,z} (\bigtriangledown m_i)^2 + K_1 f_K(\underline{m}.\underline{u}) \tag{2.18}$$

where A = exchange stiffness; K_1 = local magnetocrystalline anisotropy; f_K = angular variation in the anisotropy energy respect to local symmetry axis, $\underline{u}$. The f_K is dimensionless; while $\underline{m}$ is the direction of the magnetization vector [51]. In this equation, if the magnetization direction changes on length L, the exchange energy scale is A/L^2. The exchange energy then would be greater than the local anisotropy energy ($A/L^2 > K_1$), if the local anisotropy length is smaller than the ferromagnetic exchange length:

$$L_0 = \phi_0 \sqrt{(A/K_1)} \tag{2.19}$$

where the L_0 represents the minimum length, where the magnetization is roughly constant despite the fluctuation of local anisotropy, whereby ϕ_0 is dimensionless parameter in order of one. The value of K_1 for a $3d$-based amorphous alloy is 5 x 10^4 J/m^3 and 10^6 J/m^3 for $4f$-rich alloys. Hence the exchange length for Fe-based alloys is in the range 20

nm to 40 nm [35, 51]. For both amorphous and nanocrystalline alloys, D is smaller than the local correlation length, L_0. With $D \approx$ atomic scale for amorphous and for $D \approx$ 5-20 nm for nanocrystalline. Consequently, the local anisotropy which orients randomly is averaged out over several units by the domination of the exchange interactions.

Consider for $D < L_0$, the magnetic anisotropy which is related to magnetization over the volume, $V_{ex} = L_{ex}^3$ and within this volume the magnetization is constant due to the exchange coupling. The schematic of the random of anisotropy model with local anisotropy K_1 over the volume (shown by the area in a grey color) and the exchange length, L_{ex} is illustrated in Figure 2.7. The results for the number of grains N, the average anisotropy constant can be shown by:

$$\langle K \rangle = \frac{K_1}{\sqrt{N}} = K_1.(D/L_{ex})^{3/2} \tag{2.20}$$

Thus, the easy axes for N grains randomly oriented which have magnetization favourable along these axis. Hence the exchange energy coupling will be A/L_{ex}^2. Substituting the $\langle K \rangle$ for K_1 in Equation 2.18, the exchange length therefore can be correlated to the average anisotropy:

$$L_{ex} = \phi_0 \sqrt{(A/\langle K \rangle)} \tag{2.21}$$

with ϕ_0 corresponds to both the symmetry of anisotropy and the angle between the easiest axes of the adjacent exchange interactions of the spins. By combining Equation 2.19 and 2.20, one can determine:

$$\langle K \rangle = K_1.(D/L_0)^6 \tag{2.22}$$

where L_0 is ferromagnetic exchange length as provided in Equation 2.18. It showed that the magnetic anisotropy of amorphous has dependence on the sixth power of grain size [18, 50, 51].

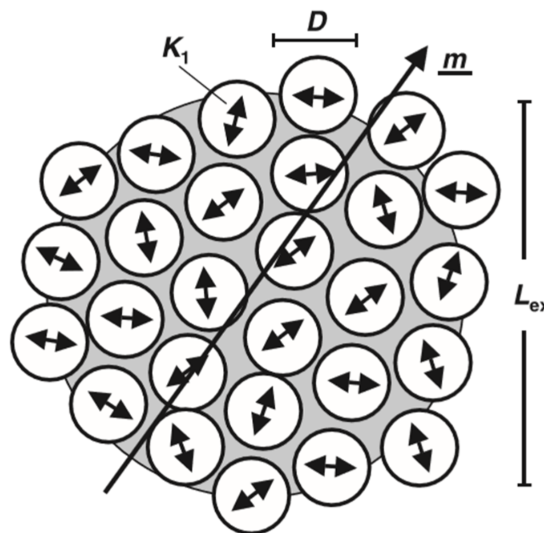

Figure 2.7: The random anisotropy model for amorphous showing that the correlation length, D is much smaller compare to the exchange length, L_{ex} [51].

2.5 Induced Anisotropy

To design magnetic materials for the needs of specific applications, it is possible to induce the magnetic anisotropy by appropriate methods. Induced anisotropy can purposely be achieved by methods such as annealing treatments or during the sample preparation [37]. There are several treatments, which can induce the anisotropy such as magnetic annealing (field annealing), plastic deformation, stress annealing and magnetic irradiation.

2.5.1 Magnetic Annealing

The induced anisotropy by magnetic annealing was discovered on the superlattice of Permalloy (Fe-Ni) alloy [52]. At 490^oC, this alloy was in order-disorder states, then at 500^oC the phase changed to the ordered phase whereby the anisotropy disappeared approaching the completely ordered state. Chikazumi [53] introduced the "directional order" which leads to the existence of induced anisotropy by magnetic annealing. Their specimens were heated in a furnace for about an hour then cooled in longitudinal magnetic field, 30 Oe. He explained that magnetic anisotropy due to the different atomic

pairs of Ni-Ni, Fe-Fe or Ni-Fe. The directional order described is similar to magnetocrystalline anisotropy arises from the spin-orbit coupling. There is magnetic interaction between the axis of like-atom pairs with the local magnetization, hence these two tends to be in the same directions. The atomic pairs interaction gives rise to the anisotropy when they were always pointing in the same direction. The anisotropy is the same as for materials which have uniaxial anisotropy.

2.5.2 Roll Anisotropy

The magnetic anisotropy can be induced by cold-rolling and this effect is also referred as roll magnetic anisotropy. This kind of anisotropy was observed in Fe-Ni (50:50) alloys. The Fe-Ni alloy (001) plane is cold-rolled with the direction of rolling [100]. A large magnetic anisotropy is induced after rolling to 50% thickness reduction. The mechanism of anisotropy induced in cold-rolling also can be caused by the directional order which there are an increased number of Fe-Fe and Ni-Ni neighbouring atoms which the applied field direction is perpendicular to the rolling direction. [33].

2.5.3 Stress Annealing

According to O'Handley [35], there are several mechanisms which occur when materials undergo stress upon heating. During annealing, materials under stress will either be elastically strained, or may undergo irreversible strain (creep), such that at certain annealing temperatures this leads to an easy magnetization. These mechanisms give rise to anisotropy. It is also possible to induce the anisotropy by placing the sample under stress and subsequently annealing below the crystalline temperature. After annealing, the sample is released, leaving the sample in a stress state [54].

2.6 Magnetostriction Principle

The phenomenon under which ferromagnetic materials change their dimensions when subjected to a magnetic field is known as the magnetostriction effect. Typically, the deformation is very small in magnitude of 10^{-5} to 10^{-6}. The first magnetostriction effect was discovered by James Joule in 1842 [13] and found that the Iron having positive and

negative magnetostriction constants (λ_{100} = 21 ppm ; λ_{111} = -21 ppm) depending on the crystal direction. Thus, a material can have positive and negative magnetostriction constants. The magnetostriction constant, λ is defined as the fractional change in length $\delta L'/L$ by the magnetic field. This effect occurs because of the rotation and reorientation of small magnetic domains, which cause internal strains. For positive magnetostriction, the strain is in the direction of magnetic field while for negative magnetostriction, the strain is opposed to the magnetic field. By applying a higher magnetic field, more domains have become aligned until it reaches saturation where at this point it is called saturation magnetostriction, λ_s [55].

The physical origin of magnetostriction can be explained by spin-orbit coupling as depicted in Figure 2.8. The arrows and black dots represent the net magnetic moments and atomic nuclei, respectively. There are two kinds of magnetostriction, which are spontaneous magnetostriction and field-induced magnetostriction. Above the Curie temperature, T_C the magnetic moments have completely a disordered arrangement. If the magnetic moments have very strong spin-orbit coupling below T_C, then spontaneous magnetostriction occurs and the spins and the electron clouds rotate into a particular orientation due to the crystal anisotropy. If the atomic nuclei are forced further apart, the spontaneous magnetostriction would be $\delta L'/L$. Field-induced magnetostriction occurs when a strong field is applied perpendicular to the spin direction, this results in the spins and electron clouds rotating through 90°, such that the domains are magnetostrictively strained by an amount of $\delta L'/L$.

Magnetostriction can also be introduced by applying a mechanical stress onto the specimen. As a result the sample magnetization is affected as the stress causes the magnetization to rotate either along the stress direction (positive magnetostriction) or away (negative magnetostriction). This mechanism is called the inverse Joule effect or Villari effect or the magnetomechanical effect or the stress-induced anisotropy. This effect plays an important role as one can control the magnetization and the domain structures by applying a stress rather than a field [37].

2.6.1 Magnetostriction for Different Materials

There are two independent magnetostriction constants for cubic materials, which are λ_{100} and λ_{111}. The saturation magnetostriction for a single domain or single crystal

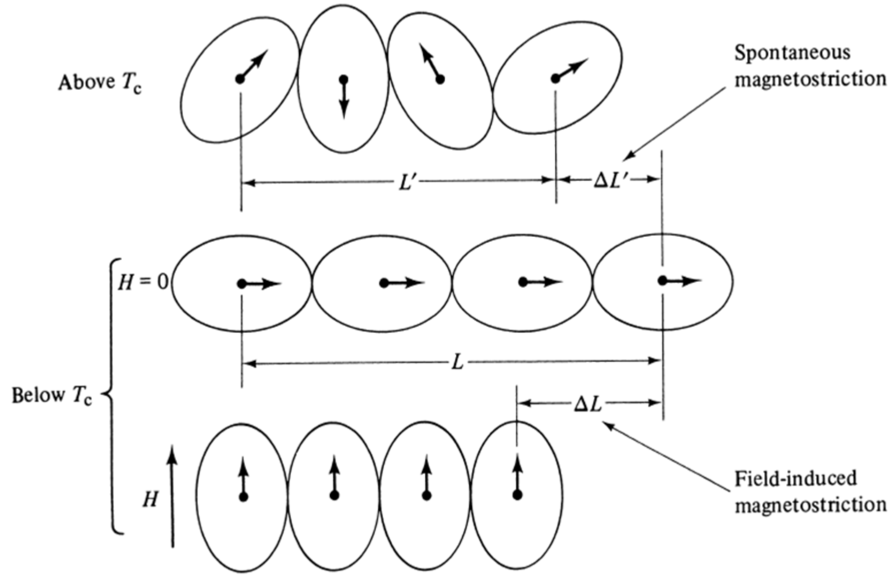

Figure 2.8: Magnetostriction due to the spin orbit coupling. Taken from [36].

cubic materials can be given by:

$$\lambda_s = \frac{3}{2}\lambda_{100}\left(\alpha_1^2\beta_1^2 + \alpha_2^2\beta_2^2 + \alpha_3^2\beta_3^2 - \frac{1}{3}\right) + 3\lambda_{111}\left(\alpha_1\alpha_2\beta_1\beta_2 + \alpha_2\alpha_3\beta_2\beta_3 + \alpha_3\alpha_1\beta_3\beta_1\right) \tag{2.23}$$

where λ_{100} and λ_{111} are saturation magnetostriction measured along $< 100 >$ directions and along $< 111 >$ directions, respectively. The terms α_1, α_2, α_2 refer to the direction cosines of magnetization, whereas the β_1, β_2, β_3 are the direction cosines for the magnetostriction in relation to the field direction [23]. The magnetostriction in the direction $< 110 >$ is not independent of λ_{100} and λ_{111}, is given by [37]:

$$\lambda_{110} = \frac{1}{4}\lambda_{100} + \frac{3}{4}\lambda_{111} \tag{2.24}$$

For a completely isotropic material, $\lambda = \lambda_{100} = \lambda_{111} = \lambda_{110}$. In the case of polycrystalline material with no texture, i.e. randomly orientated grains, the overall magnetostriction is averaged from each grain, even though $\lambda_{100} \neq \lambda_{111}$. Thus the average magnetostriction of this material is expressed by [37]:

$$\overline{\lambda} = \frac{2}{5}\lambda_{100} + \frac{3}{5}\lambda_{111} \tag{2.25}$$

2.6.2 Surface Magnetostriction

The magnetostriction of a thin film has been observed to be different from the bulk. According to O'Handley and Sun [56] it is affected by the symmetry on the surface which has been altered due to the changes in the number of nearest-neighbor atoms. It has been found that for multilayer films, the magnetostriction constant changed with multilayer thickness caused by the magnetostrictive strain which is localized at the interface. This leads to the linear dependence of effective magnetostriction constant on the inverse thickness, t^{-1} [57]. This effective magnetostriction for thin film which has contribution from the volume magnetostriction, λ_v and the surface or interdiffusion layers, magnetostriction, $\lambda_{s/i}$ it is given by:

$$\lambda_{eff} = \lambda_v + (2\lambda_{s/i})/t \tag{2.26}$$

where t is the thickness of the film or layer. Lafford and Gibbs [58] extended the model for finite thicknesses at the interface region between the magnetic and nonmagnetic layer, which was not given in the model proposed by Szymczak [57]. Thus equation 2.25 becomes:

$$\lambda_s t_{mag} = \lambda_s^{mag} t_{mag} + \frac{2(\lambda_{s/i} - \lambda_s^{mag})t_{int}}{1 + \left(\frac{t_{int}}{t_{mag}}\right)} \tag{2.27}$$

where λ_s is effective magnetostriction constant, which is similar with the λ_{eff} in the Equation 2.25; $\lambda_{s/i}$ is magnetostriction constant of the interface; λ_s^{mag} is magnetostriction constant of magnetic layer, t_{mag} is a thickness of magnetic layer and t_{int} is a thickness of the interface. In some cases, the second term is constant when $t_{int} \ll t_{mag}$. The equation above yields the linear regression from the plot of λ_s t_{mag} against t_{mag} [59, 60].

2.7 Theory on Nanoidentation for Measuring the Mechanical Properties

Measuring the mechanical properties of thin films on different substrates by load and depth-sensing indentation technique allows the force and depth of penetration into a material to be recorded. Hence the hardness and the Young's modulus of that material

can be determined directly. Sneddon [61] have derived the relationship between the force, P, displacement, h and the contact area for different types of tips indenter (flat cylinders, cones, and spheres) and this can be expressed by the power of law equation:

$$P = \alpha h^m \tag{2.28}$$

where α and m are constants.The values of m depends on the geometry of the tip.

According to the method proposed by Doerner and Nix [62], the contact area between the indenter and sample remains the same when the tip is withdrawn, and the curve of load-displacement at unloading is linear. However, Oliver and Pharr [63] experimentally found that the unloading part is clearly curved with m which in the range $1.2 \leq m \leq 1.6$ and determined that Equation 2.27 becomes:

$$P = \alpha(h - h_f)^m \tag{2.29}$$

which h_f is the final depth of contact after unloading.

Measurement of the hardness properties of the sample requires the indenter area function, A. Thus, Oliver and Pharr [64] have introduced a method that accounts for the non-linear behaviour of the unloading data, in contrast with a linear part which proposed by Doerner and Nix method. The measurement of Young's Modulus, E and hardness, H was proposed by Oliver and Pharr and are based on the unloading process during one cycle. A typical load-displacement plot is illustrated in Figure 2.9 (after[64]). Both elastic and plastic deformation occurs when the tip is driven into the film and the contact area changes with the depth. The unloading curve is dominated by the elastic displacement. The important parameters determined from the curve shown in the Figure 2.9 are the peak load, P_{max}, the depth at the peak load, h_{max}, the contact stiffness at the unloading curve, $S = dP/dH$ and the final depth, h_f which the depth after the indenter is completely unloaded.

For the Berkovich indenter, the contact area, A and the contact depth, h_c are related by:

$$A = 24.5h_c^2 \tag{2.30}$$

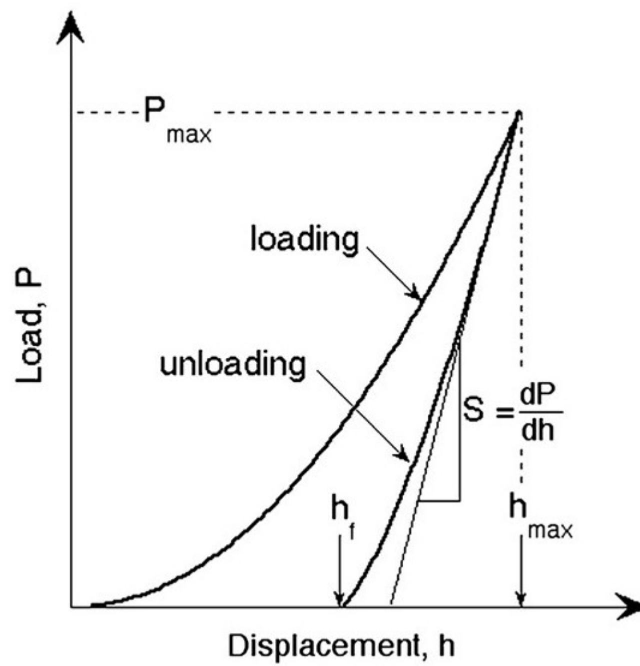

Figure 2.9: The load-displacement curve. Figure taken from [63].

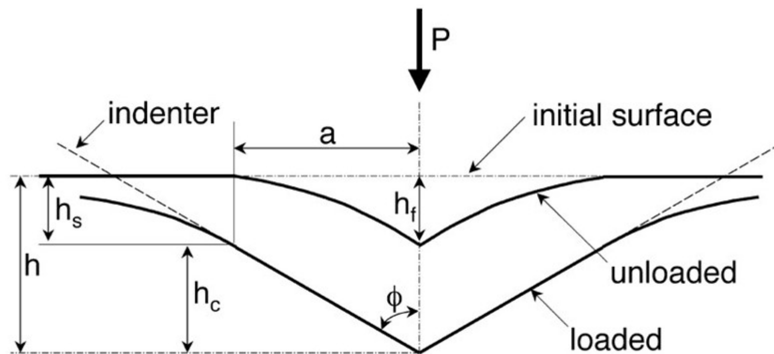

Figure 2.10: The schematic diagram of unloading and loading process of indenter tip into sample. Figure taken from [63].

The exact process of how Young's modulus and hardness are measured by the Berkovich tip during the unloading process is based on the illustration shown in Figure 2.10. They assumed that the Berkovich tip can be modeled by a conical indenter with a half-included angle, $\phi = 70.3^o$. The contact depth, $h_c = h_{max}$ - h_s is the depth contact between the tip and the sample given by:

$$h_c = h_{max} - \epsilon \frac{P_{max}}{S} \tag{2.31}$$

Where ϵ is geometric constant depending on indenter geometry. In this case, the $\epsilon = 0.75$ to account for edge effects (sink-in), and the pile-up is negligible.

This method also determines the depth and the contact area that the indentation makes with Berkovich geometry, whereby this kind of tip are not described in Sneddon analysis. The contact of area, A at the peak load, is determined by:

$$A = F(h_c) \tag{2.32}$$

Where F is area function or cross-sectional area of indenter to the distance from its tip, h_c. By taking deviations from Berkovich geometry due to blunting at the tip, the area function, A in equation 2.29 can be extended as:

$$A = 24.5h_c^2 + C_1h_c^1 + C_2h_c^{1/2} + C_3h_c^{1/4} + ... + C_8h_c^{1/128} \tag{2.33}$$

which C_1 to C_8 are constants obtained by fitting the A against h_c data.

The reduced elastic modulus, E_r which has contribution from both the Young's Modulus and Poisson ratio, ν of the film and the indenter tip can be written as:

$$\frac{1}{E_r} = \left(\frac{1 - \nu_{film}^2}{E_{film}}\right) + \left(\frac{1 - \nu_{indenter}^2}{E_{indenter}}\right) \tag{2.34}$$

where the $E_{indenter}$ and $\nu_{indenter}$ of a standard diamond tip are 1140 GPa and 0.07, respectively. The value of Poisson's ratio is usually between 0 and 0.5, depending on the material. From the load-displacement curve, Oliver and Pharr analysis define the equation for E_r for any axisymmetric indenter given as:

$$E_r = \frac{\sqrt{\pi}}{2}\beta\frac{S}{\sqrt{A}} \tag{2.35}$$

where β is a dimensionless parameter equal to unity. However, β has value greater than 1 ($\beta = 1.05$) when taking into account a deviation in stiffness caused by the non-axisymmetric of the indenter. Apart from the reduced modulus, Oliver and Pharr analysis also gives a solution in determining the hardness, H_r of the sample once the

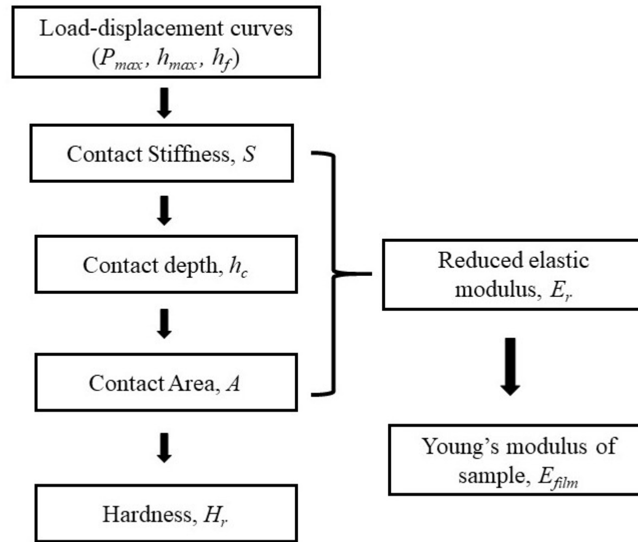

Figure 2.11: Process of nanoindentation involves measurement of some parameters in obtaining the hardness, reduced elastic modulus and Young's modulus. [63].

contact area of function is obtained:

$$H_r = \frac{P_{max}}{A} \tag{2.36}$$

Figure 2.11 shows an overall nanoindentation process in which the hardness, reduced elastic modulus and Young's modulus of sample can be obtained.

There is another type of indenter used to investigate the mechanical properties of material which the projected contact area are different with Berkovich contact area. The Knoop indenter, has an elongated four-sided pyramid indenter with two unequal face angles; θ_1= 86.25^o and θ_2= 65° as shown in Figure 2.12a. The contact area, A for Knoop indenter is A= $2h_c^2$ $\tan_{\theta_1}\tan_{\theta_2}$. The advantage of this tip geometry is it provides very shallow depths of penetration and able to respond to the difference in the ratio of hardness to modulus of material [65].The spherical indenter, however, has an advantage as this tip able to measure mechanical properties from elastic to elastic-plastic region. The projected area for this indenter is A=$\pi 2Rh_c$, which R is a radius of contact and α is effective cone angle as shown in Figure 2.12b. The geometries and the SEM images of both Knoop and spherical indenter are shown in Figure 2.12.

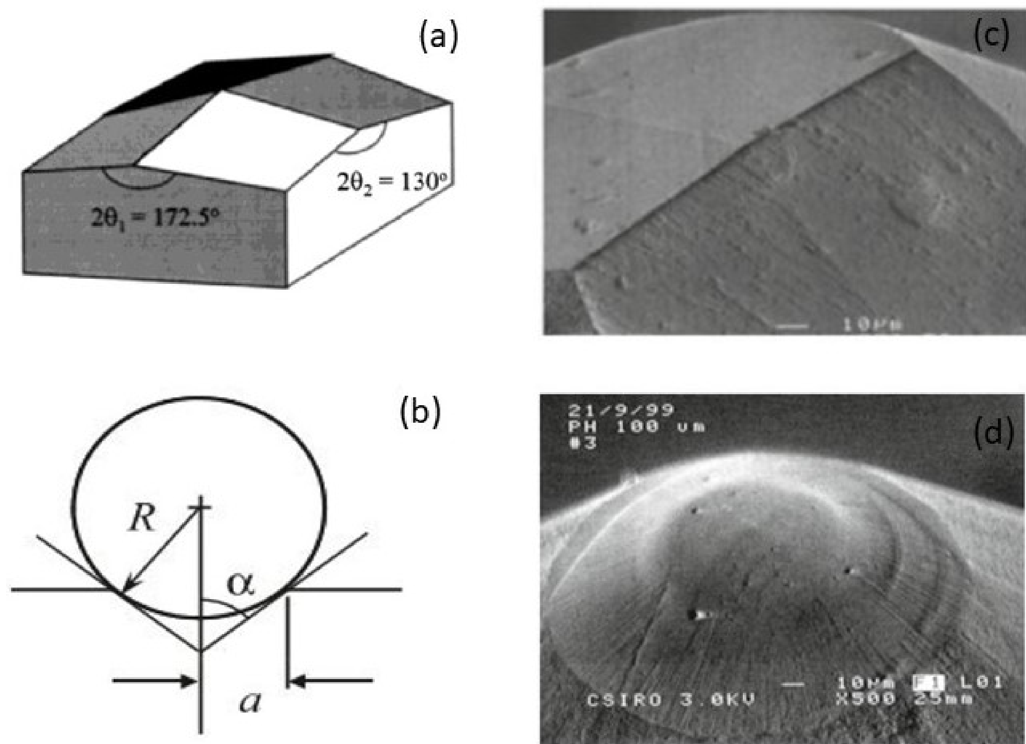

Figure 2.12: Geometry of (a) Knoop indenter (b) spherical indenter and SEM images of (c) Knoop indenter (d) spherical indenter. Figure taken from [65].

Chapter 3

Literature Review

Soft magnetic materials have received considerable interest with numerous reports having been published on the properties of soft magnetic materials including FeCo-based alloy and films. The driving force behind these efforts is the potential for FeCo to be used in many applications such as MagMEMS sensors and actuators, additionally spintronic devices. This chapter reviews the wide range of studies focusing on the structure, magnetic and magnetostrictive properties of FeCo-based alloys and thin films. Several factors (compositions, annealing, multilayer films, elements doping) which influenced the films properties will be outlined in the first section in this chapter. This chapter also describes the previous works by other groups on soft FeCo-based material for microwave studies in high frequency ranges. Further, a literature review on the mechanical studies using nanoindentation method are given at the end of this chapter.

3.1 Structural, Magnetic and Magnetostrictive of FeCo

The purpose of studying the magnetostriction properties is to understand how a ferromagnetic material respond to an external magnetic field or strain acting on it. This phenomenon enable us to engineer high performance of magneto-electromechanical transducers of magnetostrictive bulk, ribbons and thin films. However, many factors need to be considered to attain a large magnetostrictive effect especially in thin films, which are affected by a number of intrinsic (composition) and extrinsic (for example : pressure,

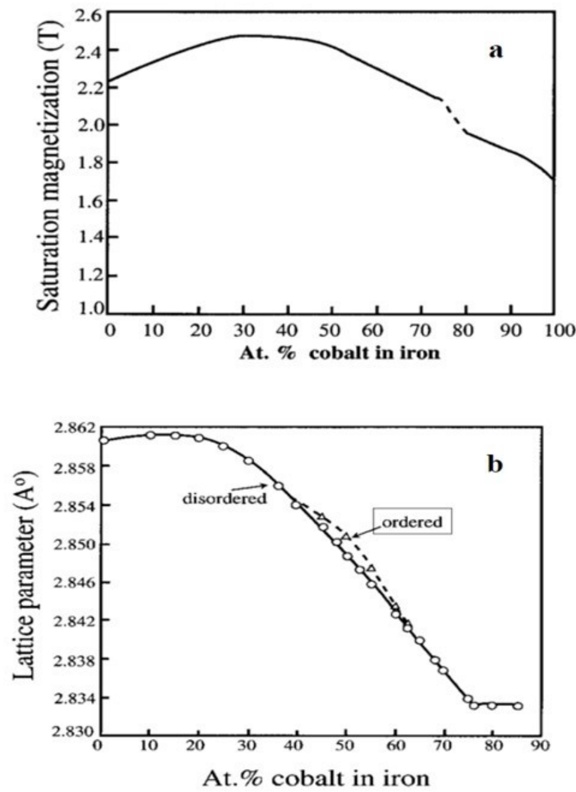

Figure 3.1: The saturation magnetisation of FeCo at varied composition (a) and (b)the lattice parameter in disordered and ordered structure. Figure taken from [23].

power, substrate temperature, annealing) factors [66]. Numerous studies on the structure, magnetic and magnetostrictive properties of FeCo either in bulk or thin films have been published since the discovery of the high saturation magnetisation (2.4 Tesla) of Fe-Co at near equiatomic composition as shown in Figure 3.1.

3.1.1 Effect of Fe and Co Compositions

An early study on Fe-Co magnetostrictive materials was reported in 1932 [67]. There was a substantial change in the magnetostriction constant when Fe was alloyed with 40, 50 and 60% Co. The magnetostriction constants values at those percent of Co found to be 60 to 70 ppm. The value of magnetostriction constant was found nearly -20 ppm at 100% Co and less than -10 ppm with no addition of Co . In 1960, an experiment was performed on annealed bulk $Fe_{50}Co_{50}$, which showed high magnetostriction of λ_{100}=150 ppm [68]. At this composition, it is in the B2 ordering phases and close to

zero anisotropy. Different concentration of Fe-Co films were prepared by electrodeposition and then annealed in vacuum 400°C with an applied magnetic field were studied by Yokoshima et. al [69]. They reported that the coercivity, H_c decreased for films with 30 to 65 at.% Fe and claimed due to the lattice distortion relaxation. For higher concentration 90 at.% Fe, they found that annealing was not effective in reducing the H_c. They concluded that the high H_c at higher concentration of Fe, was due to a large magnetocrystalline anisotropy. Nevertheless, the study did not reported the magnitude of the magnetocrystalline anisotropy for their films. In another study, variation of Co composition in FeCo films deposited by using magnetron sputtering have been reported by Lin et al. [70]. The lower coercivity was found with $Fe_{80}Co_{20}$ and increased as the Co concentration increased. The magnetisation squareness increased close to 1 with the percentage of Co. They also studied how surface roughness affects the magnetic properties of their samples. Films with smaller roughness had lower coercivity and vice versa for larger roughness. The higher coercivity for larger surface roughness was believed to be due to the defects in films causing the impediment of domain wall movement.

Magnetostrictive properties of FeCo at composition 50:50 grown by two different sputtering methods namely DC and RF sputtering have been determined by Morley et.al [71]. They also investigated how fabrication parameters such as temperature (300 K and 600K), rotating and keeping the sample stationary during sputtering, as well as film thicknesses influenced the magnetic and structural properties of their films. The films' thicknesses were in range between 10 nm and 100nm. Their results showed that at 300 K for DC sputtered films with various thicknesses and rotating the sample during growth, the magnetostriction constant (λ = 11 ppm) did not changed over the film thickness. Meanwhile, samples at 600 K for DC sputtered (rotated) and RF (non-rotated), the magnetostriction followed the Néel's model of surface magnetostriction with the contributions of volume, λ_v and interface, $\lambda_{s/i}$. For films (DC) the λ_v and $\lambda_{s/i}$ found to be 63 ppm and -1199 ppm.m, respectively. The λ_v was found to 53 ppm and $\lambda_{s/i}$ was 669 ppm.m for films grown by RF sputtering method. The uniaxial anisotropy were found for both non-rotated DC and RF caused by the stray field from magnetron sputtering. For structural analysis, XRD peaks at $2\theta = 44.97^o$ were observed in all films. They concluded that the films uniformity in thickness for the DC rotated samples was determined and decreasing in anisotropy field and internal stress also were possible to be reduced by fabricating films at elevated temperature and rotating the sample.

Fu et.al [72] investigated the magnetic properties of $Fe_{100-x}Co_x$ ($30 \leq x \leq 40$) films prepared by co-sputtering. They found that the films had isotropic behaviour with saturation magnetisation in the Co composition (30 at.% to 40 at.%) of 2.4 Tesla, so had similar value as bulk FeCo. The minimum value of coercivity was 1 kAm^{-1} for FeCo film of 34 at.% but it increased markedly afterwards in the range of ($36 \leq x \leq 40$) Co concentration. They also found that by growing $Fe_{65}Co_{35}$ (100 nm) on the seed layer ($Co_{93}Fe_7$) thickness varied from 0 to 10 nm could change the behaviour of the films. They found that films showed uniaxial anisotropy at high Co concentration. The coercivity of the hard axis and easy axis was reduced to 0.2 kAm^{-1} and 1 kAm^{-1}, respectively. There was no magnetostriction measurement conducted in the study.

The influence of Fe ($20\% \leq Fe \leq 51\%$) and Co ($49\% \leq Co \leq 80\%$) compositions on the magnetic properties and microstructure of FeCo thin films have been reported by Yang et.al [73]. In this paper, they prepared FeCo films on the Si substrate by sputtering the Co target with Fe chips. They varied the film compositions by changing the number of Fe chips. From the structural study they found that the peak of FeCo (110) at $2\theta = 45^o$ disappeared when the composition was $Fe_{51}Co_{49}$ but revealed the peak of $FeSi_2$ (042) at about $2\theta = 53^o$. For magnetic studies, they performed Vibrating Sample Magnetometer measurement at room temperature with the findings of the coercive field increased gradually with Fe compositions from 8 kAm^{-1} to 19 kAm^{-1}. This paper however did not investigated the magnetostrictive properties of their films.

Summary

Based on reported studies of Fe and Co concentrations used, it can be summarised that the amount of Fe or Co had significantly affected the coercive field, H_c and anisotropy field, H_k of thin films. It has been claimed that the concentration of Fe within 30 to 65 at.% have reduced the H_c, while the concentration of Co from 30 at.% to 40 at.% on other studies have found the H_c also decreased. However, the study also determined that for compositions of Fe and Co at an equal concentration (50:50), the anisotropy field also could be reduced by controlling the deposition temperature and applying a different method during thin film deposition of thin films can affect film properties. Therefore, a different technique would use in this current study to vary the concentrations of Fe and Co by adjusting the sputtering power to investigate if the coercivity or anisotropy fields have shown a substantial difference.

3.1.2 Effect of Annealing

The magnetic properties of ferromagnetic thin film also can be tailored by annealing either by applying a magnetic field during deposition or by temperature (post-deposition). The effect of annealing on the magnetic properties of 300 nm $Fe_{50}Co_{50}$ films had been studied by Cooke et.al [27]. The films were grown by rf sputtering onto different substrates silicon (001) and sodium glass. This study found that the coercivity reduced when the annealing temperatures were above 375°C. The change in grain size when samples were annealed from 30 nm - 60 nm to 100 nm - 150 nm. The magnetostriction constants were also found to be different for both group of films, for the films deposited on sodium glass substrate was larger (76 ppm) than on Si substrate (63 ppm).

Research on $Fe_{50}Co_{50}$ films which annealed by means of an applied field had been studied by Coisson et. al [74]. They deposited films onto glass substrate with film thicknesses of 30 nm and 4 nm. They annealed the films in a vacuum with pressure of 2 x 10^4 mbar, annealing time was varied between 20 and 120 minutes and under magnetic field of 100 Oe. The film with thickness of 4 nm annealed for 20 minutes had a coercive field H_c = 10 Oe which was three times lower than the as prepared film which was 30 Oe. However the film coercivity increased to 80 Oe as the annealing times increased to 40 and 100 minutes. All samples showed an isotropic behaviour. Thus annealing at longer periods for the 4 nm thick film did not markedly reduce the coercivity and did not change the magnetic behaviour of the films. This is contradicting to the 30 nm thickness, where magnetic annealing at 60 minutes reduce the coercivity and magnetic anisotropy was developed. They suggested that the magnetic field applied at 100 Oe and film deposited for 60 minutes was sufficient to induce a moderate magnetic anisotropy for their thicker film.

Investigation of the different thermal processes on the magnetic properties of Fe-Co has been highlighted by Hunter et al. [75]. The Co-Fe films were sputtered on the Si/SiO_2 substrate. The films were divided into three different conditions which were as deposited Co-Fe, annealed at 800°C for 1 hour (slow-cooled) and another one was annealed at 800°C for 1 hour (water quenched). The change of magnetrostriction constant with Co concentration in their study for the as deposited films with a comparison for the bulk and thin film forms from other studies is shown in Figure 3.2a. Their films subjected to different heat treatment(slow-cooled, quenched), the magnetostriction constants is

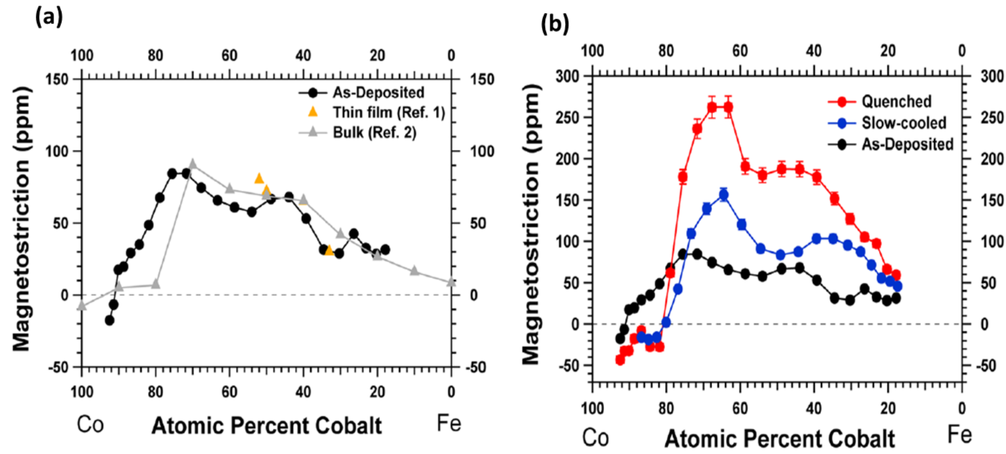

Figure 3.2: The plot of magnetostriction of FeCo with percentages Co (a) as-deposited films and (b) samples at different heat treatment. Figure taken from [75].

presented in Figure 3.2b. They determined that the annealed film with water quenched showed the highest value of magnetostriction constant. As the composition increased between 60 and 75 at.% Co the maximum magnetostriction was found to be 260 ppm as opposed to film annealed (slow-cooled) with a maximum value was 156 ppm. For the as deposited films the value was much lower (67 ppm). They reported that by annealing the sample at the temperature and composition near to the fcc+bcc/bcc phase boundary and subsequently quenching the film could results in the enhancement of magnetostriction at low saturation field $\sim 100Oe$.

Another study was performed by Nakajima et al. [76] in which $Fe_{32}Co_{68}$ films with thickness of 240 nm were annealed from 673 K to 1153 K for 60 minutes and quenched in an ice tube. They found that two phases were observed, which correspond to BCC and FCC at annealing temperature of 1113 K as depicted in Figure 3.3. However, at the higher temperature of 1153 K only the FCC phases occurred, and for films below 1113 K only BCC phase observed. The surface morphologies of their films also changed with temperature as at lower temperature the films exhibited the uniform surface roughness compared to the film at higher temperature with discontinuous morphology. The saturation magnetostriction was found to be maximum at 159 ppm for film at 1073 K (BCC phase) which was three times higher than film at very low temperature (673K). On the other hand, as the existence of both FCC and BCC phases decreased the magnetostriction and they suggested it was related to the discontinuous surface of samples at higher temperature. From the magnetisation measurement, the coercivity also decreased with

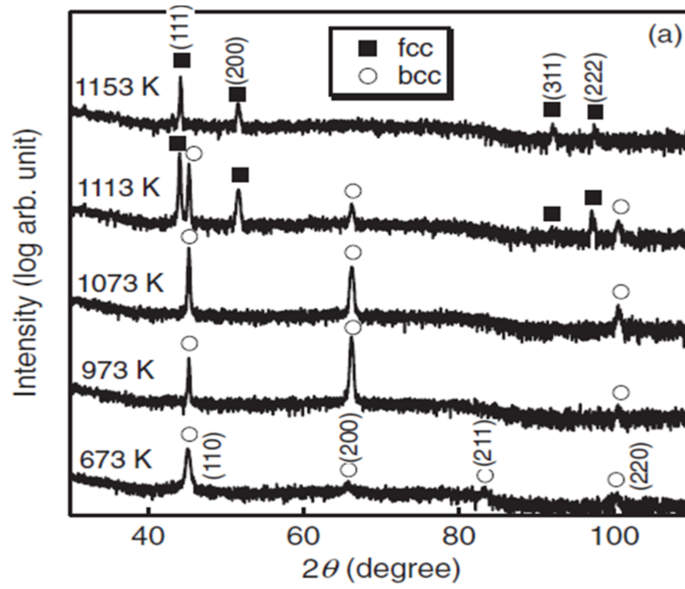

Figure 3.3: XRD pattern for $Fe_{32}Co_{68}$ at different annealing temperature showing the existence of FCC phases at higher temperature. Figure taken from [76].

temperature possibly due to stress between films and the substrate interface.

Varvaro et.al [77] fabricated FeCo films onto MgO substrates with body centered cubic phase confirmed by high resolution transmission electron microscopy. They successfully produced highly textured FeCo by using low temperature pulsed laser deposition. They fabricated the films at different substrate temperatures (25°C and 150°C). The thickness were 12 nm (25°C) and 16 nm (150°C). They characterized the in-plane hysteresis loops of films using VSM at room temperature by varying the angles and applying field of 1 Tesla and found FeCo showed in-plane magnetic anisotropy. For different substrate temperature they found that increasing temperature also slightly increased the coercivity. This was caused by the pinning sites which hindered the magnetization. These sites are expected to be from the grain size or the microstructure defects at the interface.

The effect of annealing on the magnetostriction of $Fe_{1-x}Co_x$ (x = 50, 55, 60, 66, 70, 75, 80, 85, 90 at%) were measured by Yamaura et.al [24]. The FeCo alloys in ingots were forged and heat treated at different temperature (873K - 1073K) for 3 hours under vacuum. The magnetostriction of samples annealed at 1073K after forging showed higher magnetostriction constant in between 80 ppm to 100 ppm for composition of Co at.% 60 to 70. They suggested that the increase in magnetostriction values with annealing were caused by the internal stress being released and the formation of grains. Between the

similar ranges of compositions, the magnetostriction for as-forged samples were found below than 60 ppm. Surprisingly by increasing Co content more than 75 at.%, they also found a negative magnetostriction constant with increasing annealing temperature. A discussion on the negative values of magnetostriction obtained was not given in this paper.

Recently, well-defined uniaxial properties of the soft amorphous FeCoNbB have been reported [78]. The FeCoBNb films on Si substrate were sputtered from a source target composed of $Fe_{32}Co_{57}Nb_4B_7$ by ion beam sputtering at room temperature; thicknesses 16 nm and 75 nm. Both as-prepared samples showed strong angular dependencies of the remanence measured by longitudinal MOKE, hence the films were magnetically uniaxial. The XRD diffraction reflected that the films were amorphous with broad peak observed. They expanded the study by figuring out how the thermal annealing (473K to 773K) affected the structure and magnetic anistropy of the as deposited films. The transformation of structure from amorphous to nanocrystalline were determined when annealed at 503K, with three phases (110), (200) and (211). For the magnetic study they found that increasing the temperature gradually degraded the magnetic anisotropy and at the highest temperature 773 K, the films were isotropic, they suggested it was caused by internal stress relaxation.

Summary

Based on findings from the mentioned literature above, it have shown that the structural, grain size, magnetostriction constant, and the coercive field can be tailored by annealing. These changes depend on the applied temperature and the duration of the annealing. Annealing $Fe_{50}Co_{50}$ thin films have lowered the H_c but, as the time of annealing increased, another literature also found that annealing was no longer significant to reduce the H_c for a very thin of $Fe_{50}Co_{50}$. The FeCo reported a change in the crystallographic structure from the bcc to fcc when annealed at a higher temperature (1153 K). Also, the relaxation of internal stresses within the film can result in the reduction of magnetic anisotropy for films annealled at certain temperature. It also showed that annealed the FeCo samples at the composition of Co % to 75% near the boundary of fcc+bcc and bcc led to an enhancement of the magnetostriction constant as high as 260 ppm.

3.1.3 Effect of underlayer/multilayers films

It has been found that the structure and magnetostrictive properties of FeCo films were also affected by depositing onto underlayer or multilayers films. For example, preparation of Fe-Co on double underlayer films have affected the magnetostrictive properties of the films [79]. This study investigated the saturation magnetostriction of FeCo on underlayers of ruthenium/copper (Ru/Cu) by fixing the Cu thickness, and Cu/Ru with fixed Ru. They found that the films deposited on Ru with fixed Cu layer showed a positively large magnetostriction when Ru thickness was increased. In contrary, the films which were fabricated on Cu layer with thickness varying to 2 nm at fixed Ru thickness, had negatively large on magnetostriction with thickness. They discussed that the contribution of the films' magnetostriction deposited on double-underlayer may be attributed to the strain model. This is because of the Ru has large atomic radius while Cu has a smaller radius, it was expected that the atomic spacing of Cu was in strain when the thickness of the Cu layer was reduced. On the other hand, they also stated that changing on magnetostriction of their ultrathin films with range of thickness did not fitted to the Néel's model (the model has contribution from both bulk and the interface effect).

Cakmaktepe et.al [80] have suggested the coercivity of films with nonmagnetic underlayer could also enhance the magnetic properties of FeCo. It was related to the changes in texture as a result of grain size reduction. In their study, they grew $Fe_{10}Co_{90}$ with thickness 40nm, on to underlayers of Cu, Cr, Au and magnetic underlayer of $Ni_{80}Fe_{20}$ with 6 nm thickness. They found that for films grown on Au, NiFe and Cu the coercivity was markedly reduced to below than 10 Oe compared to the coercivity field without a layer which were higher; 49 Oe (easy axis) and 37 Oe (hard axis). The reduction in coercivity with the change in film structure from (110) and (220), indicated the reduction in grain sizes and the stress relief. Similarly reported in this study [81] they found that there was a decrease in coercivity for $Fe_{65}Co_{35}$ with thickness 50 nm deposited onto multilayers films (glass, Ru, Cu, Ta and NiFe). Films grown on a Cu layer presented a remarkable reduction in the anisotropy field from 2000 Oe to 40 Oe with the magnetostriction constant, λ being 47 ppm, but independent of the FeCo and Cu thickness. All the films deposited on underlayers had a well-defined anisotropy, except the film grown without an underlayer (glass substrate) which was isotropic. Growing FeCo with

an underlayer improved the structure of the films. From XRD, films grown on Ta, Cu, NiFe and Ru all had FeCo (110) with a sharp peak at 45°. In contrast, the XRD pattern was found to be different for the film with no underlayer where there was no (110) peak revealed at 45°, but a (200) peak at 65° appeared.

Caruanka et.al [82] determined the difference in magnetic properties and grain size of $Fe_{10}Co_{90}$ films grown with and without underlayer. They deposited the Metglas with $Ni_{81}Fe_{19}$ acts as underlayer by using sputtering technique. The coercivity for films grown on underlayer reduce while the grain size increased. They also performed magnetostriction measurement and found that the bilayer film Metglas/$Fe_{10}Co_{90}$ has $\lambda = 17$ ppm. However by growing film with 35nm $Ni_{81}Fe_{19}$/$Fe_{10}Co_{90}$, they determined the negative magnetostriction which was λ = -12 ppm. The λ for $Ni_{81}Fe_{19}$ film is in the range between -5 ppm and 5 ppm. They suggested the underlayer thickness and the growth parameter had affected the value of magnetostriction.

The magnetic properties of $Fe_{70}Co_{30}$ films with various thicknesses of multilayers have been studied [83]. The top layer was Ta/NiFe while the bottom layer was NiFe/Ta with the Ta layer being introduced as a protective layer. The films were deposited by ultrahigh vacuum dc magnetron sputtering with a magnetic field of 600 Oe being applied during the film growth. In their study, the thicknesses of the top and bottom layers were fixed at 5nm while the thickness of $Fe_{70}Co_{30}$ was varied up to 400 nm. The coercivity of the hard axis dropped to below 4 Oe when the film thickness was up to 100 nm, however the coercivity increased as the thickness further increased beyond 100 nm. They assumed that the existence of a large strain in the FeCo layer near the interface between FeCo and NiFe to be the factor, which contributed to larger coercivity. The value of the magnetostriction of Ta/NiFe/$Fe_{70}Co_{30}$/NiFe/Ta film at 100nm of $Fe_{70}Co_{30}$ was found to be 30 ppm.

Different underlayers such as Au, Ag and Cu have been fabricated with Fe–Co–Al–O films deposited on the top by sputtering technique [84]. They found that the value of coercivity intensely decreased for Au underlayer with thickness 0.2 to 0.5 nm for both as deposited and annealed films. The annealed film showed a remarkable reduction in coercivity, which was less than 2 Oe. They also studied the relationship between the intensity of the Fe-Co (110) peaks and the coercivity, from which they concluded that a dropped in the coercivity was related to the grain size and the surface free

energy. The crystallographic axis of all films presented was the BCC (110) peak. The magnetic properties of the films also changed when grown on underlayers with different thicknesses. In the study on the underlayer effect of $Ni_{81}Fe_{19}$, the anisotropy field of $Fe_{30}Co_{70}$ reduced with the thicknesses [85]. This study found that there was a decrease in the in-plane stress; therefore the anisotropy field decrease can be related to the stress in the film. This study reported that the overall of uniaxial anisotropy within the films was maintained, though the anisotropy and coercive field were found to be reduced.

Research done by Gupta et al [86] has shown that depositing of Fe/Co and Co/Fe bilayers on silicon substrate using ion beam sputtering technique also reduce the coercivity of the Si/Fe/Co films with Ni ion implantation up to 20 x 10^{15} ions cm^{-2}. They suggested that the stress relaxation during ion implantation occurred, thus the stress affected the coercivity of the films. Both films showed different magnetic behaviour, the Si/Co/Fe film was uniaxial anisotropic, while the Si/Fe/Co was isotropic. The effect of Co underlayer on the magnetic and microstructure of the FeCo films was also investigated by Fu et al. [87]. Growing on a Co underlayer (2nm), the FeCo films exhibited significant reduction in coercivity, as it dropped from 94 Oe to 10 Oe when measured along the easy axis; whilst the H_c reduced from 85 Oe to about 3 Oe when measured along the hard axis. By increasing the FeCo thickness, the texture also changed from (200) to (110). From their study, the found that there was a huge difference between grain size for the films with and without underlayer. They found a smaller grain size which was about $D = 8.2$ nm for film with an underlayer as opposed to $D = 70$ nm for the film without a Co layer.

Summary

In summary, depositing FeCo onto underlayer films could alter the magnetic properties, depending on the underlayer's material. It showed that the changes related to the internal strain within the film and the grain size. The coercive field of the FeCo grown on the Au underlayer and the magnetic underlayer, i.e., Permalloy, was due to a reduction in the grain size. However, when a thin film deposited on the Co underlayer, the grain size was larger than the films without the Co underlayer. On the other hand, the study found that when magnetic thin films grown onto the magnetic underlayer such as the Metglas onto the Permalloy drop the coercivity, the grain size increased. Changing the magnetic film on the same magnetic underlayer has resulted in a different value of magnetostriction constant. For instance fabricated the NiFe/$Fe_{10}Co_{90}$ and Metglas/$Fe_{10}Co_{90}$ have shown

negative and positive magnetostriction constant, respectively. Another published study also concluded that a large strain near the interface of FeCo and NiFe has contributed to a larger coercivity.

3.1.4 Effect of Additives

There are considerable amount of studies which have focused on structural, magnetic and magnetostriction properties of FeCo with addition of a two or more elements into FeCo. For example, FeCo with Ni concentrations grown by electrodeposition technique was studied by Yoo et. al [88]. The coercivity for both in-plane and out-of-plane were measured by a vibrating sample magnetometer, and the results showed that between 3% and 13% Ni concentration, the coercivity decreased steadily presumably due to the grain size. The grain sizes were reduced from 110 nm to 40 nm. Both coercivities in-plane and out-plane increased from 26 Oe to 31 Oe, and 160 Oe to 305 Oe, respectively for the Ni content range from 13% to 48%. This was found to be influenced by the internal stress and also the phase structure transition. Increasing the Ni content had increased the film stress. They also found that columnar structure at 13% Ni changed to lamellar structure once Ni increased to 48%, with the predominant phase of FCC (111) detected at this composition. By adding Boron into FeCo it was also found that the coercivity reduced by a factor five to about 5 Oe at.% 15 [89]. This study also found that the structure of FeCo films was affected by the addition of B above at.% 11. The lattice parameters increased and FeCo (110) XRD peaks became broader, indicating the reduction in grain sizes from 20 nm to 10 nm at higher Boron content (at.% 17). They correlated the decreased in coercivity with the reduction in grain size as well as the existence of internal stress. However the data for the stress were not included in this paper. Similar result were reported in [90] where this study also found coercivity decreased in FeCoB measured both along the hard and easy axes. Between at.% 1.5 and at.% 10 B, the coercivity decreased from 100 Oe to 10 Oe for $Fe_{25}Co_{75}$ concentrations. This study also found that as Boron concentrations increased, the grain size decreased from 30 nm to 10 nm, which lead to the reduction in coercivity. They related the dependence of the coercivity of their films to the grain size, using the Random Magnetic Anisotropy Model (RAM) [18].

Dai et. al [3] investigated the effect of substitution of Co in FeGa to the magnetostriction properties of FeCoGa alloys. In their study, the composition of Co varied up to at.% 10, while Ga concentrations up to at.% 17. They quenched the samples in the ice water at 900^0C prior to the magnetostriction measurement. They measured the magnetostriction by using strain gauge method. The results showed that by increasing the Ga content at fixed Co percentage (at.% 7), the magnetostriction constants were found more pronounced, for example they found that the $Fe_{76}Ga_{17}Co_7$ sample showed a higher magnetostriction more than 90 ppm than the $Fe_{86}Ga_7Co_7$, which was about 30 ppm. On the other hand, when Co was increased to 10%, the magnetostriction values were reduced to below 60 ppm for Ga compositions (7%, 12% and 17%). The explanation on how the Co percentages modified the magnetostriction constants in FeGa films were not discussed further in their report.

The magnetic properties of thick film 500 nm film fabricated from $Fe_{70}Co_{30}$ and Al_2O_3 source targets have been grown by RF Magnetron sputtering [91] at room temperature with Ar pressure at 4 mTorr. The FeCoAlO films exhibited good soft magnetic properties with an uniaxial anisotropy and lower coercivity between 4 Oe and 8 Oe were obtained. As they sputtered the sample in an absence of magnetic field, thus they inferred that the well defined anisotropy originated from stress-induced anisotropy. Apart from that, they assumed that magnetic anisotropy contributed by the high resonance frequency response at 3.0 GHz, which they measured by Vector Network Analyzer (VNA). In another paper [92] also published by the same authors, the structural properties and magnetic anisotropy of FeCoAlO films with thickness 460nm grown in a presence of magnetic field was reported. The peaks of FeCo (110) shifted to lower angle by adding Al_2O_3. The peaks shift lead to the expansion of the lattice constant which may due in part to the Al atoms entering the FeCo lattice. They also obtained a smaller grain size, which was 15 nm smaller than the exchange length ($\approx$ 35nm) of FeCo-based alloy. Their films showed uniaxial anistoropy, which they concluded due to the magnetic field during sputtering as well as the contribution from magnetoelastic anisotropy. They obtained positive magnetostriction constant and compressive stress in their films. They also suggested the magnetic anisotropy was from the magnetoelastic contribution, yet no magnetostriction value was given in this paper.

Wang et.al [29] reported the properties of Fe-Co-Cr films in terms of its magnetic and structural properties. They used magnetron co-sputtering to grow 240 nm thick films

with $Fe_{65}Co_{35}$ target and Cr plate target (99.99% purity). During the fabrication the target power of Cr was varied between 0 and 100 W to obtain the difference composition of Cr, while the $Fe_{65}Co_{35}$ power was maintained at 90 W. Magnetic studies were performed by Vibrating Sample Magnetometer (VSM) and the results showed that both the coercivity field and saturation magnetisation of the films dropped sharply for the Cr power between 40 and 80 W. From the structure analysis they found a sharp peaks of Fe-Co-Cr at $2\theta = 45^o$ (110) and $2\theta = 81^o$ (211), shown in Figure 3.4. The addition of Cr by increasing the power lead to the expansion of the lattice constants and it was believed due to Cr atom replacing the Fe and Co atomic sites. Further, they investigated the FeCoCr film with thickness 75 nm deposited by electron beam evaporation and the Cr-ion was implanted with 35 keV and 100 keV under different concentration of ions. The ion concentration were 1 x 10^{15} ions/ cm^2, 5 x 10^{15} ions/ cm^2, 1 x 10^{16} ions/ cm^2 and 1 x 10^{17} ions/ cm^2. They found that, the XRD main peaks indicated a BCC (100) structure with the grain size and the lattice constant increase over Cr concentration. From MOKE measurement, the coercivity decreased from 140 Oe to 44 Oe. They also determined that the films have different magnetic behaviour, with the as-deposited film having isotropic behaviour while at higher Cr concentrations (10^{16} and 10^{17}) exhibited magnetic anisotropy. One shortcoming of this paper was they did not carry out a magnetostriction studies of Fe-Co-Cr films.

Summary

Overall, adding other elements in some proportion into FeCo could reduce the H_c. It was linked to the grain size, and therefore can modify the structure of the FeCo-based films. Adding other materials changed the FeCo from polycrystalline/crystalline into the amorphous structure. The reduction in H_c was seen in the FeCo when Ni concentration increased to 13%. Similarly adding boron at 15% was related to a lower of H_c as a result of the grain size became smaller. For the FeCo-based amorphous thin films, the coercive field's dependence on the grain sizes associated with the Random Anisotropy Model.

3.2 Magnetostrictive materials of Fe-X based (X=Tb,Dy,Ga)

This section review several published researches on magnetic and magnetostrictive properties of soft materials other than the FeCo. It is well known that the materials from

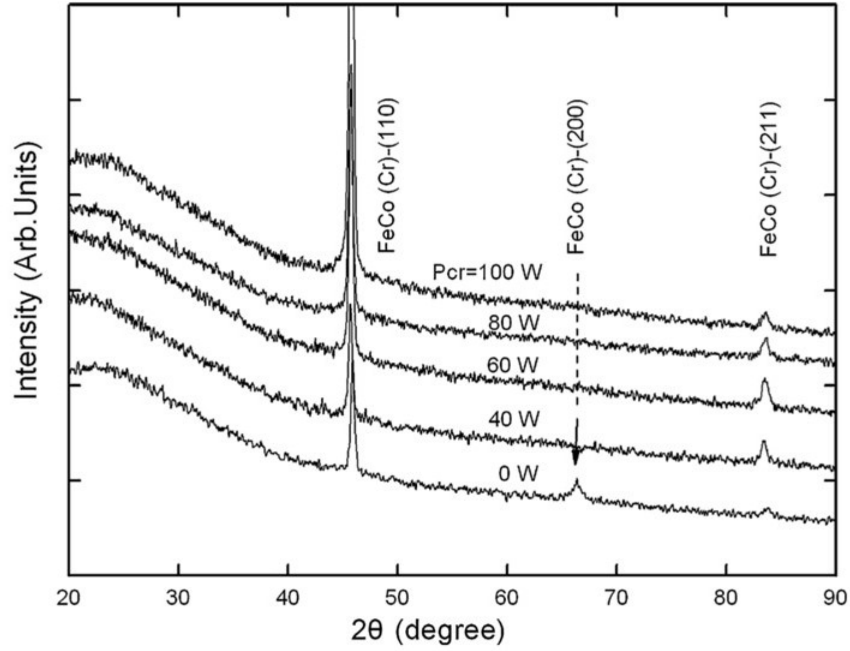

Figure 3.4: XRD pattern for FeCoCr grown at varied power. Figure taken from [29].

rare-earth (RE) alloys; Terbium (Tb) and Dysprosium (Dy) have been subject of interest for decades due to its remarkable magnetostriction constant, $\lambda = 2000$ ppm [14, 15]. Following the breakthrough of giant magnetostriction from the RE group, combining these RE with Fe has became a promising candidates as well as an alternative route in achieving amorphous structure. The amorphous are needed to lower the magnetocrystalline anisotropy particularly, so that they are suitable for microactuators which require small magnetic fields.

Miyazki et.al [93] investigated the magnetostriction properties of Tb_xFe_{100-x} alloy films on glass substrate prepared by RF sputtering. The optical cantilever technique was used to measure the magnetostriction by applying a magnetic field. The amorphous structure was obtained in the compositions of Tb_xFe_{100-x} ($7 \leq x \leq 51$). Soft magnetostrictive properties were successfully achieved at composition x= 42 with lowest magnetic field (1 kOe) and $\lambda = 220$ ppm. The highest magnetostriction constant attained at composition x=33 but at larger field 7 kOe. They suggested a larger magnetostriction at higher field arose from the $TbFe_2$ Laves phase which appeared when they investigated the dependence of magnetostriction on annealing temperature for composition around $Tb_{31}Fe_{69}$ and $Tb_{34}Fe_{66}$. They found that by increasing the annealing temperatures beyond crystallization temperature, the $TbFe_2$ Laves phase decomposed and made the films become

harder with larger magnetocrystalline anisotropy.

The influence of substrate temperature, T_s which ranged from 330^0C to 510^0C during sputtering for the structural and magnetostrictive studies of $(Tb_{0.3}Dy_{0.7})_{39}Fe_{61}$ were carried out [94]. Two different phases at different range of T_s were observed where the films were amorphous at T_s=330°C to 400°C and crystalline at T_s= 425°C to 510°C. They mentioned that the films at lower temperatures were in compressive stress as opposed to higher temperature films which were in tensile stress. The measured magnetostriction for the amorphous films were between 185 and 400 ppm, while the crystalline films had much higher range from 360 to 750 ppm. This paper however did not addressed in detail the relationship between the microstructure and the magnetic properties of these material.

Duc et.al [95] investigated thick TbFe films (t= 1μm) by adding Co as they made assumption that the interaction energy between transition metals (T) i.e Fe-Co was stronger than in solely Fe or Co-based alloys. In addition to this the intersublattice exchange constant of RE is equal to T (Fe and Co). Thereby a combination of both RE material and transition metal should increase the RE moments, hence the magnetostriction. $(Tb_{1-x}Dy_x)(Fe_{0.45}Co_{0.55})y$ films were prepared by rf magnetron sputtering with applied power 300 W and pressure 10^{-2} mbar. Samples were annealed in a magnetic field 2.2 T from 150^oC to 250^oC. At T = 250^oC, films were found to have amorphous structure. The magnetostriction constants of their samples were obtained through substrate bending and measured by an optical deflectometer. The amorphous samples annealed at 250^oC had the highest magnetostriction, λ = 1020 ppm. They suggested that the reason for the significant difference in λ between their amorphous films and crystalline $TbFe_2$ was primarily contributed by the existence of sperimagnetic structure in the amorphous alloys.

Fe-Ga became the focus in magnetostriction studies after rare earth elements as this alloy can overcome the mechanical problems on Tb-Dy groups. The rare-earth magnetostrictives are brittle, therefore were not the best material to be used and operated in shock-prone environment [10]. The study on Fe-Ga was initiated by [16] which showed λ =350 ppm in low field. Similarly to other materials, FeGa thin films are also critically influenced by composition and fabrication parameters. Basantkumar et.al [96] studied Fe-Ga for different thickness, sputtering power (60 to 100 W) and Ar pressure (10 to

50 mTorr) on $Fe_{1-x}Ga_x$. They used the cantilever capacitance technique to measure the magnetostriction. They found fluctuation in λ_s against the Ga composition and the sputtering power but discussion on why λ_s of their films varied was not emphasized in details in this paper. Nevertheless a sample sputtered at 80 W, 146 nm thick and at.% 24 Ga had higher $\lambda_s = 147$ ppm.

Wang et.al [97] investigated magnetostriction constant of the $Fe_{81}Ga_{19}$ films annealed at 300°C, 400°C and 500°C. Their findings showed that by increasing the annealing temperatures, the magnetostriction was reduced. The as-deposited film exhibited larger $\lambda = 42$ ppm at 5 kAm^{-1} compared to the annealed samples. The precipitation of DO3 phase and the large grain size as the annealing temperature increase were believed to be the factor in decreasing of λ. They also fabricated their films with and without magnetic field and the difference of magnetostriction constants between these two film sets was also determined. Films produced under magnetic field had higher magnetostrictions which reached a maximum, $\lambda = 60$ ppm as opposed to films grown without applied field with λ below 50 ppm.

Javed et.al [98, 99] also reported the effect of the growth parameters (pressure,power, Ga rate) on the magnetostriction of Fe-Ga films using their novel co-sputtering evaporation system. The magnetostriction constants of the $Fe_{100x}Ga_x$ films increased with the Ga composition, $Fe_{86}Ga_{14}$ films had λ= 51 ppm, while $Fe_{86.4}Ga_{13.6}$ had λ= 31 ppm, as comparison to the pure Fe, λ= 4 ppm. They also concluded that varying the Ar pressure did not significantly affected the magnetostriction constants of their film, but the saturation field of their films were strongly dependent on the Ar pressure as indicating stress changes in the FeGa films.

The magnetostriction constants value reported from the past researches for different materials with respect to the single crystal, polycrystalline and amorphous either in bulk or thin films are summarized in Table 3.1.

3.3 Measurement Techniques of Magnetostriction

A variety of methods for measuring magnetostriction have been developed, which includes different techniques either direct or indirect measurements. For measurements of the saturation magnetostriction, λ_s indirect methods are used, whilst direct methods

Table 3.1: Magnetostriction constants of some materials from previous studies.

Material	λ_{100}**(ppm)**	λ_{111}**(ppm)**	λ_s**(ppm)**	**Remarks and References**
Fe	21	-21	-	bulk [100]
Ni	-46	-24	-	bulk [100]
Tb	-	-	1250	bulk (78 K) [14]
Dy	-	-	1400	bulk (78 K) [14]
Tb Fe_2	-	-	1753	bulk [14]
$Tb_{0.27}Dy_{0.73}Fe_2$	-	2000	-	bulk [15]
$NiFe_2O_4$	-42	-14	-	bulk [101]
CoFe	-	-	68	bulk [67]
Fe_{30} Co_{70}	-	-	90	bulk [102]
$Fe_{60}Co_{40}$	-	-	70	bulk [102]
Fe at.16% Al	86	-2	-	bulk [103]
Fe at.15.6% V	43	-10	-	bulk [103]
Fe at.15.6% Cr	51	-6	-	bulk [103]
$Fe_{55}Co_{15}$ Cr_{30}	-	-	61	bulk [28]
$Fe_{34}Co_{66}$	-	-	260	quenched thin film [75]
Metglas / $Fe_{10}Co_{90}$	-	-	17	bilayer thin film [82]
$Ni_{81}Fe_{19}$ / $Fe_{10}Co_{90}$	-	-	- 12	bilayer thin film [82]
$Fe_{50}Co_{50}$ / $Ni_{81}Fe_{19}$	-	-	50	bilayer thin film [104]
Fe_xCo_{1-x}	-	-	up to 80	annealed thin film [105]
$Fe_{10}Co_{90}$	-	-	47	thin film with underlayer [80]
$Fe_{70}Co_{30}$	-	-	30	thin film multilayer [83]
$Fe_{32}Co_{68}$	-	-	159	quenched thin film [76]
$Fe_{73}Co_{10}Ga_{17}$	118	10	54	bulk [3]
$Fe_{68}Co_{15}Ga_{17}$	43	29	48	bulk [3]
$Fe_{1-x}Ga_x$	-	-	450	bulk [106]
$Fe_{83}Ga_{17}$	-	-	311	bulk [16]
Fe at.13% Ga	153	-16	-	bulk [16]
$Fe_{86.2}Ga_{12.4}Sn_{1.4}$	-	-	35	bulk [107]
$Fe_{81}Ga_{19}$	-	-	42	thin film [97]
$Fe_{81}Si_{3.5}B_{13.5}C_2$	-	-	31	[54]
$Fe_{78}Si_9B_{13}$	-	-	27	commercial Metglas
FeGaSiB	-	-	17	thin film [6]

are associated with the magnetostriction strain as a function of applied field [55]. Some examples from both of techniques are described in the following subsection.

3.3.1 Direct Measurement

3.3.1.1 Strain Gauge Technique

This method was developed in 1947 by Goldman [108] and is commonly used to measure the magnetostriction of crystal and amorphous materials over various temperature ranges. The strain can be measured down to 10^{-6} and principally measures the change in resistance when the specimen has been elongated. The changes in the resistance can

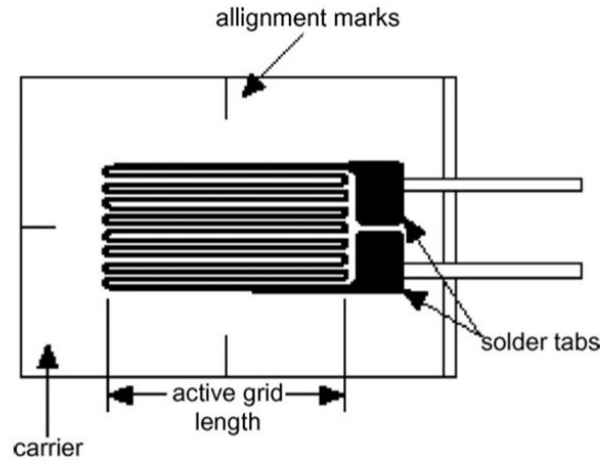

Figure 3.5: Set-up of strain gauge technique. Figure taken from [55].

be measured by the sensitive bridge circuit. The voltage chance, ΔV across the bridge is associated to the gauge factor, G and the strain by $\varepsilon = 4\Delta V/(GV_0)$, where V_0 is the applied voltage to the bridge. The gauge factor, G is the ratio between the fractional resistance change and the fractional length change which is $\Delta R/R = G\varepsilon$. The strain causes the elongation $\Delta L/L$. The schematic diagram of strain gauge set-up is shown in Figure 3.5. For measurement due to temperature and magnetic field, the dummy gauges were mounted onto a nonmagnetic material near the specimen so that it experiences the same temperature and magnetic field. This dummy gauge must have the same thermal properties with the one on the sample as if there is any thermal drift, it will change the strain of both gauges, so that as temperature coefficient is the same, so that there is no change in the output. The same way with any magnetic field changes, hence the magnetoresistance for both are similar [109]. This then provides the accuracy of measurement of magnetostriction using the strain gauge technique [110].

3.3.1.2 Capacitance Method

Tsuya [111] designed the capacitance cell method to measure the magnetostriction of spherical samples. This method measures the variation in capacitance across two electrodes, one of the electrodes moves with the samples dimension change and the other one is fixed. The schematic diagram of capacitance cell in measuring magnetostriction of spherical sample is presented in Figure 3.6. In this method, capacitance cell was put in a uniform magnetic field. The capacitance across these two electrodes was measured

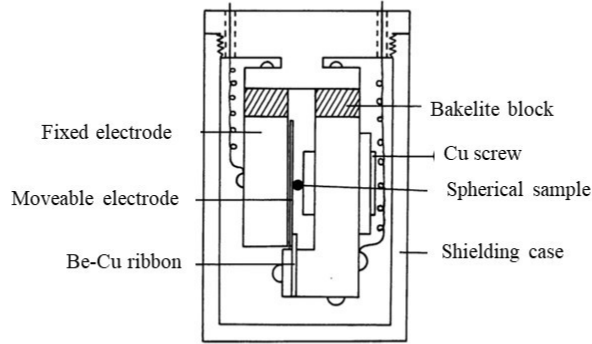

Figure 3.6: Schematic diagram of capacitance cell. Figure taken from [111].

by the capacitance bridge and lock in amplifier. When the change of dimension of the sample changed by Δd from d (the distance between two electrodes), the capacitance, C also change to $\Delta C + C$. The relationship between Δd and ΔC can be shown by:

$$\Delta d = -\varepsilon_0 S \Delta C/(C – C_0)^2 \tag{3.1}$$

where ε_0 is the dielectric constant, S is the area of electrode and C_0 is the stray capacitance between the lead wires which determined experimentally from the relationship between capacitance and the distance. From this equation, the magnetostriction (dimension change) can be determined and its proportional to change in capacitance, ΔC. A similar technique was also been discussed by Boley [112] whereby they observed the capacitance change at a high frequency rate by a capacitance bridge meter.

3.3.2 Indirect Measurement

3.3.2.1 Cantilever Deflection Method

For an indirect technique, an external stress is applied by either stretching, pressing or bending the sample, thus the magnetostrictive strain can be determined [113]. One example is the cantilever deflection method under a magnetic field, which was introduced by Klokholm [114]. The laser beam deflection method was then established by du Tremolet de Lacheisserie et.al [115] as shown in Figure 3.7. A film with length, L (distance between O and A) attached on a non-magnetic substrate are in a deformation

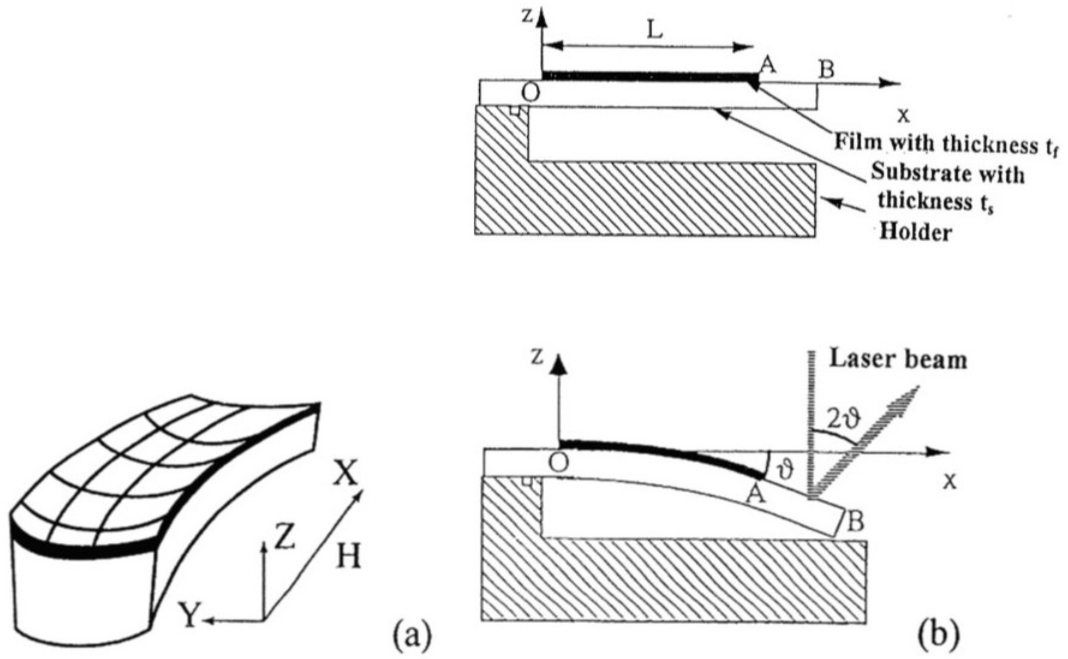

Figure 3.7: Cantilever deflection method. Figure taken from [115].

state (A-B) when a magnetic field is applied, H. In that figure the positive magnetostriction is along its length, while the deflection angle, θ is derived in terms of the mechanical properties (elastic modulus and Poisson's ratio) and thicknesses of both film and substrate. This method has been applied by Hunter [75] in measuring the effective magnetostriction constant, λ_{eff} of their FeCo films. In their experiment, the cantilevers are bent as the magnetic field is applied. The displacement of the cantilever when the field was applied parallel and perpendicular was recorded by a sensitive detector. The magnetostriction constant was then determined by using the following equation:

$$\lambda_{eff} = \frac{2(D_{||} - D_{\perp})E_s t_s^2(1+\nu_f)}{9E_f L^2 t_f(1+\nu_s)} \tag{3.2}$$

where E_s, E_f, L, t_f, t_s, ν_f and ν_s represent the Young Modulus, sample length, thickness and Poisson's ratio of the substrate (s) and film (f). The $D_{||}$ and $D_{\perp}$ are the measurement of displacement when the applied field is along the length and perpendicular to the width of cantilever, respectively.

3.3.2.2 Strain-Modulated Ferromagnetic Resonance (SMFMR)

This technique was employed by Smith [116] on their investigation of the temperature dependence of magnetostriction for nickel ferittes, nickel ferittes doped Cobalt and Yttrium Iron Garnet (YIG) specimens. Then, Henning and Boef [117] had developed a novel method known as Strain-Modulated Ferromagnetic Resonance (SMFMR) for measuring magnetostriction constants when a strain gauge technique is unable to measure very thin specimen. In this technique, the ferromagnetic resonance line was modulated due to an applied strain. The strain is applied periodically where the sample is placed in the resonator cavity. The magnetostriction constant,λ_s determined by SMFMR technique is related to the resonance field, H_r. The shifted of resonance field, ΔH_r as a result of an applied stress, $\Delta\sigma$ can be expressed by [118]:

$$\frac{\Delta H_r}{\Delta\sigma} = \frac{-3\lambda_s}{M_s} \tag{3.3}$$

where M_s is saturation magnetisation. This technique also had been applied in measuring magnetostriction in the range of temperature from 4.2 K to room temperature [119]. Magnetostriction due to either surface or interdiffusion effects can be distinguished by using this technique [120].

3.4 Ferromagnetic Resonance studies on FeCo-based thin films

Since the characteristics of soft amorphous magnetic materials often include high magnetostrictive, low anisotropy field, other advantages of this material are low damping and high permeability. These properties are demanded for spin-transfer switching devices. The increased development of these kind of materials, occurs along with the development of electronic devices operating at high frequency.

Compositional dependence of the total Gilbert damping, α_{tot} parameter in $Fe_{1-x}Co_x$ grown on Cu/Ta layers have been conducted by Schoen et. al [121]. In their study, the α_{tot} for different phases of CoFe corresponding to BCC, FCC and mixed phases were determined from the fitted frequency linewidth from 5GHz to 40 GHz. A minimum

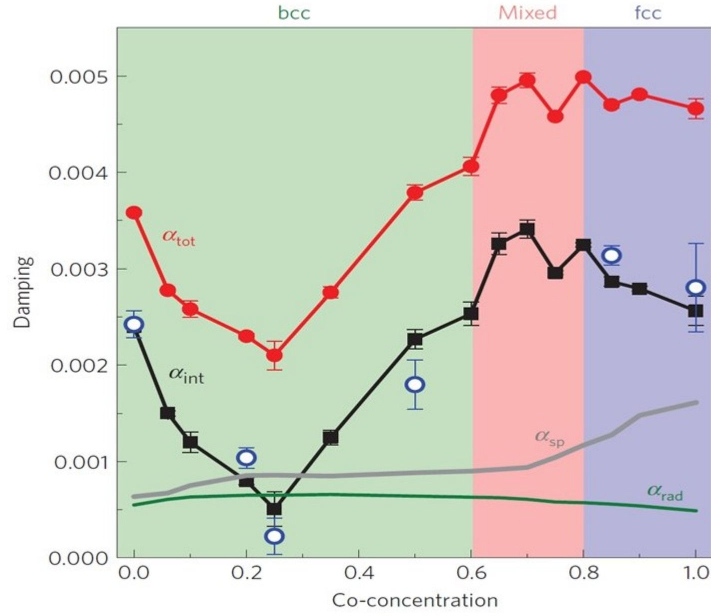

Figure 3.8: Compositional dependence of $Fe_{1-x}Co_x$ on the damping parameters in the regions of phases structures (bcc, fcc and mixed). It presenting damping from radiative, α_{rad} (green); spin-pump, α_{sp} (grey) and calculated intrinsic, α_{int} (black). The total of damping,α_{tot} contributed by α_{rad}, α_{sp} and α_{int} shown by red-line. Also shown the α_b for bulk value (open-circle). Figure taken from [121].

α_{tot} was found at the Co composition 25% (α_{tot}= 0.0021) in the BCC phase. Their total damping results showed the contribution from radiative damping, α_{rad} due to the inductive coupling of the co-planar waveguide and precession magnetization. For very thin films at low magnetization, the α_{rad} could be neglected. Another contribution was from the damping spin pump, α_{sp} into adjacent Cu/Ta layers. These are extrinsic contribution factors, thus allowed them to determine the intrinsic damping ($\alpha_{tot} = \alpha_{rad} + \alpha_{sp} + \alpha_{int}$). The graph of dependence on those damping parameters with the Co concentration within diffrent CoFe structures are presented in Figure 3.8. The obtained α_{int} from this study had a very low magnitude ($\alpha_{int} = 10^{-4}$) and they suggested due to the band structure of the CoFe systems.

The dynamic properties of polycrystalline $Fe_{1-x}Co_x$ (thickness = 10 nm) on different substrate (sapphire, MgO and silicone) were studied by Weber et. al [122]. A seed layer of Ta was deposited prior the FeCo growth, then followed by depositing a Cu layer. The Cu interlayer was grown to suppress the intermixing between the CoFe and Ta and to promote the growth of films with low damping properties. At compositions around 18% to 33% on Si and MgO, the minimum damping factor were identified, but there was

no remarkable difference on the value of damping between the three substrates. They reported that the low damping for all substrates for the same compositions originated from electron-magnon scattering with the effective damping of the CoFe below 5x10^{-3}. They further investigated the annealing effect on the damping magnitude of the films whereby they obtained a reduction in the magnitude with annealing, with the lowest magnitude at α = 3.6x10^{-3} for film grown on the Si. The improvement of crystallinity by annealing CoFe at $530^{o}C$ was believed to reduce the damping value.

Conca et.al [42] studied the magnetic properties of amorphous $Co_{40}Fe_{40}B_{20}$ as-deposited thin films by rf sputtering with thickness of 75 nm. The saturation magnetisation and damping properties were measured by means of a Vector Network Analyzer (VNA). The magnetic anisotropy of the films was determined by a MOKE system. They identified a smooth surface of the film reflecting the amorphous structure of CoFeB. The films also showed weak uniaxial property with the coercive field along the easy axis was found to be 240 Am^{-1}. Their film's value for the saturation magnetisation were fitted according to the Kittel's formula was 1250 kAm^{-1}. An example of their fitted plot is shown in Figure 3.9, where they found a damping parameter, α = 0.0042. Another study of CoFeB was performed by Devolder et.al [123]. This paper reported how compositions of Fe-Co in two different states; amorphous (as-grown) and crystalline (annealed for 2 hours) affected the gyromagnetic factor, g and the damping constant of CoFeB films. The films grown for both as deposited and annealed compositions were $Co_{20}Fe_{60}B_{20}$, $Co_{40}Fe_{40}B_{20}$ and $Co_{60}Fe_{20}B_{20}$. For the as-grown (amorphous) films, the Fe-rich films had g-factors close to 2.16, which were smaller than the Co-rich(2.18) films for amorphous and crystalline samples. This implies that the g-factor of Co is larger than Fe, as it has a 28% larger spin-orbit coupling. The damping constant of the crystalline sample films increased, which they suggested was due to the increase in the g-factor. For instance the crystalline sample $Co_{60}Fe_{20}B_{20}$ had α= 0.016 larger than the amorphous $Co_{40}Fe_{40}B_{20}$, α= 0.014. The high damping constant of their materials made them less interesting to be used in spin-torque based application.

Bi et.al [124] carried out the effect of variation in film thickness on the microwave properties of amorphous FeCoNbBCu. The films grown by rf magnetron sputtering at room temperature varied in thickness from 70 nm to 450 nm. The films showed higher permeability both in real ($\mu^{'}$ = 852) and imaginary ($\mu^{''}$ = 1495) as function of film thickness. One drawback of this research was the damping constants for their films were

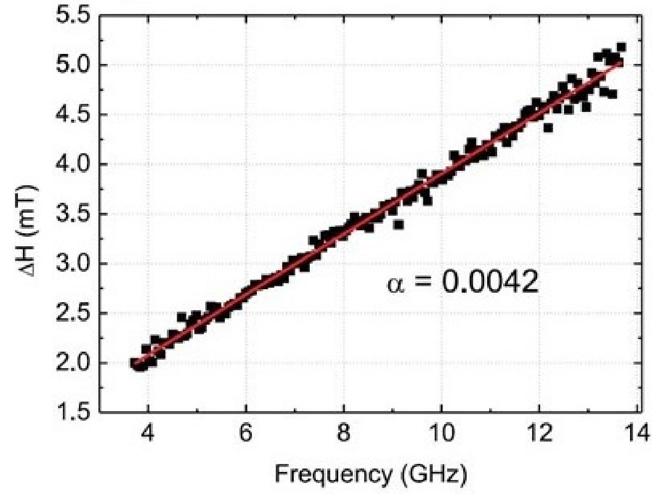

Figure 3.9: The plot showing linewidth dependence on the FMR frequency of CoFeB film thickness 75nm that fitted to Kittle's formula. Figure taken from [42].

Table 3.2: Magnetic damping constant, α of ranges of thin film materials.

Material	**t(nm)**	**Method**	**Damping constant (α)**	**References**
$Fe_{52}Co_{48}$	540	electrodeposition	0.109	[125]
$Fe_{1-x}Co_x$	10	co-sputtering	0.0036	annealed [122]
$Fe_{20}Co_{80}$	40	ion-beam	0.013	as-deposited [126]
$Fe_{18}Co_{72}B_{10}$	25	ion-beam	0.006	as-deposited [126]
$Fe_{18}Co_{72}B_{10}$	25	ion-beam	0.0019	annealed [126]
$Fe_{40}Co_{40}B_{20}$	75	rf magnetron sputtering	0.0042	[42]
$Fe_{60}Co_{20}B_{20}$	1	dc sputtering	0.014	as-deposited [123]
$Fe_{40}Co_{40}B_{20}$	1	dc sputtering	0.012	annealed [123]
FeCo	110	magnetron sputtering	0.018	[127]
$(FeCo)_{0.84}Gd_{0.20}$	110	magnetron sputtering	0.008	[127]
FeGa	21	molecule beam expitaxy	0.017	[12]
FeGaC	40	sputtering	0.0027 (9% C)	[128]
$Ni_{80}Fe_{20}$	3	dc magnetron sputtering	0.0136	[129]
$Ni_{80}Fe_{20}$	10	dc magnetron sputtering	0.0080	[129]
NiFeCr	20	Cr-ion implantation	0.024 (4% Cr)	[130]

larger, between 0.0151 and 0.0368. They showed relatively higher damping for thinner films, which they deduced was attributed to the presence of interface defects for instance, the stress. The damping constants determined from previous studies is summarized in Table 3.2.

3.5 Mechanical Properties of FeCo-based Films

Compared to the conventional measurement on the elastic modulus and the hardness of material, a measurement of elastic and plastic deformation of thin film material in nanometer scale can be probed by using depth-sensing indentation also known as the nanoindentation technique. However there was a very little studies have been reported on the investigation of the mechanical property notably of FeCo in thin films. Chan et.al [131] studied the mechanical testing on different thickness of FeCo films which were deposited on Ti–6Al–4V substrate. The substrate surface was prepared by different conditions such as EDM (electrodischarge machining), electropolished and mechanical polished. The elastic modulus, hardness and yield strength were measured by using standard Berkovich diamond tip by technique of MTS® Continuous Stiffness Measurement (CSM). The FeCo (4.1 μm) deposited onto EDM Ti–6Al–4V substrate had the highest Young's modulus (206 GPa) among the other substrates surface, but the lower hardness (8.7 GPa) and yield strength (2830 GPa) compared to the 0.9 μm sample, on the same substrate surface; whose hardness was 165 GPa and yield strength was 3470 GPa. The 4 μm sample on the substrate mechanically polished had smaller values of hardness (8.2 GPa) and yield strength (2730 GPa) as compared to the 1 μm sample (hardness = 8.8 GPa; yield strength = 2930 GPa). However the FeCo/Ti–6Al–4V (eletropolished) sample had a very large hardness about 10 GPa compared to the others. The mechanical properties of FeCo/Si were also evaluated, and were found to be smaller than FeCo/Ti–6Al–4V. The values were found 165 GPa, 5.5 GPa and 1830 GPa in respective to Young's modulus, hardness and yield strength.

The mechanical properties of magnetostrictive FeCoGa were reported by Jen et. al [132], however the details on nanoidentation experimental was not described in the paper. The films prepared on the glass Corning substrate by dc magnetron sputtering with 250 nm thick and different composition of Co. They compared the elastic modulus, E_f and the hardness, H_f to the bulk and found that their findings did not agreed with the bulk result. In the reported bulk, the Young's Modulus, E_b increased monotonically with increasing the Co contents. Their analysis found that the Young's Modulus of film, E_f initially increased when the Co composition increased to at.% 3 (140 GPa). Then it dropped to 125 GPa for film at.% 11, before it jumped again to 145 GPa (at.% 15). The hardness reduced from 7.5 GPa to 5.7 GPa in the range of Co = at.% 11 to at.% 19.

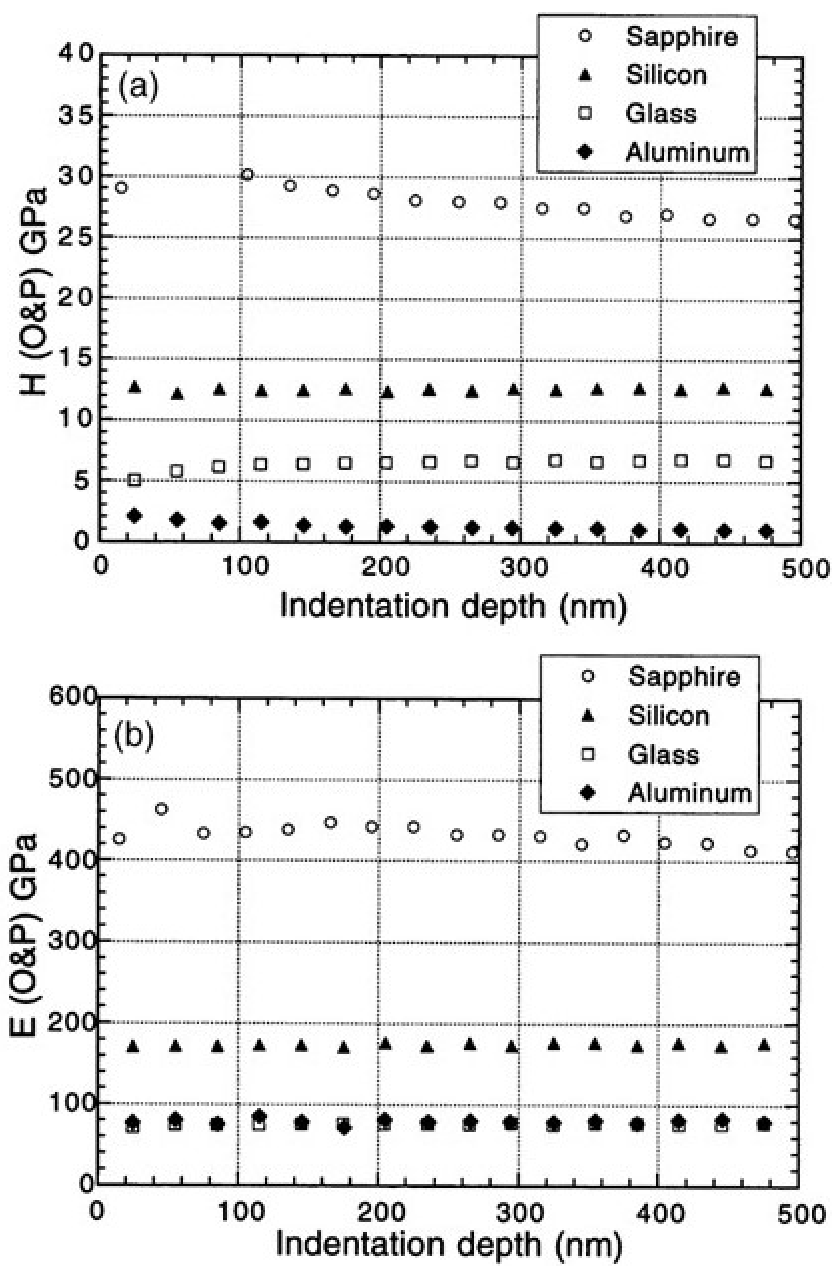

Figure 3.10: The average of hardness and modulus of different substrates. The values determined by standard method of Oliver and Pharr. Figure taken from [133].

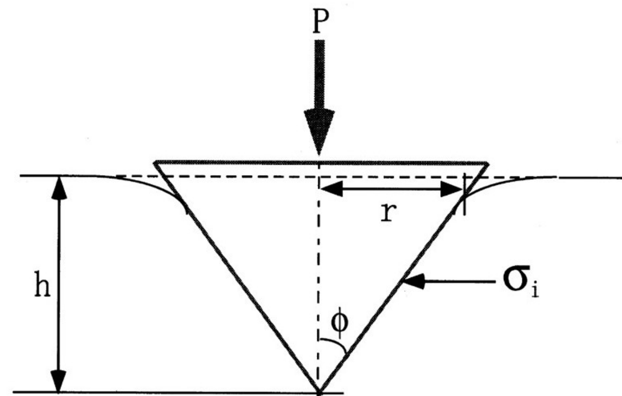

Figure 3.11: The schematic diagram of indenter pressing the film surface, showing the existence of internal stresses based on Sneddon's analysis. Figure taken from [134].

In order to ensure only the true film's contact area and hardness are being measured, it is necessary to investigate the effect of substrate during conducting the nanoidentation experiment on thin film materials. The effect of different substrates (sapphire, glass, silicon and aluminum) on the mechanical properties of aluminum had been studied by Saha and Nix [133]. The Al films fabricated by the sputtering method with a range of thicknesses (Al = 0.5, 1.0, 1.5, and 2.0μm). The nanoidentation measurement performed by a Berkovich tip and operated in continuous stiffness mode (CSM). There were 10 indentations made for each sample to a depth of 500 nm. They determined that Sapphire had the largest hardness (30 GPa) and modulus (440 GPa), followed by the Si with hardness and modulus 12.75 GPa and 172 GPa, respectively. For glass and Al, they were found to have almost the same modulus (Al = 75 GPa and glass = 73 GPa). The hardness for Al was found lower (0.95 GPa) than the glass with 6.8 GPa. The plot of these properties are presented in Figure 3.10. Further, they did nanoidentation to the Al films on these four substrates in order to determine the substrate contributed to the measurement. Their analysis showed that in the range $0.05 < h/t < 0.2$; (h/t = depth of indentation as function of film thickness), the values were constant for all substrates. Nevertheless, an increase in hardness with depth was observed at $0.2 < h/t < 1$ which was more pronounced at $h/t > 1$. This reflects the influence of the substrate to this measurement. They suggested due to the Al was being a soft material compared to glass, sapphire and Si results in a much smaller load. Hence, the indenter tip start to penetrates the hard substrates. For modulus measurement, again they found a substrate contribution at smaller film thickness, with a very significant effect on sapphire substrate.

The effect of internal stress on the mechanical properties have also been studied by Chuang et.al [134] as they suggested that internal stress induced from the fabrication process also contributed to modulus and the strength of the measured materials. This paper investigated the Ti films thickness 200 nm on Si substrate evaporated with different deposition rate (0.1, 0.3, and 0.5 $\text{Å}s^{-1}$). The internal stresses of their films were defined from the substrate curvature method, which were measured by a surface profiler. Both hardness and modulus properties were calculated according to Oliver and Pharr standard method. Their results showed an increase in internal stresses with rate of deposition. The increase in internal stress affected both hardness and elastic modulus, whereby these mechanical properties decreased linearly with stress. The elastic modulus reduced by 6 GPa when the internal stress increased from 0.3 GPa to 0.6 GPa. They suggested that the internal stress, σ_i increased with the indent depth based on the interpretation from Sneddon's analysis [61] :

$$P_i = \left[\left(\frac{2}{\pi} \frac{E}{(1-\nu^2)} \tan\phi \right) - \pi\sigma_i(\mu\sin\phi - \tan^2\phi\cos\phi) \right] h^2 \tag{3.4}$$

where P_i is total force due internal stress, ϕ represents the half angle of conical indenter that pressing against the film surface and μ is the friction coefficient between the indenter and thin film, as depicted in Figure 3.11.

Recently, the mechanical properties of FeSiB (t= 668 nm) and FeGaSiB (t=640 nm) on Si substrate have been studied by Abbas [135]. This study found that the reduced modulus of elasticity, E_r of FeSiB/Si was 110 GPa and the reduced modulus for FeGaSiB/Si was slightly higher (E_r = 120 GPa) than FeSiB/Si. However, Young's Modulus, E_s for FeSiB/Si was found to be larger (140 GPa) than FeGaSiB/Si (120 GPa), so they concluded that adding Ga reduced the mechanical properties due to the Ga changing the atomic distribution within the film.

Chapter 4

Experimental Techniques

This chapter is devoted to the experimental techniques used in the work, starting from the fabrication of films to the characterization techniques. Understanding the cornerstones of each experimental technique is indispensable in order to investigate the surface topography, structure, magnetic, magnetostrictive, magnetic dynamics and the mechanical properties of the materials. Therefore, various techniques are described in this chapter namely, RF Magnetron Sputtering, Atomic Force Microscopy (AFM), Scanning Electron Microscope - Energy Dispersive X-Ray (SEM-EDX), X-ray Diffraction (XRD), Transmission Electron Microscope (TEM), Magneto-Optical Kerr Effect (MOKE), Magnetostriction Measurement by Villari Effect, Vector Network Analyzer - Ferromagnetic Resonance (VNA-FMR), Superconducting Quantum Interference Device (SQUID) and Nanoidentation.

4.1 Film Fabrication

4.1.1 Sputtering Principle

There are two common techniques of transferring atoms from one or more sources onto a substrate, which are physical vapour deposition (PVD) and chemical vapour deposition (CVD). Physical deposition technique is performed in vacuum condition with the base pressure usually in the range of 10^{-2} to 10^{-6} Torr. For chemical vapour deposition technique usually incorporate thermal cracking of precursors for example silane (SiH_4)

to deposit Si onto the substrate. Common CVD techniques include plasma-enhanced CVD (PECVD), low-pressure CVD (LPCVD) and metalorganic CVD (MOCVD) [136–138]. Unlike CVD, materials to be deposited by physical vapor deposition (PVD) do not involve chemical reactions, but instead the material is condensed directly onto the substrate via a physical process. The most frequent techniques used are thermal evaporation and sputtering. Sputtering is commonly used for different practical applications such as reactive sputtering, DC sputtering, RF sputtering and RF magnetron sputtering that uses a gas such as argon to create a plasma. Reactive sputtering uses reactive gases (oxygen or nitrogen) and targets of metal alloys (for example Al) in order to produce the oxide thin films. In DC sputtering, the target source must be electrically conductive, i.e it has the ability to emit electrons. Different to the DC sputtering, for RF sputtering the target are often insulator materials, which are not electrically conductive. In the RF mechanism, the electrical potential is supplied to the targets in a frequency range between 5-30 MHz, leading to argon gas to become ionised. In RF sputtering technique, a magnetron used as a source that contains magnets which focus the sputtered species to increase deposition rate. The generated magnetic field will confine secondary electrons close to the target. Electrons ejected from the target experience both electric force and magnetic force based on the Lorentz force, (F = qv x B). This allows more electrons to be trapped close to the target and increases the ionization. The advantages of the sputtering methods over the thermal evaporation are the uniform thickness and stoichiometry of the film which can be produced as well as the flexibility to fabricate amorphous and crystalline materials [136].

The basic principle of sputtering, is that atoms are ejected from the target when high energetic particles for example inert gas plasma (Ar^+ ions) strike the target. In this process, the energetic ions are produced by the ionisation of the argon gas to form a plasma. Plasma is the fourth state of matter and in this case the source is Ar^+ ions. When the target is supplied with a high negative voltage, the Ar ions which have positive charges are attracted towards the target. The collision between the target atoms and ions yield knocked out atoms, which travel across the deposition chamber, and are then deposited onto the substrate as films. The ratio between the number of incident ion and the number of sputtered atoms is refer to the sputter yields, Y [139] or the efficiency of sputtering [140]. The yields are related to binding energy of an atom to the surface of solid material [138]. It is well known that the properties of sputtered

films (microstructure, magnetic, optical and electrical) are influenced by the sputtering parameters.

Gas Pressure

To optimize the films properties, it is necessary to carefully choose the appropriate argon gas sputtering pressure. At high sputtering pressure, the number of sputtered atoms increase but the mean free path of the atoms decrease. This is caused by the collisions between the sputtered atom and the ionised gas which are increased before the atom reaches the substrate, leading to a lower deposition rate. Inversely, at low gas pressure, the mean free path increases, thereby the sputtered atoms will deposited onto the substrate at a higher deposition rate as the number of collisions are reduced. Also the pressure of the gas can be correlated to the film thickness and the element concentrations as reported in the literature [141] by study the effect of sputtering parameters on Tb-Fe films. They found by increasing the Ar pressure, the film thickness reduced, which attributed to the large number of collision between the atoms and the Ar ions. They also found at higher pressure, the concentration of Fe reduced, indicating that the scattering of Fe by Ar ions is more pronounced than Tb atom, due to Tb being heavier than Fe.

Substrate Temperature

The substrate temperature, T_s affects the microstructure of sputtered films similarly to the gas pressure. The effect on substrate temperature is given by the Model of Zone Structure by Thorton [142] described in Section 4.2. For the final stages of microstructure formation, increasing the the substrate temperature tends to promote coarser grains, hence the single crystal growth. It was inferred that the deposition rate increased with the substrate temperature [136].

Sputtering Power

The sputtering power also plays a role in changing the structural phase and the roughness of the sputtered films. The morphology of the films is dependent on the sputtering power, as previous research found that at higher sputtering power the surface roughness of films increased with the formation of coarser islands. At fixed pressure but higher power, many atoms are sputtered from the target reflecting the higher kinetic energy in the form of thermal energy. This energy increase the number and momentum of the atoms and reduces the mean free path. This means at the substrate, there is a

greater surface diffusion. This implies that the films crystallinity could be improved by increasing the sputtering power [141, 143].

Target-Substrate Distance

The geometry of the sputtering system such as target-substrate distance also affects the sputtering rate, similarly to the sputtering pressure [144]. The surface diffusion of the atoms are greater when the target-substrate distance decreases. The films stress also depends on product of the pressure and target-substrate distance ($P - d$). Films with compressive stress are grown at a lower Pd, while for a higher Pd, films with tensile stress were produced.

4.2 Thin Film Growth and Film Stress

4.2.1 Modes of Film Growth and Microstructure

As this study deals with samples in thin film form, it is beneficial to understand what are the mechanisms associated with the deposition of thin films onto a substrate. The formation of thin films involves four stages; nucleation, islands formation, islands coalescence and the growth. In the early stage of nucleation, small nuclei or vapor atoms are condensed and deposited onto the substrate. When they impinge on the substrate, they lose their energy in order to accommodate themselves on the substrate surface. As the nuclei grow, cluster or island formation takes place and rapidly saturate [145]. Following islands formation is coalescence. The islands coalescence is believed to involve with different transport mechanisms, including Ostwald ripening. In Ostwald ripening, when there are two islands, which are different size and are not very far from each other, there is a difference in concentration gradient of the adatoms. This is because since the adatom density near the smaller island is higher than the larger island. Therefore the diffusion of atoms is from the higher density to the lower one. The smaller adatom will shrink and the larger one then will grow or "ripen" with time, so is referred to as Ostwald ripening. This mechanism does not involved the direct contact between the two islands. Another mechanism of islands coalescence is cluster migration when the two separated islands that are assumed to be like a droplets collide on the substrate surface. This cluster migration is related to the thermal energy, E_C and the surface diffusion,

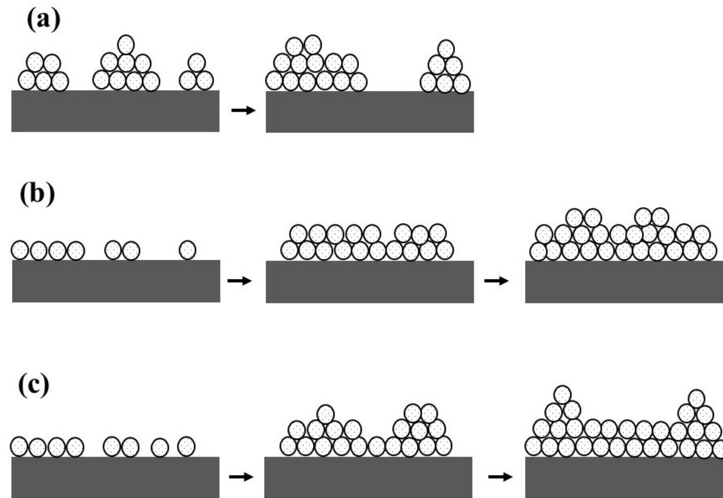

Figure 4.1: Three categories of thin film growth modes (a) Volmer - Weber (b) Frank - van der Merwe and (c) Stranski - Krastanov. Figure adapted from [140].

the smaller the cluster the higher the migration. Then, the islands continues to merge, filling the gap between them until a continuous film is formed. It is said that the film thickness in these early stages of film formation is about few hundred Å of film thickness [140].

It has generally been accepted that the thin film structure formation is incorporated by three basic growth modes which largely involve adsorption, atoms diffusion and the binding between atoms and surfaces. The schematic diagram of each growth mode is shown in Figure 4.1. In Volmer - Weber growth also known as islands formation, the small atoms impinge on the substrate are strongly bound to each other rather than to the substrate and have a slow diffusion. Therefore, they form islands and grow in the three dimension. Conversely with the Frank - van der Merwe mode, the diffusion is very fast as the atoms are more strongly bound to the substrate. When the first monoloyer is completed, then the growth continues by forming another layer. Thus this mode is also defined as layer-by-layer and such that a single crystal (expitaxial) structure can be produced from this mechanism. A third mechanism of film growth, which combines layer-by-layer and islands growth is called Stranski - Krastanov. The atoms tends to attached to the substrate to form a monolayer and once the layer has been established, the atoms gather to continue the growth in islands form [136].

The film growth determines the characteristics of the material in terms of its surface

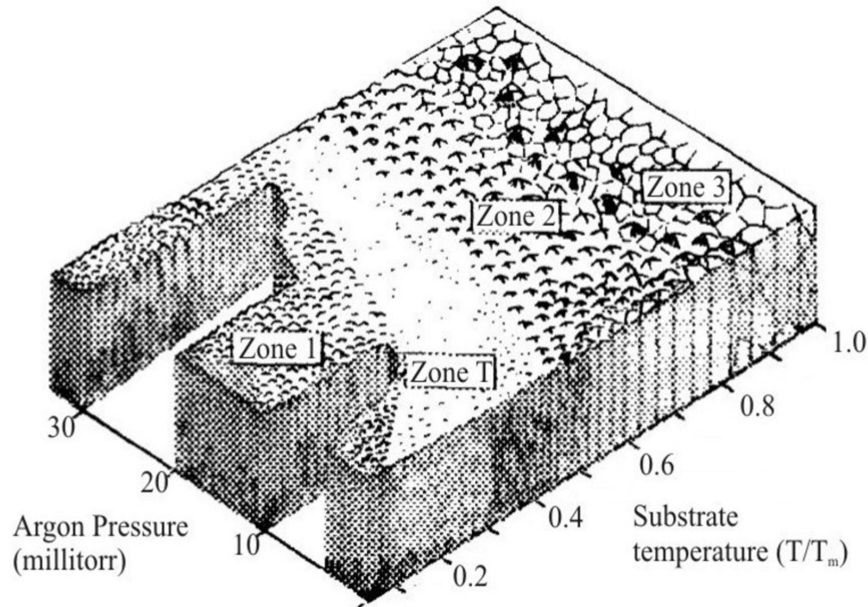

Figure 4.2: Model of Zone Structure for sputtered materials. Taken from [142].

morphology and the grain size. Movchan and Demchishin [146], who first introduced the structure zone model for evaporated coating describes the morphology of materials as function of substrate temperature. Later, Thornton [142] introduced the structure zone model for thick sputtered films by adding the factor of argon pressure from the original model proposed by Movchan and Demchishin. The structure zone model by Thornton as shown in Figure 4.2 can be described as follows :

(a) Zone 1 : In this zone, a porous structure with voided boundaries is produced as a result of the substrate roughness and oblique deposition.
(b) Zone T : This zone is the transition between Zone I and II where a fibrous structure without voided boundary due to the high bombardment particles from the sputtering target at low argon pressure occurs.
(c) Zone 2 : This region is dominated by the surface diffusion of adatom ($T/T_m > 0.3$), which T_m is melting temperature, columnar grains forms and increase in the grain size.
(d) Zone 3 : High columnar structural can be observed in this region occurs at high substrate temperature ($T/T_m > 0.5$) as characterized by bulk diffusion, which allows recrystallization and densification.

4.2.2 Stress in Thin Film

Knowledge and understanding about stress in thin film is very important because the stress can lead to several problem like fracture, delamination and affects to the microstructural feature of materials, which can be detrimental for MEMs devices. The origin of film stress can be divided into two categories; intrinsic (growth stresses) or extrinsic (induced stresses) [147]. For the intrinsic stress it can be affected by the deposition conditions and substrate temperature, while the extrinsic stress usually arises after deposition from the different thermal expansion between the thin film and the substrate [136]. The origin of the stress due to the growth was initially proposed by Hoffman [148] where the tensile stress in polycrystalline films was created during the early stage of film growth (island coalescence), as a result of grain boundaries formation. The grains which are separated by atomic distance, d pull together to form a boundary, such that the tensile stress is developed more as the coalescence continues. Tensile stress can become relaxed when as the film growth continues to develop and eventually compressive stress is introduced. The compressive stress is believed to be due to the excess number of the adatoms into the grain boundaries, which are driven by the surface chemical potential [149].

In general, films bonded with the substrate are in a stressed state either in compressive stress or tensile stress. For films which are grown at elevated temperature, thermal stress can be introduced. This thermal stress also dubbed as thermal mismatch stress occurs when two materials are attached together having different thermal expansion coefficient, $\alpha_{T,s}$. Consider a thin film deposited at a deposition temperature, T_d on the substrate, both film and substrate are at initial, T_d and film is said to be in a stress and strain free. However, when film and substrate were allowed to cool down to room temperature, T_r, an extrinsic stress occur due to the thermal mismatch between two different materials. Because of the film attached to the substrate, both of substrate and film must have the same strain when they were cooled down. Since the substrate thickness is thicker than the film, the strain experienced by both materials is similar as the thermal strain of the substrate alone. By assuming a constant thermal expansion coefficient for the substrate, $\alpha_{T,s}$, the total of strain experienced by the substrate, ε_s can be written as:

$$\varepsilon = \varepsilon_s = \varepsilon_s(T_d) + \alpha_{T,s}(T_r - T_d) = \alpha_{T,s}(T_r - T_d) \tag{4.1}$$

where $\alpha_{T,s}$ (T_r - T_d) is a thermal strain when substrate was cooled to room temperature and ε_s (T_d) is the initial strain at deposition temperature and it is assumed to be strain free. The same with the strain free experienced by the film at initial deposition temperature, ε_f (T_d), therefore the total strain of the film, ε_f can be expressed by:

$$\varepsilon = \varepsilon_f = \varepsilon_f(T_d) + \alpha_{T,f}(T_r - T_d) + \varepsilon_{extra} = \alpha_{T,s}(T_r - T_d) + \varepsilon_{extra} \tag{4.2}$$

Based on the above equation however, film experiences with two different thermal strains one from its own thermal expansion when the temperature is cooled down to room temperature, $\alpha_{T,s}$ (T_r - T_d) and the other strain is due to the film dragged along with the substrate, ε_{extra}. Because both materials must have experienced the same strain, so solving both equations above, the resulting extra strain, ε_{extra}, which leads to the thermal mismatch stress. This can be shown by :

$$\varepsilon_{mismatch} = \varepsilon_{extra} = (\alpha_{T,f} - \alpha_{T,s})(T_d - T_r) \tag{4.3}$$

The relationship between the strain and stress for in-plane directions is denoted by :

$$\varepsilon_x = \frac{1}{E}(\sigma_x - \nu\sigma_y) \tag{4.4}$$

$$\varepsilon_y = \frac{1}{E}(\sigma_y - \nu\sigma_x) \tag{4.5}$$

where E is Young's Modulus, ν is Poisson's ratio, σ_x and σ_y are stress with respect to x and y-direction. As the thermal expansion is the same for all directions, $\varepsilon_x = \varepsilon_y = \varepsilon_{mismatch}$, this results in the biaxial stress:

$$\sigma = \frac{E}{1-\nu}.\varepsilon \tag{4.6}$$

By substitute the Equation 4.3 into Equation 4.6, the thermal mismatch stress due to the different thermal expansion can be finally written as :

$$\sigma = \frac{E}{1-\nu}.(\alpha_{T,f} - \alpha_{T,s})(T_d - T_r) \tag{4.7}$$

The film is said in tensile stress when $\alpha_{T,f} > \alpha_{T,s}$ and compressive stress when $\alpha_{T,f} < \alpha_{T,s}$ [137].

4.2.3 Deposition of Films by Nordiko Sputter System

In this project, all the films were fabricated by using the RF Magnetron Sputtering Nordiko NM2000 system. The advantage of using a magnetron sputtering system is that it relies on the magnetron to trap the electrons close to the target, so generates more ionization, causing a higher sputtering rate [150]. The Nordiko Sputter system consists of three main parts; (i) vacuum chamber (ii) pumps system (iii) power control panel. Inside the main chamber, there are three different targets, which are fitted on the same stage. It is also rotatable, allowing one to deposit multilayer films without breaking the vacuum. Each target is clamped by a stainless steel ring and then covered by the earth shields, which is grounded, to avoid contact with the plasma. The mechanical hoist is located the outside and connected to the chamber, so that it can be lifted up for target mounting purpose. The substrate holder positioned above the target, at a fixed distance 6 cm, hence the target-substrate distance is the same for all deposited films. The substrate holder is always stationary during film growth due to the limitation of this system. In the middle of the target and substrate there is a shutter, which can only be opened manually to start the film growth. Beforehand, the Argon gas flows into the chamber through the needle valve to ignite as the plasma. Once the plasma is ignited, it is left for about 10 minutes prior to film fabrication, to stabilize. Argon gas is commonly used in sputtering as it does not react with the sputtered as it is an inert gas.

The second important part in sputtering is the pumping system. There are two types of pumps according to the vacuum range which are mechanical pump (low vacuum pressure) and diffusion pump (high vacuum pressure). The combination of these two pumps creates and maintains high vacuum in the chamber. Initially, the chamber is brought to base pressure $\sim 10^{-2}$ Torr by mechanical pump and monitored by the Pirani gauge sensor (A2). This can be done by opening the roughing valve, which is connected to the mechanical pump, while the others valve is closed. After the pressure in this range is achieved, the roughing valve is closed and then the chamber is exposed to the diffusion pump to achieve a higher vacuum. This is done with the foreline valve and the high vacuum valve being opened to obtain a lower pressure, usually in the range

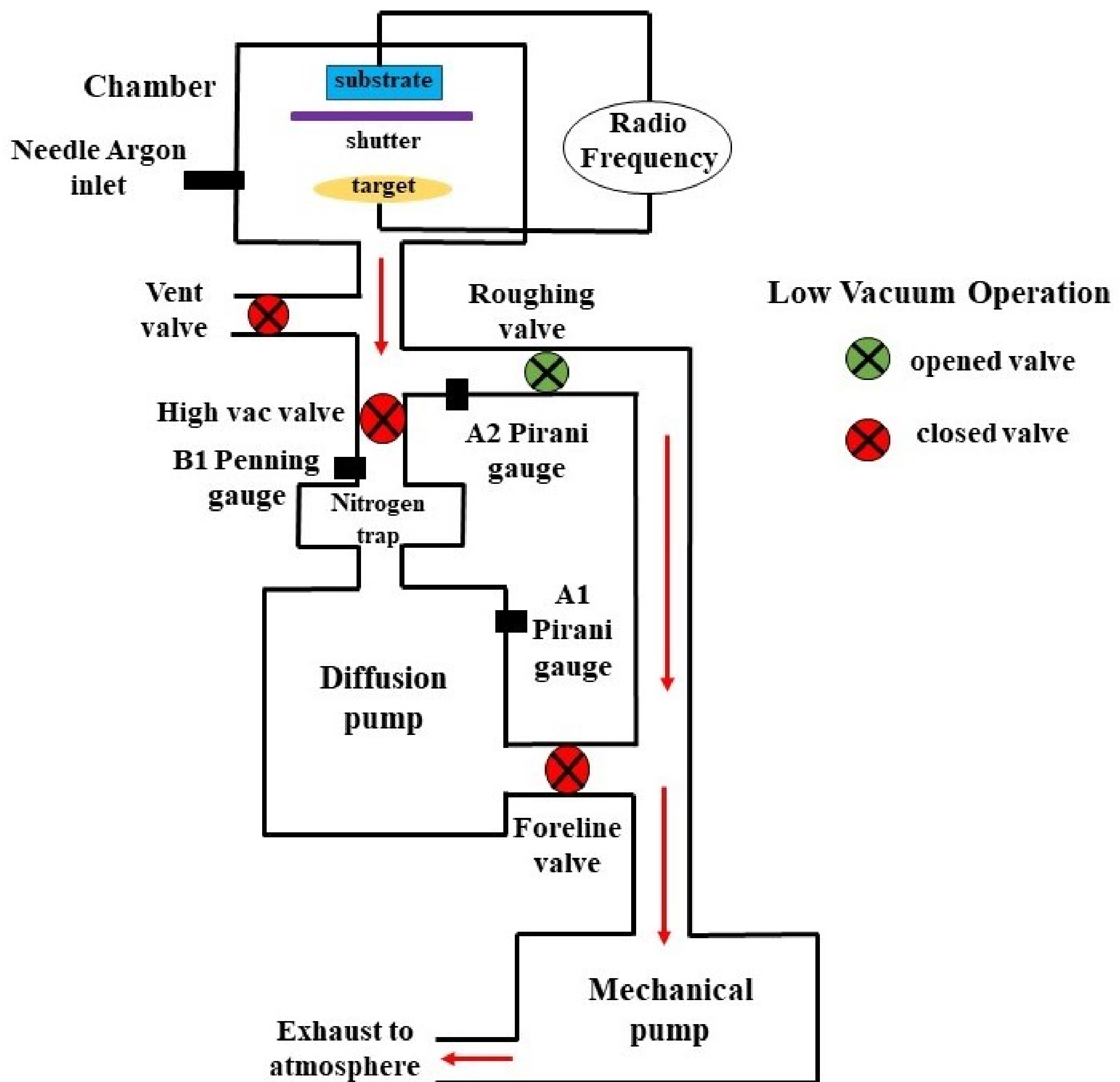

Figure 4.3: The sputter system operation for obtaining low vacuum down to 10^{-2} Torr by mechanical pump through roughing valve.

from $\sim 10^{-5}$ to 10^{-8} Torr. The pressure is observed with Penning gauge (B1) sensor while the pressure for diffusion pump is checked by a second Pirani gauge sensor (A1). The schematic operations of the mechanical pump and diffusion pump in obtaining a lower and higher vacuum in the Nordiko sputter system are illustrated in Figure 4.3 and Figure 4.4, respectively. The system is also supplied with water and equipped with the liquid nitrogen trap between the diffusion pump and the chamber. The liquid nitrogen trap can be filled when the high vacuum valve already opened. The liquid nitrogen is to prevent backstreaming, due to the oils pump entering the system. This situation can affect the efficiency of the diffusion pump [151].

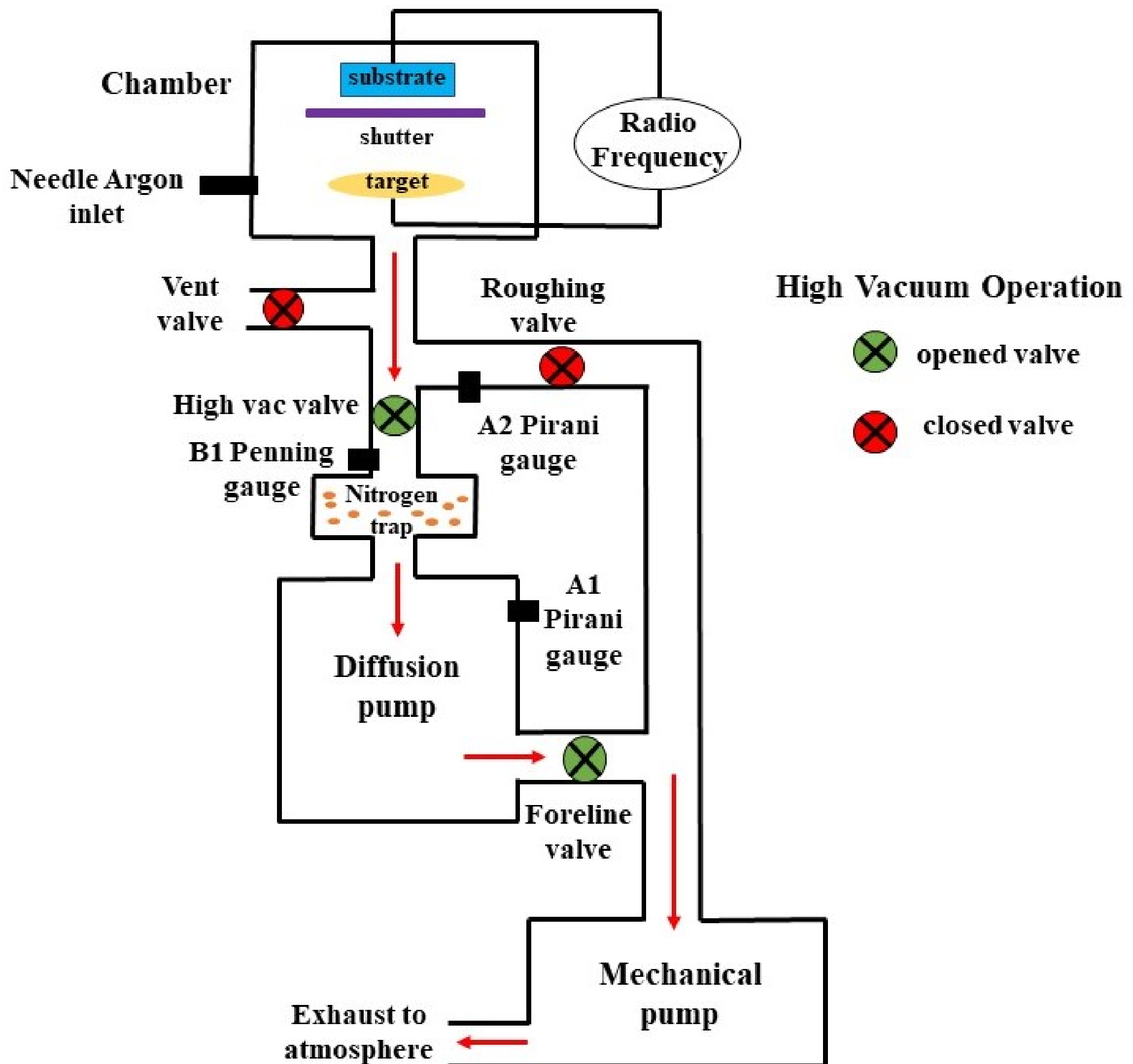

Figure 4.4: The sputter system operation for obtaining higher vacuum down to 10^{-5} to 10^{-8} Torr by diffusion pump through high vacuum and foreline valve.

The third significant part is the RF amplifier which supplies power to the electrodes (target and substrate). The power between the target and substrate is achieved by matching the impedance between them. This enables a higher forward power, with the reflected power being minimized as lowest as possible, to maintain the plasma.

4.2.4 Substrate Preparation and Thin Film Deposition

Prior to deposition, the substrates were cleaned according to the procedures reported in the literature [6]. First, the substrate was put into a beaker and immersed with acetone. Second, it was placed in the ultrasonic bath for couples of minutes to allow the substrate

surface to be free from any contaminants. The substrate was repeatedly clean used the isopropyl alcohol (IPA) before it was dried using the nitrogen. The type of substrate used in this study was silicon wafer (polished) which had a crystal orientation (100), thickness = 380 μm and resistivity (0.001-0.005 Ω.cm).

To characterize the properties of films in terms of its morphology, structural, magnetic, magnetostrictive and mechanical as well as to determine whether the sputtering conditions have significant effect on those properties, various set of films were deposited and divided into different categories as follows :

(i) FeCo : different thickness (50 nm, 70 nm, 100 nm and 120 nm) by applying magnetic field (120 kAm^{-1}) and sputtering power 75 W during growth;

(ii) FeCo : having the same thicknesses as (i) but with no magnetic field during growth;

(iii) FeCoCr : different thickness (56nm, 80 nm, 100 nm, 125 nm and 165 nm) with sputtering power 75 W and magnetic field (120 kAm^{-1});

(iv) FeCoCr : different sputtering power (75 W, 100 W, 120 W and 150 W) with constant thickness, 100 $\pm$ 5 nm thick with magnetic field (120 kAm^{-1}) ;

(v) FeCoCr : different Cr compositions (2.6 at.%, 5.6 at.%, 7.2 at.%, 9.6 at.%) fabricated at the same thickness, 65.1 $\pm$ 0.3 nm, magnetic field during growth was 22.3 kAm^{-1}, and sputtering power of 75 W;

(vi) FeCo and FeCoCr : thicker films ($>$ 400 nm) for nanoidentation measurement were fabricated. The reason for growing thicker films is to meet requirement of minimum thickness that suitable for the size of nanoidentation tip. For this set of films grown at sputtering power 75 W in a presence of magnetic field (22.3 kAm^{-1}).

It is important to note that for the set of FeCoCr films mentioned in (iii) were deposited to determine which thickness had magnetic properties with lowest coercivity, lowest anisotropy field and highest magnetostriction. Later that, film thickness was selected to grow another set of FeCoCr films as stated in (iv) in order to investigate how the sputtering power could affect the properties of the films. From that, the optimized power was chosen to fabricate the next batch of films at different composition of Cr, as mentioned in (v). In this study, the deposition of FeCo film acts as a control sample

to allow a justification on whether the structural, magnetostrictive, magnetic damping and mechanical characteristics of FeCo films could be tuned by adding Cr.

The thin films were sputtered from FeCo and FeCoCr material targets. The FeCo target size was 15 cm in diameter, while a piece of Cr in foil form with dimension (5 mm x 5 mm x 1 mm) was placed on the top of FeCo target for the preparation of FeCoCr films. These two targets were used to deposit films as described in parts (iii) and (iv). Furthermore, to prepare films at different compositions of Cr, the Cr foil was cut into four pieces with dimension for each piece was 2.5 mm x 2.5 mm x 1 mm. This was to vary the Cr percentages, so that a number of Cr pieces can be placed on the top of the FeCo. The sputtering pressure during film growth was kept similar for all films, with a base pressure = 1.0 x 10^{-7} Torr and the Argon pressure = 4.8 x 10^{-3} Torr. All the films were deposited at room temperature and the substrate kept stationary.

4.2.5 Thickness Calibration

For films which were deposited from different sources of targets, the thickness must be calibrated by means of Atomic Force Microscope (AFM). This calibration was needed because different materials have different growth deposition rates. Prior to film growth, a blob of PMMA was put on the surface of the silicon substrate. Then, after the film was deposited, the PMMA were washed away in acetone, to leave behind a small area without film covering. The step height difference between these two areas on the silicon substrate could be measured by Atomic Force Microscope (AFM). Three different areas were scanned and measured to obtain more accuracy on the film thickness. The image of the step height for representative FeCoCr is shown in Figure 4.5. The thickness calibration of FeCoCr is plotted in Figure 4.6. It can be seen that the calibration of FeCoCr did not intercept at the zero point and this was due to the Nordiko Sputter system not having a thickness or growth rate monitor. Instead, the shutter had to be opened and closed manually before and after film deposition. This may have led to some error on the deposition time, hence a perfect calibration graph could not be achieved. In this work, deposition time was adjusted to obtain a series of film thicknesses.

4.3 Atomic Force Microscopy (AFM)

The Atomic Force Microscope (AFM) is one of the microscopy techniques based on the interaction between a cantilever tip and the surface of sample, allowing surface images of different ranges of material to be analyzed. There are three types of operation modes which are contact, non-contact and tapping mode. Principally there are two forces generated either repulsive or attractive depending on the distance between the surface and cantilever tip. The cantilever is bent as a result of the forces between the tip and the sample. When the tip and sample are separated by some distance, the attractive force increases, while as the atom of the tip and the sample are brought closer to each other the repulsive forces progressively increase weakens the attractive forces [152].

In this study, tapping mode or also known as intermittent mode was employed using the AFM DimensionTM 3000 in order to measure the thickness and the surface roughness, R_a and the root mean square roughness, R_{ms} of the films. The cantilever tip was mounted at the end of piezoelectric tube. The tip used was made of silicon, had a resonant frequency 300 kHz, spring constant = 26 N/m, and dimensions 160 μm x 40μm. The back side of the tip was coated with aluminum to act as a mirror to reflect a laser beam. Before measurement of the surface roughness or thickness, the laser and detector alignment had to be adjusted. Good alignment was needed to ensure the cantilever drive frequency could be tuned. The drive frequency determines the frequency at which the cantilever oscillates near to the resonant frequency of the cantilever and must be 10 percent off the voltage amplitude. The drive frequency is very important to improve the performance of scanning in the AFM tapping mode. The cantilever oscillated by the piezoelectric tube at or near the cantilever resonant frequency. When the tip is in non-contact with the surface, the cantilever will oscillate at a higher amplitude and its magnitude will reduce once the tip makes a contact with the sample. The tip is deflected when it encounters the sample's surface, as a consequence this deflection changes the laser beam position in the photodetector and the signal from the photodetector is rectified. In tapping mode, the RMS voltage is compared to a setpoint voltage by the feedback system, as the RMS magnitude is proportional to the amount of cantilever motion. The tip engagement requires the setpoint voltage to be smaller than the RMS voltage. The schematic operation of AFM in tapping mode is depicted in Figure 4.7 [153].

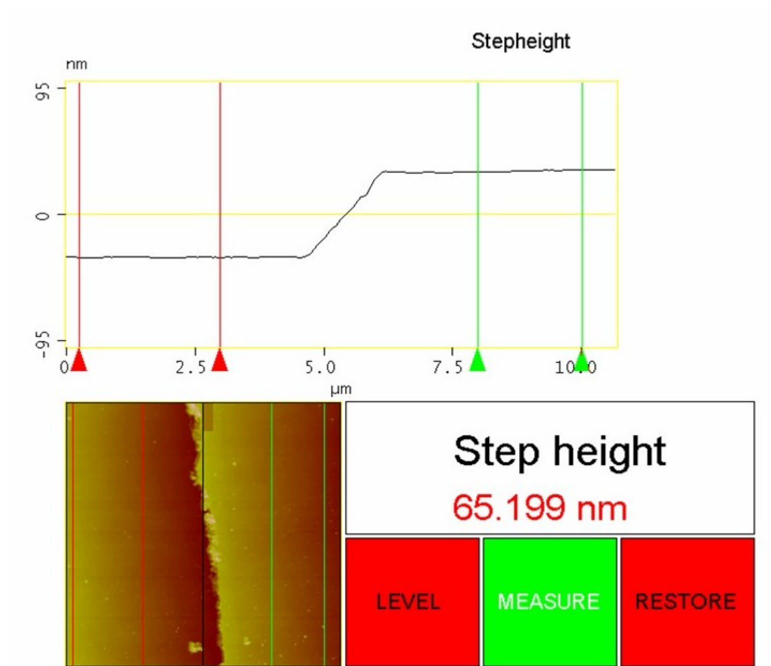

Figure 4.5: An image on difference in stepheight between FeCoCr film and substrate to determine the film thickness.

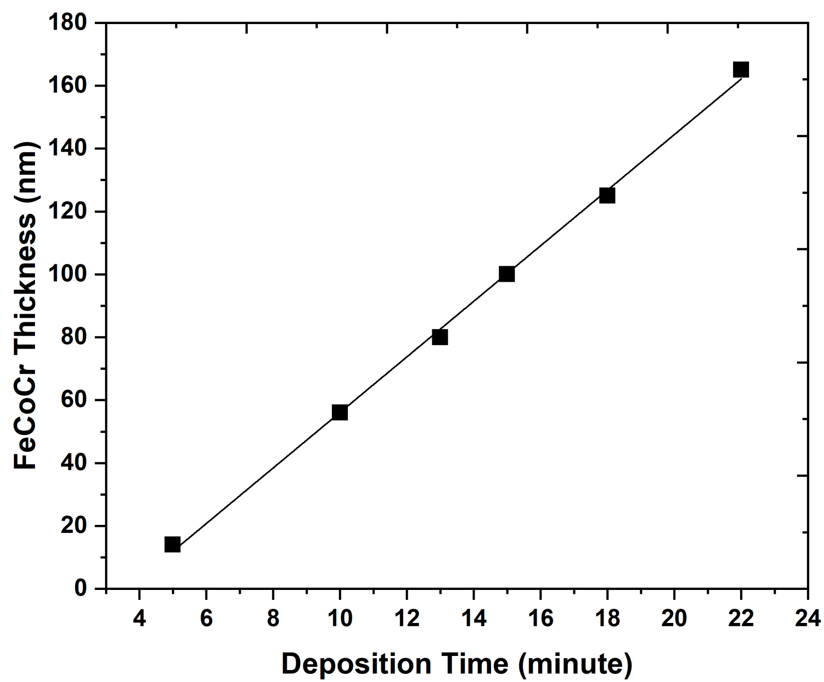

Figure 4.6: Graph of thickness calibration of FeCoCr with varied deposition time

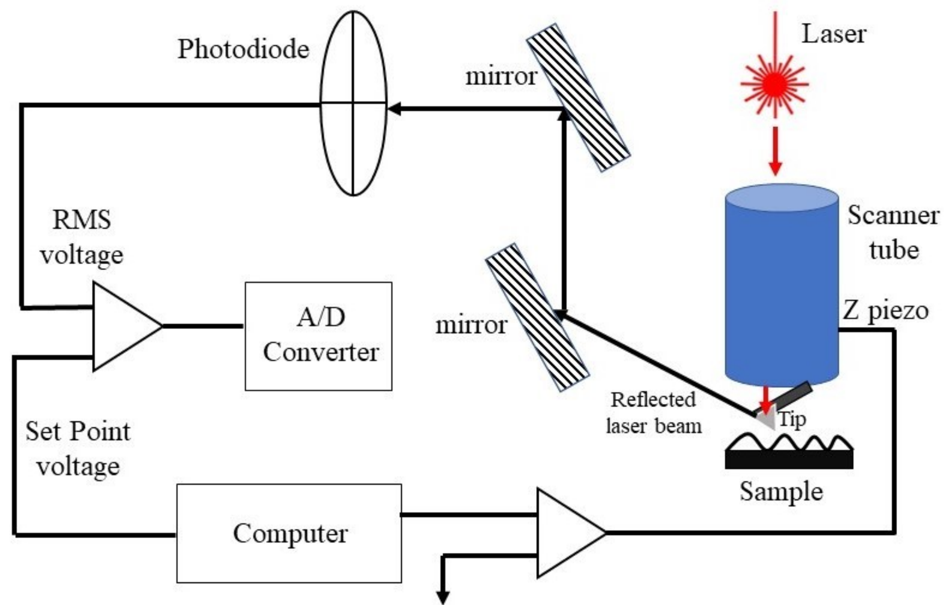

Figure 4.7: Schematic operation of AFM in tapping mode. Figure adapted from [153]

4.4 Scanning Electron Microscope and Energy Dispersive X-Ray (SEM-EDX)

A Scanning Electron Microscope is used to image and analyze the topography of a wide ranges of bulk samples, based on the principles of electron acceleration through a difference voltage, from 0.1 keV to as high as 50 keV. The electron beam is emitted thermionically from the electron gun made of tungsten, then is focused usually by two condensers. A double deflection coils deflect the beams in x and y axes which scans the images in a raster across the specimen [154]. Basically, the interaction between electron and different penetrations depth or interaction volume of matter will produce different electron energies as illustrated in Figure 4.8. The image resolution in SEM is determined by the characteristics of the interaction volume. The release of secondary electron (SE) and Auger electron (AE) are from the interaction between the electron beam and a thin section at the surface of specimen which is nanometer thick, thus this provides the surface morphology of the specimen. For backscattered electrons (BSE), it is used to distinguished the contrast of heavy elements i.e. those with large atomic number, Z appears more brighter in the image.

While the Scanning Electron Microscope (SEM) is utilised to image the sample's surface.

It is based on the interaction of electron both elastic and inelastic with the sample, the Energy Dispersive X-ray (EDX), which is usually integrated with SEM machine was used to analyze the elemental composition. The elemental analysis by SEM-EDX is a result of X-Ray production from the interaction between the electrons and sample. The X-Ray can be generated by two process; either by the transitions of electron from a filled state into the empty state (lower shell) with a characteristics X-ray is being released, or from the deceleration of charged particles (X-ray continuum). To enable element identification possible using the characteristic X-Ray emission line from M, K and L series. Light elements, they emit X-Rays of the K series only, intermediate elements emit K and L series X-rays, and high atomic number generate X-rays of L and M series. In the case of Fe, Co, and Cr all these elements generate X-rays of the K_α and L_α energy series [155].

In this study, two different types of SEM-EDX were used to identify the percentages of each element of Fe, Co and Cr. Firstly, samples of FeCoCr fabricated at different sputtering power were analyzed by using SEM Model Quanta FEG 650 equipped with EDX Model X-Max, Oxford Instrument with applied high voltage 10 kV. Secondly, Model BMS Tescan Vega3 LMU SEM with EDX Oxford Instrument in the Department of Biomedical Science, The University of Sheffield was used to determine the compositions of FeCoCr deposited at range percentages of Cr and a high voltage of 10.5 kV was applied. To obtain the average compositions of each elements, scans were made on several areas on the film's surface. Prior to sample imaging, the sample was placed into the chamber and the pressure of the chamber was brought down to lower vacuum until 10^{-3} Pa. Because the FeCoCr film is a conductive material, no additional coating process was necessary. The energy spectrum of materials which need to be identified can be seen on the plot of the number of X-Ray (counts) as a function of energy (keV). The normalization of elements was done to calculate the percentage of each identified elements. The energy of K_α corresponds to elements of Cr, Fe and Co are lies at 5.41 keV, 6.4 keV and 6.93 keV, respectively [155].

4.5 X-Ray Diffraction (XRD)

X-rays are an electromagnetic radiation with a shorter wavelength can be diffracted when they encountered with a crystal lattice. X-ray diffraction caused by a constructive

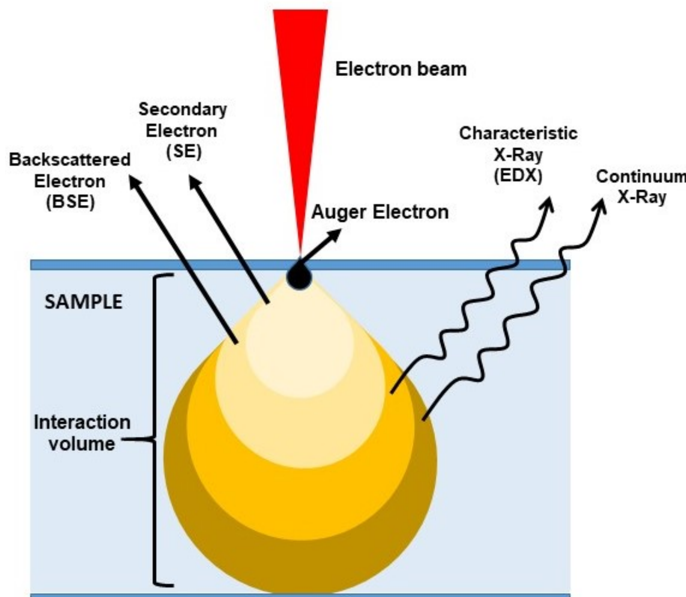

Figure 4.8: Interaction processes of electron with sample. Figure adapted from [154].

interference at specific angles. This phenomenon is known as X-ray diffraction (XRD). Since the wavelength of X-Rays are comparable to the interatomic spacing, XRD is widely used as non-destructive technique to characterize the structural properties of different classes of materials; crystals, polycrystalline and amorphous. The intensities of the diffracted X-Ray determines the sample's structure [156, 157]. Diffraction occurrs due to Bragg's Law, i.e the incident X-Ray beams must be in phase with one another and also to the diffracted beams. For instance as depicted in Figure 4.9, the diffracted beam from the second plane must travel ABC farther than the diffracted beam from the first crystal plane. For the third plane, the diffracted beam must travel at distance DEF farther then the second plane. Therefore, the distance of ABC is equal to the wavelength, λ and the distance DEF is equal to 2λ. The Bragg equation then results [158]:

$$\lambda = 2d_{hkl}.sin\theta \tag{4.8}$$

where d_{hkl} is the crystallographic plane. The Glancing-Angle X-Ray Diffraction (GA-XRD) instrument PANanalytical X'Pert Powder was used in this study to examine the types of structure of FeCo and FeCoCr films. The advantage of using this kind of geometry over the conventional one is the signal from the substrate can be minimized such that the penetration of X-ray into the a material under investigation could be

reduced. This results in an intense signal from the sample itself. By knowing the compositions, film thickness and density of materials, one can determined a suitable incident angle, ω. ω then can be calculated according to the following equation [159]:

$$I = I_0 \exp(-\mu z/\sin(\omega)) \tag{4.9}$$

where μ is the absorption coefficient which depends on the composition and density of that material, z is the distance from the surface, I_0 is the intensity at the surface. Typical values of ω used were between 0.5^o and 1.0^o, this angle was fixed during XRD measurement [160]. While in the standard XRD configuration the incident angle is equal to the angle of the detector, but with glancing angle geometry it is not the same. For GA-XRD, the incident angle and the diffracted beam is varied, while the detector was moved during the measurement. The XRD parameters applied during the measurement were $\omega = 0.8^o$ to 1.0^o, step size =0.02, time per step = 5.00 s and the scan speed = 0.004 $^o/s$. The wavelength, λ of X-Ray, $K_{\alpha 1}$ = 1.540598 Å, the voltage and the current of X-ray source were 45 kV and 40mV, respectively. The lattice parameter with corresponds to Bragg's diffraction angle 2θ of the crystalline materials can be calculated by :

$$a = \frac{\lambda\sqrt{h^2 + k^2 + l^2}}{2sin\theta} \tag{4.10}$$

Not limited to structure studies, this geometry of GA-XRD also offers a stress measurement on the multilayer deposited films [160].

The value of the full width at half-maximum (FWHM) which determines the peak broadening can be caused by the non-uniform strain. For sputtered thin films, normally stresses are produced during deposition, which have either the tensile or compressive stress [161]. The peak broadening is attributed by the particle (crystallite size) and can be from the diffractometer itself known as instrumental broadening [157]. In this present work, the FWHM from experimental data was analyzed by using Gaussian curve fitting in the OriginPro 2018 Software. Figure 4.10 presents an example of Gaussian fitting for FeCo at thickness 100 nm corresponding to BCC (110) peaks.

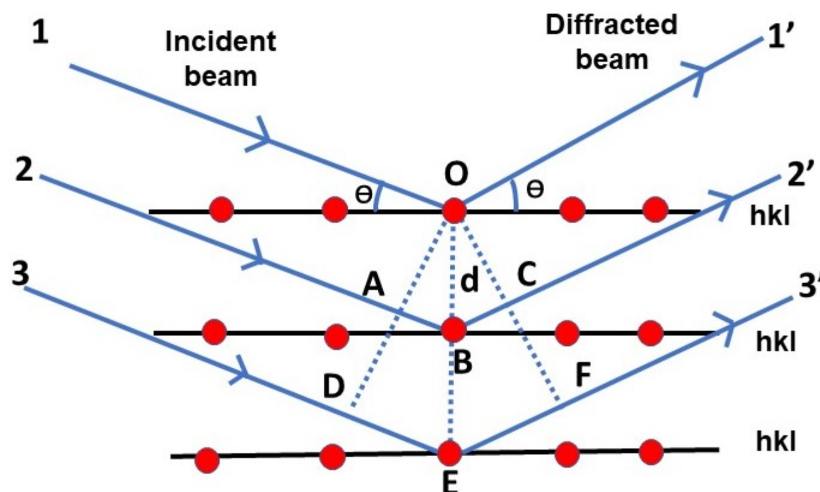

Figure 4.9: Braggs Law on X-Ray diffraction. Figure adapted from [158].

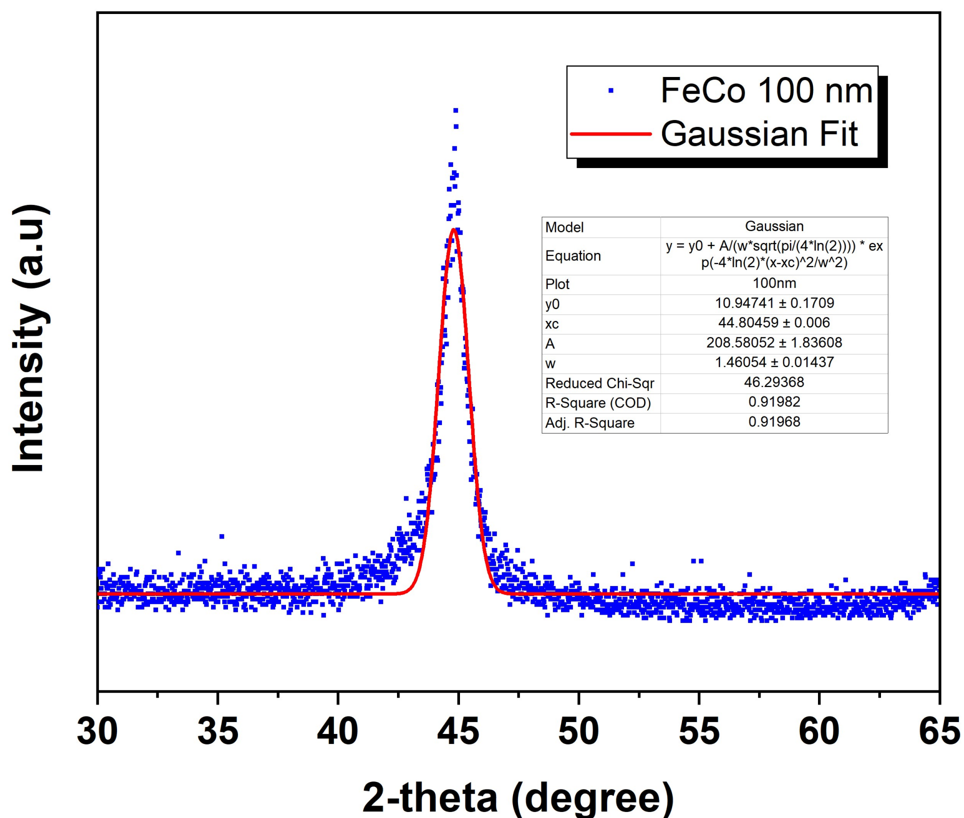

Model	Gaussian
Equation	y = y0 + A/(w*sqrt(pi/(4*ln(2)))) * exp(-4*ln(2)*(x-xc)^2/w^2)
Plot	100nm
y0	10.94741 ± 0.1709
xc	44.80459 ± 0.006
A	208.58052 ± 1.83608
w	1.46054 ± 0.01437
Reduced Chi-Sqr	46.29368
R-Square (COD)	0.91982
Adj. R-Square	0.91968

Figure 4.10: The FWHM curve fitting for the experimental data of FeCo (100nm) using the Gaussian function, whereby w = FWHM; y_0 = base; x_c = center; A = area.

4.6 Transmission Electron Microscope (TEM)

Different to SEM, the electron beam in TEM is transmitted through a very thin layer of material and produces electron diffraction. Similar to the XRD technique the diffraction occurs only when the Bragg's law is satisfied. TEM is a powerful method which not only can examine the crystallinity of a specimen but also to detect the defects for a very tiny volume of specimen 10 nm^3. TEM allows either an image or diffraction pattern to be formed in the viewing screen, depending on its lenses and aperture. For the imaging mode the objective aperture is positioned in the back focal plane of the objective lens. There are three types modes of imaging, which are bright-field (BF), dark-field (DF) and high resolution (HR-TEM). In bright-field, a small aperture used to transmit only the undiffracted beam, meanwhile DF imaging allows the diffracted electron to pass through the small aperture. The schematic imaging of BF and DF are illustrated in Figure 4.11. In BF and DF features are based on the amplitude contrast, while HR-TEM imaging relies on the phase contrast of the electron waves. HRTEM is the powerful technique to image the atomic structure of material [162]. Basically, TEM instruments can be divided into three main parts [163]:

(a) **the illumination system** which consists of the electron gun that accelerates the electrons from 40 to 200 kV, and two magnetic condenser lenses. These lenses will controls the spot size and focus the electron beam onto the specimen. In the middle of the lenses are condenser aperture which control the convergence angle;

(b) **sample stage** where the sample can be moved or kept it stationary. The sample must be very thin enough (20 nm to 100 nm) so that electrons can be transmitted. The sample is loaded on the stage through the airlock;

(c) **the imaging systems** which produces the diffraction pattern. It comprises of three lenses which were objective lens, intermediate lens and projector lens.

A selected area electron diffraction (SAED) is usually used to image the diffraction pattern of the small preferred area on the specimen. A SAED aperture can be inserted to allow the electrons pass through the small area, to form diffraction pattern.

Two representatives of FeCoCr films from the power series (75 W and 150 W) were selected and analyzed by Transmission Electron Microscope (TEM) with the objective

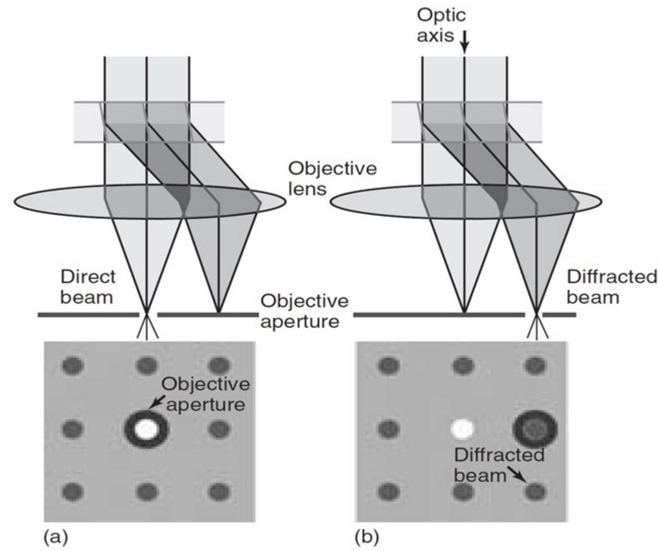

Figure 4.11: (a) Directed beam is used to image bright-field and (b) Diffracted beam which is away from optic axis is selected to form the dark-field image. Figure taken from [163].

of checking the crystallinity of the deposited FeCoCr film by selected area electron diffraction. This measurement was not conducted by the author herself, but instead with assistance from Dr. Joanne Sharp (Postdoctoral Research Associate). Samples were prepared via the the focused ion-beam (FIB) lift-out with the FIB preparation work was carried out in an FEI Helios Nanolab G3 UC dual-beam FIB. During sample preparation, platinum was deposited as a protective layer in order to prevent the film (FeCoCr) from being destroyed by thinning process. The TEM measurements were performed using a JEOL 2010F TEM at 200kV.

4.7 Magneto-Optical Kerr Effect (MOKE)

The Magneto-Optical Kerr Effect (MOKE) is a qualitative measurement technique that is used for investigating the magnetization of ferromagnetic materials in-plane and out of plane. By utilizing MOKE, one can easily study the magnetization of the magnetic surface of thin films as well as nanostructures [164]. Additionally, this method is non-destructive and works at room temperature [165].

The Kerr effect was first discovered in 19th century by John Kerr when he found that the polarization state of the reflected light was changed when it interact with a magnetic

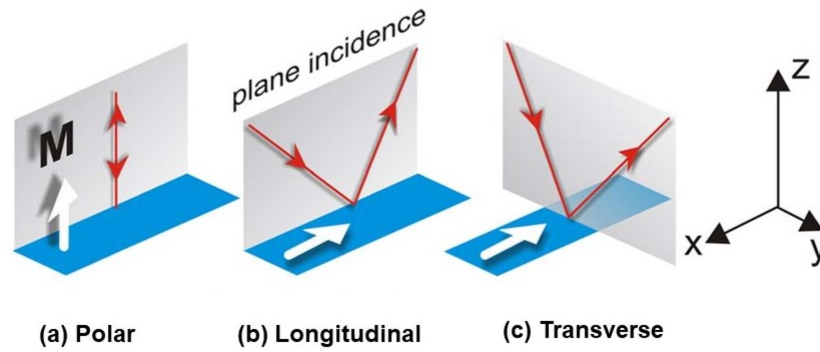

Figure 4.12: Three different of MOKE configurations. Figure taken from [168].

material with respect to the incident of light [166]. MOKE has three different configurations namely transverse, longitudinal and polar as shown in Figure 4.12. For geometry of polar and longitudinal have component of magnetisation parallel to the plane of incidence, while transverse has the magnetisation perpendicular to the plane of incidence. The light reflecting has two linear polarisations; s-polarisation refers to the electric field perpendicular to the plane of incidence and p- polarisation defines as the electric field which is parallel to the plane of incidence. Normally, a linear polarized when reflected off the non-magnetic surface it retains its polarisation. But, a linear polarized light upon reflected from magnetized sample can be changed by two ways; first, the polarisation plane of reflected light is rotated with small angle, θ_K with respect to the incidence light and second, the reflected light become elliptically polarised characterised by η_K. An example of how Kerr rotation and ellipticity occurs when light reflected from the magnetized sample in polar geometry of MOKE is illustrated in Figure 4.13.

In magnetic surface, oscillation of electrons experience a Lorentz force. As a result, an additional component of electrical field, E_K is produced which is out of phase with the reflected parallel of component electric field. The superposition of these two components gives rise to a magnetisation dependent rotation of polarisation. In both polar and longitudinal geometries, the polarisation of the incidence light (s or p) being altered to elliptically polarised with axis rotation upon reflected from magnetic surface. In the transverse effect there is no change in polarisation of s-polarised as the electric field and magnetisation being parallel. For p-polarised, there is no Kerr ellipticity, but the amplitude of reflected light will be varied due to the E_K is parallel to the plane of incidence, also normal to the reflected light [167].

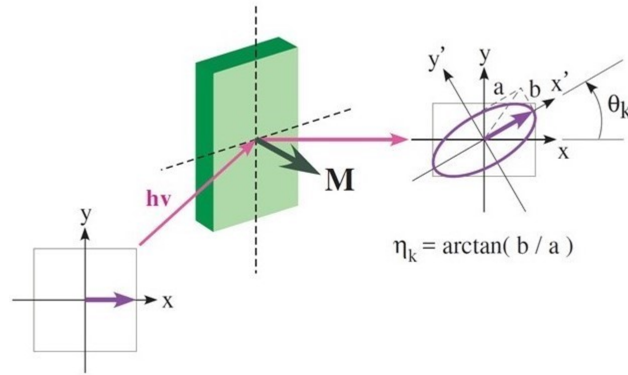

Figure 4.13: Schematic of polar MOKE showing the reflected light being rotated at angle, θ_K and elliptically polarised characterised by η_K. Figure taken from [169].

To investigate the magnetisation switching of FeCo and FeCoCr films, two different types of MOKE have been used at the Centre For Magnetics Research Lab, Department of Material Science and Engineering, The University of Sheffield. They are :
(a) High Field MOKE - to characterize FeCo and FeCoCr films (different thickness) with the magnetic field maximum of 240 kAm^{-1} and
(b) Low Field MOKE - to determine the hysteresis loops for FeCoCr films (different Cr percentages). It is important to note that, due to the FeCoCr films (different at.% Cr) having magnetic softness compared to FeCoCr films (different thickness), the Low Field MOKE was used to determine its hysteresis loops. As the name implies, the magnetic field is up to about 22.3 kAm^{-1}, which its magnitude smaller compared to the High Field MOKE.

The High Field MOKE used in this study has the transverse geometry and polariser was set-up to produce mixed polarisation s and p. The s and p are refer to polarised light which perpendicular and parallel to the plane of incidence, respectively [165]. The magnetization, M of the film in this geometry is perpendicular to the plane of incidence of the laser. The main components for the MOKE includes a laser diode He-Ne (λ= 635 nm and maximum power = 3mW), polariser, analyzer, photodetector and electromagnet. The polariser was set to certain angle to increase the signal to noise ratio. It was found that in order to obtain a symmetric hysteresis loops of FeCo and FeCoCr, the MOKE worked best at the polarizer angle, $\theta = 122^o$ and analyzer was set close to extinction in the range of, $85^o \leq \theta \leq 120^o$. The light was then reflected from the magnetic surface of sample, passed through the analyzer and then the intensity of light detected by a photodetector. The output voltage of photodetector depends upon the angle between

the analyzer and the plane of incidence [170]. To generate the magnetic field, a DC current was supplied by a KEPCO Power Supply to the electromagnet. The Hall probe was placed between two electromagnet poles near the sample stage and was connected to the Gauss/Tesla meter so that magnetic field could be measured. The sample stage can also be rotated, so that measurement of hysteresis loops were made at different angle (0° to 360°) to study the anisotropy of the films.

The Low Field MOKE differs from the High Field MOKE as for the Low Field MOKE has a longitudinal configuration with the addition of an optical lens used in this MOKE set-up. The schematic diagram of Low Field MOKE is shown in Figure 4.14. The components of MOKE are mounted on the optical table and the experiment performed in the dark environment. The requirement of performing measurement in the conditions is to prevent the reading of photodetector from being affected by the ambient light. There are three optical lenses mounted, one is between the polariser and the sample, to allow the laser light to be focused. The second lens is positioned at the front of sample after laser has been reflected, and the last one is placed in between the analyzer and the photodetector. The output signals from photodetector then is fed to analog-to-digital I/O converter. The final output of voltage as a function of magnetic field is read using a Data Acquisition (DAQ) board. The magnetisation loops is viewed on the computer by programmable LabView Software.

4.8 Measurement of Magnetostriction by the Villari Effect

Different techniques have been used to measure the magnetostriction of samples as described in Chapter 3. Measuring the magnetostriction of thin films, one needs to know the mechanical properties of the substrate such the Young's Modulus, E_s and the Poisson's ratio, ν_s. Theoretically, when the film is attached to the substrate and bent, the in-plane strains occurs in x and y-directions :

$$\varepsilon_x = \frac{\sigma_x}{E_s} - \frac{\nu_s \sigma_y}{E_s} \tag{4.11}$$

$$\varepsilon_y = \frac{\sigma_y}{E_s} - \frac{\nu_s \sigma_x}{E_s} \tag{4.12}$$

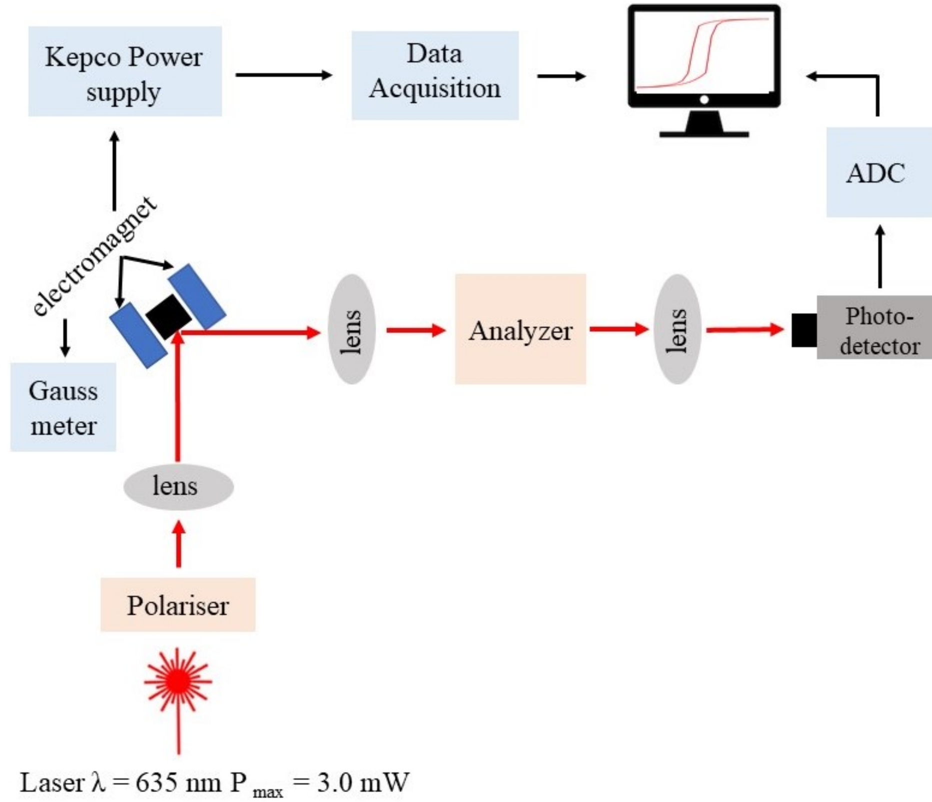

Figure 4.14: Schematic diagram of Low Field MOKE magnetometer.

In order to maintain the continuity in the film during bending, the strain in y-direction should be 0; $\varepsilon_y = 0$. The stress in y-direction can be rewritten as:

$$\sigma_y = \nu_s \sigma_x \tag{4.13}$$

Replacing the stress, σ_y into equation 4.11, the strain, ε_x then can be expressed as:

$$\varepsilon_x = (1 - \nu_s^2)\frac{\sigma_x}{E_s} \tag{4.14}$$

The stress in x-direction thus becomes:

$$\sigma_x = \frac{\varepsilon_x E_s}{(1 - \nu_s^2)} \tag{4.15}$$

It should be noted that, the strain when the wafer bent is given as:

$$\varepsilon_x = \frac{t_s}{2R} \tag{4.16}$$

where R = radius of the curvature and t_s = film thickness. By combining equation 4.15 and 4.16, then the stress in x-component becomes:

$$\sigma_x = \frac{t_s E_s}{2R(1-\nu_s^2)} \tag{4.17}$$

For magnetic material having an uniaxial anisotropy, the anisotropy field, H_k are proportional to the anisotropy constant, K_u:

$$H_k = \frac{2K_u}{\mu_o M_s} \tag{4.18}$$

where M_s is saturation magnetisation. For magnetostrictive material, the anisotropy constant is related to the stress which can be written as:

$$K_\sigma = \frac{3}{2}\lambda_s \sigma \tag{4.19}$$

By substituting the K_σ with K_u into equation 4.18 , the anisotropy field of magnetostrictive material then can be expressed by:

$$H_k = \frac{3\lambda_s \sigma}{\mu_o M_s} \tag{4.20}$$

This then lead to the determination of magnetostriction constant, λ_s by combining equation 4.20 into equation 4.17 :

$$H_k = \frac{3\lambda_s t_s E_s}{2\mu_o M_s(1-\nu_s^2)R} \tag{4.21}$$

In this current work, applying the above theory with those equation, the magnetostriction of the films then were determined through the Villari Effect by means of MOKE magnetometry. In Villari Effect measurement, stress was applied by bending the samples with three different bending radii of R = 500 mm, 400 mm and 300 mm, with the bending tools of 300 mm having the largest curvature [99]. The schematic diagram for the magnetostriction apparatus is depicted in Figure 4.15. At first, film was bent using the lowest radius bending tools, R = 500 mm followed by the R= 400 mm and lastly with R = 300 mm. The experiment needs to be conducted gently during the bending set up

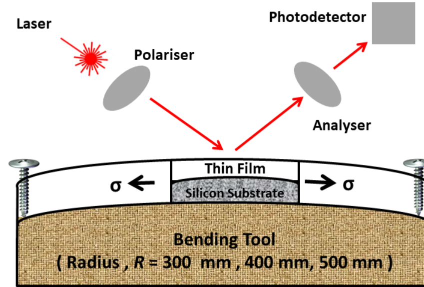

Figure 4.15: Magnetostriction measurement using different bending tools.

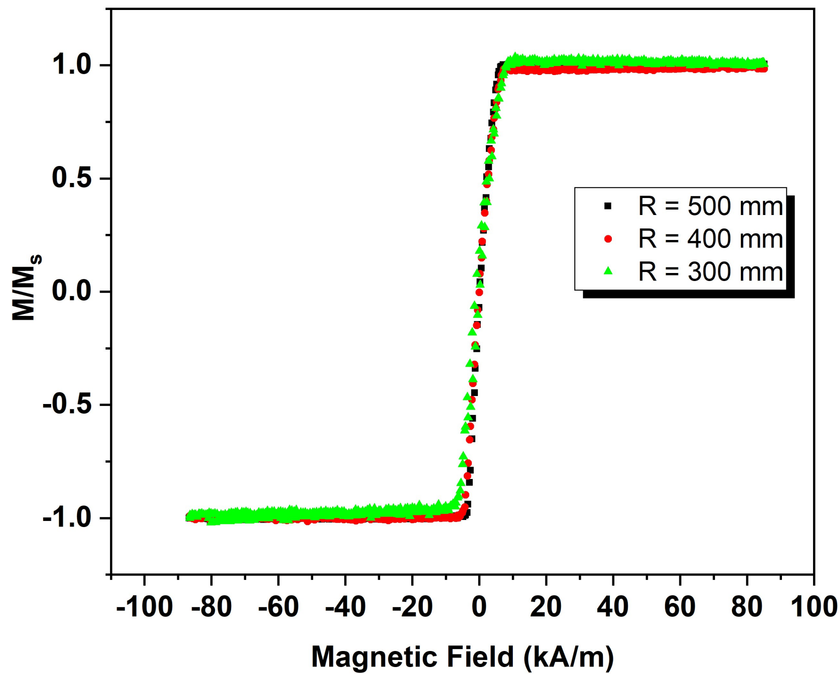

Figure 4.16: Magnetisation curves of the representative FeCoCr film after bent using three different radii tools.

since the film can easily broken especially with the highest bending radius. The change in the sample's magnetisation curve was then observed by using the MOKE system. The magnetisation curves obtained as a result of bending the film using three different bending radii is shown in Figure 4.16.

Figure 4.17 presents an example of magnetization loops, for the upper part (positive curve) due to film bent. Also shown in that figure is how the anisotropy field, H_k due to stress was determined by the straight line method. The determination of H_k also done for each bend radius, both the positive and negative parts of the loop. Accordingly, a linear graph of H_k with respect to the inverse bending radius $1/R$ was plotted and fitted

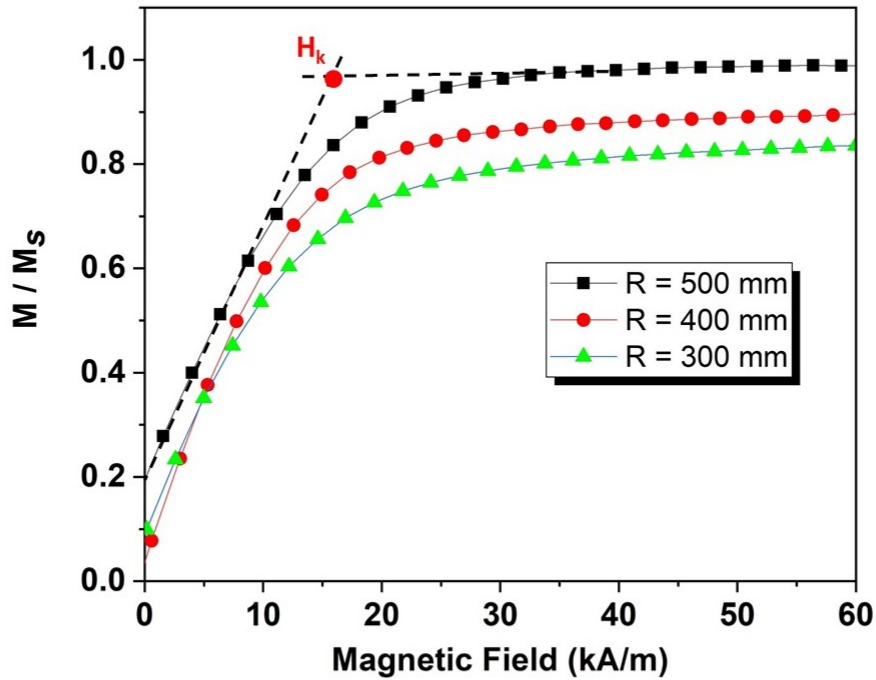

Figure 4.17: Magnetization curves upon the stress application using three different bending tools. It showing the determination of H_k at the positive part of magnetization switching.

to define its gradient, $(dH_k/d(1/R))$, as given in Figure 4.18. The magnetostriction constant can then be calculated as given in equation 4.21 which has been described in the literature [6, 82, 99, 171]. By inserting the value of gradient into the following equation:

$$\lambda_s = \frac{dH_k}{d(1/R)} \times \frac{2\mu_0 M_s(1 - v_s^2)}{3t_s E_s} \tag{4.22}$$

where R = radius curvature of bending tools (in meter); $\mu_0 M_s$ = saturation induction (in Tesla); v_s = Poisson's ratio (0.28 for silicon substrate); t_s = substrate's thickness (380 μm) and E_s = Young's Modulus of substrate (1.69 x 10^{11} Pa).

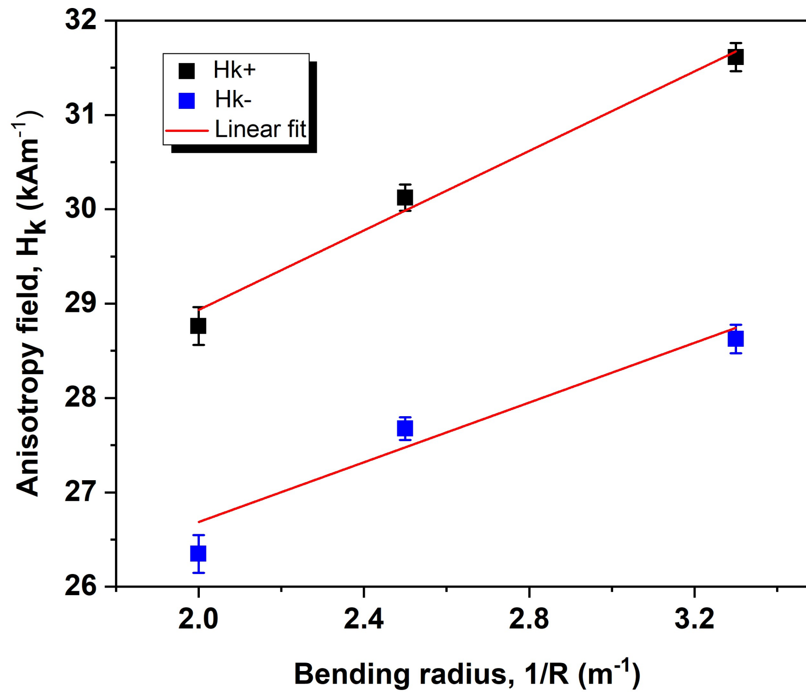

Figure 4.18: The fitted linear graph of anisotropy field, H_k as a function of inverse bending radii,$1/R$. H_k^+ and H_k^- are anisotropy measured at upper part and lower part of hysteresis loop, respectively.

4.9 Measurement of Damping Properties by Vector Network Analyzer and Ferromagnetic Resonance (VNA-FMR)

Vector Network Analyzer Model Rhode & Schwarz ZVB 20 and Ferromagnetic Resonance (FMR) was used to study the microwave properties of soft magnetic films. The important parameter to be defined were the damping constant, α, saturation magnetization, M_s and the anisotropy field, H_k [123, 126, 172]. The VNA system was equipped with two ports (Port 1 and Port 2) which operated in the range of radio frequencies from 10 MHz to 20 GHz. The schematic of two-port S-parameters is given in Figure 4.19. There are two geometries of measurement; transmission and reflection by which the S-scattering parameters (S_{mn}) can be determined either at static magnetic field while the frequency is swept or, vice versa. The subscripts m and n refer to the receiver port and the source port, respectively. For instance, transmission used both Port 1 and Port 2 and therefore, the S_{21} parameter. It measures the output from Port 2 with respect to the RF entering device under test (DUT) from Port 1. The S-parameter of S_{11} is defined

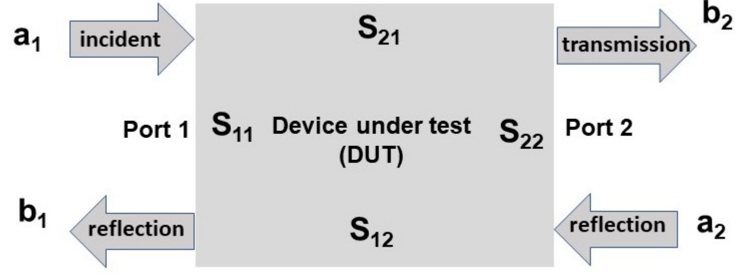

Figure 4.19: Scattering parameters for VNA with two-ports.

as the ratio between the reflection signal out from the DUT (Port 1) and the incident wave into DUT (Port 1). The other parameters, S_{22} and S_{12} also can be obtained. All those parameters can thus be expressed by:

$$S_{11} = \frac{b_1}{a_1}; (a_2 = 0) \tag{4.23}$$

$$S_{21} = \frac{b_2}{a_1}; (a_2 = 0) \tag{4.24}$$

$$S_{12} = \frac{b_1}{a_2}; (a_1 = 0) \tag{4.25}$$

$$S_{22} = \frac{b_2}{a_2}; (a_1 = 0) \tag{4.26}$$

where a_1 and a_2 refer to the wave entering the DUT and b_1 and b_2 represent the wave leaving the DUT.

For the purpose of this study, the geometry of reflection S_{11} in the field domain was chosen. To set up the measurement for this reflection geometry, co-planar waveguide was connected to the VNA at the Port 1. The device under test (DUT) was mounted faced down on the top of co-planar waveguide (CPW). The CPW was positioned in the center between of electromagnet. The sample was placed with the easy axis parallel to the field. Frequencies from 3 GHz to 12 GHz were applied with maximum field 1000 Oe. For determination of saturation of magnetization, M_s and anisotropy field, H_k the plot

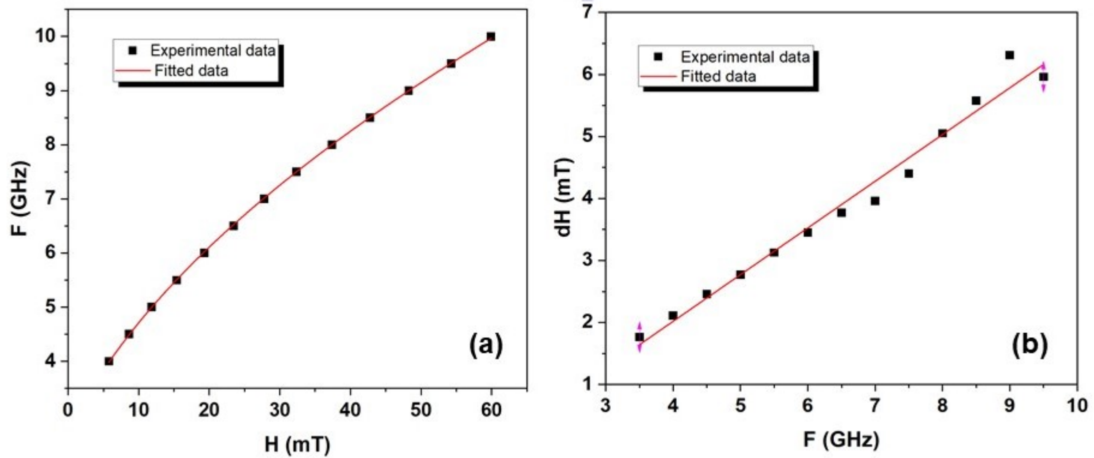

Figure 4.20: Experimental data which fitted to (a) Kittle equation and (b) FMR linewidth in obtaining the M_s, H_k and α.

of resonance frequency against the field was fitted according the Kittel's formula [173] which can be written as:

$$f_{FMR} = \frac{\gamma}{2\pi}\sqrt{[H + \mu_B H_k][H + \mu_B M_s + \mu_B H_k]} \tag{4.27}$$

where f_{FMR} is resonance frequency, γ is gyromagnetic ratio, H is external magnetic field, μ_B is the Bohr magnetron and M_s is saturation magnetization. This measurement also allow us to obtain the linear dependency between the α and FMR linewidth as expressed by the Equation 2.16 in Chapter 2. For instance, by fitting the linear plot from the linewidth in terms of field as a function of frequency, then the value of damping constant, α can be extracted. The graphs of experimental data for FeCoCr film that have been fitted are presented in Figure 4.20.

4.10 Measurement of Saturation Magnetisation by SQUID-VSM Technique

Determining the saturation magnetisation by measuring the magnetic moment is not possible using the MOKE technique. This parameter can be measured by using the Superconducting Quantum Interference Device (SQUID) system. A SQUID principally detects the magnetic flux changes of a moving the sample in a set of pickup coils. The SQUID Model MPMS 3 that used in this study has a superconducting Niobium-Titanium

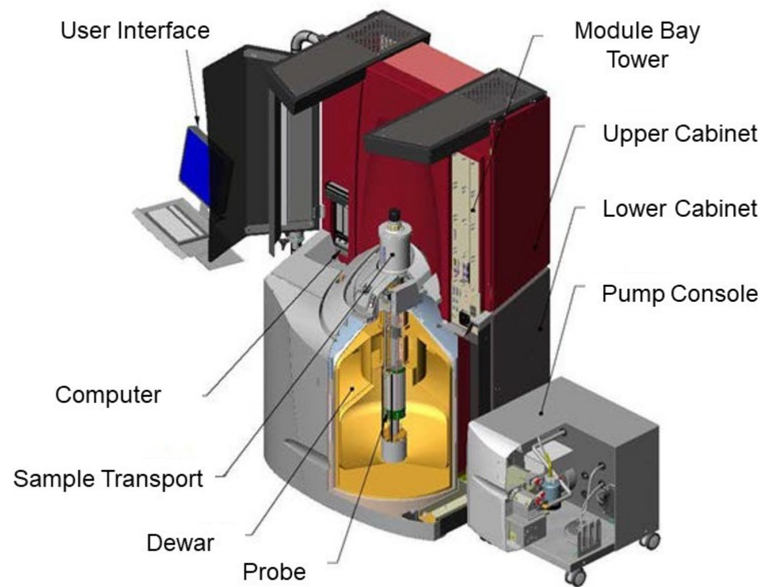

Figure 4.21: The components of SQUID MPMS 3 system. Figure taken from [174].

(NbTi) solenoid magnet in combination with a Vibrating Sample Magnetometer (VSM). As its name suggests, it vibrates the sample sinusoidally and uses a lock-in amplifier to measure the response of the sample to an applied magnetic field. The system employs a DC scan; scan up and down at constant speed, measuring the magnetic flux in superconducting loop as a function of sample position. At the start of the measurement, sample positioned at the center of the pickup coils [174]. The set-up of the SQUID-VSM system is illustrated in Figure 4.21 which has two main parts, the upper and the lower cabinet. The upper contains the computer and module bay housing (modular electronics). The lower part consists of the dewar which holds the liquid helium inside. The liquid helium is required to cooling the superconducting solenoid. The sample transport is located on the the top of the dewar.

Sample preparation involves mounting, loading and centering sample position which are need to be conducted before measurement can be run. The sample was inserted into a capsule and securely placed in the straw. To ensure the sample was in the correct position, the straw should be placed aligned with the zero point indicator. This can be done by placing the sample parallel with the marker on the mounting station, as shown in Figure 4.22. The position of sample must be in between 66 $\pm$ 3mm from the zero point. Then the sample was inserted into the sample holder (rod) and loaded into the chamber. After that, the position of sample was centered within the detection coils by

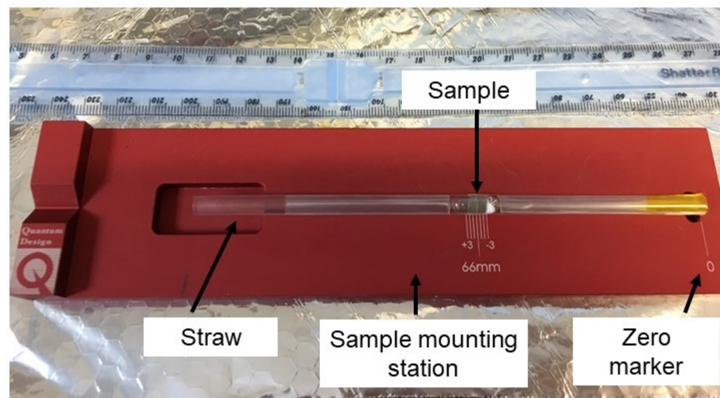

Figure 4.22: Sample position on the mounting station.

scanning the sample offset. The distance from the bottom end of the sample holder to the sample location is defined as the sample offset and is usually about 66 mm. Before single measurement or sequences were initiated, the chamber was evacuated down to about 7 mTorr and filled with He gas. In this study, the M(H) loops of films with set of Cr compositions were measured by applying magnetic field until 1 Tesla at room temperature (300 K).

4.11 Measurement of Mechanical properties by Nanoindentation

The mechanical properties of FeCo and FeCoCr thin films have been studied by the nanoindentation technique allowing for the extraction of two important parameters which are the reduced elastic modulus, E_r and the hardness, H. As described in Chapter 2, the Young's Modulus of FeCoCr films can be calculated once the E_r has been determined.

4.11.1 System Calibration

In order to achieve high accuracy in the nanoindentation data of the specimen, these three calibrations steps are need to be performed prior to the nanoindentation testing:

(a) Transducer calibration:

The transducer calibration must be performed, as the probe is installed in the transducer.

The centre plate of the transducer where the probe is attached ,is moves as the transducer is driven to the sample, and it is also connected to the spring. Thus, the movement of the center plate can cause a different value on the electrostatic constant force. Also, the electrostatic constant force can vary due to temperature and humidity. For this reason, the indentation axis calibration on the electrostatic constant and plate spacing must be conducted on a daily basis to avoid any errors that might affect the indentation test results. This calibration was performed in the air, meaning that there is a gap between the probe and the sample stage.

(b) Optic-probe tip offset calibration:

After the indentation axis calibration has been carried out, the calibration of the optic-probe tip offset needs to be performed if either transducer, nanoidentation tip or any optical camera system has been removed or changed. This tip to optic calibration is performed to record the distances in the X, Y, and Z-axis between the center of the optical focal plane and the probe (tip) and the area of interest on the film sample can be optically focused. This calibration requires a transducer with a nanoindentation tip be installed on the system and a standard sample of polycarbonate was mounted on the sample and the H-pattern indenter was made first before the nanoindentation can be done on the thin film sample. A standard sample of polycarbonate has the mechanical properties of hardness, $H = 0.18$ GPa, reduced elastic modulus, $E_r = 3.10$ GPa, Young's Modulus, $E = 2.7$ GPa and Poisson's ratio, $\nu = 0.37$. During this calibration, the tip was bring down to about 2 mm gap distance of the sample surface without crashing the tip into the sample.

(c) Probe calibration

Another most crucial calibration that had to be performed is the indenter tip calibration, as the area of the tip will changes when performing the test. Tip used in this measurement was Berkovich geometry. A tip was calibrated by a series of indentations onto a material where the elastic modulus is known; usually a fused quartz sample is used ($E_r = 69.6$ GPa ; $H = 9.25$ GPa and $E_Y = 72$ GPa) to determine the area function. From the calibration, the graph of the calculated area function, A against the contact depth, h_c, was then fitted according to Equation 2.32.

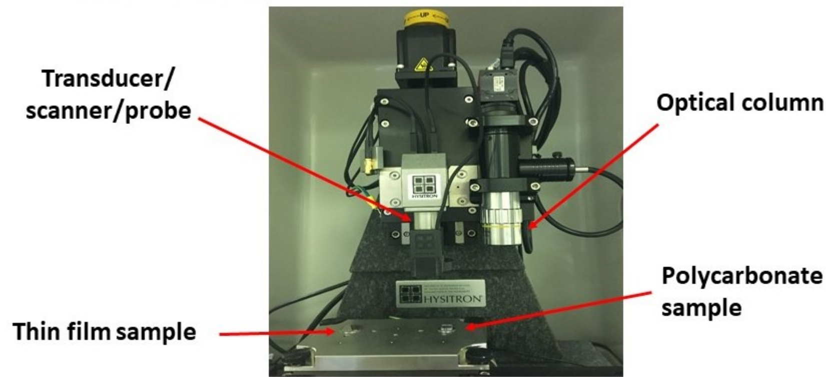

Figure 4.23: Figure showing the position of the sample mounted on the stage along with the polycarbonate sample on the TI 950 TriboIndenter Hysitron. The nanoindentation was firstly performed onto the polycarbonate before the nanoindentation is conducted on the thin film.

4.11.2 Sample Mounting

The specimen was mounted onto a metal disk by using an adhesive (super-glue) is vital to ensure that the sample is firmly attached to reduce the system compliance. The indentation tests in this study were conducted by using a TI 950 TriboIndenter Hysitron with a Berkovich indenter tip, the system used as depicted in Figure 4.23. To prevent the transducer or the probe from being damaged during calibration, the test specimen which has short height (in this case the FeCoCr thin films) was mounted on the stage at bottom of the transducer side, while the standard sample of polycarbonate (taller than the thin films) was placed underneath the side of the optical column.

A series of nanoindentation were then performed with a partial unload consisting of three segments: 5 seconds for loading, 5 seconds hold at the load maximum and 5 seconds for unloading. The load-displacement curve could then be used to obtain the reduced elastic modulus and hardness of the films.

Chapter 5

Characterisation of FeCo and FeCoCr films under different sputtering conditions

5.1 Introduction

The main purpose of this chapter is to present characterisation of the effect of growth conditions on the structural, compositions and magnetic properties of FeCo and FeCoCr thin film. The effect of applying a magnetic field during the growth of FeCo for different thickness is presented in the first section. In the case of FeCoCr films, two different series of FeCoCr films were prepared with respect to their thickness and sputtering power. Since one of the motivations of this study is to produce soft amorphous film by adding Cr, the structural properties of FeCoCr deposited at the similar conditions with FeCo were investigated by XRD and further confirmed by TEM. This then allows a valid comparison between the structure of pure FeCo and FeCoCr films. All the films were characterized by XRD,TEM, AFM, EDX, MOKE Magnetometry and Villari techniques, as detailed in this chapter.

5.2 Structural Properties of FeCo

As clarified in Chapter 4, FeCo with different thicknesses were deposited based on two growth conditions; in the presence of a magnetic field and with no field. All the films were grown at the same sputtering power: 75 W and pressure : 4.8 mTorr. Figure 5.1 compares the XRD patterns between the FeCo films. The intensity of XRD peaks of those films (applied field) increased with film thickness. It is interesting to note that the XRD peaks for films grown under magnetic field showed more texture than the samples with no applied field. No other peak was detected and only a single peak was observed at $2\theta = 44.96^o$ (50nm); 44.86^o (70nm); 44.89^o (100nm) and 44.95^o (120nm). Those peaks can be indexed as crystal lattice of body-centered cubic BCC (110). The BCC peaks for FeCo found in this study had values matched to those published in the literatures, $2\theta \approx 45^o$ [76, 175].

Conversely for the 50 nm film in the absence of a magnetic field, the peak exhibited the weakest XRD intensity at $2\theta \approx 35^o$. This could be associated to a Si peak as the X-Ray may penetrates to the Si substrate. This peak is also identical with the reported diffraction angle of the oxidized Si peak in the FeCoB film prepared at room temperature [176]. Unexpectedly, for 70nm the peak is more intense but had shifted to $2\theta = 41.82^o$, different from the 2θ for sample 70 nm with applied field. An error in sample height adjustment could be the reason why the peak was shifted. To confirm the position of the peak, the measurement was repeated on a different sample at the same thickness (70 nm), nonetheless a peak at similar position still was detected. This is most likely from the nature of the film itself for instance, the existence of a uniform strain within 70nm film. However it can be seen that the peaks became more intense as the thickness increases up to 100 nm and 120 nm. The peaks were similar to the sputtered samples with applied field, but shifted slightly to lower values of $2\theta = 44.71^o$ (100nm) and $2\theta = 44.75^o$ (120nm). This suggests that peak is associated with the structure of the film, as it is visible for all films apart from 50nm.

Table 5.1 compares the calculated lattice parameters and the FWHM values that were fitted by using Gaussian peak functions with respect to BCC peaks in the FeCo for both set of films and FeCoCr at the higher sputtering power. The errors in FWHM were taken from the Gaussian fitted data. The lattice parameters from these two different growth conditions have significant differences in their lattice constants. For films with applied

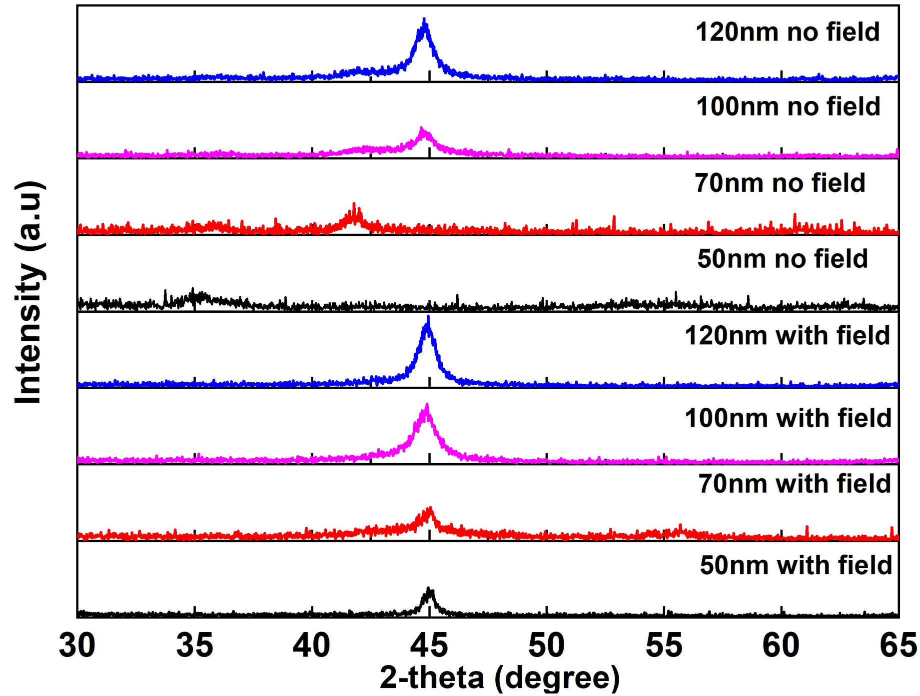

Figure 5.1: XRD profiles of FeCo with and without magnetic field during deposition for different film thicknesses.

field, they showed that the lattice constant of FeCo tends to approach the bulk constant, $a_o = 2.855$ Å[23]. The difference in lattice constant may be due to strain in the film. The standard errors for lattice parameter were calculated based on the difference between the bulk and calculated value and the errors also given in Table 5.1. It showed that the film at 100 nm with no applied field had larger FWHM (2.143^o) than films at the same thickness deposited with applied field, which may be attributed by the inhomogeneous strain within the film. By using the relationship of $\epsilon = (a - a_o)/a_o$, where ϵ = film strain; a = calculated lattice constant ; and a_o = lattice constant of FeCo (bulk) taken from literature [23], therefore the strain in the film can be estimated. For instance, by comparing the strain of FeCo films at thickness 100 nm, the calculated strain for the films grown with applied field was smaller, $\epsilon = -0.0011 \pm 3\text{x}10^{-6}$ than the FeCo with no field, $\epsilon = 0.0028 \pm 7\text{x}10^{-6}$. Based one these value, one film growth was under tensile and the other under compression. This suggests that a small compressive stress within the FeCo films at thickness 100 nm grown in the absence of applied field was generated during sputtering. It also shows that the growth within a magnetic field changes the internal homogenous and inhomogeneous stresses within the film.

Table 5.1: Lattice parameters and FWHM values with respect to BCC peaks in FeCo and FeCoCr films.

Sample	**Growth Parameter**	**Lattice Parameter (Å)**	**FWHM (degree)**
FeCo - 50 nm	applied field, 75 Watt	2.848 ± 0.007	0.720 ± 0.011
FeCo - 70 nm	applied field, 75 Watt	2.854 ± 0.007	2.573 ± 0.063
FeCo - 100 nm	applied field, 75 Watt	2.852 ± 0.007	1.461 ± 0.014
FeCo - 120 nm	applied field, 75 Watt	2.849 ± 0.007	1.078 ± 0.009
FeCo - 100 nm	no field, 75 Watt	2.863 ± 0.007	2.143 ± 0.042
FeCo - 120 nm	no field, 75 Watt	2.861 ± 0.002	1.219 ± 0.014
FeCoCr - 100 nm	field, 125 Watt	2.891 ± 0.001	3.104 ± 0.038
FeCoCr - 100 nm	field, 150 Watt	2.884 ± 0.001	1.774 ± 0.026

5.3 Structural Properties of FeCoCr

Since the FeCo films fabricated with a magnetic field have shown stronger XRD intensities than samples with no field, the XRD measurements were also conducted to evaluate the structure of FeCoCr films grown in the presence of magnetic field. The films varied in thickness between 56 nm and 165 nm but similar Cr compositions (at.% 14) as grown with similar sputtering power of 75 W (details in Table 5.2). The XRD profiles for the thickness series of FeCoCr are presented in Figure 5.2. All films show a broad peak around $2\theta = 44^o$, representing amorphous structure. The 56nm film shows the lowest signal to noise ratio (SNR) with an indistinct peak at position $2\theta = 36^o$. This is due to the Si peak; similar to the FeCo films sputtered without field. Also, a indistinct peak at around $2\theta \approx 42^o$ is also seen at this thickness. This is possible due to the short deposition time, such that the nucleated atoms did not have enough time to coalesce and form a crystalline structure. Nevertheless, the XRD intensity was improved when the thickness was increased to 80 nm, but a hump peak can still be seen at around 2θ $= 44^o$. This peak position has close resemblance to the XRD patterns of FeCo-based films in the thickness range from 70 nm to 450 nm, previously studied in [124]. All these FeCoCr films have amorphous structure irrespective of the thickness. Clearly, the structure of FeCo (50:50) films have changed from polycrystalline to amorphous at thicknesses greater than 50nm by adding Cr. XRD pattern of the 100nm FeCo deposited with the same growth parameters is also given in Figure 5.2 as comparison. The discrepancy between XRD patterns of FeCo and FeCoCr could be explained by the effect of lattice expansion. Lattice expansion may occur as a result of the Cr atom accuppying the sites of Fe and Co atoms. In addition, the Cr atom has radius larger than Co and Fe [177]. Also the peak broadening can be contributed by the non-uniform strain. Thus it can be

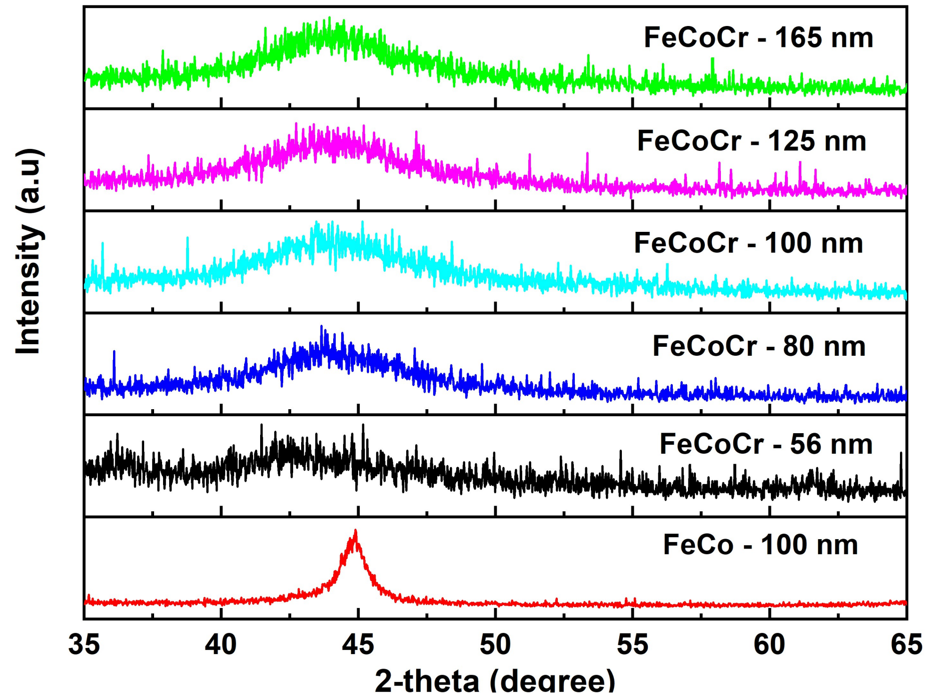

Figure 5.2: XRD profiles of FeCoCr as function of thickness at the same Cr concentration at.% 14 grown in magnetic field. Shown in plot also is the FeCo at 100nm grown with magnetic field, for a structure comparison.

assumed that strain within the films may be created during the deposition of FeCoCr in the sputtering chamber.

To enable us to study the effect of sputtering power on the structural properties, the FeCoCr films were fabricated at a fixed thickness of 100nm while varying the sputtering power from 75 W to 150 W. The reason why the samples were not deposited at a higher power more than 150 W was due to the fact that the films experienced delamination issue above this power. Therefore in this chapter, the effect of sputtering power are described for sample grown until the maximum power of 150 W.

Figure 5.3 displays the XRD profiles for FeCoCr films grown from 75 W to 150 W. It can be seen that the films grown at lower powers (75W and 100W) have broader peaks, indicating an amorphous structure. The peaks become narrower at the same diffraction angle around $2\theta = 44^o$ as the sputtering power increases above 100 W. Surprisingly, another peak with lower intensity at $2\theta = 81.61^o$ for films at 125 W and 150 W appears. Those peaks were indexed as BCC corresponding to the (211) crystal plane. This implies that the structure has become more polycrystalline at higher powers. The reason for this could be the higher power, gives a higher deposition rate, hence more sputtered atom

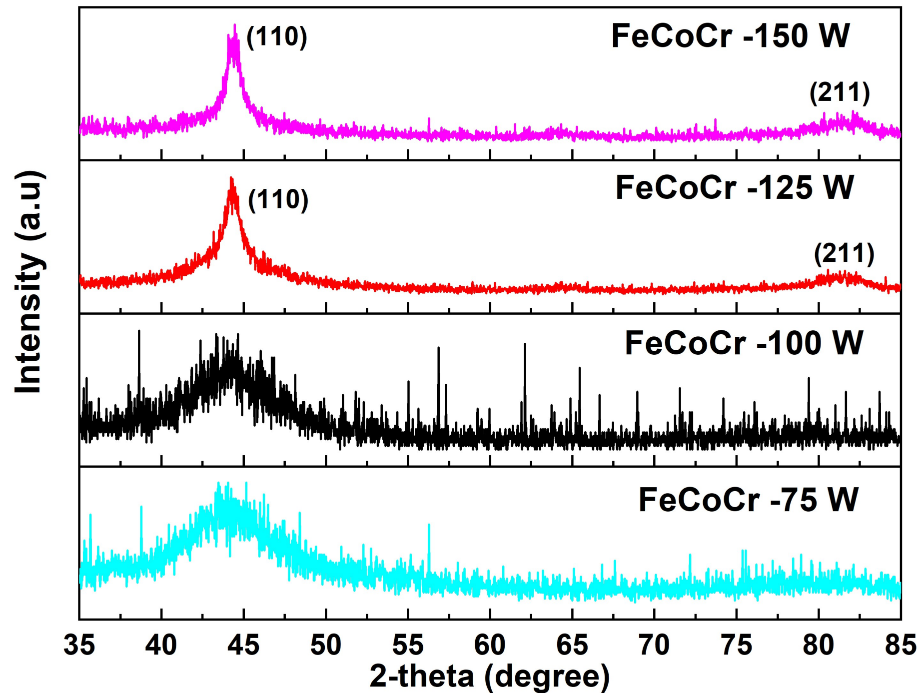

Figure 5.3: XRD profiles of FeCoCr as function of sputtering power grown at thickness 100nm deposited with magnetic field.

are moving around with a higher energy, so when they reach the substrate, this improves the grain growth of the film. At lower power however, the atom scattering events are higher, as a consequence there are fewer atoms to be deposited onto the substrate. The calculated lattice parameter and FWHM for 100 W and 150 W corresponding to BCC (110) at $2\theta = 44^o$ are included in Table 5.1. The FWHM was found to be higher for the 100 nm film grown at 125 W (FWHM $= 3.104^o$) than the FHWM of FeCoCr film at 150 W (1.774^o). This is probably due to an increase in the crystallinity of the film and a reduction in the inhomogenous strain. Different phases have been observed for films fabricated at different sputtering power which might be attributed to different compositions of Chromium within the film. To validate this assumption, EDX analysis was performed in order to examine the Cr composition. This analysis will be given in the next section as well as the TEM measurement to confirm the phase of FeCoCr for selected films (75 W and 150 W).

5.4 Compositional and Structural Studies by SEM- EDX and TEM

To examine the percentage elements of Fe, Co and Cr, a Scanning Electron Microscope (SEM) equipped with Energy Dispersive X-Ray (EDX) technique was used for films deposited with varied sputtering power. Accordingly, justification can be made on why the structure of the film has changed to polycrystalline as the sputtering power increased to 125 W.

Table 5.2 compares the percentages of the three elements Fe, Co and Cr for different applied sputtering power. Fixed thickness (100 $\pm$ 5 nm) and sputtering pressure (4.8mTorr) was applied for all films, which were deposited at room temperature. The standard errors in the table were taken from the EDX measurement at different areas for each film. As expected, the percentages of Fe and Co in films deposited at higher power (125 W and 150 W) were higher than the 75 W and 100 W films. As a result, it was found that the structure properties of 125 W and 150 W films revealed more texture, as discussed in XRD analysis section. Meanwhile, for films at lower powers (75 W and 100 W) the Cr compositions is more dominant, i.e for the 75 W film the Cr was nearly double (at.% 14.3) that of Cr in the 150 W film (at.% 7.7). This suggests the amorphous structure of the 75 W film as well as the 100 W film (refer to Figure 5.3) was a result of the larger amount of Cr. The Cr contents in 75 W film however, has a large standard error and this reflects that Cr atoms were not deposited uniformly onto the substrate, again due to the low power giving the deposited atoms has lower energy.

To confirm the amorphous and the polycrystalline structures, TEM measurements were carried out on the 75 W and 150 W films. The differences between the films grown at 75W and 150W can be seen clearly in the TEM analysis images. To ensure that the FeCoCr film was correctly identified, the imaged areas were analyzed by electron energy-dispersive X-ray spectroscopy (EDX) which integrated with TEM . Figure 5.4 shows bright field TEM images of the (a) 75 W and (b) 150 W films. The 75 W FeCoCr film shows smooth contrast with no features except for a small number of dark spots towards the edge that are due to beam damaged from the spot EDX analysis. Figure 5.4(c) shows the magnified image of 150 W in the dark field (DF) mode to visualize the grain spotted in Figure 5.4(b). It showed that the 150 W film appears to have columnar grains with

Table 5.2: The atomic percentages of Fe, Co and Cr for various sputtering power.

Sputtering Power (Watt)	**Fe at.%**	**Co at.%**	**Cr at.%**
75	40.8 ± 4.3	44.9 ± 2.8	14.3 ± 7.0
100	43.5 ± 0.4	43.9 ± 0.3	12.6 ± 0.2
125	43.8 ± 0.4	45.3 ± 0.3	10.9 ± 0.2
150	45.1 ± 0.3	47.2 ± 0.4	7.7 ± 0.1

vertical edges. The Si in these images was the silicon substrate while the part marked Pt was the platinum acts as a protective layer. In these images the growth direction of Pt is upwards and perpendicular to the interface with the silicon. From the TEM analysis, the film thicknesses were measured. It was confirmed that the thickness for 75 W film was 110 nm thick, whilst the 150 W film was 103 nm thick, with an uncertainty of 5nm due to the unevenness of the platinum growth. These film thicknesses were almost the same thickness measured by the AFM. Selected area electron diffraction (SAED) images were conducted and the respective patterns for 75 W and 150 W films are presented in Figure 5.5. The amorphous structure of the 75 W film with the diffuse rings was imaged. Interestingly, for 150 W the diffraction pattern shows rings with small diffraction spots can be seen in the image. This finding supports the amorphous nature of 75 W film and polycrystalline structure of 150 W film which were obtained from XRD analysis.

5.5 Morphology Studies of FeCoCr by AFM

A published study has reported that surface roughness is one of the factors that can affect the magnetization reversal of thin films [178]. To understand if the surface roughness might have contributed in changing the magnetization of FeCoCr and to determine whether surface roughness of FeCoCr was affected by film thickness and sputtering power, the film's surface were examined by Atomic Force Microscopy (AFM). Figure 5.6a and Figure 5.6b provide the graph of film roughness as a function of thickness with similar sputtering power of 75 W and varied sputtering power at similar thickness; 100 nm, respectively. From the graph, it can be seen clearly that film thickness does not have a significant affect on the roughness R_a, as their values are similar. It revealed that the FeCoCr films have smooth surface with R_a in the range between 0.3 nm and 0.5 nm. The images also indicate the amorphous structure as no features of grains (AFM micrographs are not provided). Although the R_a as a function of sputtering

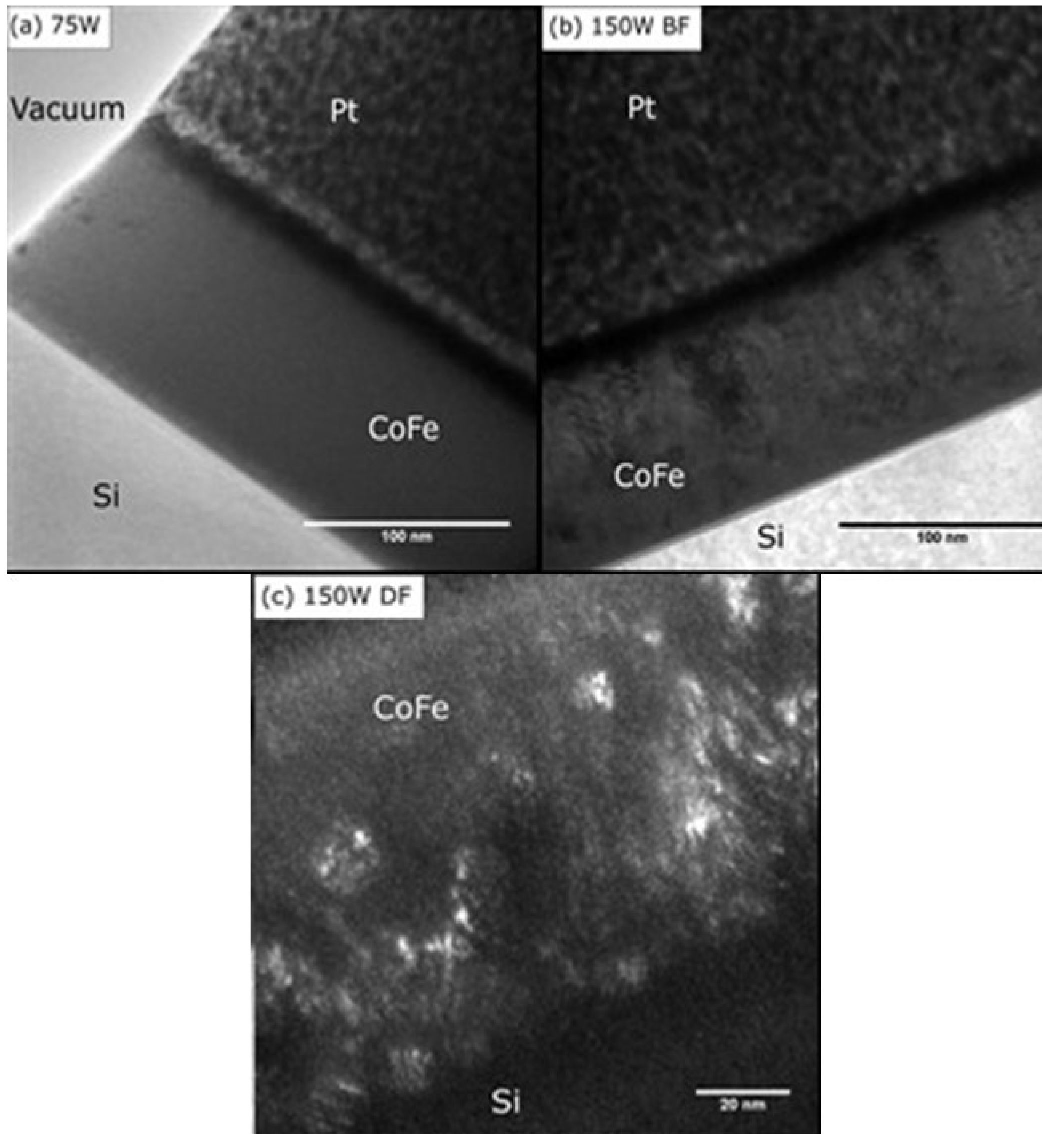

Figure 5.4: Bright field images of FeCoCr films deposited at sputtering power (a) 75 W (b) 150 W (c) dark field image of FeCoCr film at 150 W showing columnar structure.

power exhibited a monotonic increase from 75 W to 125 W, their values are within the error bars. Thus, varying the sputtering power did not change the surface roughness of film. Similarly to the study done by [179], they also found the insignificant effect on sputtering power to the roughness of FeCo-based films. The error bars represent the standard error of different areas measured on each sample. It also identified that the root-mean square roughness, R_{ms} of FeCoCr films was not influenced by the power as their difference were not significant as well. The representative images of FeCoCr films grown with sputtering powers by using data scale: 10 nm ; scan size 2μm $\times 2\mu$m are given in Figure 5.7. Some of the areas on the film's surface were found to be contaminated,

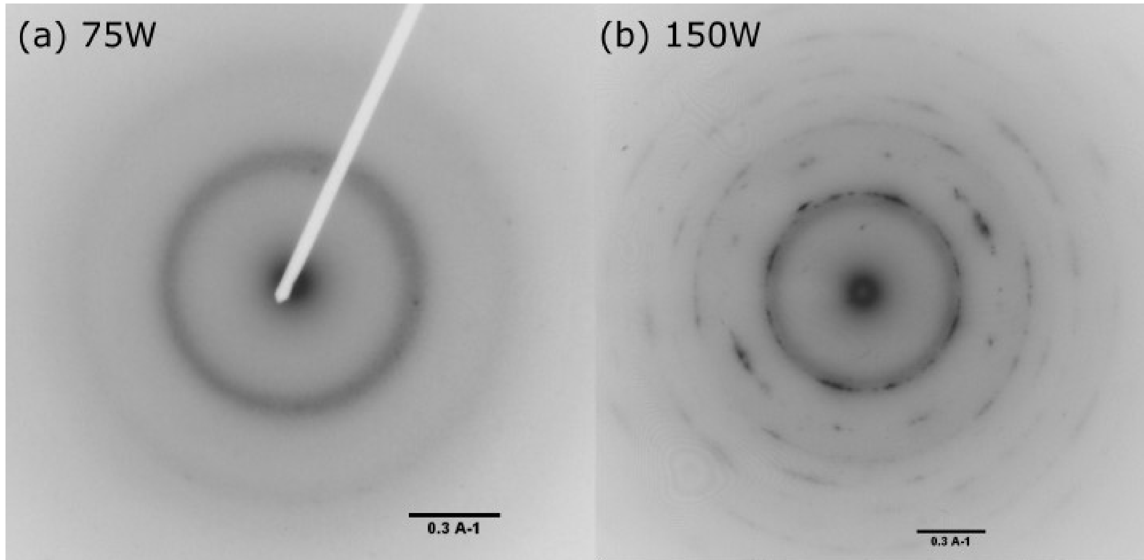

Figure 5.5: SAED images of FeCoCr films sputtered at power (a) 75 W (b) 150 W.

thus the images with defects were identified. These image defects made the standard error higher. The R_{ms} values for the FeCoCr films were 0.562 ± 0.100 nm (75 W), 0.532 ± 0.001 nm (100 W), 0.517 ± 0.010 nm (125 W) and 0.502 ± 0.002 nm (150 W). Figure 5.8 displays an example of roughness analysis from the AFM image of the FeCoCr film with thickness 100nm for film deposited at power of 125 W. From the AFM examination, neither thickness nor sputtering power affects the surface roughness of FeCoCr. It can be inferred that the surface roughness would not responsible for any differences on magnetization switching of FeCoCr grown under different sputtering paramaters. Further investigation on magnetic characteristics will be discussed in the next section.

5.6 Studies on Magnetic Properties

Following the microstructural characterizations, MOKE measurements were used to investigate the difference in magnetic properties between the FeCoCr and pure FeCo films. The magnetic properties of FeCo for films thickness from 70 nm to 120 nm (with and no applied field) will be characterized and analyzed first. Then, followed by the magnetic characterization of FeCoCr films with series of thicknesses (56 nm to 165 nm). Lastly, the characterization of films for different sputtering power will be described. To study the magnetic properties, the coercive field (H_c), saturation field (H_s) or anisotropy

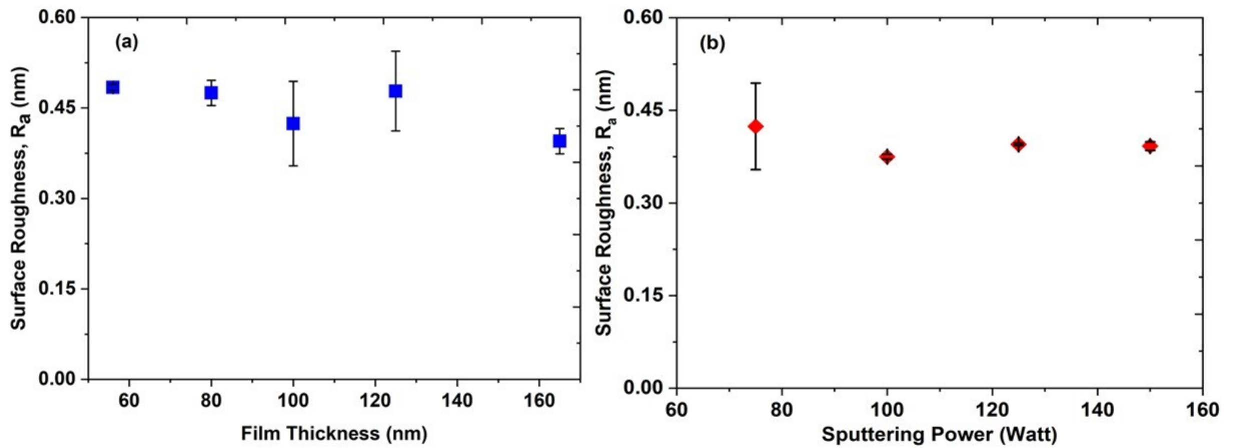

Figure 5.6: Surface roughness of FeCoCr (a) as a function of film thicknesses (fixed sputtering power 75 W) and (b) as a function of sputtering power (constant thickness 100 nm).

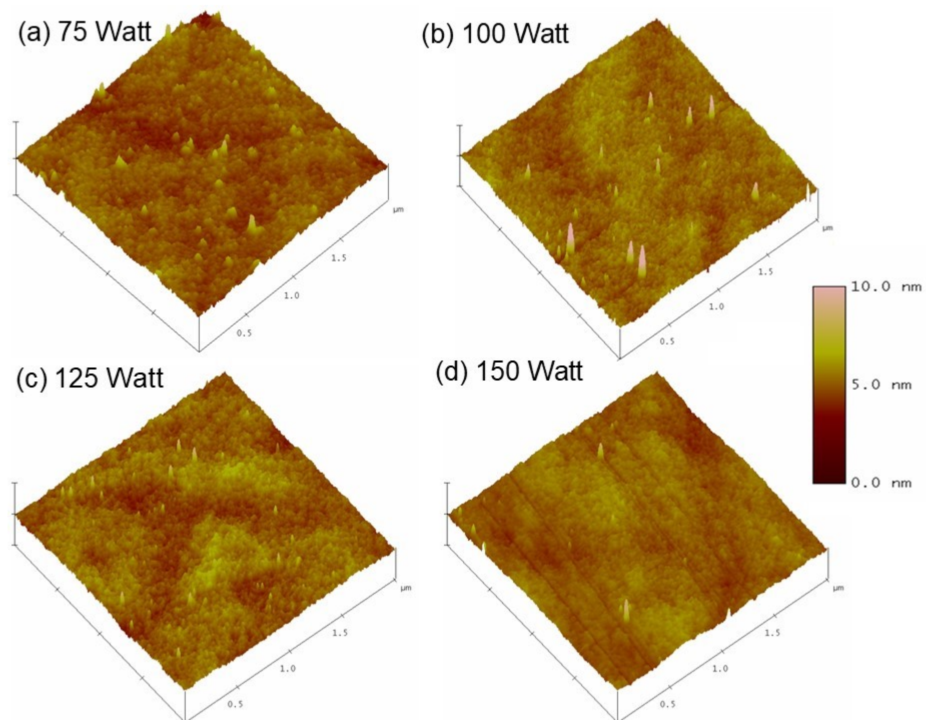

Figure 5.7: AFM micrographs of 100 nm thick FeCoCr films grown with sputtering power (a) 75 W (b) 100 W (c) 125 W and (d) 150 W in the presence of magnetic field. Data scale: 10nm; Scan size $2\mu m \times 2\mu m$.

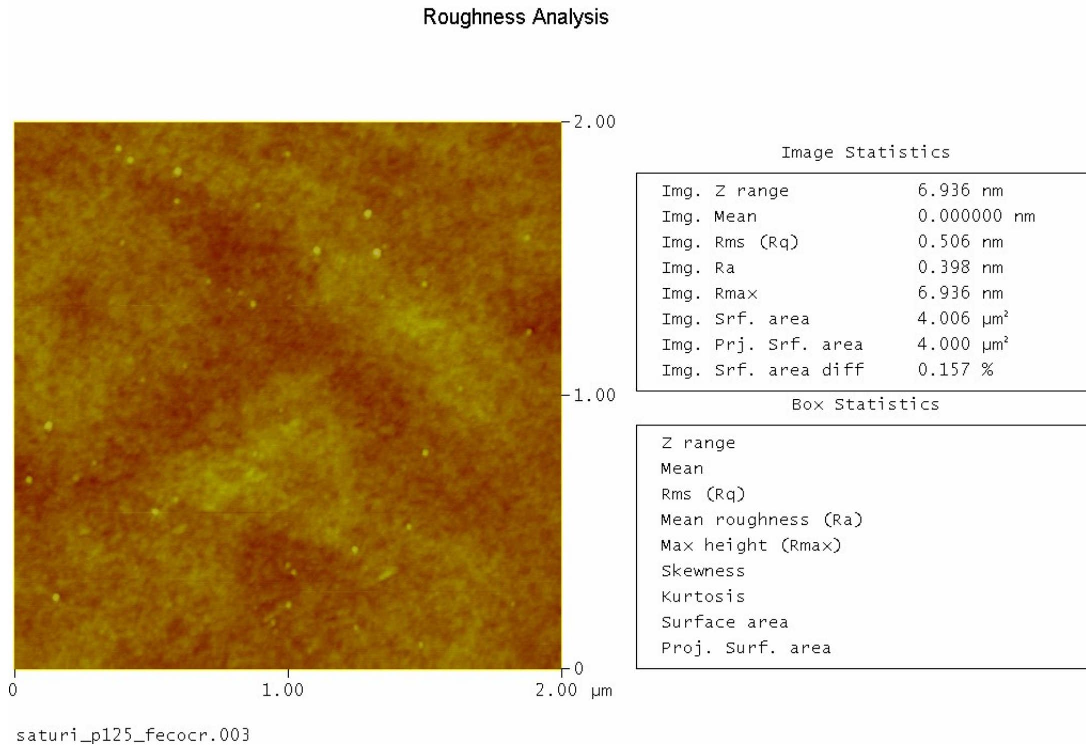

Figure 5.8: Roughness analysis with scan size $2\mu m \times 2\mu m$ of 100 nm thick at 125 W sputtering power. The image also shows the presence of particles due to contamination on the film surface.

field (H_k) and normalised magnetic remanence (M_r/M_s) are the paramount parameters determined from MOKE measurement.

5.6.1 Magnetic Properties of FeCo

The normalised magnetization with respect to FeCo (applied field) and FeCo (no field) are given in respective Figure 5.9 and Figure 5.10. It is noticeable that the magnetization loops of these two types fabrication conditions show different loop shapes. The hysteresis loops for thicker films (100 nm and 120nm) grown with no field have shown a wider loops than films grown under magnetic field. From the normalised graph, the values of H_c, H_s and M_r/M_s can be deduced directly. To see the difference on their magnetic values, the graph of the coercive field and saturation field for these categories of films as function of thickness are plotted in Figure 5.11 and Figure 5.12, respectively. They clearly shows that H_c and H_s increase with film thickness with both 70 nm films (applied field and no field) the H_c was below 5 kAm^{-1}. The H_c for thicker films with applied field are lower than the films grown in an absence of a magnetic field. For instance, the 100 nm film

(applied field) has $H_c = 9.2 \pm 0.7$ kAm^{-1} which is lower than film with no field $H_c = 13.8 \pm 0.5$ kAm^{-1}. It also showed that, the H_c for 120 nm film with no field 17.2 ± 0.7 kAm^{-1} is nearly double the H_c of the same film thickness sputtered with a field (9.8 ± 0.3 kAm^{-1}). Similarly, the 100 nm and 120 nm films deposited in presence of magnetic field yields smaller saturation fields, H_s than the films deposited in the absence of a magnetic field. The H_s for 100 nm and 120 nm (applied field) are 35.5 ± 0.7 kAm^{-1} and 79.2 ± 3.4 kAm^{-1}, respectively. Meanwhile, a larger field was needed to saturate films grown without field as the $H_s = 64 \pm 3.5$ kAm^{-1} for 100 nm and $H_s = 106 \pm 1.1$ kAm^{-1} for 120 nm film. This is proves that, by applying a magnetic field during film fabrication can facilitate a softer magnetic films, thus reducing the field required to saturate the magnetic moments.

To investigate the magnetic anisotropy for all films, the MOKE measurement were carried out at different angles from 0° to 360° at 30° intervals. Then, the remanence ratio M_r/M_s was determined from the normalised graph. The M_r/M_s as a function of angle were plotted as a polar graph and presented in Figure 5.13. The 70 nm and 100 nm films grown with magnetic field had a very weak anisotropy (not well-defined anisotropy shape), while the polar shape for 120 nm (applied field) resembles the polar shape of the 120 nm film (no field). Apparently, FeCo films are magnetically isotropic for both film groups. These findings are supported by the evidence from previous studies on the isotropic behaviour of $Fe_{50}Co_{50}$. Their films deposited at thickness 10 nm $\leqslant t \leqslant$ 100 nm at elevated temperatures (300 K and 600 K) [171] and FeCo (30 nm) [180] grown at room temperature were also found to be isotropic. From the polar remanence analysis, it can be assumed that the application of a magnetic field during the sputtering process was not sufficient enough to induce magnetic anisotropy into FeCo. The 70 nm films from both film sets have no substantial difference in their H_s and H_c. Growing the FeCo thicker than 100 nm in the presence of magnetic field allow the coercive and the saturation fields to be reduced.

5.6.2 Magnetic Properties of FeCoCr films

As the magnetic properties of FeCo were described previously, this study aims to further investigates and to understand whether the addition of Chromium can tailor the properties of FeCo or, if adding Cr insignificantly affects the magnetic as well as the

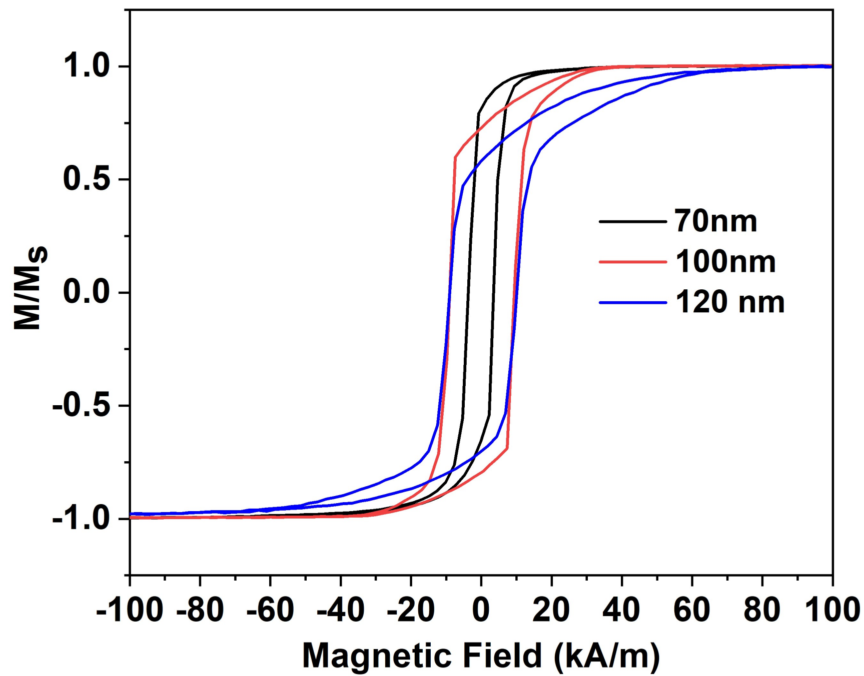

Figure 5.9: Normalised magnetization measured at easy axis of FeCo films sputtered with applied field (120 kAm^{-1}) at different thicknesses.

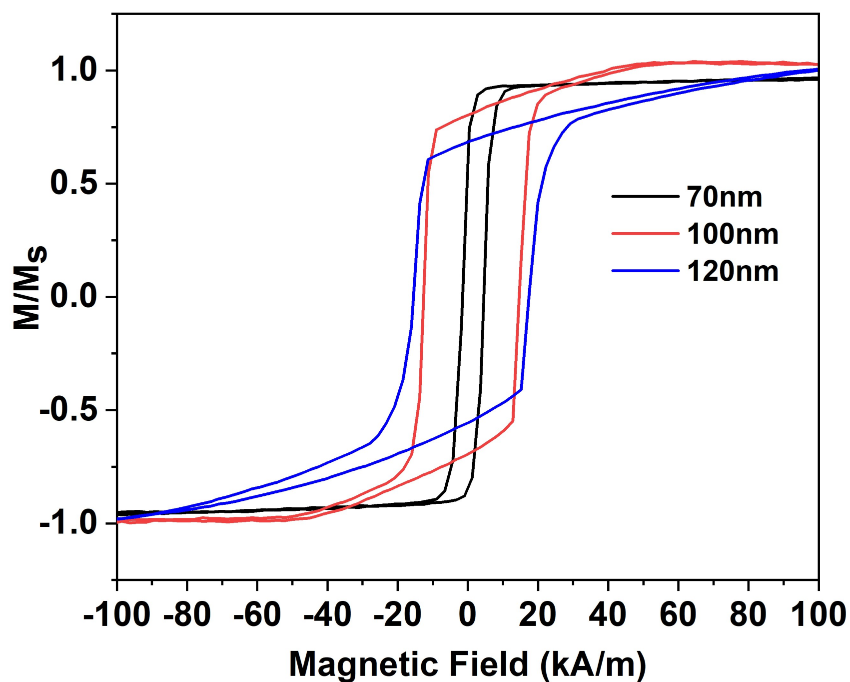

Figure 5.10: Normalised magnetization measured at easy axis of FeCo films sputtered without applied field at different thicknesses.

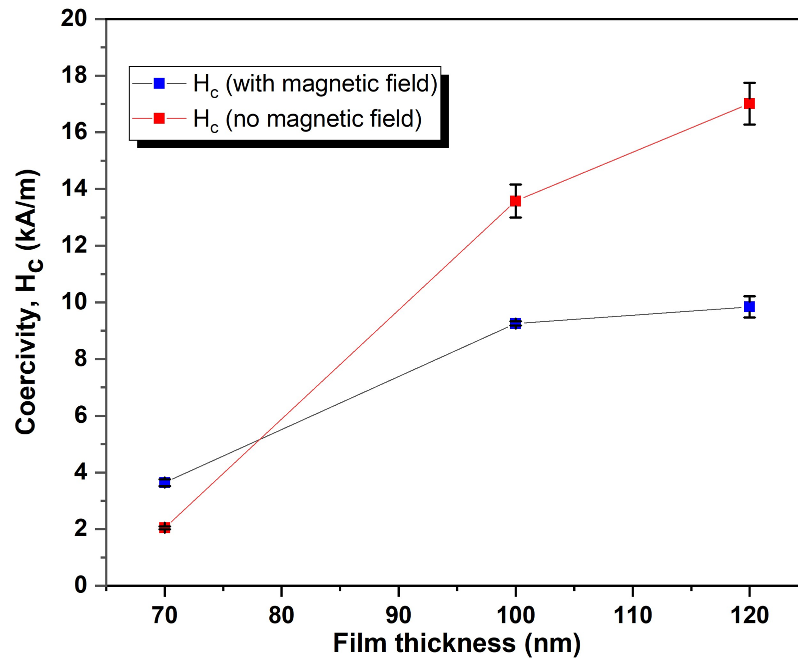

Figure 5.11: The average of coercive field of FeCo sputtered under magnetic field and no field with the shown error bars represent the standard error calculated from three different samples for each film thickness.

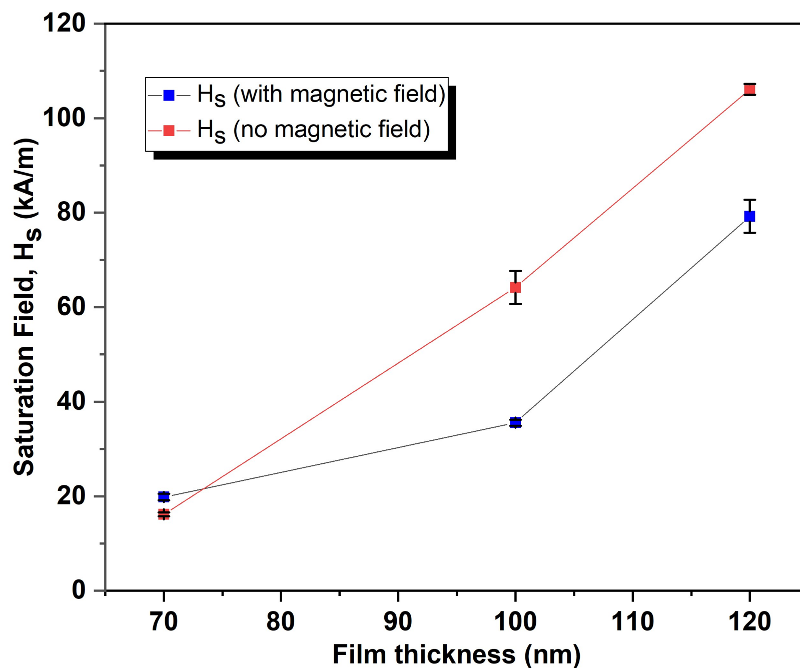

Figure 5.12: The average of saturation field of FeCo sputtered under magnetic field and no field with the shown error bars indicate the standard error calculated from three different samples for each film thickness.

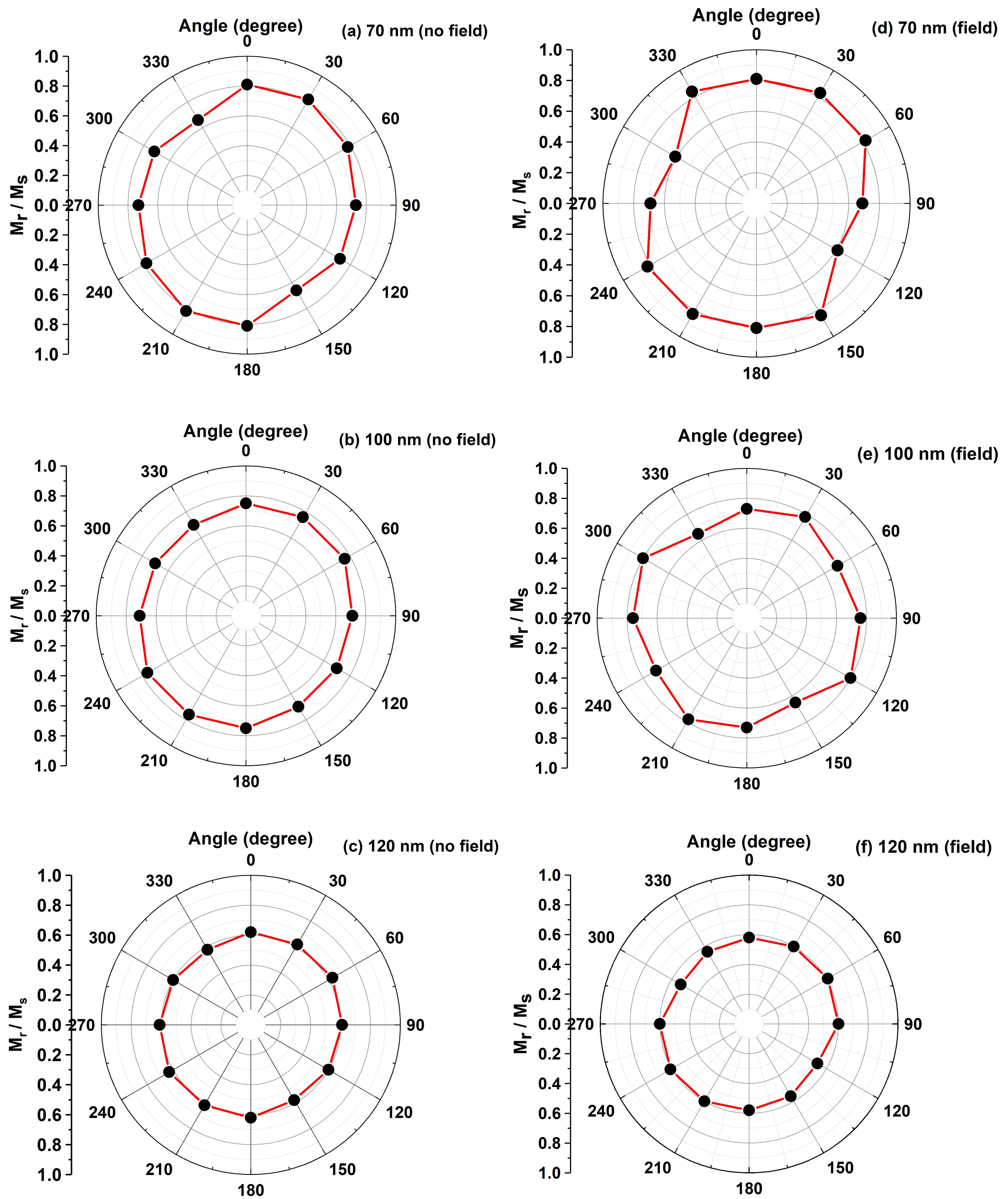

Figure 5.13: Angular dependence of remanence ratio, M_r/M_s of two different set of FeCo films grown with no magnetic field (a) 70 nm (b) 100 nm (c) 120 nm and with magnetic field (d) 70 nm (e) 100 nm (f) 120 nm.

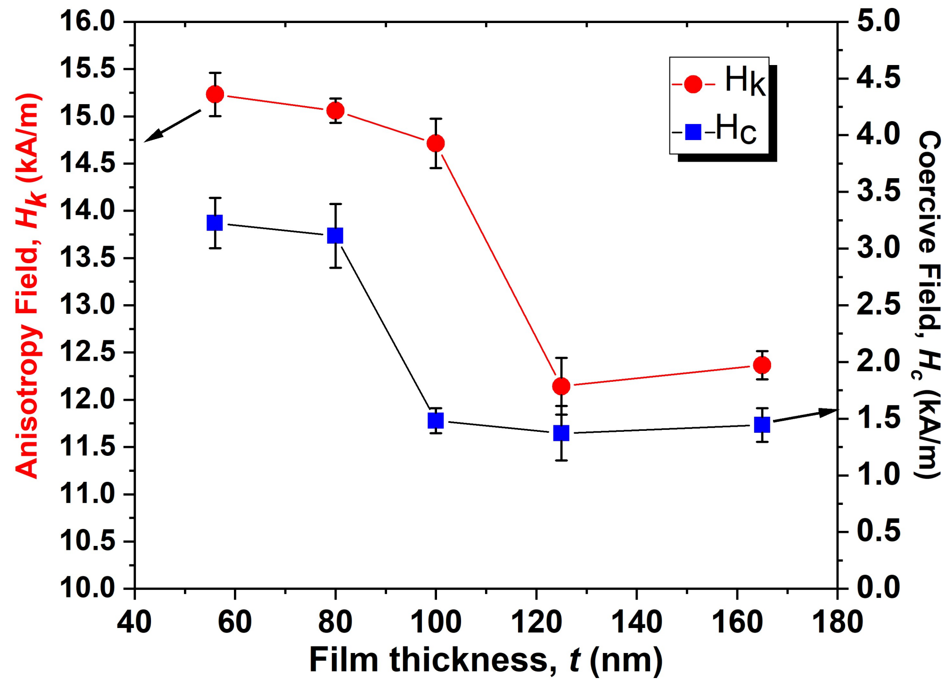

Figure 5.14: The average of coercive field and anisotropy field of FeCoCr as function of thickness (sputtering power 75 W). The error bars represent the standard errors calculated from three different samples.

magnetostrictive properties of FeCo. Figure 5.14 and Figure 5.15 demonstrate the dependence of coercive, H_c, and anisotropy field, H_k, with film thicknesses and sputtering power. It is important to note that the value of the anisotropy fields of FeCoCr in this study were determined at the saturation point taken from along the hard axes, meanwhile the saturation field, H_s as given in previous section on FeCo was taken from the saturation point along the easy axis. From the given figure (Figure 5.14), the anisotropy field H_k was slightly reduced from 15 kAm^{-1} to 12 kAm^{-1} (125 nm) when the thickness is above 100 nm. The H_k for 165 nm film was similar to the 125 nm film. The H_c was found to decrease with thickness up to 100 nm, then almost remained constant as thickness increased up to 165 nm. The coercive field was about 3.22 $\pm$ 0.22 kAm^{-1} for 56 nm and reduced by half to 1.48 $\pm$ 0.11 kAm^{-1} at thickness 100 nm. The results of magnetic properties of FeCoCr were found contrary to FeCo film as previously discussed whereby the coercive and saturation/anisotropy fields of FeCo increased with film thicknesses.

Figure 5.16 compares the normalised magnetization loops of FeCo and FeCoCr at t = 100 nm. It clearly shows that the addition of Cr changed the magnetic properties of FeCo such that, the H_c for FeCoCr (1.48 $\pm$ 0.11 kAm^{-1}) was a factor of 6 lower than the H_c of FeCo (H_c = 9.26 $\pm$ 0.07 kAm^{-1}). One possible reason for the difference in

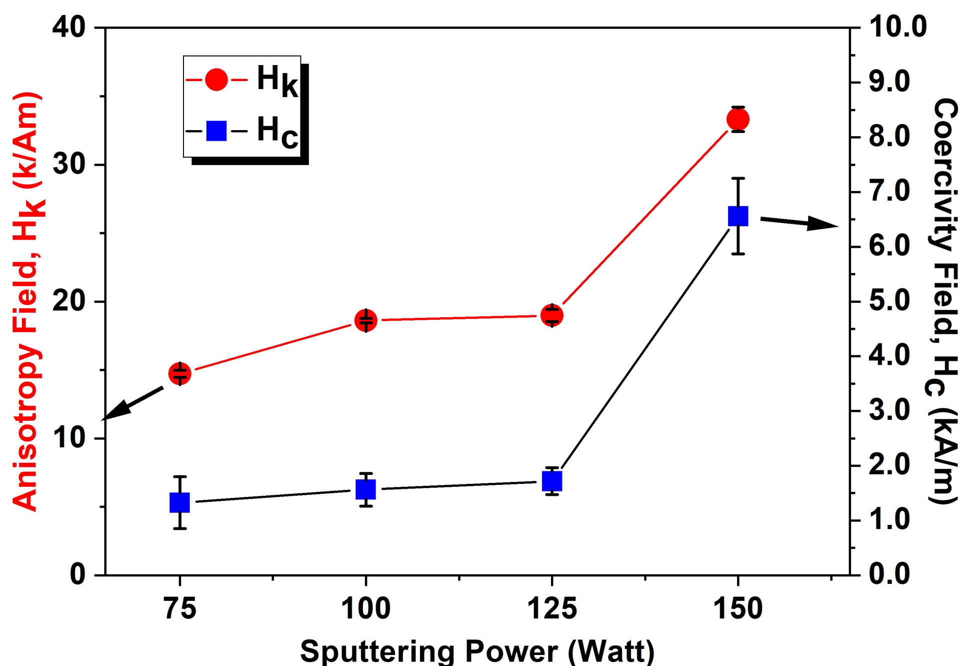

Figure 5.15: The average coercive field of FeCoCr films as a function of sputtering power. Also shown the anisotropy field of films sputtered from 75 W to 125 W (grown under magnetic field at the same film thickness of 100 nm). The error bars indicate the standard error calculated from three different samples.

the coercive field of FeCo larger is due to the grain size, as the FeCo film was found to have a texture phase, with a grain size much larger than the amorphous nature of the FeCoCr film with no grains. It had been found elsewhere that as-deposited FeCo films have shown higher coercivity attributed by domain wall pinning at larger grain boundaries, thus increasing the coercive field [180].

It may be worth comparing the values of H_c and H_k of FeCoCr with those found by earlier research on the addition of boron into FeCo [181]. They found that for FeCoB at thickness 100 nm grown by Magnetron Sputtering, the H_k was 30.33 kAm^{-1}, while the H_c was 3.98 kAm^{-1}, larger than the values of FeCoCr. Rather than adding boron to reduce and induce disorder structure, the results found in this present study supports the hypothesis that Cr addition also could lower the anisotropy and coercive fields.

In contrast to film thickness, the coercive and anisotropy field were found to increase with sputtering power to 125 W, as presented in Figure 5.15. The value for H_c and H_k gradually increased for powers between 75 W to 125 W but then increased noticeably to $H_c = 6.56 \pm 0.69$ kAm^{-1}. As there is no anisotropy was observed for the sample at high power, thus the saturation field, H_s for the film at 150 W (measured at hard

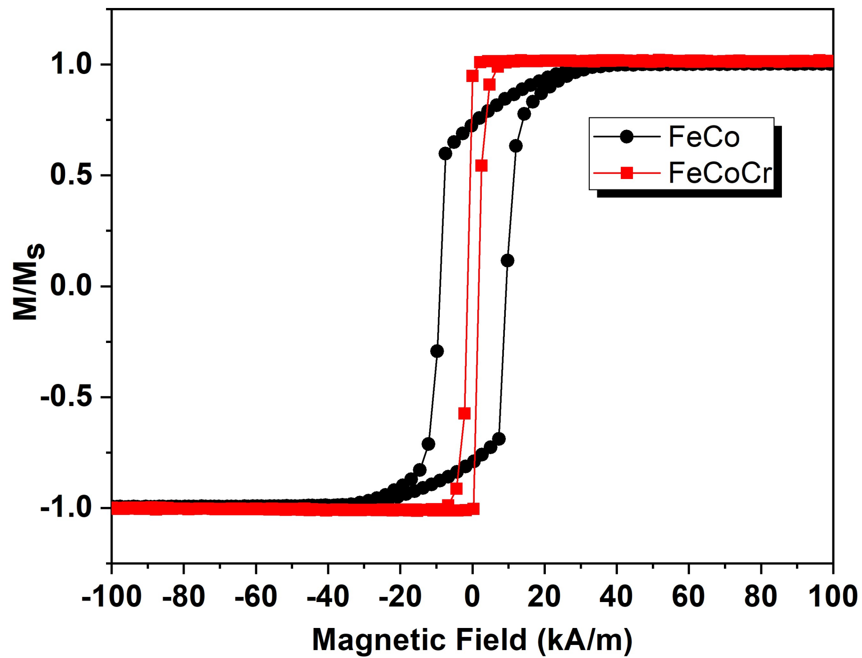

Figure 5.16: Comparison of normalised magnetization between FeCo and FeCoCr (t= 100nm) grown at similar sputtering conditions.

axis) was 33.31 $\pm$ 0.89 kAm^{-1}, which was double the value of the anisotropy field of sample grown at 75 W ($H_k = 14.71 \pm 0.26$ kAm^{-1}). The increment in both coercive and anisotropy fields may have arisen from the change from amorphous to polycrystalline structure as described in the previous section on XRD analysis. It can thus be suggested that, Cr addition can change the structure of FeCo to amorphous, hence tailoring its magnetic property to be softner with lower coercive and anisotropy fields. It is shown by increasing the sputtering power to 150 W, the soft magnetic property were degraded compared to the lower powers. The easy and hard axes loops of representative film thickness is given in Figure 5.17 and for sputtering power the easy and hard axes loops are shown in Figure 5.18.

The angular dependence of the normalised remanence to saturation magnetization, M_r/M_s for different thicknesses of FeCoCr is shown in Figure 5.19. Despite growing the FeCo films under magnetic field (120 kAm^{-1}) in our sputtering system, the field was not enough to induce anisotropy as the films were isotropic in the plane of the film, but the FeCoCr films showed different behaviour, as they had uniaxial anisotropy (Figure 5.19). The strong magnetic anisotropy in amorphous FeCoCr films may be influenced by two reasons. Firstly, the application of a magnetic field (120 kAm^{-1}) during deposition clearly was able to induced the anisotropy into FeCoCr films. Secondly, the

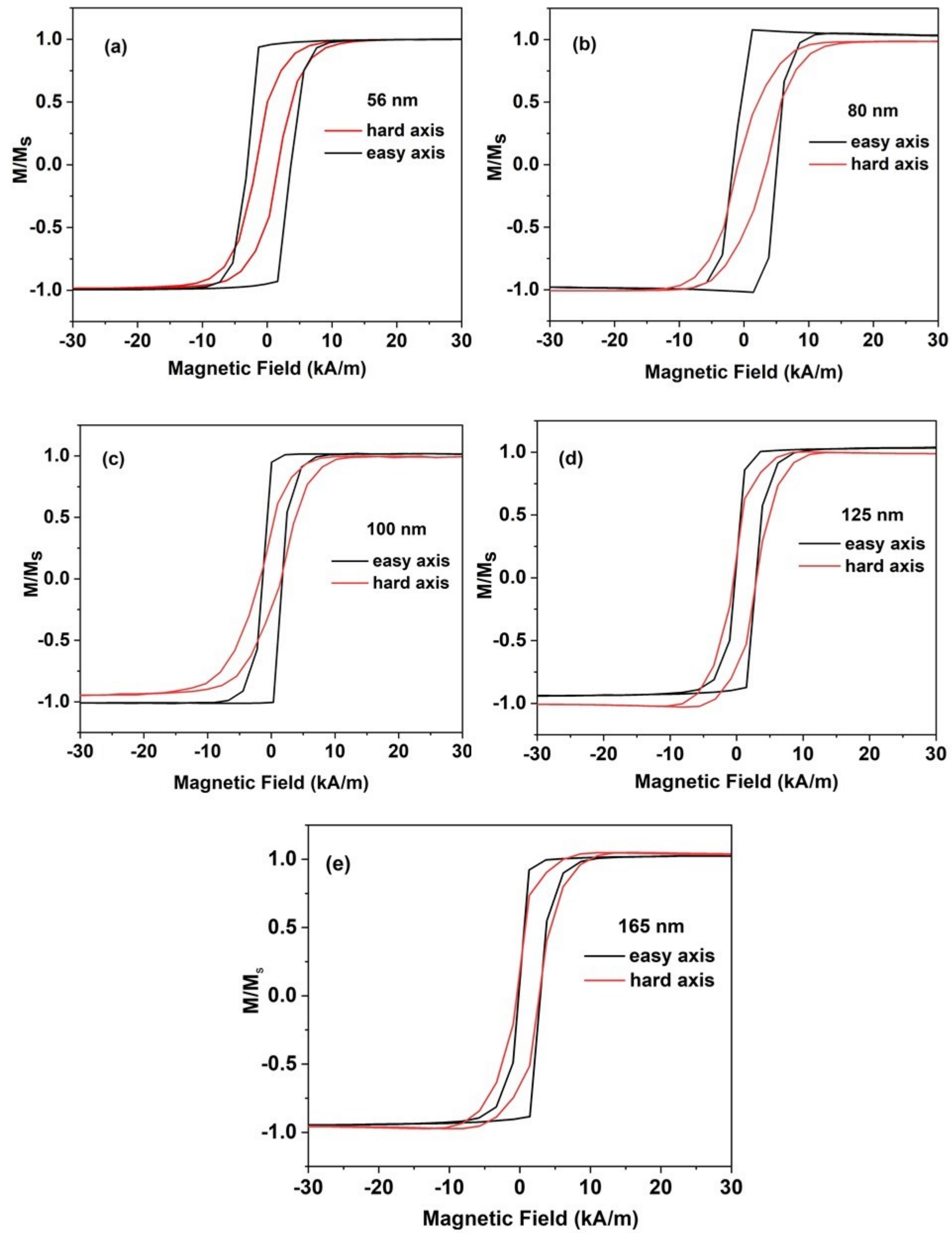

Figure 5.17: Normalised magnetization on easy and hard axes for series of thickness FeCoCr (a) 56 nm (b) 80 nm (c) 100 nm (d) 125 nm and (e) 165 nm grown at sputtering power 75 W.

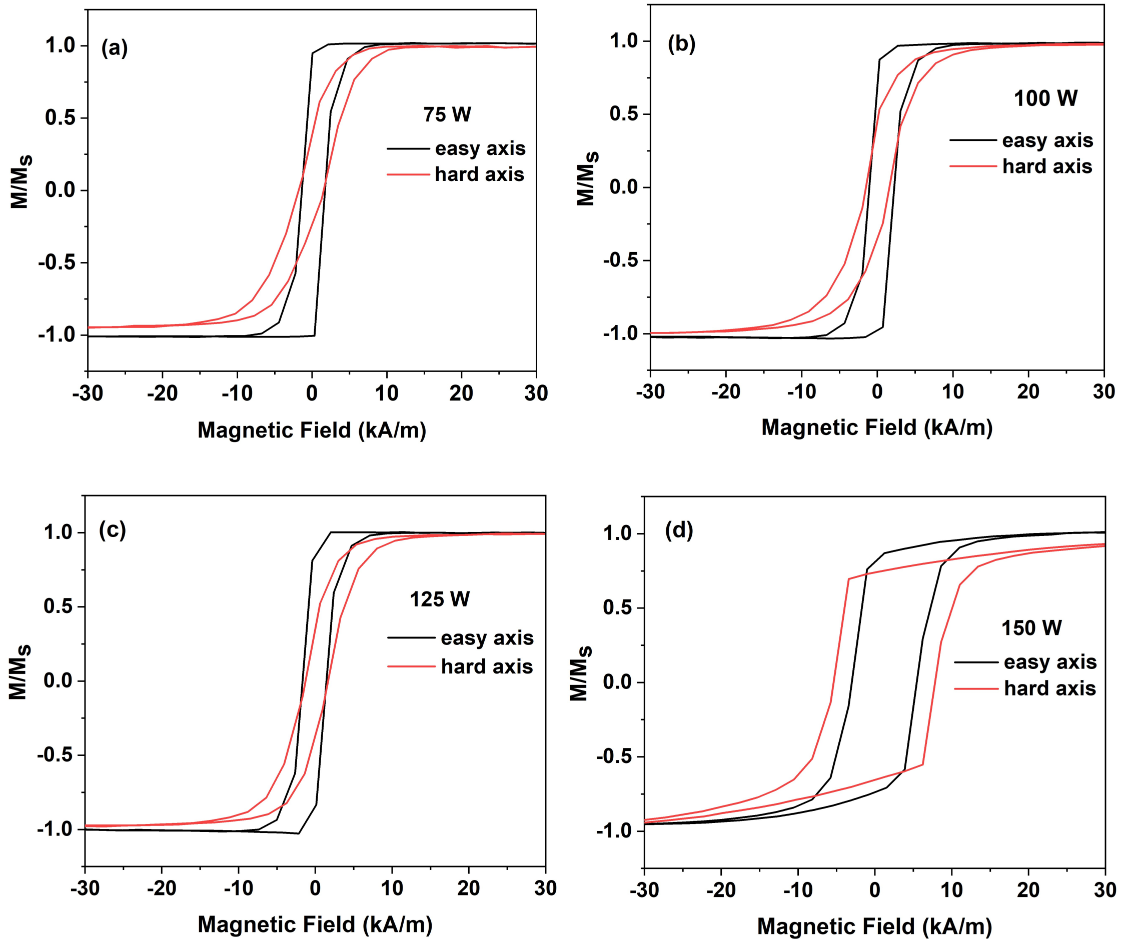

Figure 5.18: Plots of easy and hard axes for FeCoCr at different sputtering power (a) 75 Watt, (b) 100 Watt (c) 125 Watt (d) 150 Watt at fixed thickness 100 nm.

.

magnetic anisotropy for amorphous material can be explained by the random anisotropy model (RAM) [18, 49, 50]. In this theory, the exchange interaction was dominant such that the correlation length, d is much smaller compared to the ferromagnetic exchange length, L_{ex}. As given in the Chapter 2 the typical value of the exchange length for Fe-based was 20 nm to 40 nm [35]. As consequence the local magnetocrystalline anisotropy was averaged out due to the short-range order in amorphous films [182]. Thus it can be expected that magnetic anisotropy for FeCoCr films also has contribution from the local random anisotropy due to the disorder structural [182]. Figure 5.20 compares the difference in polar graphs for films grown at sputtering 75 W and 150 W. It revealed that increasing the sputtering power to 150 W led to the degradation of anisotropy as it can be seen that the anisotropy is weaker than the film at the lowest power. This most

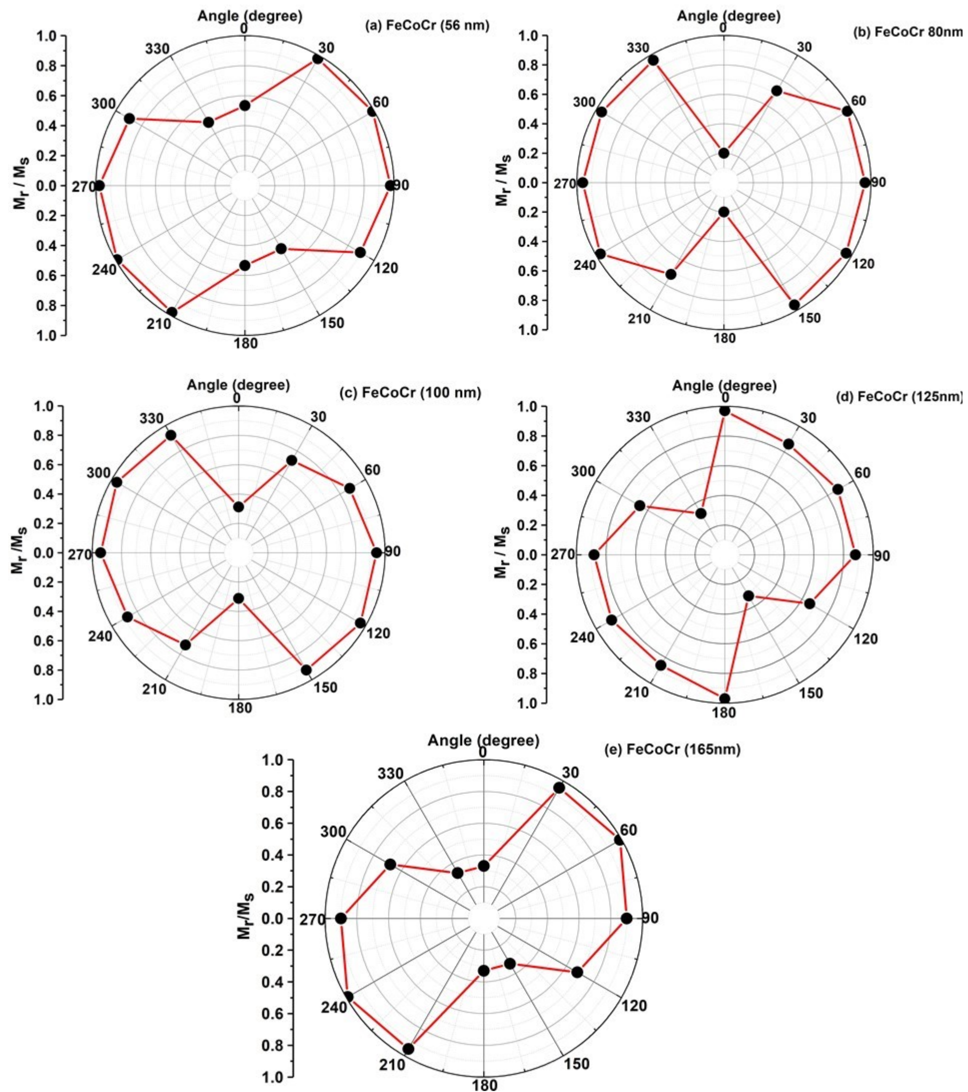

Figure 5.19: Angular dependence of FeCoCr at varied thickness (a) 56 nm (b) 80 nm (c) 100 nm (d) 125 nm and (e) 165 nm.

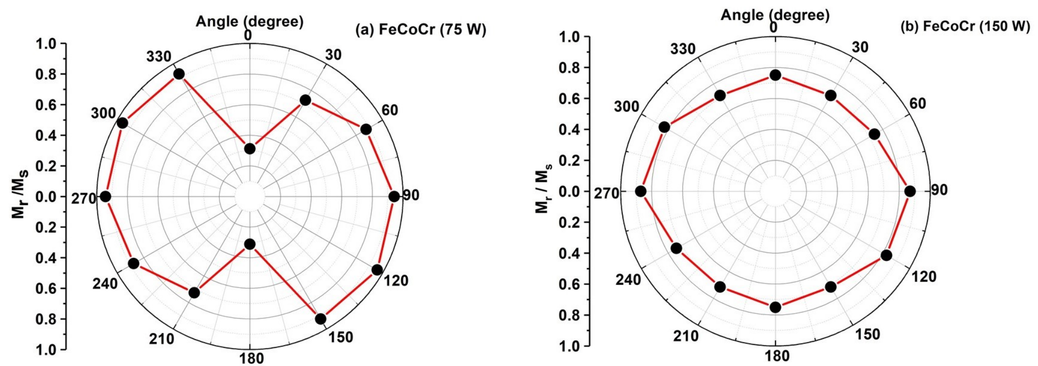

Figure 5.20: Comparison of angular dependence of M_r/M_s between films grown at sputtering power of (a) 75 W and (b) 150 W.

likely to the structure of film at highest power was different to the film grown at lowest power as described in Section 5.3. Therefore, the optimize sputtering power for FeCoCr films to have a strong magnetic anisotropy with low coercivity and anisotropy fields was at 75 W.

5.7 Magnetostriction Studies on FeCo and FeCoCr

In this section, an investigation into the magnetostrictive properties of the two different FeCo structure (FeCo with texture structure and FeCoCr films in amorphous) was carried out. The total effective magnetostriction constant, λ_s was determined by Villari effect through film bending using an Equation 4.22 as given in details in Chapter 4. That equation includes the saturation magnetisation of the film, therefore the saturation induction ($\mu_0 M_s$) of FeCo was taken as 2.4 T from the literature [23]. The saturation induction of FeCoCr was measured by using a VSM and it was found to be lower which was 0.96 T, due to existence of Cr, which is antiferromagnetic, hence reduced the magnetisation of those films. Figure 5.21 depicts the magnetostriction constant as a function of FeCoCr thickness. It was determined that λ_s for FeCoCr ranged from 22ppm to 28ppm for film thickness up to 100nm. While the 100nm film having the magnetostriction (λ_s= 28 ± 5ppm), 56nm film having a λ_s = 22 ± 3ppm. However, it can be said that the magnetostriction constants of FeCoCr films were independent of film thickness, as all the values were within error of each other. This means that the interfacial/surface magnetostriction constant does not strongly influence the total effective magnetostriction constant of the films. The same plot also (Figure 5.21) shows the magnetostriction constants for FeCo films. The λ_s of FeCo were observed to reduce with thickness. The results of the FeCoCr films contradict the previous findings on the dependency of the total effective magnetostriction on film thickness as proposed by Szymczak [183]. The model was based on Neel's model ($\lambda_s = \lambda_b + \lambda_{s/i}/t$), where λ_b = magnetostriction of bulk, $\lambda_{s/i}$ = magnetostriction due to surface or interface contribution to the magnetostriction and t = film thickness. Notwithstanding, the λ_s for 100 nm (FeCo), was 26 ± 6 ppm, which this figure insignificantly different to λ_s for 100nm FeCoCr (λ_s = 28 ± 5 ppm). Film for 70 nm FeCo film had magnetostriction, (λ_s = 35 ± 5 ppm) which was lower from the value of FeCo films ($\lambda_s \approx$ 50 ppm) reported by [105]. They measured the λ_s for the same compositions of FeCo deposited onto sodium glass films by using

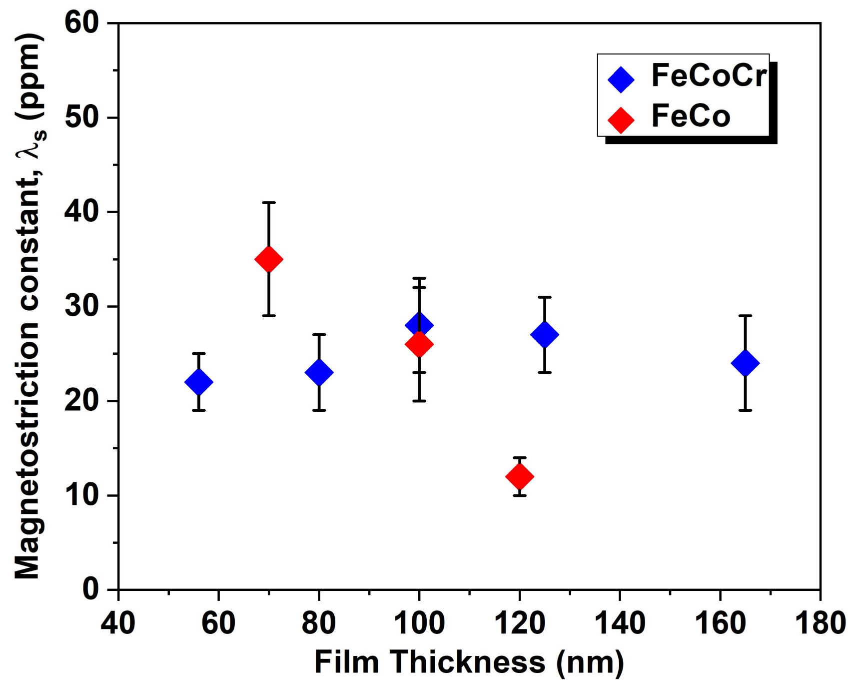

Figure 5.21: Comparison of magnetostriction constant, λ_s between FeCo and FeCoCr as function of film thickness at fixed sputtering power 75 W. The data point and error bars represent the average of λ_s from a number of measurements on the same sample, respectively.

cantilever method. The value of λ_s determined from the present study are also far below the reported bulk value of FeCoCr due to the compositions of Co and Cr being different [28] where this paper reported the λ_s = 61 ppm at composition of 30 wt.% Cr and 15 wt.% Co. This also may be explained by the fact that the local atomic arrangement between thin film and bulk are different [184], leading to the different magnetoelastic behaviour, as the FeCoCr film exhibited the amorphous structure with the atoms being randomly oriented.

Figure 5.22 reveals the magnetostriction constant of the films grown at different powers. While the magnetostriction of FeCoCr films demonstrated the independency upon thickness, by contrast the magnetostriction decreased as the sputtering power increased. The film grown at 75 W exhibited the highest magnetostriction ($\lambda_s = 28 \pm 5$ ppm). When the power increased to 100 W, λ_s reduced to 18 ± 6 ppm then at 150W considerably dropped to $\lambda_s = 6 \pm 1$ ppm, which is nearly five times lower than the 75W film. One plausible reason attributed to the higher magnetostriction at lower power (75 W) is because of the internal stress may occur during sputtering process. The higher the stress, the higher the elastic properties, hence the magnetostriction. Thus it can be concluded

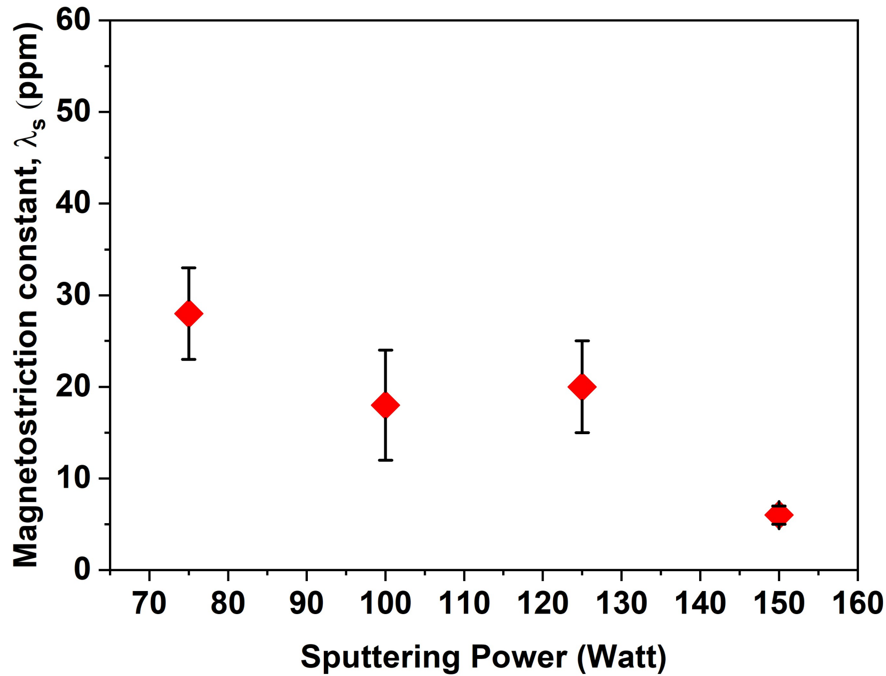

Figure 5.22: Magnetostriction constant, λ_s of FeCoCr against sputtering power with each film has thickness 100 nm. The data point and error bars represent the average of λ_s and the standard error of a number of measurements on the same sample, respectively.

that the disorder structural of 75 W had higher magnetostriction due to a larger internal stress than the 150 W with polycrystalline structure.

5.7.1 Summary

To summarize, the characterization of FeCo and FeCoCr films grown by varying growth conditions have been described and discussed. For FeCo films the application of a magnetic field during growth affected the coercive and saturation fields but not considerably significant to induce anisotropy in these films. Depositing film in the absence of magnetic field made the films harder, hence the coercive and saturation fields increased in comparison to the FeCo films grown under magnetic field. All FeCoCr films with different thicknesses were found to be amorphous and magnetically soft. On the other hand, increasing the sputtering power above 100 W changed the structure to polycrystalline with two peaks of body-centered cubic (BCC) phase at $2\theta \approx 45^0$ and $2\theta \approx 81^0$. The structural order obtained in XRD agrees with the TEM analysis. The element percentages of Cr in FeCo decreased with sputtering power. The changes in surface roughness of films were insignificant regardless of thickness and sputtering power. Although the addition of Cr

have not shown huge affects on the magnetostriction constant compared to FeCo films over the film thickness, it did significantly affects the coercive and anisotropy fields by reducing them. Contrarily, increasing sputtering power reduced the magnetostriction constant by five times. The induced magnetic anisotropy in soft magnetic amorphous FeCoCr films gives promising results, which could be exploited in magnetic sensors and spintronic applications. The outcomes from the characterization of FeCo and FeCoCr films in this present study have contributed to the current literature, as the feasibility to achieve soft amorphous magnetostrictive of FeCoCr films with lower anisotropy field while still maintaining higher magnetostriction, $\lambda_s = 26$ ppm has been achieved.

Chapter 6

Structural, Magnetostrictive and Magnetic Damping Properties of Soft FeCoCr Thin Films

6.1 Introduction

As given in preceding chapter, soft amorphous FeCo films have been successfully achieved by doping with Cr. This Chapter extends the investigation on how much Cr concentrations can be added into FeCo to achieve the ideal magnetostrictive properties with high saturation magnetostriction (> 20 ppm) and lower H_c (< 10 kAm^{-1}). Other than structural and magnetostrictive properties, one further feature worth studying is the magnetic damping of soft magnetic materials. It has been found that, the development of MagMEMS sensors and microwave spintronics devices have become a driving force to expand experimental works and studies on the magnetostrictive and high frequencies properties of soft amorphous thin films notably, Fe-based amorphous materials. To minimize the power consumption in spin devices such as in magnetic random access memory (MRAM), small damping values are absolutely necessary [12]. The characteristics of soft magnetic film having large magnetostriction, at the same time possessing small resonant linewidth and low damping have become topics of interest for tunable microwave magnetoelectric devices. For instance, Lou et.al [185] investigated the magnetostriction and microwave properties of FeGaB thin films. The FeGaB films were sputtered from two

different targets of FeGa and boron, which the B compositions were varied by adjusting the gun power of the Boron target. They found for FeGa films at the composition of at.% 12 of B, the magnetostriction constant was enhanced by a factor of 3 (70 ppm) from the value of pure FeGa. Their investigation on the FMR linewidth with B contents have found that the FMR linewidth dropped from 700 Oe to 20 Oe with an increase of B compositions. Liu et.al [186] have reported thickness dependence on the damping constant of FeCoB. They found that the damping constant dropped from $\alpha = 0.008$ ($t=$ 10nm) to 0.001 ($t=$ 1nm) with decreasing film thickness. Another study by Parkes et.al [12] claimed that their Galfenol films ($Fe_{81}Ga_{19}$) grown on GaAs substrate via molecule beam epitaxy had magnetostriction constants as large as bulk single crystal, which they obtained $(3/2)\lambda_{100} = 3.95\text{x}10^{-4}$ with low magnetic damping ($\alpha = 0.017$). Recently, the addition of C from 2% to 16% into FeGa was studied to determine its effect on the magnetostriction, microstructure and microwave properties [128]. The analysis showed that the magnetostriction constant of FeGaC reached a peaked with $\lambda \approx$ 70ppm at about 10% of C and dropped dramatically to 23 ppm when C was further increased. The Gilbert damping constants of FeGaC were reduced with the C contents with minimum value of 0.0027.

The effects of dopants on the magnetic properties of FeCo films have been widely explored, with most reported work focusing on the effect of thickness and compositions of FeCo thin films alloyed with B or C [42, 123, 124, 126]. To the best of the author's knowledge there is no report yet on investigating the effect of Cr doping on especially on its effects on both the magnetostrictive and magnetic damping properties of FeCoCr films. Generally Cr has been used as an underlayer to achieve a good adhesion between film and substrate. Therefore in this chapter, particular attention has been paid to the effect of the Cr dopants on the structural, magnetic, magnetostrictive and magnetic damping of FeCoCr films. It would be expected that by incorporation of Cr into the FeCo thin films, the soft amorphous of FeCoCr thin films can be produced which would exhibit a high saturation magnetostriction constant ($\lambda_s > 20$ ppm), low anisotropy field ($H_k < 15$ kAm^{-1} and small magnetic damping ($\alpha \leq 0.01$). The structure and magnetic properties of the films were characterized by XRD, MOKE and SQUID-VSM (see Chapter 4). The composition of Cr was examined by Energy Dispersive X-Ray Spectroscopy (EDX). The magnetostriction constant, λ with different compositions was measured by Villari technique. The anisotropy field,H_k, saturation magnetisation, M_s and Gilbert damping

constant, α were also determined by using a Vector Network Analyzer Ferromagnetic Resonance (VNA-FMR) measurement.

6.2 Sample Fabrication

FeCoCr films with a range of Cr compositions were deposited by using RF Magnetron Sputtering technique in which the Cr compositions were controlled by using different number of Cr foil targets as described in section 4.2.4. The Cr targets which had 99.99% purity and were mounted on top of the 15 cm diameter FeCo target. A maximum of four pieces of Cr target were used with each having size of 2.5 mm x 2.5 mm x 1 mm. Accordingly, four groups of samples with different compositions of Cr were fabricated on silicon substrates. Samples were then labeled and denoted as C1, C2, C3 and C4 for further characterization analysis based on the number of foil pieces being used. For example C1 refers to the sample grown when one piece of Cr placed on FeCo target and etc. The sputtering parameters such as power, pressure and target-substrate distance were kept constant for all films, the optimized sputtering power 75 W used, the working pressure 4.8 x 10^{-3} Torr and the target-substrate distance 6 cm . The films were deposited under the presence of an in-plane magnetic field (22 kAm^{-1}) at room temperature, while deposition time was maintained such that the thickness for all samples were the same in order to make valid comparison between range of FeCoCr concentrations. Film thicknesses were examined and confirmed by Atomic Force Microscopy to be t= 65.1 $\pm$ 0.3 nm.

6.3 Compositions Analysis by EDX

To characterise how the concentration of Cr varied across the deposited films, Energy Dispersive X-Ray spectroscopy (EDX) was used for compositional analysis. Figure 6.1 presents a graph of elemental composition analysis. It is shows that the Co and Fe compositions were found to decrease with the increase in the number of Cr targets. The Cr percentages were found to vary from at.% 2.6 to at.% 9.6. The concentrations of Fe ranging between at.% 43 and at.% 45, whilst the Co were found in the ranged of at.% 47 to at.% 52. The composition of FeCo as a control sample, which initially was assumed to be 50:50, shows higher Co percentages (at.% 52.8) compared to Fe content

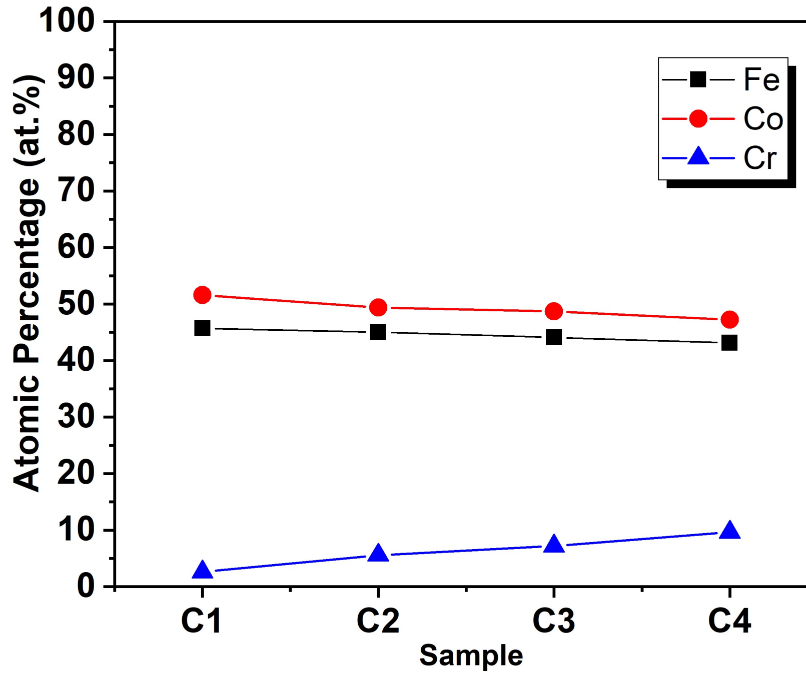

Figure 6.1: Plot of element concentrations determined in fabricated sample based on number of Cr target used.

Table 6.1: Concentrations level of Fe, Co and Cr in atomic percentage (at.%) determined by EDX Spectroscopy.

Sample	**Fe at.%**	**Co at.%**	**Cr at.%**
C1	45.7 ± 0.1	51.6 ± 0.1	2.6 ± 0.1
C2	45.0 ± 0.1	49.4 ± 0.1	5.60 ± 0.03
C3	44.1 ± 0.1	48.7 ± 0.2	7.2 ± 0.1
C4	43.1 ± 0.2	47.2 ± 0.1	9.60 ± 0.03
Control sample	47.2 ± 0.1	52.8 ± 0.1	-

(at.% 47.2). Table 6.1 summarizes the concentrations of the respective Fe, Co and Cr for each set of films.

6.4 Structural Analysis by XRD

Figure 6.2 displays the XRD profiles of the as-deposited FeCoCr films grown on Si substrate with different Cr compositions. It is clearly observed that broad peaks were measured at $2\theta = 44.7^0$, implying an amorphous nature of FeCoCr with no other intense peaks due to a crystalline phase. This outcome was found contradict to the previous study [30] who examined a textured BCC (110) at $2\theta = 45^0$ in their films $(Fe_{54}Co_{46})_{1-x}Cr_x$ with the Cr concentration from 0 to 13% and film thickness 100 nm

grown by magnetron sputtering. An intense Bragg diffraction with textured structure was also determined by Wang et.al [29] on the XRD profiles of FeCoCr films sputtered with higher Cr target power up to 100 W. The structure discrepancy found in this present study with those literature seems possible to be explained by the different thicknesses and sputtering parameters. The film thickness of FeCoCr from the reported studies were thicker (250 nm) compared to our film, where the thickness was only 65 nm. As the film becomes thicker, there is a higher diffraction volume [187] therefore, the diffraction intensity is likely to increase with thickness, which leads to the formation of intense peaks, hence the BCC phase was observed in the study [29]. In addition, sputtering power is one of the factor which decisively influence the deposition rate, thus when a film is prepared at higher Cr power a textured phase film, such as those in the literature are possible to grow. This is also observed in the film growth at 150 W in Chapter 5, which films had (110) texture phase. Meanwhile in this study, the sputtering parameters were maintained at 75 W thus, all as-deposited films were amorphous in nature. As one of the motivation of this study is to determine the possibility of producing amorphous structure, it can be deduced that by adding Cr as low as at.% 2.6 Cr, the amorphous structure was successfully achieved. The Cr seems to disrupt the polycrystalline structure of FeCo at low power (75 W).

6.5 Magnetic Properties of FeCoCr films

Magnetic characterization of FeCoCr thin films with different Cr concentrations have been studied by two different methods. First, qualitative measurement where the magnetization of magnetic sample at the surface level were analyzed by a MOKE magnetometer. Second, quantitative measurement by SQUID-VSM which measures the magnetic moment. Through this measurement a calculation of saturation magnetization, M_s can be made by knowing the volume of the films.

6.5.1 Magnetic Properties by MOKE

The influence of Cr concentrations on the magnetization hysteresis loops of FeCoCr measured on a MOKE magnetometer are shown in Figure 6.3(a)-(d). It is apparent from the figure that, the uniaxial anisotropy of the FeCoCr films can be determined.

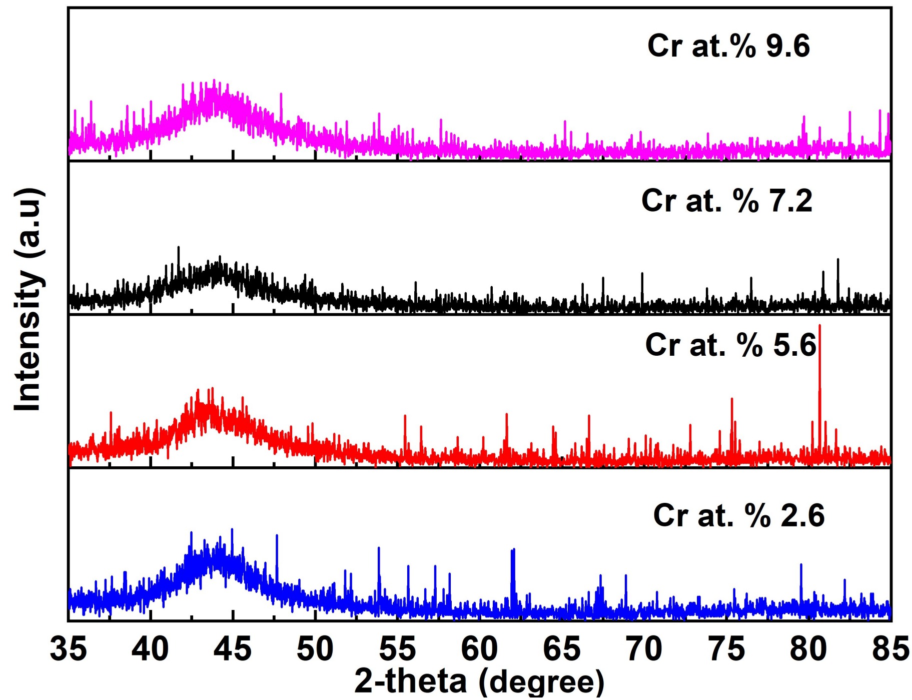

Figure 6.2: The XRD diffraction pattern of films at varied Cr percentages with thickness of samples, $t = 65$ nm.

The loops measured along the easy axis are indicated by a black line, while the loops measured along the hard axis is shown by a red line. It is clearly reveals that FeCoCr films have rectangular shaped loops measured along the easy axis as opposed to the hard axis which small coercivity of films and magnetically uniaxial, regardless of Cr concentrations. All the hysteresis loops are shown as normalised magnetisation, M/M_s. To further investigate the magnetic anisotropy, measurement of films at different angle were performed by rotating the sample from 0^0 to 360^0. The remanence ratio (M_r/M_s) as a function of angle rotation is plotted as a polar graph, as shown in Figure 6.4. It clearly showed that when sample was rotated from 0^0 to 90^0, the magnetization involves the domain wall motion. The squareness of $M_r/M_s \approx 1$ is noticeable when the angle rotation was 90^0 as presented in Figure 6.3.

It is well known that for crystalline materials the magnetic anisotropy is mainly attributed to the magnetocrystalline anisotropy due to origins of spin-orbit coupling, which is the interaction between the magnetic moment and the crystalline lattice [36]. However, even in amorphous materials uniaxial anisotropies can be induced by an application of a magnetic field during the fabrication process [37]. Previous studies related the induced anisotropy based on Néel's pair-ordering anisotropy (POA) [53] as well as the

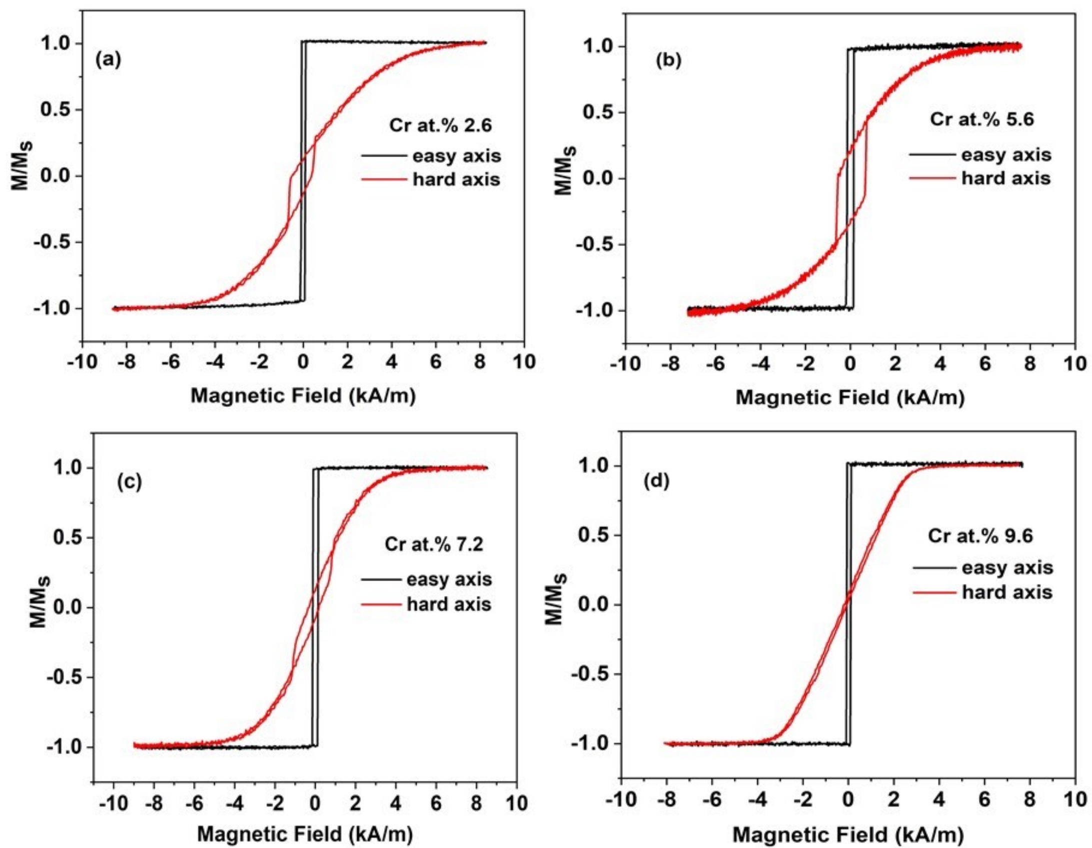

Figure 6.3: Normalised magnetization at easy and hard axes for representative FeCoCr film at varied Cr compositions.

Random Anisotropy Model (RAM). The existence of magnetic anisotropy in amorphous ferromagnetic materials according to POA are caused by the difference in the number of like and unlike nearest-neighbor distances for the in-plane and out-of-plane directions. This model has been widely used in explaining the origin of the induced uniaxial magnetic anisotropy particularly in amorphous transition metals-metalloid (TM-M) based magnetic thin films, for example FeCo-B [182, 188, 189]. A well defined uniaxial magnetic anisotropy induced in amorphous FeCoCr films was observed in all concentrations caused by an applied field during film growth, which leads to the directional order on the number of Fe-Fe, Co-Co and Cr-Cr neighbors atoms aligned with the magnetic field. By contrast, the FeCo films also grown in a presence of magnetic field, but with larger coercivity were found to be magnetically isotropic as discussed previously in Chapter 5. Although the magnetic anisotropy in FeCoCr at varied compositions was clearly induced by the magnetic field during fabrication, one could not rule out any other possible mechanism which causes anisotropy in magnetic films. Another mechanism which possibly contributed to the magnetic anisotropy in these films is from internal stresses. In the

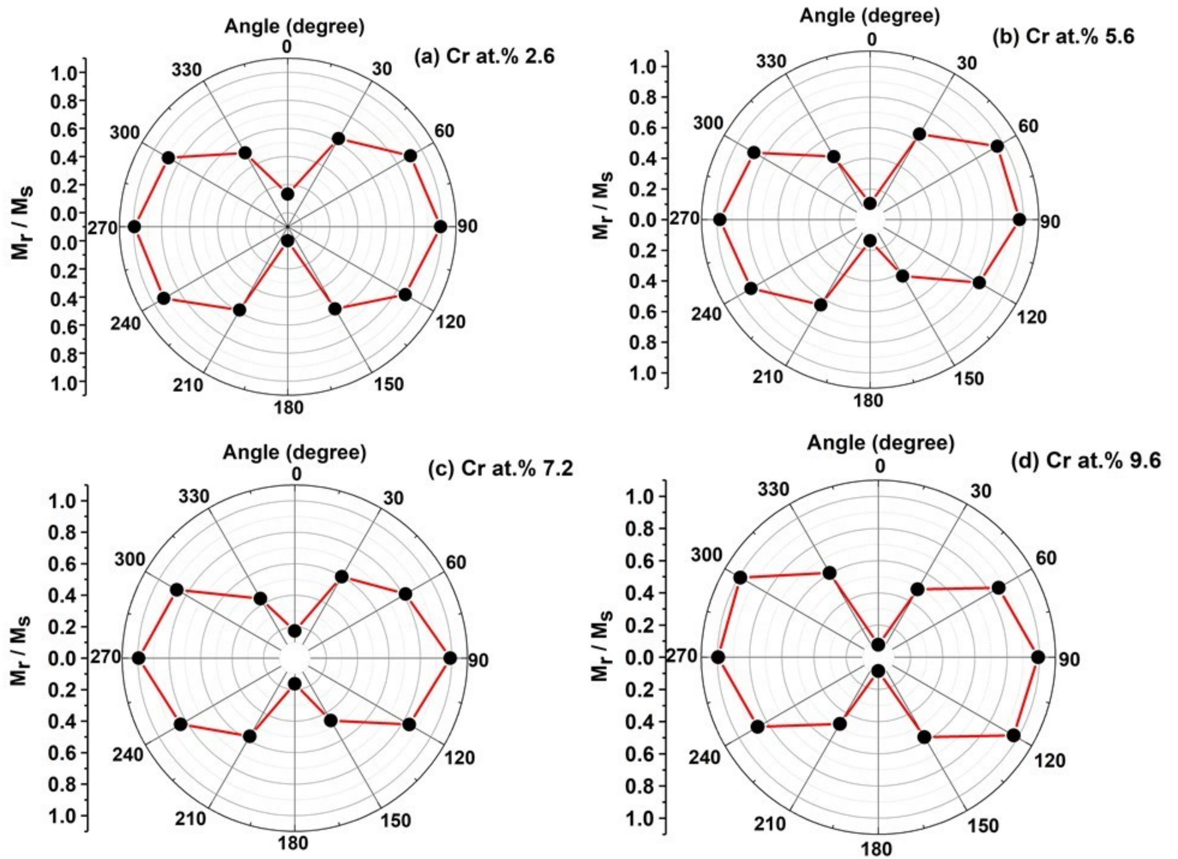

Figure 6.4: Angular dependence of remanence ratio, M_r/M_s of FeCoCr varying Cr concentrations showing a strong uniaxial anisotropy.

case of this present work, the magnetic anisotropy may also be caused by the internal stresses within the films due to the magnetoelastic properties of FeCo itself, since the FeCo has a high magnetostriction constant. It has been reported that for films grown by magnetron sputtering process, the growth induced-stresses may be developed [190], normally the compressive stress as a result of gas incorporation with substrate bias and self implantation [191].

The dependence of the coercive field, H_c and saturation field, H_s as a function of Cr percentages is plotted in Figure 6.5. The graph shows that there is a sharp drop in the H_c and H_s as Cr concentration increased to 5.6% before it remains steady upon increasing the concentration up to 9.6%. FeCoCr films at 2.6% had the highest H_c and H_s, which are 173 ± 5 Am^{-1} and 255 ± 2 Am^{-1}, respectively. This may be ascribed to the highest amounts of Fe and Co in those sample (C1) as determined by EDX. The higher coercivity for FeCo films (discussed in Chapter 5) are mainly from the large magnetocrystalline anisotropy and the grain size effect [23, 27], but since the FeCoCr films were very soft

and had an amorphous structure, so have no grain size, the coercive field found to be larger for the film at.2.6% was probably attributed by the large anisotropy due to higher proportions of Fe and Co in that film. In the Cr compositions range between 5.6% and 9.6% , the value of H_c seems to remain constant at about 140 Am^{-1}. In similar manner, the H_s did not changed within this compositions range as it was found to be around 180 Am^{-1}. The shown error bars in both measured H_c and H_s fields were determined along easy axes for different samples from each group of film.

On the other hand, the anisotropy field, H_k of films was determined along the hard axis. The H_k with respect to the Cr concentration is illustrated in Figure 6.6. It can be seen that the anisotropy field markedly reduced when Cr percentage increased to at.%7.2. It is also interesting to note that the measured H_k for Cr content at.2.6% was double (6000 Am^{-1}) the value of H_k at.9.6% ($\approx$ 2700 Am^{-1}). Therefore it can be suggested that by increasing the amount of Cr up to at.9.6% it is possible to reduce the anisotropy field of the amorphous FeCoCr films. Since these films exhibited the uniaxial anisotropy, thus it enable us to estimate the anisotropy constant, K_U of the amorphous FeCoCr films according to the equation, $K_U = \mu_0 M_s H_k/2$, [35] where the M_s is the saturation magnetization measured by VSM. The estimation of K_U enable in supporting the assumption on the highest H_k in sample C1 (at.2.6%) presumably due to the larger magnetic anisotropy energy. The anisotropy constant will be discussed in the following subsection.

6.5.2 Magnetic Properties by SQUID-VSM

Saturation magnetisation of the films at different Cr compositions was further studied using a SQUID-VSM. As the FeCoCr films are soft magnetic materials, an applied magnetic field of maximum 1 T was sufficient to saturate the films. The hysteresis (M-H) curves for each sample for the different Cr concentrations measured at room temperature are presented in Figure 6.7. The saturation magnetisation was measured for different films for each concentration, and an average of M_s determined. As expected, the magnetization of the FeCoCr films decreases with Cr concentrations, as a result of Cr being an antiferromagnetic material. It can be seen clearly that the films with the lowest Cr (at.%2.6) had the highest saturation magnetisation, $M_s = 1042 \pm 26$ kAm^{-1}, followed by the at.% 5.6 Cr sample ($M_s = 859 \pm 3$ kAm^{-1}). For the at.%7.2 Cr sample

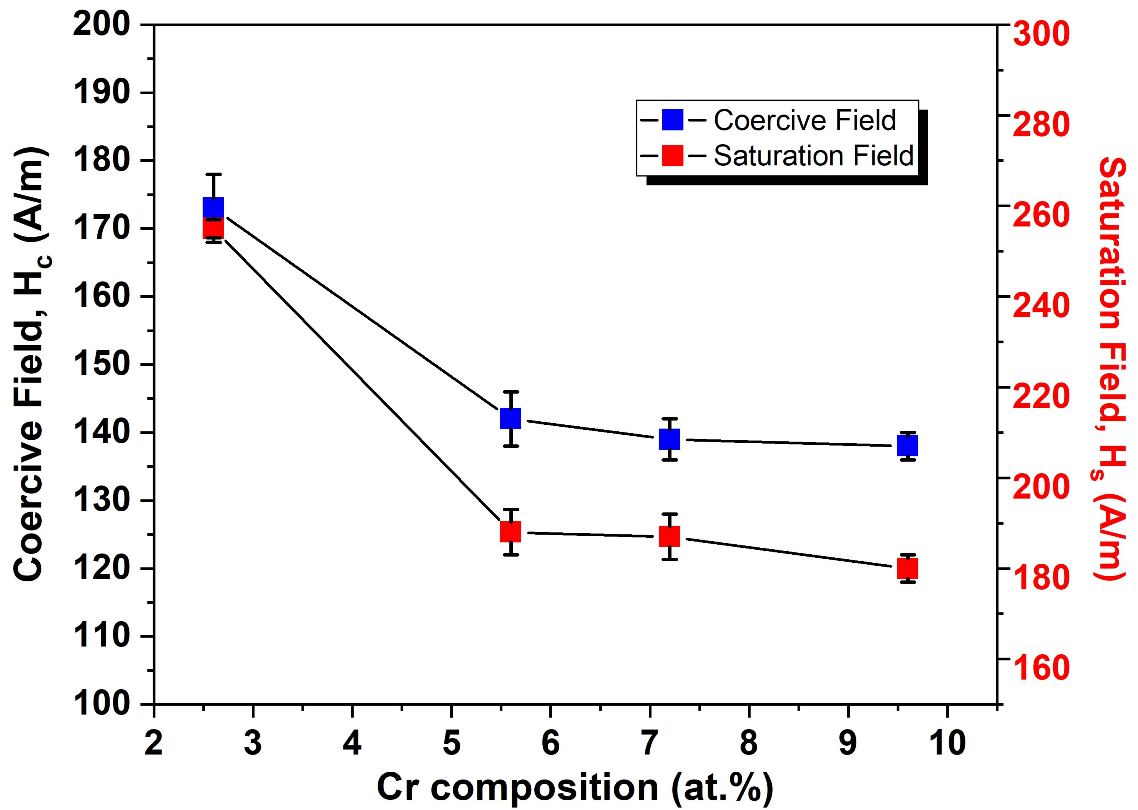

Figure 6.5: The dependence of the average of coercive and saturation fields of FeCoCr against Cr compositions with the error bars represent the standard error of three different samples.

the $M_s = 742 \pm 11$ kAm^{-1}, which is slightly higher than the M_s of the at.%9.6 Cr sample ($M_s = 726 \pm 5$ kAm^{-1}) though both groups of films exhibit almost the same M_s within the standard error. The obtained value of M_s allow the estimation of the anisotropy constant by using the relation of $K_U = \mu_0 M_s H_k/2$, where $\mu_0 M_s$ is saturation induction in Tesla. Therefore, the K_U was calculated and the values for all samples are presented in Table 6.2.

Figure 6.8 presents the saturation magnetisation and the anisotropy constants as a function of Cr compositions. It shows that there is a decrease in K_U with increasing the Cr compositions. At the lowest Cr (2.6%) the K_U was found to be higher (3930 Jm^{-3}) than the K_U at the highest Cr concentration at.% 9.6 (1269 Jm^{-3}). These results reflect those in previously reported work [192] which also found that increasing of Cr content from 1% to 5% decreased the K_U from 2550 (at.1% Cr) to 2100 Jm^{-3} (at.5% Cr) for $Fe_{73.5-x}Cr_xSi_{13.5}B_9Nb_3Cu_1$ films, which have been subjected to stress-induced annealing at 520^{0}C and 150 MPa for 2 hours. The FeCoCr films in this study, however,

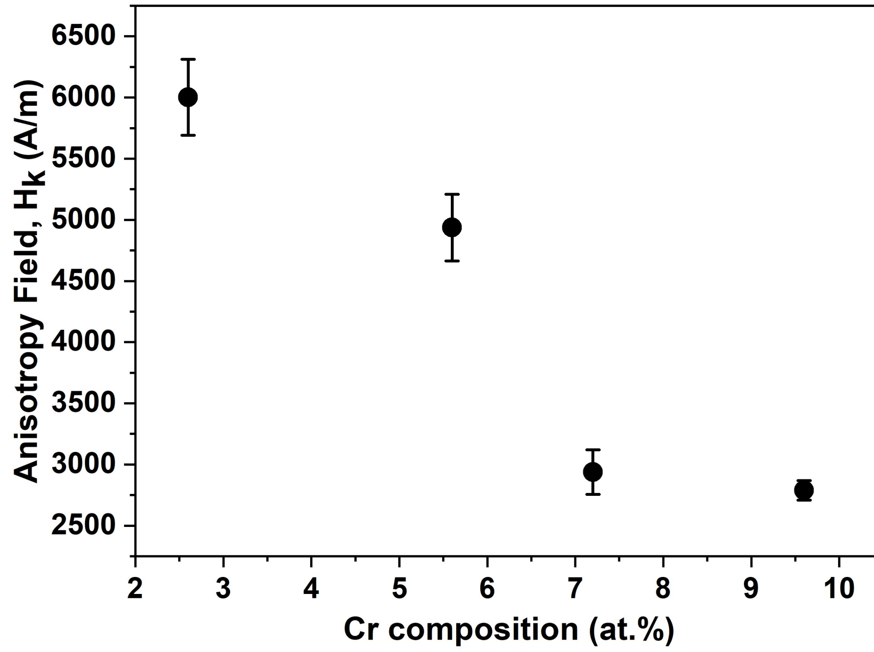

Figure 6.6: The average of anisotropy field, H_k of FeCoCr films as a function of Cr concentration determined from hard axis loops measured on the MOKE magnetometer with the error bars indicate measurement of three different samples.

Table 6.2: The magnetic parameters of FeCoCr at varied compositions determined by MOKE and SQUID-VSM.

Sample	H_c **(A/m)**	H_k **(A/m)**	M_s **(kA/m)**	K_U $(10^3 J/m^3)$
2.6 at.%	173 ± 5	6001 ± 310	1042 ± 26	3.930 ± 1.184
5.6 at.%	142 ± 4	4937 ± 273	859 ± 3	2.665 ± 0.156
7.2 at.%	138 ± 3	2938 ± 183	742 ± 11	1.366 ± 0.104
9.6 at.%	137 ± 2	2790 ± 80	726 ± 5	1.269 ± 0.045

had a slightly higher K_U than those in the literature, notably compositions around at.2% Cr. The K_U calculated from this study implies that introducing the Cr into FeCo films can reduce the anisotropy energy. Therefore, the assumption made previously on decreasing the coercive and anisotropy fields with increasing Cr concentrations due to the reduction in anisotropy energy is supported. Additionally, films with Cr at. 7.2% and at.9.6% show nearly the same magnitude of the H_c and H_k as both films have similar anisotropy constants, hence anisotropy energies.

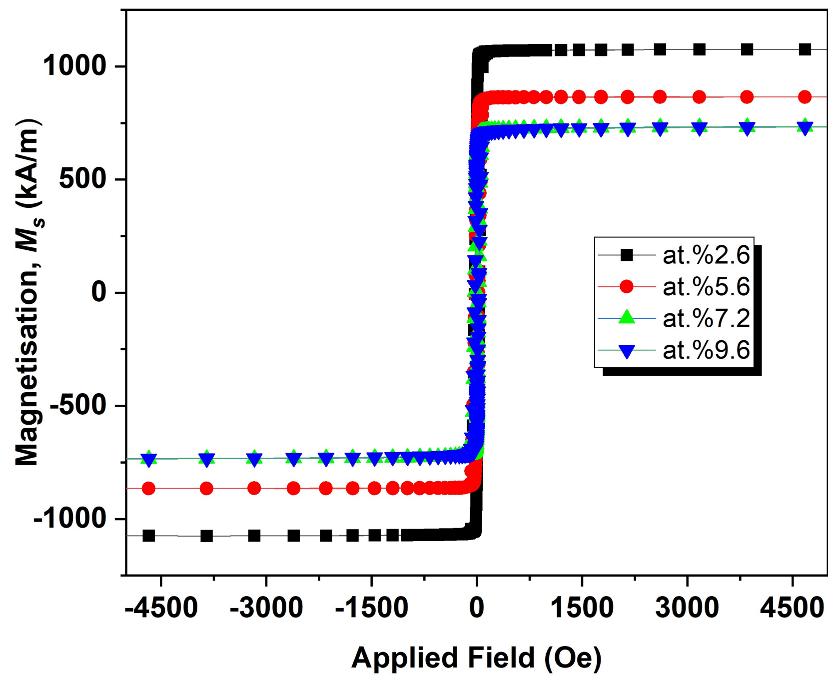

Figure 6.7: The magnetisation (M-H) curves of FeCoCr at varied composition measured at room temperature.

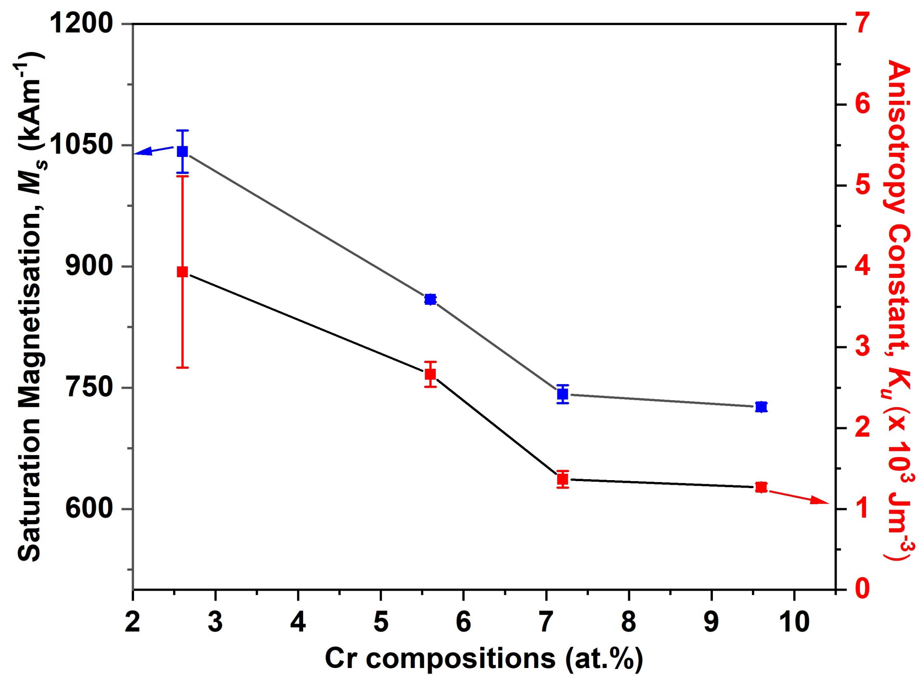

Figure 6.8: The average saturation magnetisation of FeCoCr measured by the SQUID-VSM and error bars indicate the standard error of three different samples. Also shown in the graph the calculated value of the anisotropy constant, K_u and the error bars as a function of Cr concentrations.

6.6 Magnetostriction Analysis

To answer the research question on how much Cr concentrations that can be added into FeCo films to achieve a high magnetostriction constant ($\lambda_s > 20$ ppm), the magnetostrictive properties of films were measured by using the Villari technique (see section 4.8). The dependence of λ_s on the Cr compositions is presented in Figure 6.9. It is determined that when the Cr concentrations increase, the λ_s decreases sharply by almost a factor of three from 39 ± 3 ppm (at.% 2.6 Cr) to 14 ± 2 ppm (at.% 7.2). However, the λ_s remains unchanged upon increasing the Cr amount of at.% 9.6 as the $\lambda_s = 13\pm$ 3 ppm, which is nearly the same with the film at.% 7.2 Cr. The observed decrease in the magnetostriction constant with increasing the Cr compositions may be ascribed by a reduction in the Fe and Co concentrations. Previous work reported that the FeCo at composition near 50:50 grown on the glass substrate had a magnetostriction ≈ 50 ppm [105]. This reported value is higher than the λ_s determined in our films, though the level amount of Cr added into the FeCo was only at 2.6%. It means that the incorporation of Cr atoms into the FeCo system reduced the magnetoelastic properties and change the internal stresses within the films. Also, it has been suggested in the literature [128, 185] that the higher magnetostriction constant at a small concentration of an additive element can be associated with the atomic pairs, for instance, the atomic pairs of B-B or Ga-Ga in FeGaB, or C-C in FeGaC. At higher concentrations of additive elements, it is believed that the atomic pairs form clusters, such that the magnetostriction tends to level off with further increasing the elements concentrations [193]. This behavior is observed in the studied FeCoCr films, as the magnetostriction constants of FeCoCr determined decreased up to 7.2% Cr, and then was constant within the error for the further increase up to 9.6% Cr.

This study determines that films with the lowest Cr concentrations ($Fe_{45.7}Co_{51.6}Cr_{2.6}$), demonstrate the highest magnetostriction constant compared to those films with higher Cr but less Fe and Co. A previous study on the magnetostriction in Fe-Co-Cr bulk alloys, reported that while decreasing the Fe ($15 \leq$ Fe ≤ 35) and increasing the Co ($15 \leq$ Co ≤ 25) concentrations but maintaining the Cr concentration at.% 50, the λ_s of these alloys were found to decrease from 21 ppm to 8 ppm [28]. Based on our findings, any further increase in the Cr concentrations will have no significant effect to enhance the λ_s of FeCo films, instead it likely to reduce the λ_s lower than 13 ppm. Therefore it can

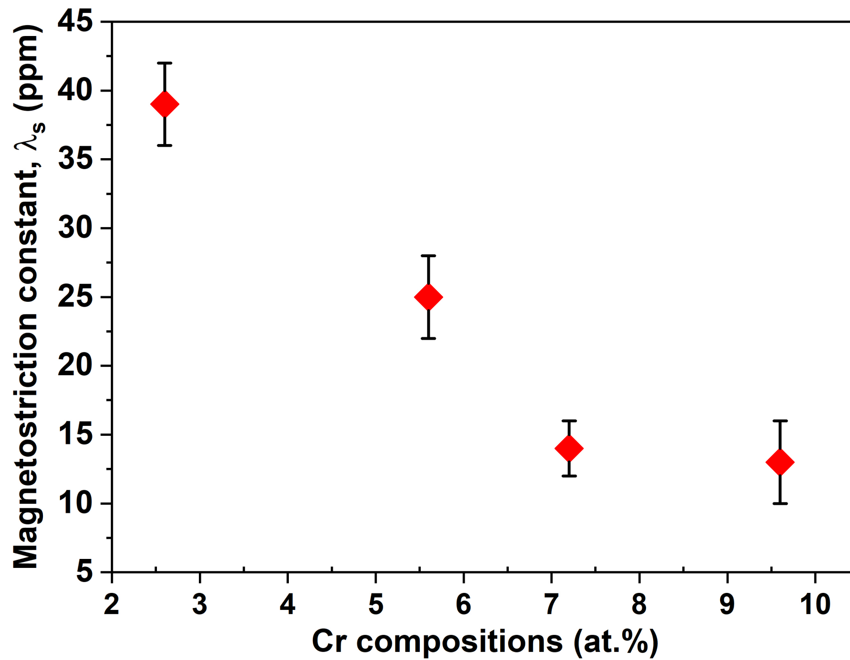

Figure 6.9: The dependence of the average magnetostriction constant, λ_s on the Cr percentages with the error bars represent a different number of measurements on the same samples.

be inferred that to maintain a higher magnetostriction constant in FeCo films from this study, a lower concentrations of Cr need to be added which was about at.2%, any more than this concentration, significantly reduces the λ_s.

6.7 Ferromagnetic Resonance Analysis by VNA-FMR

The characteristic of FeCoCr films with varied Cr concentrations have further been studied in the high-frequency range by using the VNA-FMR technique (see Section 4.9) to develop a fundamental understanding of the magnetic damping of soft magnetic FeCoCr films. For this purpose, the one-port reflection, S_{11} configuration in field domain was set-up and the raw data of one of representative sample obtained from S_{11} parameter is shown in Figure 6.10. The data together with fits to the real part of response (Figure 6.10a) and imaginary part of response (Figure 6.10b) related to the dynamic susceptibility of the sample [194]. This allows to determine the centre of the peak which gives the resonance frequency to derive the Kittel's curve. Also, the width of the peak is related to the damping with the frequency. Figure 6.11 represents an example of a

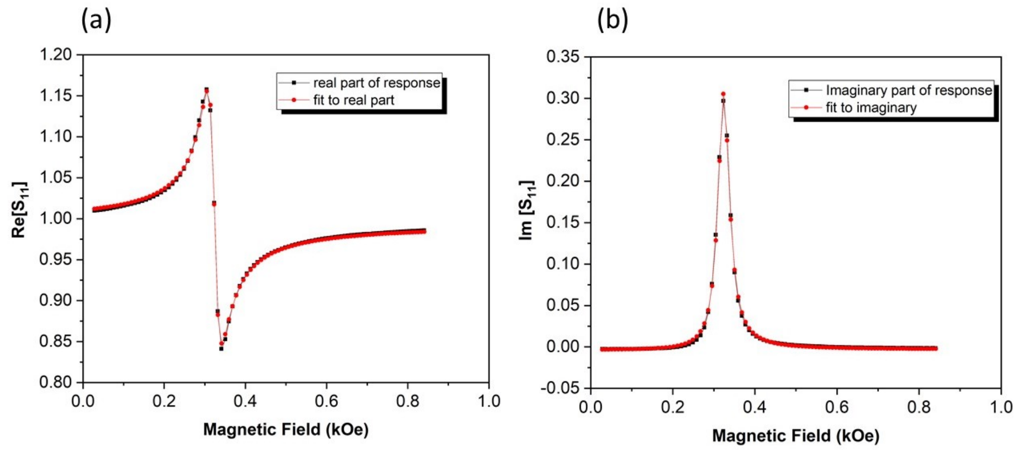

Figure 6.10: Ferromagnetic spectra from reflection data, S_{11} of the representative sample of the FeCo at.2.6% Cr. The raw data with the fits to (a) real part of response and (b) imaginary part of response. The data then fitted to extract the resonant frequency and the linewidth.

Kittel's curves in the FMR frequency range up to 10GHz for the different Cr concentrations, which then enable us to define the parameters of H_k and M_s. In Figure 6.11, the experimental data (shown as square symbol) are well fitted to the Kittel's equation (see equation 4.27). Figure 6.12 presents the H_k as a function of the Cr concentrations. The figure reveals that a steady decline in the magnitude of H_k as the Cr concentrations increases from 2.6% to 7.6%. H_k for these concentrations reduced from 3700 Am^{-1} to about 2700 Am^{-1}. H_k seems to be constant for Cr between 7.2% and 9.6%. It is apparent that the H_k for at. 2.6% Cr, particularly measured by the VNA-FMR technique, is two orders of magnitude lower than the value of H_k determined by MOKE (refer to Figure 6.6). The explanation for this discrepancy is from the method of data fitting has been used, which the VNA-FMR method yields a (3700 $\pm$ 19 Am^{-1}), compared by the H_k the MOKE method as the H_k for the MOKE was obtained by extrapolation from the linear part of graph along the hard axis (6001 $\pm$ 310 Am^{-1}). Despite this, both techniques have shown the same behavior in measuring the anisotropy fields of FeCoCr films, such that the H_k reduces with increasing the Cr content.

As the VNA-FMR measurement also allows the determination of the saturation magnetisation, therefore the measured values of M_s between VSM and VNA-FMR are presented in Figure 6.13. Similar to the anisotropy field, the saturation magnetisation, M_s, also found to reduce when the composition increase to 7.2%, but the M_s did not change much at. 9.6% Cr when measured by VSM and VNA-FMR. Both techniques measured the

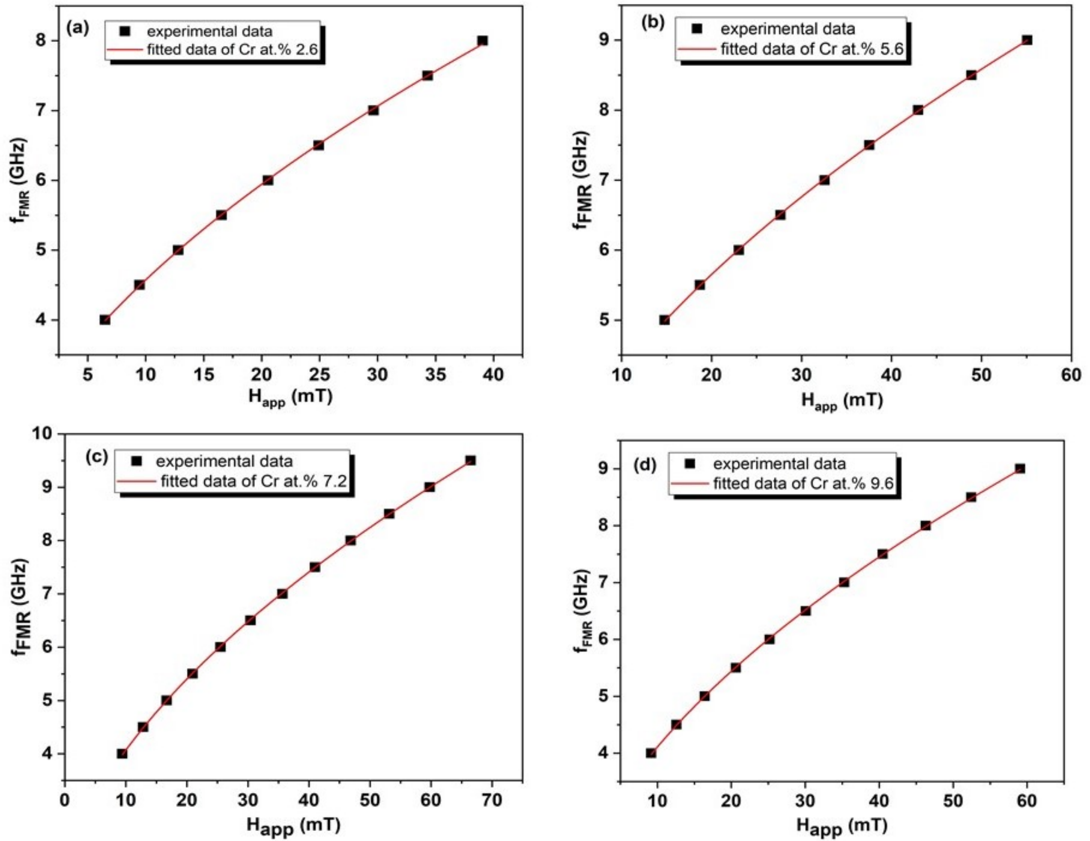

Figure 6.11: The curves of FMR frequency (S_{11}) fitted by Kittel's formula in obtaining the H_k and M_s at varied Cr concentration (a) 2.6% (b) 5.6% (c) 7.2% (d) 9.6% Cr compositions.

highest M_s for the Cr composition of 2.6% where from VSM the $M_s = 1042 \pm 26$ kAm^{-1} and from VNA-FMR the $M_s = 1440 \pm 3$ kAm^{-1}. For the Cr at 5.6% sample, the M_s measured from VNA-FMR was found to be 1350 $\pm$ 3 kAm^{-1}, which was higher than the value obtained from the VSM, $M_s = 859 \pm 3$ kAm^{-1}. On the other hand, the M_s of the Cr at 7.2% and 9.6% samples had a slight difference between them. For example, the M_s for Cr at.7.2% and at.9.6% measured from VSM were 742 $\pm$ 11 kAm^{-1} and 726 $\pm$ 5 kAm^{-1}, respectively. While, from VNA-FMR, the $M_s = 1250 \pm 4$ kAm^{-1} for Cr at 7.2% films and 1270 $\pm$ 1 kAm^{-1} for Cr at 9.6% films, these values are larger than those measured by the VSM. A full understanding of the difference of the saturation magnetisation and the anisotropy field values obtained between these two techniques, however would required further study.

Since magnetic damping, α is a crucial parameter that controls the dynamic behaviors of magnetic switching in the high-frequency range; further analysis has been conducted to determine the damping of the FeCoCr films. Generally, the measured FMR linewidth

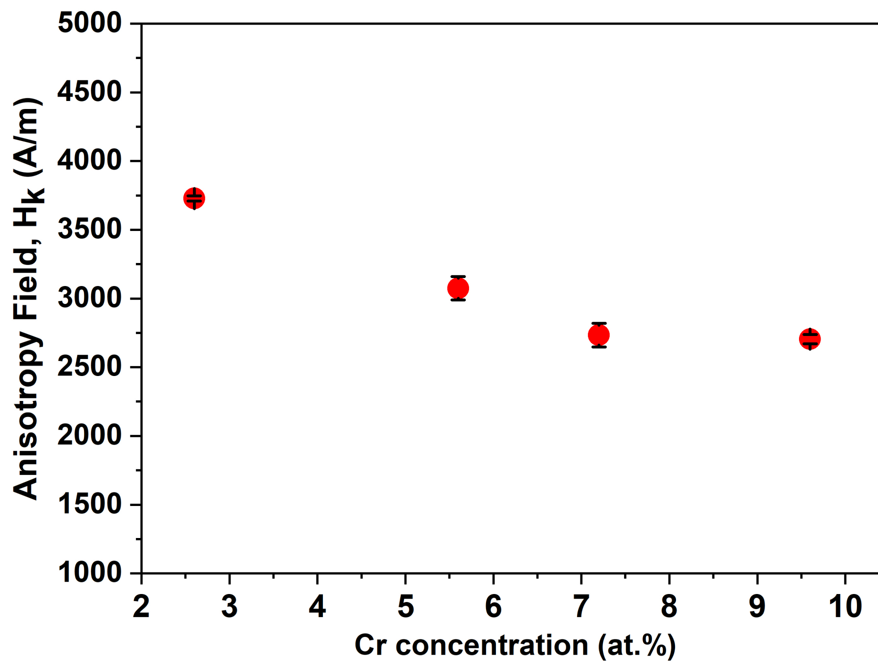

Figure 6.12: The average of anisotropy field, H_k determined from VNA-FMR fitting line as a function of Cr concentrations. The error bars shows standard error determined from three different samples.

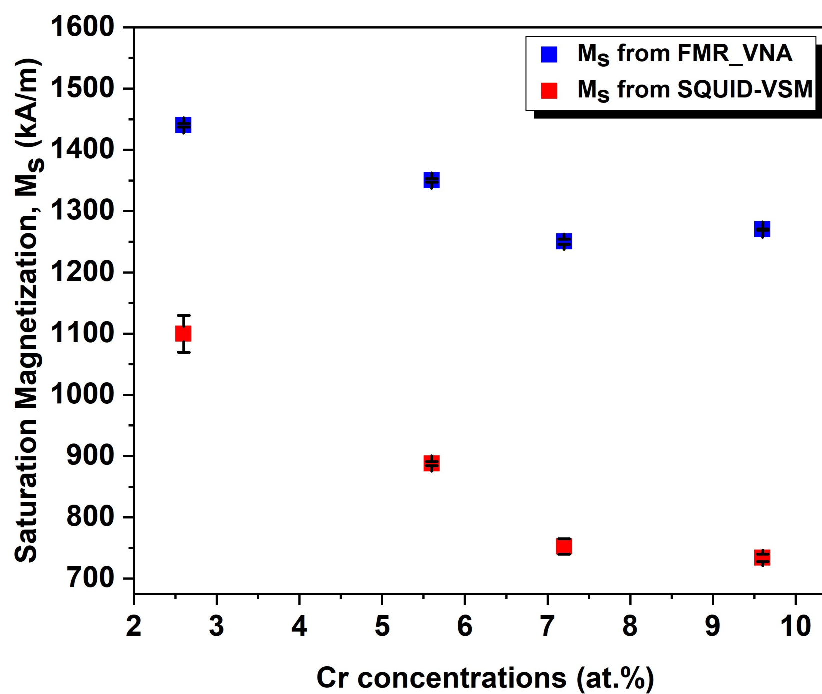

Figure 6.13: Saturation magnetization of FeCoCr films as a function of Cr concentration measured by two different techniques; VNA-FMR (blue) and SQUID-VSM (red).The error bars represent the standard errors measured from three different samples.

arises from intrinsic linewidth contribution, which is related to Gilbert damping constant: $\Delta H = \frac{4\pi\alpha f}{\gamma}$ [43, 44, 195]. From this equation, it allows the extraction of α by fitting the graph of the FMR linewidth. The slope on the linear graph determines the α, as the FMR linewidth, ΔH is proportional to the frequency, f. An example of ΔH data, which has been fitted, is presented in Figure 6.14. It is shown that there is a linear relationship with frequency. However, it has also been observed that our experimental data has intercept with the linewidth axis, which means there is an additional contribution to the FMR linewidth in FeCoCr films apart from the intrinsic Gilbert factor, as according to Equation 2.16 in section 2.3. It has been described in the published study [39] that the inhomogeneity is a result of local structure defects caused by impurities, inhomogeneous of the sample surface, film thickness and strain due to the lattice mismatch. Also, the inhomogeneity may be linked to the variation in local anisotropy field and magnetization [47, 48, 196]. The presence of in-plane uniaxial anisotropy can also be the reason for the inhomogeneity [197], and this is in good agreement with a well-defined uniaxial anisotropy exhibited in the FeCoCr films (refer Figure 6.4).

To ensure the damping constant of the FeCoCr films is reliable, the measurement was repeated three times on different samples for each Cr composition, as shown in Figure 6.15. The shown error bars in each point were determined from the fitting on FMR linewidth. Accordingly, the dependencies of the average α on the Cr compositions were calculated and plotted in Figure 6.16. It was found that the damping constant increases non-linearly with an increase of Cr concentrations. Cr at.% 2.6 sample had the lowest $\alpha = 0.0065$, which then increase to 0.0074 (Cr at.% 5.6). The damping value reached a maximum at $\alpha = 0.0100$ for the Cr at.7.2% film before dropping slightly by 0.002 when the concentration is increased up to 9.6%. In contrast, previous studies on the pure FeCo (52:48) [125] had found a larger magnetic damping of $\alpha = 0.109$. Interestingly, in this study, a smaller damping constant of FeCo when doping with 2.6% Cr measured which was two times lower than the reported damping constant of pure FeCo. The discrepancies in the magnitude of the damping constant could be due to the fact that there is a difference in the crystal structure between these two systems (FeCoCr and pure FeCo), suggesting that the crystal structure affects the magnetic damping as reported in the previous study [198]. Recently, it has been reported that the ultra-low magnetic damping was found for FeCo at nearly composition 75:25 the damping constant was about 0.0021 as due to the unique band structure of the CoFe systems [121]. It has also

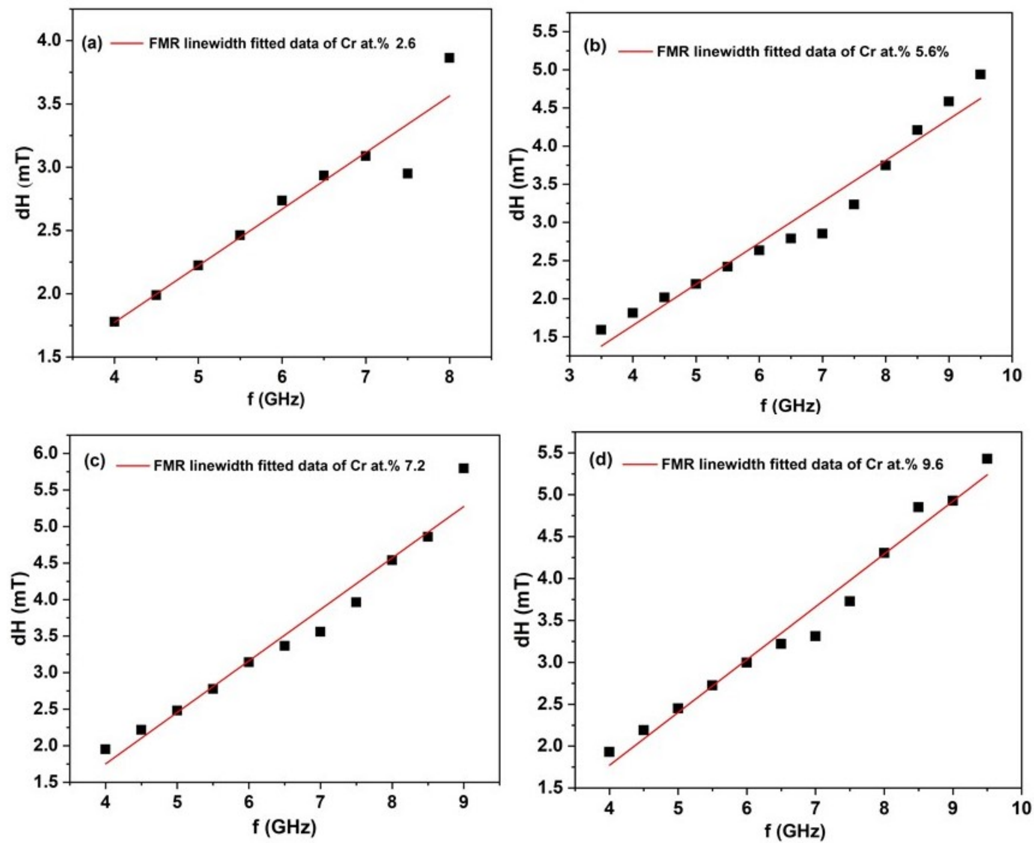

Figure 6.14: The fitted FMR linewidth for samples at varies Cr concentration showing the dependencies on the frequency (a) 2.6%, (b) 5.6%, (c) 7.2% and (d) 9.6%.

been suggested that doping with other elements increases the damping [39]. In our case increasing the Cr concentration up to 7.2% did increase the damping constant. This can be attributed to an extrinsic effect, as a result of the doping element breaking the symmetry of the FeCo crystal system, which then may create a centre for two-magnon scattering mechanisms [199]. In comparison, a more recent study [122] found a lower magnetic damping constant for FeCo without doping with another element, but instead, they annealed the films at 530^0C. They obtained $\alpha \approx 0.004$ at composition of 28% of Co [122], which is slightly lower than the damping constant (α= 0.006) of our as-deposited FeCoCr film. Their films were grown with the seed layer Ta(3nm)/Cu(3nm)/$Fe_{1-x}Co_x$ (10nm)/Cu(3nm)Ta(3nm). The study deduced that annealing could play a role in lowering the damping constant of thin films caused by the enhancement of the crystallinity and magnetic homogeneity [200]. The magnetic damping as a function of the reciprocal thickness has been studied and showed an increase in damping with t^{-1}, due to the surface contribution dominating the bulk value [39]. Studies of the thickness dependence

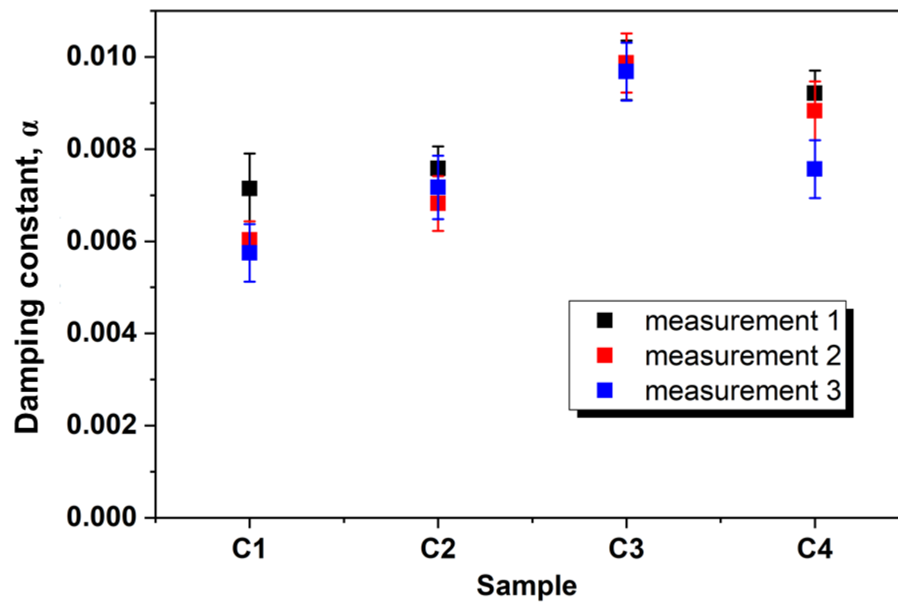

Figure 6.15: The repeatable measurement of FMR linewidth fitting allowing the extraction of the damping constant, α of C1 = 2.6%, C2 = 5.6%, C3 = 7.2% and C4 = 9.6%. The point represent a single measurement and the error bars indicate the standard error from each fitting.

of Permalloy and FeCo-based thin films grown onto a non-magnetic capping layer (for example, Pt and Pd) showed an increase the magnetic damping due to the heavy metal used and it has been reported to be linked with the spin angular momentum pumped into the non-magnetic layer [201, 202].

Thus, further study to be considered is the thickness dependence of magnetic damping on FeCoCr films. It should be noted that the measurement for thickness dependence of FeCoCr on magnetic damping were performed only to the films at thickness of 56 nm, 80 nm and 100 nm grown in the presence of magnetic field (120 kAm^{-1}) with sputtering power of 75 Watt but without any capping layer. These samples are different with those batch of films as presented in Figure 6.16. See Chapter 4 section 4.2.4(iii) and 4.2.4(v) for the lists of films batches grown in this study. An increase in magnetic damping with the film thickness of the $Fe_{41}Co_{45}Cr_{14}$ grown with magnetic field (120 kAm^{-1}) was observed as presented in Figure 6.17. The lowest magnetic damping was 0.012 for sample at 50 nm. For film at 100 nm had a highest magnetic damping which was 0.023. The magnetic damping found in this study for thickness 50 nm and 100 nm are comparable with the magnetic damping reported on FeCo (50:50) at nearly the same thickness [127]. The value of magnetic damping of FeCo (50:50) with thickness 50 nm and 110 nm in

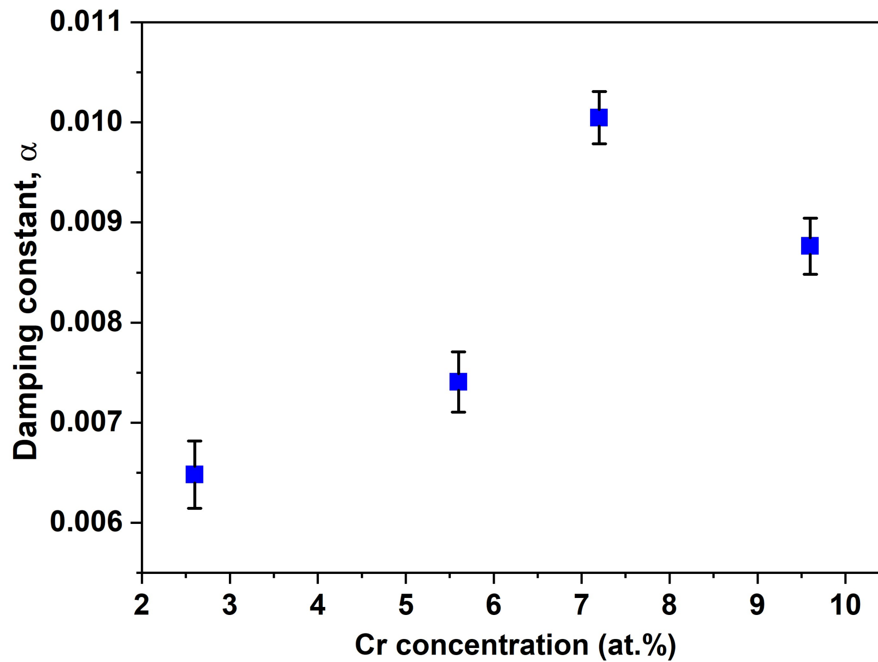

Figure 6.16: The dependence of the average damping constant, α_{ave} on the Cr concentrations of films with a similar thicknesses, 65 nm with the data point and the error bars represent the average value of damping and standard errors from three different samples, respectively.

those study were found to be 0.015 and 0.018, respectively.

6.8 Comparison between FeCoCr and other Soft Magnetic Materials

As the FeCoCr films in this study have shown soft magnetic behaviour, it is therefore interesting to compare the properties of these FeCoCr films to several other soft magnetic thin films that have been previously studied. Two of the most important soft magnetic properties are a high saturation magnetisation and a small coercive field, H_c. Figure 6.18 presents a selection of soft magnetic thin film materials reported in the literature [29, 89, 91, 171, 185, 203–207] including the bulk value of FeCo and Permalloy [23]. The plot compares the coercivity, H_c and saturation induction, $\mu_0 M_s$ values for each material. In this plot, bulk Permalloy $Ni_{78.5}Fe_{21.5}$ becomes a reference as its very soft properties, having the lowest coercive field, $H_c = 4$ Am^{-1} in comparison to the bulk FeCo. Nevertheless, the bulk Permalloy had a lower saturation induction than the bulk FeCo. As described in Chapter 5 on the characterisation of FeCo thin films which were

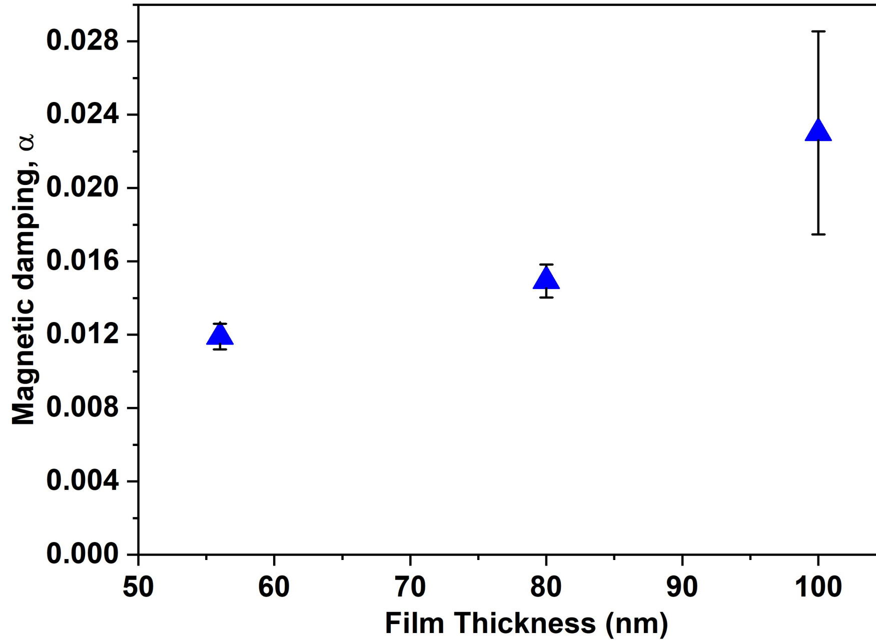

Figure 6.17: Damping parameter, α as a function of $Fe_{41}Co_{45}Cr_{14}$ film thickness grown with magnetic field at sputtering power of 75 W. The error bars shows the standard error determined from the fitting.

grown using the sputtering technique, the as-deposited FeCo films (70 nm) had a larger $H_c \approx 4$ kAm^{-1} (not shown in the plot) which was higher compared to FeCo bulk $H_c =$ 150 Am^{-1} (denoted by **). The huge difference between these two samples is due to the fact that the difference in the magnetic properties of thin film is greatly influenced by the method of fabrication. Also, it is observed that our as-deposited FeCo film had a larger grain size, indicated by a narrower width XRD peaks (refer to Figure 5.1), which contributes to the higher H_c. Despite the large coercive field found in FeCo films, they show a remarkable reduction in coercivity when doping with Cr. By comparing the H_c of FeCoCr films which were investigated in this study with other soft materials, it was found that the FeCoCr films sputtered with varied Cr concentrations have a smaller H_c in the range between 100 and 200 Am^{-1} than the other materials such as FeCoCrN, FeCoAlO, FeCoO, FeCoB and FeCoNi, as shown in the plot. The H_c of FeCoCr thin films were in the middle of the H_c values of bulk Permalloy and FeCo. The saturation induction of FeCoCr films obtained were lower and comparable to the reported value on the saturation induction of Permalloy and FeGaB. It is shown that the soft amorphous FeCoCr thin films with combination of low saturation induction, low coercive field (H_c 200 Am^{-1}), magnetic damping, α as low as 0.0065, and the magnetostriction constant, λ as high as 39 ppm have shown remarkable properties. Thus, the FeCoCr films are

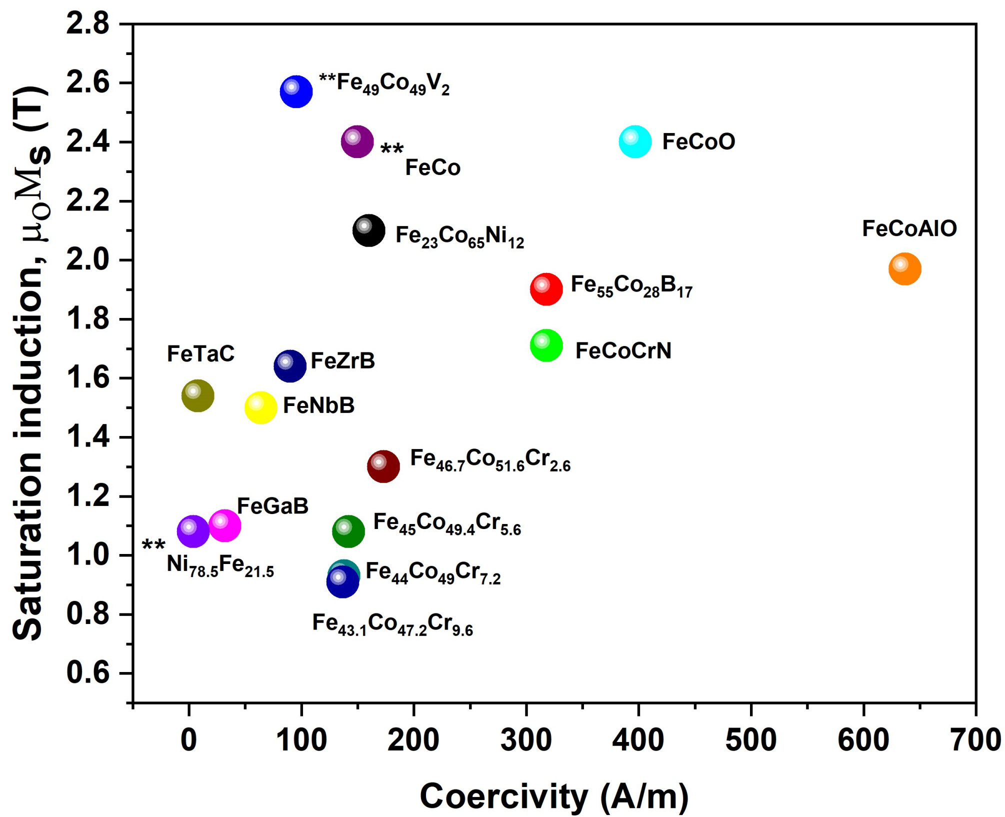

Figure 6.18: Ranges of soft magnetic thin films reported in the literature with the saturation induction, $\mu_0 M_s$ and the coercivity, H_c. The plot also presenting the magnitude of saturation magnetisation of Permendur (FeCo), Permalloy (NiFe) and $Fe_{49}Co_{49}V_2$ in bulk (shown by ** symbols) and the measured FeCoCr thin films with varied Cr concentration presented in this study [29,71,89,91,186,204-209].

promising candidate to be used in MagMEMS spin waves devices or possibly in spintronic devices that require those combination of soft magnetic properties including a low magnetic damping.

6.9 Summary

The structure study on FeCoCr films at different Cr concentrations have shown a similar amorphous structure regardless of Cr concentrations as opposed to the magnetic properties where the coercive and saturation fields were found to decrease when the compositions increased to 5.6% Cr. The measurement of anisotropy field, H_k with two different methods, namely VSM and VNA-FMR have shown interesting trends where this parameter reduced significantly with Cr compositions up to 9.6% Cr. It was also

obtained that the Cr substitutions reduced the saturation magnetisation with the highest saturation magnetization for both films at 2.6% Cr, $M_s = 1042$ kAm^{-1} as measured by SQUID-VSM and $M_s = 1440$ kAm^{-1} from VNA-FMR. Nevertheless, increasing the Cr concentrations reduced the magnetostriction constant. The film at 2.6% Cr had the highest $\lambda_s = 39$ ppm with also had lowest magnetic damping, $\alpha = 0.0065$ measured in high frequency by FMR measurement. By comparing the FeCoCr films with other soft magnetic materials with respect to theirs' coercive field and saturation inductions, it can be concluded that our FeCoCr films are softer than the majority of soft amorphous film published in previous studies (i.e FeCoB, FeCoAlO, FeCoNi, FeCoCrN). Additionally FeCoCr films had a lower magnetic damping thus would be interesting as material in MagMEMs, spinwave applications and spintronic devices applications.

Chapter 7

The Mechanical Properties of FeCo and FeCoCr thin films using the Nanoindentation Technique

7.1 Introduction

The development of soft magnetic materials with excellent mechanical properties (high hardness and yield strength), which can also operate at both room and elevated temperatures, are required but without sacrificing their magnetic properties. From previous work, the magnetic properties were often degraded (saturation magnetisation reduced while the coercivity increased) when the mechanical properties of FeCo were improved. It is reported that for binary FeCo alloys which are brittle at room temperature, alloying with other metals i.e vanadium can improve the mechanical properties to suit specific applications [207]. Soft magnetic materials with low coercivity and excellent mechanical strength would be advantageous for embedding in strain sensors due to their miniature size [131].

While conventional microindentation is suitable for investigating the mechanical behavior of materials on the micrometer-scale thickness range, the nanoindentation method has proven to be the best technique to probe the elastic-plastic behaviour of nanoscale materials. Mechanical properties such as hardness, elastic modulus and elastic recovery of the specimen under test can be extracted directly from this technique. Nevertheless,

an error in calculating these mechanical parameters is associated with the contact area between the tip indenter and the specimen under test. Several factors can influence the actual contact area. One of the significant factors is a contribution from the substrate which occurs if the sample is very thin. The commonly used indentation depth is limited to less than 10 percent of the film thickness to avoid the measurement of the substrate [64]. However, this rule of thumb is not always practicable, as it depends on the nature of the sample. In a reported study, for instance, about 20% of the Al-Ti film thickness was used to avoid the surface roughness and the pile-up effect instead of 10% of film thickness to minimize the uncertainties in their hardness data [208].

Surface roughness is also believed to affect the precision of the indentation data. When an indentation is made on a rougher surface compared to a smoother surface, it results in different contact areas, hence different penetration depth occur even under the same load [209]. Another factor that causes an error in defining the hardness is the events of sink-in and pile-up. According to Saha and Nix [133] soft films tend to have pile-up when deposited on a hard substrate, leading to an underestimate of the contact area of the indenter. On the other hand, the contact area is overestimated when the event of a sink-in occurs for hard material deposited on a soft substrate.

A number of studies have been undertaken to investigate the mechanical properties of a wide range of materials not only the bulk alloys, but also thin films and nanowire samples [208, 210, 211]. Mechanical characterization of amorphous magnetostrictive thin films in the nanoscale range, has not been widely studied. As these films are integrated into MagMEMs sensors, studying the mechanical properties is of crucial importance to understand their fundamental features. Thereby, this chapter aims to develop an understanding of the mechanical properties of amorphous magnetostrictive FeCoCr films and also polycrystalline FeCo thick films by investigating the mechanical properties at different thicknesses greater than 400 nm. Hardness, Young's modulus, elastic recovery and yield strength were investigated and are described in this chapter. The effect of Cr concentrations into FeCo has also been studied to determine whether the addition of Cr had a significant impact on the mechanical behavior of the FeCo films. Another reason to study the mechanical properties of FeCo and FeCoCr was to provide further information on the Young's Modulus of these films, which has not been investigated yet. As given in Chapter 4, the determination of the magnetostriction constant, λ_s of thin films by Villari method only takes into the account of the Young's modulus of the Si substrate. For the

cantilever technique the Young's modulus of the film is also required. This is a popular technique used to measure the magnetostriction constant of thin films, but assumes the film's Young's modulus is the same as the bulk. [54]. Hence from studying the mechanical properties of FeCoCr thin films through nanoindentation technique allows the determination of magnetostriction constants precisely in future studies. It will also help to determine how accurate the cantilever technique is to measuring the magnetostriction constants.

7.2 Sample Preparation of Thick Films

To probe the elastic and plastic properties of FeCo and FeCoCr films and to avoid the effect of the substrate, the film thickness should be thicker than the radius of the tip. Hence two different sets of thick films with thickness more than 400 nm were fabricated onto Si substrate using RF Magnetron Sputtering. All the sputtering parameters used to fabricate the thick films were kept the same, i.e the sputtering power and the argon pressure were 75 Watt and 4.8 mTorr, respectively. Three sets of FeCo films were deposited with different deposition time to vary the thickness. The measured thickness were found to be 431 nm, 603 nm, and 758 nm. For a second set of films, FeCoCr films with different Cr compositions grown with the same deposition time. It was found that the measured thickness for films for at.%2.6 Cr was 604 nm, 590 nm (for at.%5.6 Cr), 600 nm (for at.%7.2 Cr) and 601 nm (for at.%9.6 Cr). The film thickness and the surface roughness of the films were examined using an Atomic Force Microscopy (AFM).

7.3 Nanoindentation Measurement

The nanoindentation test were first performed on a Si substrate to provide a reference for the measurement of the films. The hardness and reduced modulus of the substrate and the films were extracted by performing the nanoindentation test using the TI 950 Triboindenter Hysitron. The Berkovich tip used in this study had a radius of 120 nm, included angle, ϕ = 142.30, Young's Modulus, E_Y = 1140 GPa and Poisson's ratio, ν = 0.07. Instead of using one cycle single indentation, the measurement was performed with 25 cycles. A partial unload profile was chosen, meaning that the maximum load was increased in each cycle. This partial unload profile had three segments, which are 5

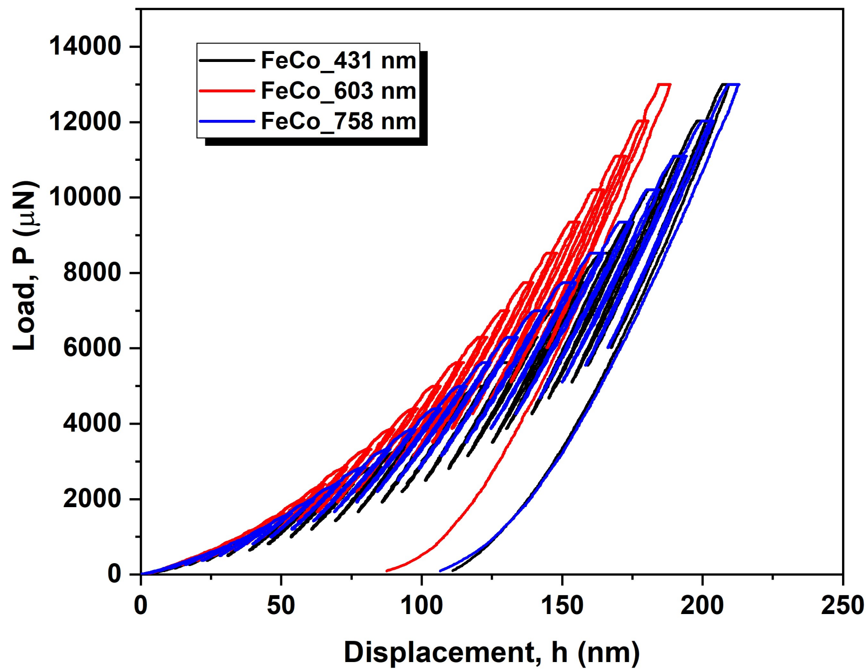

Figure 7.1: Graph of force versus displacement on the FeCo films at different thickness that involved 25 cycles of indenter with maximum of force, 13000μN was applied.

seconds for loading, 5 seconds hold at the load maximum and 5 seconds for unloading. A series of indentations were made on each sample through 3 μm x 3 μm arrays with an indent distance of 50 μm. The maximum load applied was 13000 μN. From this measurement, the parameters such as contact stiffness, S, projected contact area, A and maximum load, P_{max} were obtained from the load-displacement curve. The data for the unloading curve then were fitted based on the method developed by Oliver and Pharr, leading to the extraction of the hardness, H_r and the reduced modulus, E_r data (see section 2.7). Figure 7.1 shows an example of the measured curve of applied force versus displacement for 25 cycles, for FeCo films with different thicknesses.

7.4 Mechanical properties of Si substrate

Nanoindentation was first conducted on a bare Si substrate, which was 360 μm thick. It was necessary to do the indentation test on the Si substrate to ensure that, when analyzing the mechanical properties of thin film samples with thickness less than 1μm, there was no contribution from the substrate. This ensured that the calculation of the mechanical properties of the thick films are reliable. The hardness as a function of

penetration depth, h_c for the Silicon substrate is plotted in Figure 7.2. It is clearly seen that there is a pronounced increase in hardness at the lower penetration depths between 7 nm and 20 nm. The increase in the hardness at smaller depth is usually associated with the radius of the indenter tip. The hardness value becomes irregular when the contact depth approaches nearly the 1/3 of the radius tip. The radius of the Berkovich tip used in this study is 120 nm.

It is also possible that, tip rounding also contributed to the sudden increase in the hardness at the lower depth. It is generally accepted that the Berkovich tip does not have a perfectly sharp tip. As the tip penetrates the sample, a constant value of the hardness should be observed. In the case of silicon, however, the constant hardness value can only be observed for the contact depth ranging from 20 nm to 40 nm. After this range, the hardness is seen to increase gradually with increasing depth. Nevertheless, the increment in the hardness is still in the range of the error bars, therefore the hardness of the Si in this study was calculated from the displacement between 20 nm to 140 nm. The measured hardness of the Si was found to be 16 $\pm$ 1 GPa, which is higher than those reported in the literature of 12.75 GPa [133]. Unlike to the hardness, the measured reduced modulus, E_r seemed to be constant even at a smaller contact depth. This parameter was determined from Equation 2.33 as described in Chapter 2. The plot of E_r with penetration depth for Si is presented in Figure 7.3. The average value of E_r was 165 $\pm$ 2 GPa. The calculated value of Young's Modulus for Si substrate will be given and compared with the FeCo films in the following section.

7.5 Mechanical properties of FeCo thin films

The effect of film thickness on the mechanical properties of FeCo films was investigated with 18 indentations being made at different locations on each film. To illustrate this impact, the result from the hardness of FeCo films as a function of displacement depth for three different thicknesses (431 nm, 603 nm, and 758 nm) is shown in Figure 7.4. The hardness of the Si is also included in the plot. It was determined that the hardness increased abruptly up to 20 nm depth, as similar as observed in the Si hardness due to contact depth being comparable to the tip radius. It is interesting to note that the hardness value reached a plateau between 20 nm to 110 nm contact depth for all FeCo film thicknesses. Beyond this depth, the hardness of the 431 nm films increased slightly

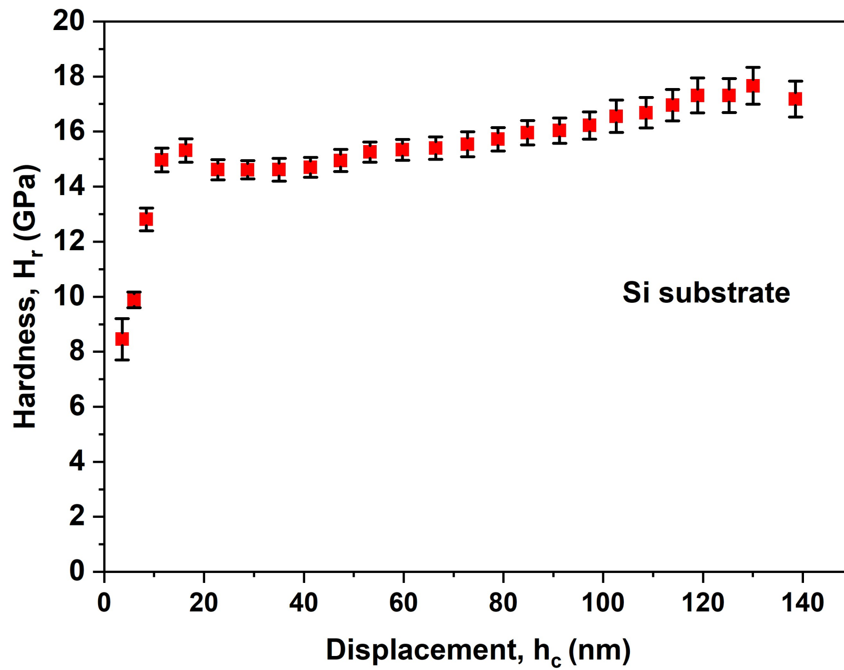

Figure 7.2: Graph of the average hardness, H_r as a function of displacement for the Si substrate with thickness 360 μm with the error bars are the standard errors from a series of nanoindentation. An abrupt increase in hardness at low penetration depth is observed.

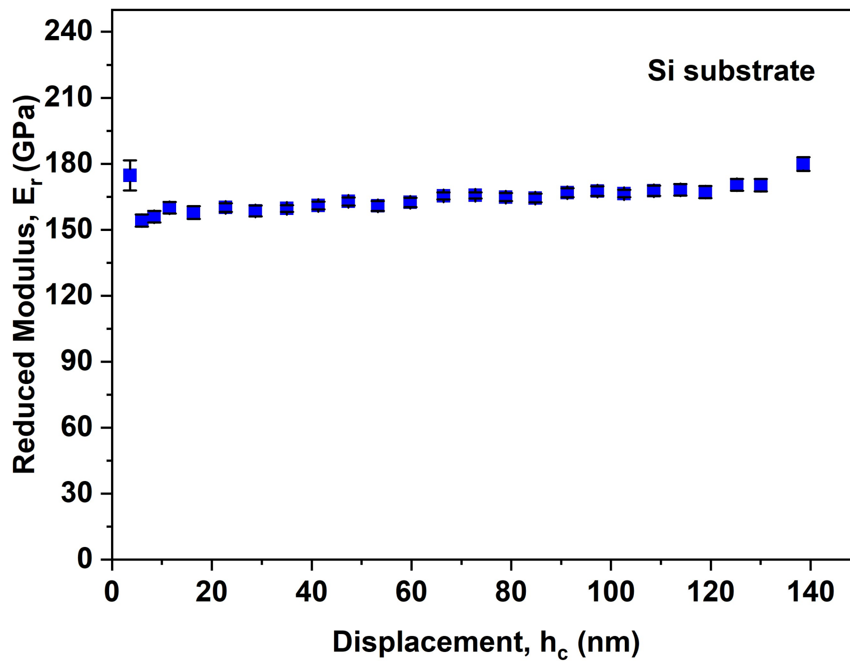

Figure 7.3: Graph of the average reduced modulus of elasticity, E_r of Si substrate as a function of contact depth with the error bars are the standard errors from a series of nanoindentation.

with depth, while for the 603 nm and 758 nm films, it appears to decrease with increasing depth.

Nonetheless, these changes in hardness are still in the range of the hardness uncertainties and do not have a significant effect on the average value of the hardness data for each sample. Interestingly, the plot shows that the hardness improved with increasing film thickness. For example, for the 758 nm film has the highest hardness of 15.1 $\pm$ 0.4 GPa, followed by the 603 nm film, which a hardness of 14.8 $\pm$ 0.2 GPa. The lowest hardness of 12.7 $\pm$ 0.4 GPa was found at the smallest thickness, 431 nm. It is worth comparing the hardness of the FeCo films determined in this study with the FeCo films that have been reported in a previous study [131]. They deposited thicker films of FeCo (thickness 2μm and 7μm) onto Si substrate by using magnetron sputtering with the Ar pressure between 0.04 and 0.2 Pa. The study found that the hardness of their films were 5.5 GPa (2μm) and 5.4 GPa (7μm). These values are a factor of 2 smaller than the hardness of the FeCo films determined in this current study. This is interesting that, the hardness of FeCo films in this study, which were fabricated onto a similar substrate have exhibited remarkable different in mechanical properties. From the graph of hardness (Figure 7.4) also clearly showed that there is no influence from the substrate on the hardness data for all samples. Generally, the substrate effect is observed when there is a continuous increase in the hardness as the penetration depth increases. The error bars shown in the plot represent the standard errors calculated from the series of nanoindentations data.

The graph of reduced modulus of elasticity, E_r for the FeCo films as a function of contact depth is presented in Figure 7.5. While the values of the hardness of FeCo films increased with thickness, the E_r was measured to be constant with the thickness, mainly at the lower thickness. For example, the E_r for the 431nm and 603 nm films are the same, 180 $\pm$ 4 GPa and 181 $\pm$ 2 GPa, respectively. The value was reduced to 172 $\pm$ 2 GPa as the thickness increased to 758 nm. The reduced modulus for the FeCo, however was found to be higher than the E_r for the Si substrate.

The value of the reduced modulus then is used to define the Young's modulus of the film, E_f. By taking the value of the Poisson ratio of the FeCo film as 0.27 [212] and mechanical parameters of the Berkovich indenter (supplied by Bruker) to be; Young's Modulus, $E_i = 1140$ GPa and Poisson ratio, $\nu = 0.07$, the Young's Modulus of the FeCo thin films can be estimated according to Equation 2.33. A comparison of the Young's

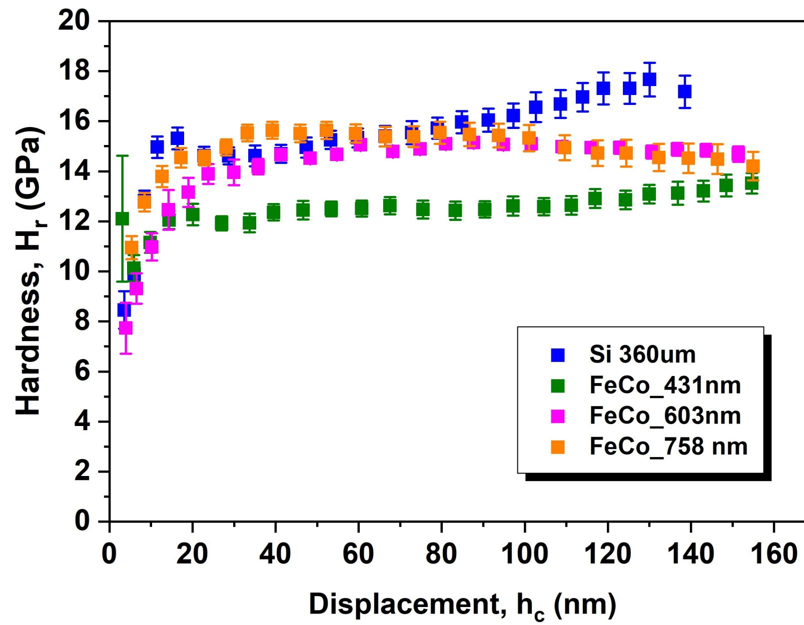

Figure 7.4: The average hardness, H_r against the displacement, h_c of FeCo at thickness 431 nm, 603 nm and 758 nm. The graph also presenting the average hardness for Si substrate at thickness 360 μm.The error bars in each plot represent the standard errors from a series of nanoindentation.

Modulus of Si and FeCo thin films is presented in Figure 7.6. Similarly to the trend observed in the reduced modulus, the Young's modulus of the thicker films, 758 nm was slightly lower (159 $\pm$ 2 GPa) than the thinner films, where the E_Y of the 431 nm was 166 $\pm$ 2 GPa and the 603 nm film was 167 $\pm$ 1 GPa. These values are comparable to the E_Y of FeCo/Si (165 GPa) in the literature [131]. For Si substrate, the E_Y obtained was 155 $\pm$ 2 GPa, which is lower than the E_Y of Si (172 GPa) published in this previous study [133].

7.6 Mechanical properties of FeCoCr thin films

Nanoindentation testing was performed on the four sets of films with different Cr concentrations to investigate the effect of Cr on the mechanical properties of FeCo films. The result of the hardness of the FeCoCr films are shown in Figure 7.7. For the initial penetration depth below 40 nm, the hardness dropped sharply, contrary to the hardness found in the FeCo films at the same range of penetration depth. It was found that the hardness of FeCoCr films was in the range of 12 GPa to 13 GPa, which varied slightly different over the Cr concentrations range. This indicates that the substitution of Cr

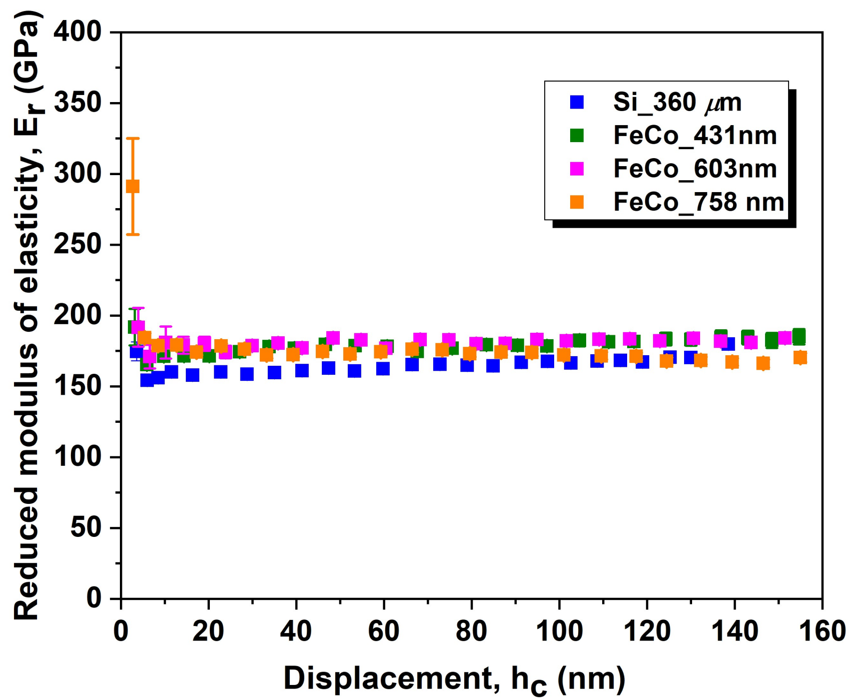

Figure 7.5: Plot of the average reduced modulus of elasticity, E_r of the different thicknesses of FeCo and the average reduced modulus of Si substrate as a function of displacement.The error bars in each plot represent the standard errors from a series of nanoindentation.

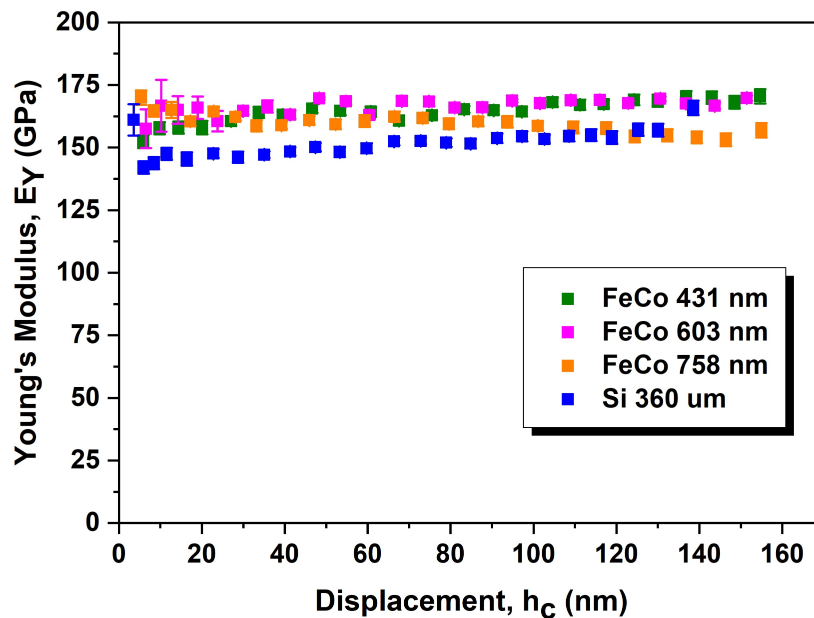

Figure 7.6: Plot of Young's modulus, E_Y calculated from the measured of reduced modulus showing that the magnitude of E_Y have less influenced on film thickness.

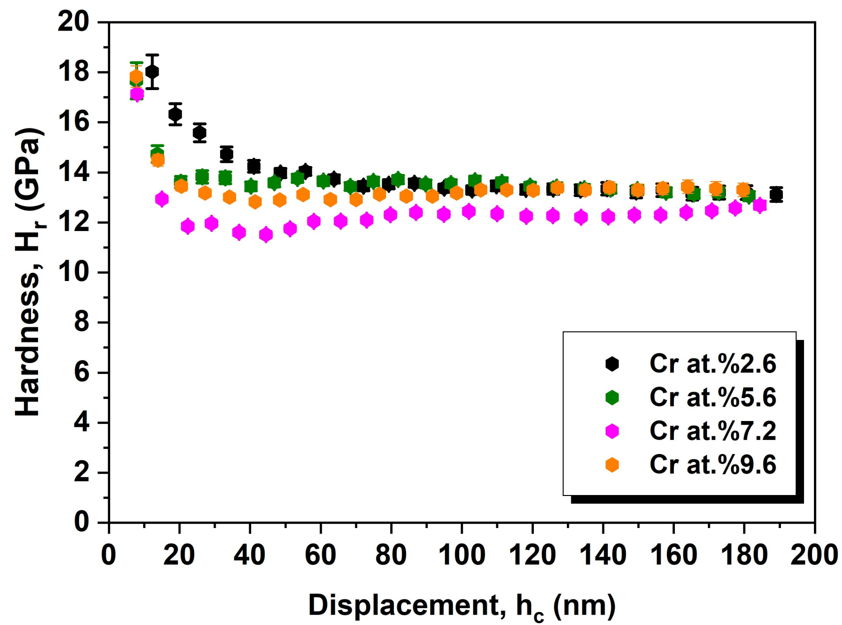

Figure 7.7: The average hardness, H_r as function of displacement for FeCoCr at varies Cr concentrations at.2.6% (604 nm), at.5.6% (590 nm), at.7.2% (600 nm),and at.9.6% (601 nm) from a series of nanoindentation.

atoms into FeCo did not significantly improve the hardness of FeCo, although the Cr was added up to at.9.6%. It is also interesting to note that, however, the E_r of FeCoCr films increased with Cr concentrations, although the E_r of FeCoCr is still lower compared to the E_r of FeCo films. As shown in Figure 7.8, the E_r of the at.2.6% Cr film, was found to be lower than those films at higher Cr concentrations, notably between penetration depth from 40 nm to 190 nm. By comparing the average E_r between these films, the E_r of films at.2.6% Cr film was 150 GPa $\pm$ 1 GPa, and smaller than the films at highest concentration (at.9.6% Cr), where the $E_r = 170 \pm 1$ GPa.

Figure 7.9 shows the graph of the average of Young's Modulus, E_Y of FeCoCr films from a series of nanoindentations. As the determination of E_Y is related to the reduced modulus, E_r, hence the E_Y as functions of Cr concentrations show similar tendency with the E_r plot, whereby the E_Y are constant for contact depths between 40 nm and 190 nm, except for at.2.6% Cr films. The plot clearly shows that E_Y of the at.2.6% Cr film decreased gradually with increasing penetration depth, giving the lowest average value of $E_Y = 144 \pm 1$ GPa. As the Cr concentrations increased to at.5.6% and up to at.9.6% Cr, the average E_Y were nearly the same at about 156 to 157 GPa, for all Cr concentrations.

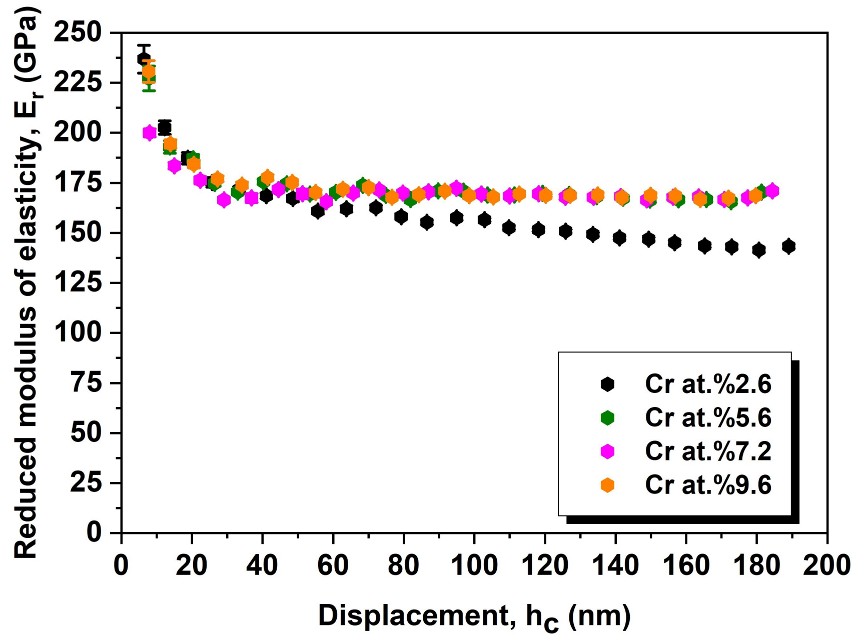

Figure 7.8: The average reduced modulus of elasticity, E_r as function of displacement for FeCoCr at varies Cr concentrations at.2.6% (604 nm), at.5.6% (590 nm), at.7.2% (600 nm),and at.9.6% (601 nm) from a series of nanoindentation.

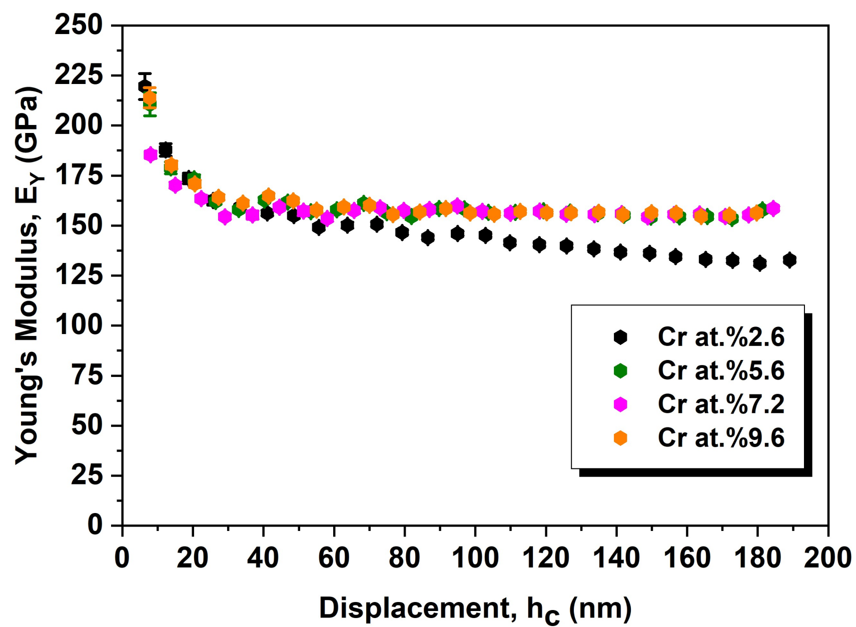

Figure 7.9: Young's modulus, E_Y of FeCoCr films at varied Cr concentrations as a function of tip displacement.

Table 7.1: The mechanical parameters of FeCo and Si at different thickness determined from the nanoidentation with E_r: reduced modulus of elasticity; H_r: hardness; E_Y: Young's modulus.

Sample	E_r **(GPa)**	H_r **(GPa)**	E_Y **(GPa)**
Si (380 μm)	165 ± 2	16 ± 1	155 ± 2
FeCo (431 nm)	180 ± 4	12.7 ± 0.4	166 ± 2
FeCo (603 nm)	181 ± 2	14.8 ± 0.2	167 ± 1
FeCo (758 nm)	172 ± 2	15.1 ± 0.4	159 ± 2
Cr at.% 2.6 (604 nm)	150 ± 1	13.3 ± 0.2	144 ± 1
Cr at.% 5.6 (590 nm)	169 ± 1	13.5 ± 0.2	157 ± 1
Cr at.% 7.2 (600 nm)	169 ± 1	12.2 ± 0.1	156 ± 1
Cr at.% 9.6 (601 nm)	170 ± 1	13.2 ± 0.2	157 ± 1

The measured mechanical parameters of Si, FeCo, and FeCoCr films are compared in Table 7.1. It is noticeable that the average hardness and the Young's Modulus of FeCo films obtained were higher than the FeCoCr films, suggesting that the addition of Cr into FeCo has changed the elastic property of the FeCo. One plausible reason for the degradation in the hardness and the Young's Modulus when Cr is added into the FeCo system likely attributed to the different microstructure between these films. This is supported by the AFM images as illustrated in Figure 7.10. The representative of FeCoCr film at the highest Cr concentration (at.9.6%) with a thickness of 601 nm has a smooth surface and no grains were observed (Figure 7.10d), though the film thickness is comparable to the thickness of the FeCo film (Figure 7.10b).

In contrast, for the FeCo films, the grains became more significant with increasing the film thickness, such that the crystallinity of the FeCo improved. The surface roughness also increased with increasing the film thickness, such that 758 nm films had the largest surface roughness (R_a=1.68 ± 0.04 nm). On the other hand, the FeCoCr film has a smooth roughness of R_a=0.48 ± 0.01 nm. To further study whether these different groups of films have different structures, XRD measurement was performed on the selected thickness of FeCo and FeCoCr films. As shown in Figure 7.11 it was observed that the FeCo thick film (758nm) showed a sharper and higher intensity for a peak at $2\theta = 45^0$ compared to the FeCoCr at.9.6% film a broad peak at the same diffraction angle. Thus, it can be implied that the surface roughness and the grains have influenced the mechanical behavior of the FeCo thin films such that the increase in hardness and reduction in Young's modulus with FeCo thickness are due to the different films' morphology and structure. Also, the Cr substitution degraded the mechanical properties of the FeCo films as the morphology and compositions had changed.

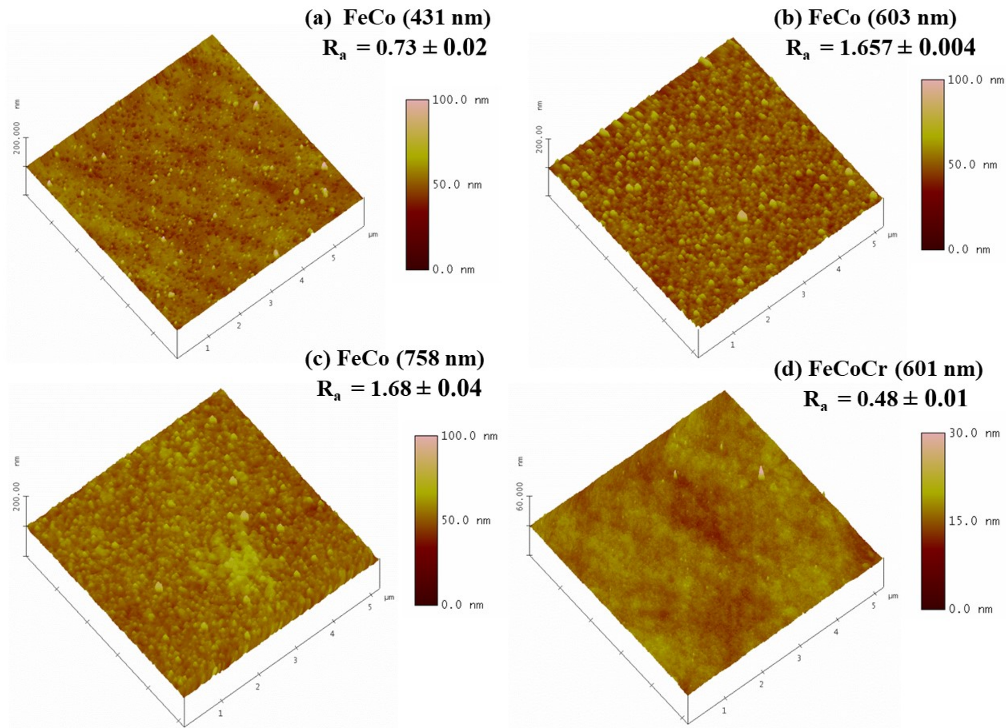

Figure 7.10: AFM images on the surface roughness demonstrating different microstructure between FeCo and FeCoCr films. Scan size 5μm x 5μm.

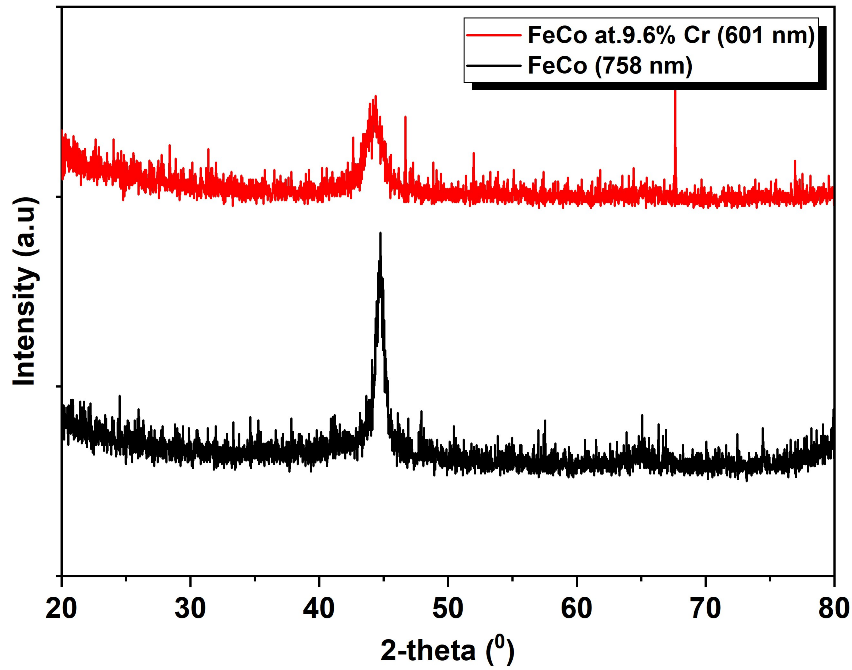

Figure 7.11: XRD profiles showing different structure between selected thick of FeCo and FeCoCr films.

Table 7.2: The calculated of elastic recovery, h_e from the difference between the parameter of the contact depth at the maximum load, h_{max} and the final contact depth, h_f taken from the part of an unloading curve.

Sample	**Elastic Recovery, h_e(nm)**
FeCo 431 nm	103.3 ± 0.4
FeCo 603 nm	92.7 ± 0.2
FeCo 758 nm	101.2 ± 0.2
Cr at.% 2.6 604 nm	112.2 ± 0.5
Cr at.% 5.6 590 nm	100.3 ± 0.2
Cr at.% 7.2 600 nm	106.0 ± 0.5
Cr at.% 9.6 601 nm	95.3 ± 0.2

7.7 Elastic recovery of FeCo and FeCoCr films

The elastic recovery, h_e of the FeCo and FeCoCr thick films were investigated by calculating a difference between the indentation depth at maximum, h_{max} and the final depth, h_f at part of unloading in a load-displacement curve. The elastic recovery is defined as the ability of a material to return to its original shape when the load is removed. Figure 7.12 presents the average elastic recovery as a function of the Cr concentrations. The average value of this parameter was calculated on a series of indentations, similar to the analysis done on the hardness and the reduced modulus. It is observed from the figure that the elastic recovery of FeCoCr films reduced with increasing the Cr concentrations to 5.6%. The highest h_e of 112.2 ± 0.4 nm was observed in Cr at.2.6%. It then dropped to 100.3 ± 0.1 nm as the Cr increases to at.5.6%. By increasing the amount of Cr up to at.7.2%, the elastic recovery of FeCoCr was increased slightly to 106.1 ± 0.5 nm. The lowest amount of elastic recovery was observed for a sample at the highest Cr concentration, 9.6% Cr with the h_e of 95.3 ± 0.2 nm. To compare the amount of elastic recovery between the FeCo and FeCoCr films, the h_e as a function of FeCo thickness and the FeCoCr films is given in Table 7.2. For the 603 nm thick FeCo film which is comparable to the thickness of the FeCoCr films, the elastic recovery of FeCo was obtained to be 92.7 ± 0.2 nm, lower than the FeCoCr films. The difference between FeCo and FeCoCr in the same thickness is also observed in the load-displacement curves in Figure 7.13. In addition, for the thicker 758 nm of FeCo film, the h_e of this film was still found to be lower (101.2 ± 0.2 nm) than the FeCoCr films, suggesting that the FeCoCr thick films are more easily deformed than the FeCo films.

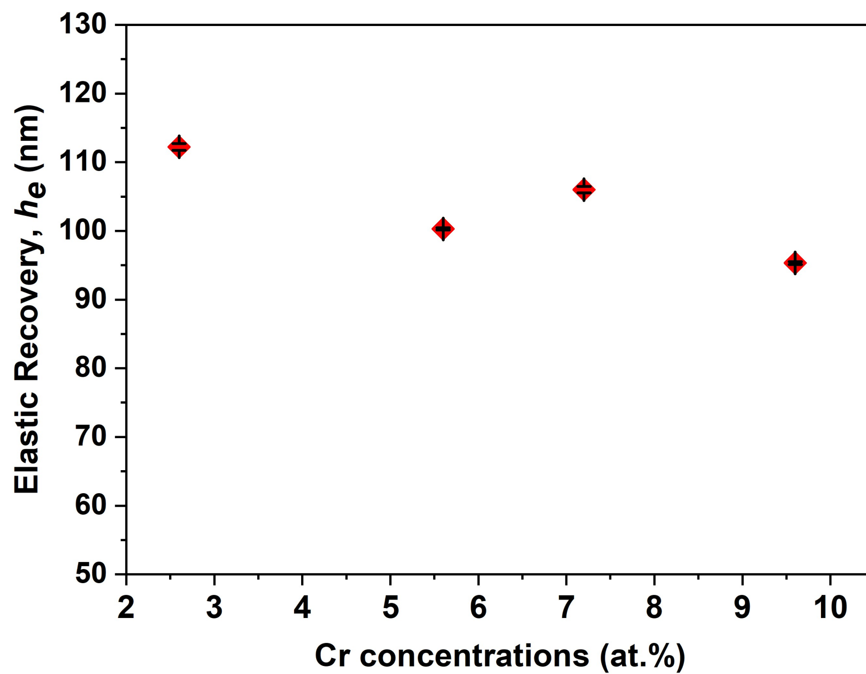

Figure 7.12: The average of elastic recovery, h_e of FeCoCr films as a function of Cr concentration .

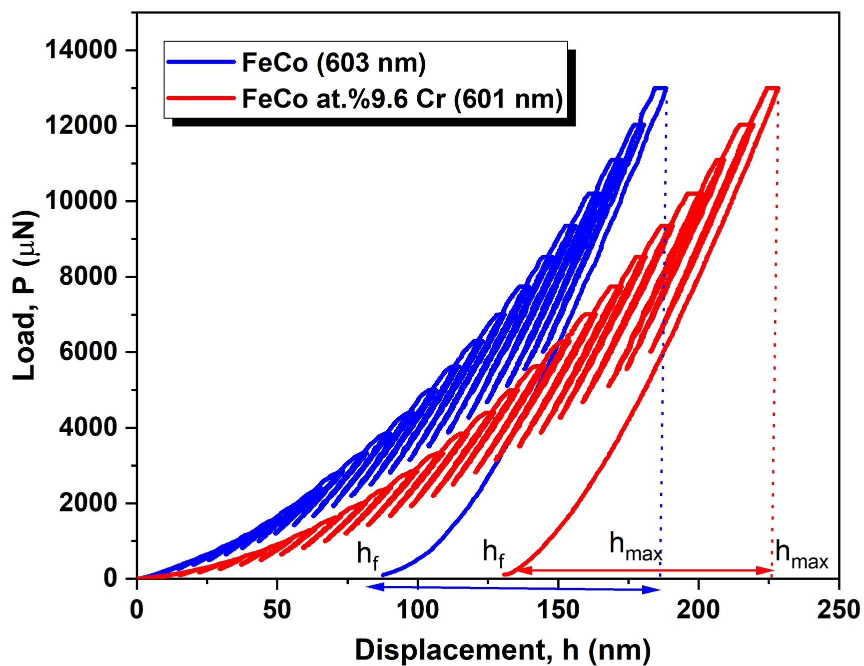

Figure 7.13: Comparison of a load-displacement curves between the FeCo (603 nm) and FeCoCr at.%9.6 (601 nm) films presenting that the elastic recovery, h_e of FeCoCr is slightly higher than the FeCo film. The h_e is calculated from the difference between the maximum displacement, h_{max} and the final depth, h_f.

7.8 Analysis of the Material Effect

It is well known that when the indenter tip makes contact into an elastic material, surface deformation may occur, either as sink-in or pile-up around the indenter. Depending on the strain hardening of the specimen, the pile-up event is more pronounced for non-strain hardening material (metal) with a large value of the ratio between the Young's modulus and yield strength, E/σ_Y, while sink-in tends to happen for a material with a low value of E/σ_Y [213]. On the other hand, both events also can be associated with a measurable parameter from the load-displacement curve, i.e the ratio of h_f/h_{max}. Pile-up is more significant when h_f/h_{max} is close to 1 and sink-in occurs when $h_f/h_{max} < 0.7$. These material effects can also influence the determination of the contact area, hence the measurement of the real hardness and modulus of the specimen. It has been reported that an underestimated of the contact area can be as much as 60% due to a large pile-up phenomena, which results in an overestimation of the hardness and modulus properties [214]. For this reason, it is important to study the pile-up or sink-in behaviour on the tested materials.

To examine whether the FeCo and FeCoCr films have undergone either these effects, AFM images were taken after the indentations had been performed. It should be noted for this analysis, a Triboscope Nanodindentation equipped with AFM was used, which is different from the TI 950 Triboindenter Hysitron used to measure the hardness and reduced modulus. The reason for using the Triboscope with AFM rather than using Scanning Probe Microscopy (SPM) on the TI 950 Triboindenter is because the AFM gives a better image of the pile-up or sink-in events. A similar Berkovich tip has been used with a load applied at a maximum of 13 mN, a total of 25 cycles with loading, holding and unloading at 5 seconds for each segment was carried out. To distinguish the material effect between the FeCo and FeCoCr films, the measurement was performed on selected samples only which were the FeCo film at thickness 758 nm and the FeCoCr films with the lowest and highest concentrations; at.%2.6 Cr and at.%9.6 Cr samples.

Figure 7.14 displays a cross-sectional analysis and the 3D images of the four indentations which were performed on the 758 nm FeCo film. From the 3D image, there were no sink-in events observed. Nonetheless, a small pile-up occurred on the one side of indenter. The pile-up is measured by the height of the pile-up relative to the surface which does

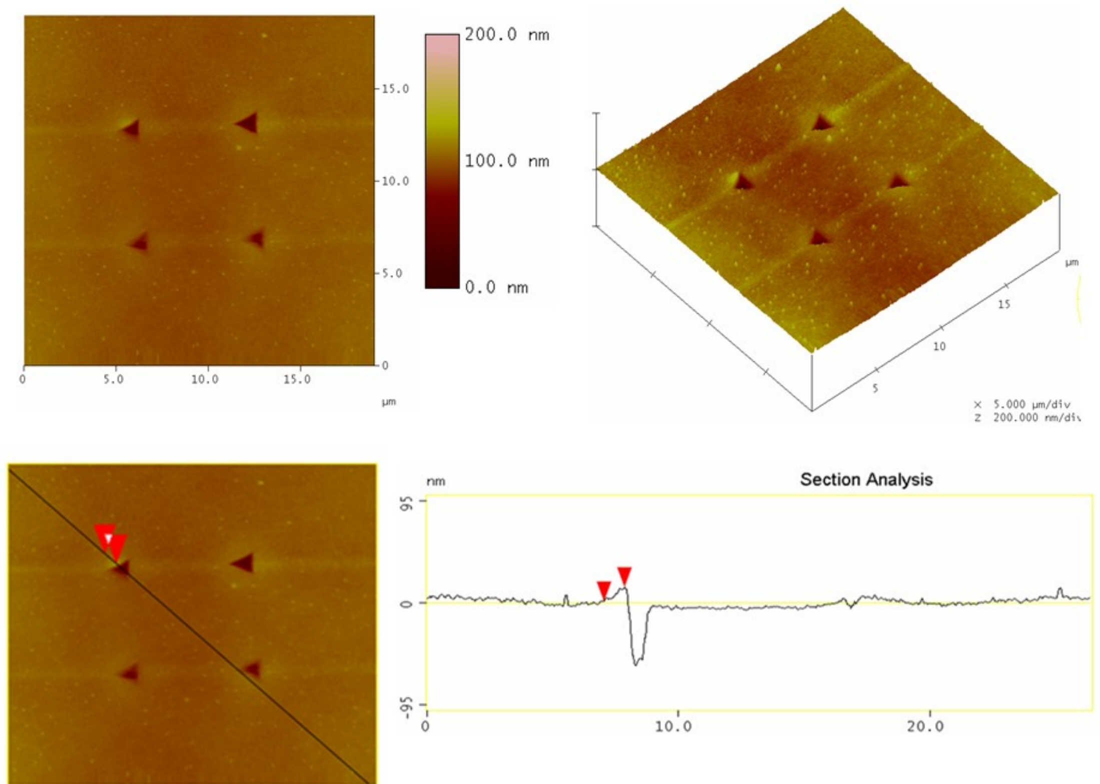

Figure 7.14: The images of a cross-section analysis (on the bottom) and 3D view (on the top-right) showing a small pile-up has occurred on FeCo film thickness 758 nm after indentation with load of 13 mN. Data scale is 200 nm with the scan size of 19 μm x 19 μm.

not experience any deformation by the indenter. The shown red marker on the cross-section analysis measured the pile-up on the FeCo film, and found the height to be about 13.21 nm. The images of the indentation on the sample of FeCoCr at.% 2.6 film are schematically shown in Figure 7.15. It is apparent that a significant variation of pile-up happens around the three sides of the triangle indenter tip in the FeCoCr films, as demonstrated in the 3D image. The cross-section analysis measured the amount of pile-up on the three different locations of the indenter represented by the green, black and red lines. It was found that the vertical distance of the pile-up on the films at.% 2.6 was between 18.65 nm and 25.58 nm.

Similarly, the material pile-up is clearly visible for the at.% 9.6 Cr film, with a measured height varying from 15.27 nm to 24.41 nm as shown in Figure 7.16. From the material pile-up analysis, this indicates that the material pile-up is considerably larger on the soft amorphous FeCoCr compared to the FeCo films. This is supported by the reported

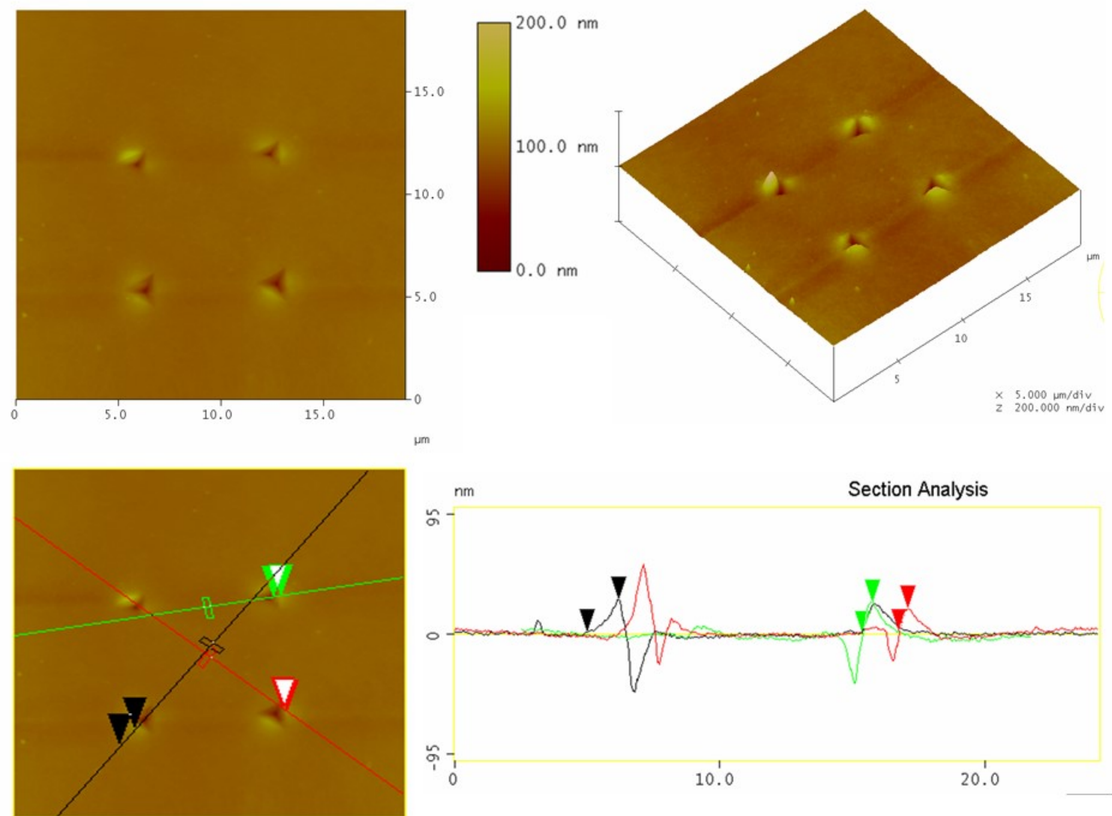

Figure 7.15: The images of a cross-section analysis (on the bottom) and 3D view (on the top-right) showing a significant pile-up has occurred on FeCoCr film at.% 2.6 Cr after indentation with load of 13 mN. Data scale is 200 nm with the scan size of 19 μm x 19 μm.

studies that a soft material deposited on the hard substrate tends to experience with the pile-up effect [133]. Another study has also suggested that thin films deposited on a hard substrate have a larger pile-up compare to the bulk sample. The mechanism of the pile-up can be explained by the dislocation movement being reduced as they are confined near the surface. As a result, more cross slip on the slip plane occurs close to the indenter, hence forming the pile-up. The amount of pile-up depends on how far the dislocations move into the material [215].

As the Oliver and Pharr method has been used to calculate the hardness and Young's modulus, which does not take into account the pile-up effect, this implies that the presented value of the hardness and Young's modulus for the FeCoCr films in the preceding section probably higher than the actual value due to the effect of pile-up which have been visualized from AFM measurement. According to Bolshakov and Pharr [214], depending on the amount of the pile-up effect, the value of hardness and Young's Modulus

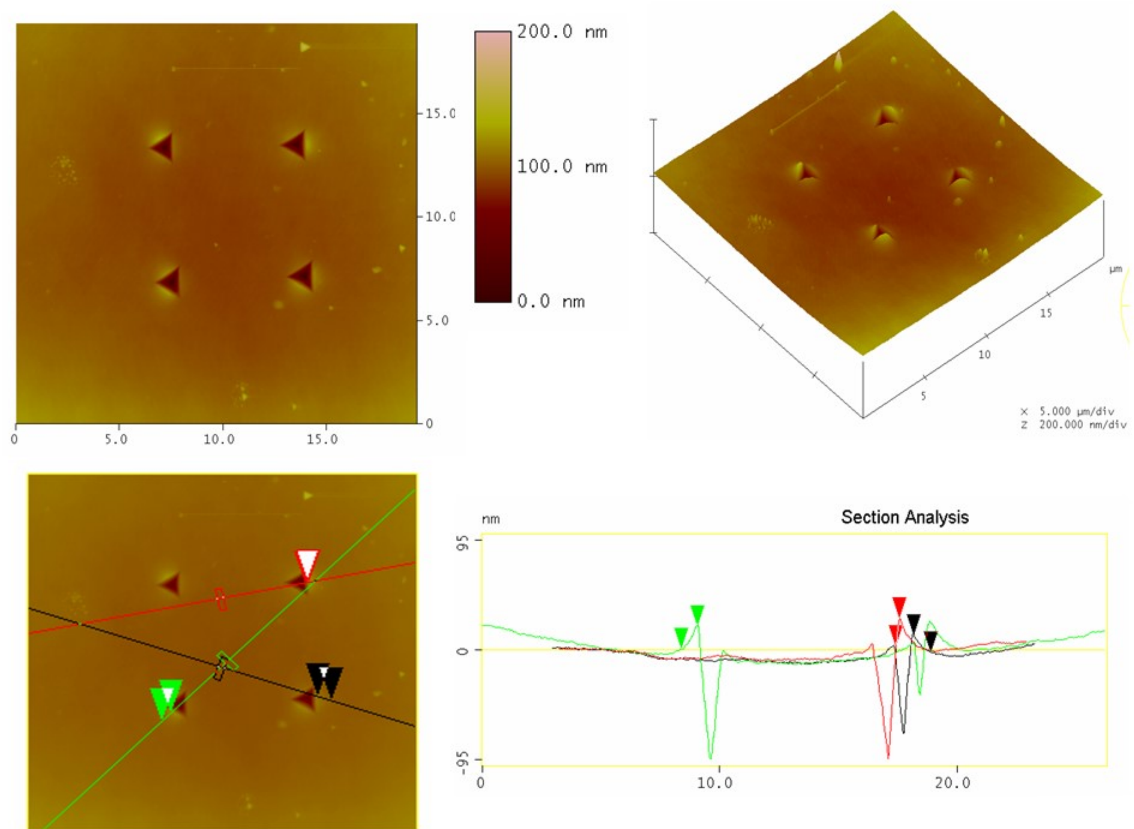

Figure 7.16: The images of a cross-section analysis (on the bottom) and 3D view (on the top-right) showing a significant pile-up has occurred on FeCoCr film at.% 9.6 Cr after indentation with load of 13 mN. Data scale is 200 nm with the scan size of 19 μm x 19 μm.

can be overestimated up to 60% and 16%, respectively.

7.9 Yield Strength of FeCo and FeCoCr films

Another important parameter that is also of interest to extend the knowledge on the mechanical behavior of FeCoCr thick films is the yield strength, σ_y. The yield strength determines the amount of stress than can be applied to the material before it is deformed from elastic to plastic behaviour. To obtain the yield strength of the sample, a microindentation test was performed by the NanoTest Vantage equipment. In the microindentation, a spherical tip with a radius of 19 μm was used, which is different from the Berkovich tip used in nanoindentation test. The major advantage of using the spherical tips over the sharper tip (Berkovich) in this measurement is the spherical tip

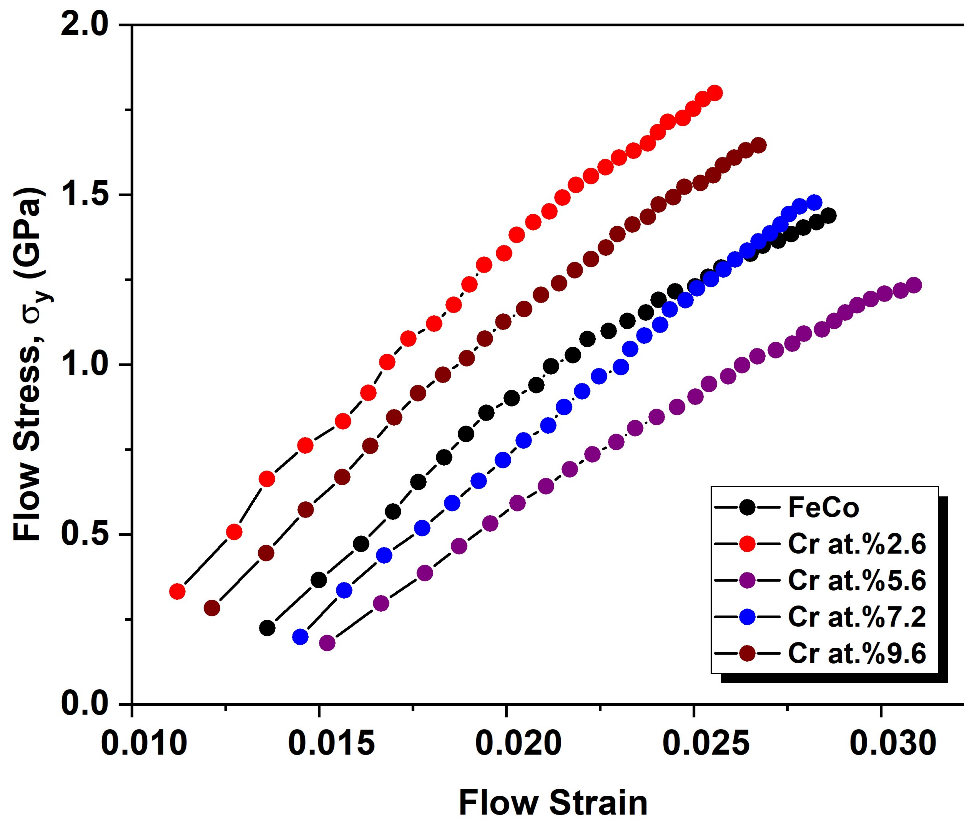

Figure 7.17: The plot of strain-stress curves of FeCo and FeCoCr determined from a representative of indentation.

allows one to determine the response of material from initial elasticity to initial plasticity regions, then until post-yield at a finite plastic strain [216].

A load of 100 mN was applied for 30 cycles for a series of indentation performed on several areas of interest for each film. The microindentation was performed using a spherical indentation. The load and displacement curve data were subsequently analyzed based on the Field and Swain measurement [217]. The data was then converted into a stress and strain plot. From the plot, the σ_y point can be determined directly. Examples of the stress and strain curves determined from this measurement are presented in Figure 7.17. It should be noted that the shown curves are a representative of the stress-strain curves determined from the series indentations for each sample. Based on the determined stress-strain curves as shown in Figure 7.17, the changing from elastic to plastic deformation occurred at the average flow stress between 0.020 and 0.024. It has been generally accepted that, the 0.2% offset is a method, which is commonly applied to estimate the $\sigma_{y0.2}$ that corresponds to the plastic strain at 0.002 [218]. As the obtained stress-strain plots of the FeCo and FeCoCr films in this current study do not show a perfect

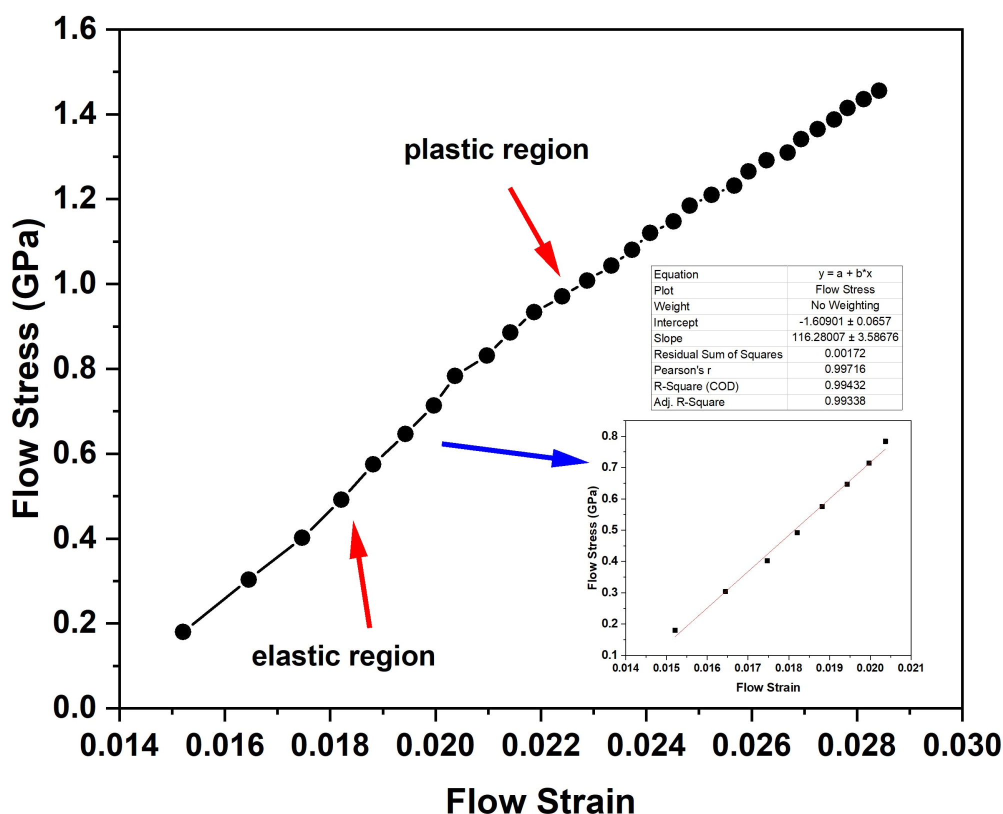

Figure 7.18: The representative of stress-strain curve of FeCoCr film at.% 9.6 Cr from microindentation using spherical tip (19 μm) with load applied of 100 mN. In the plot showing an estimation of a yield point by a linear fit of elastic region as shown in inserted graph.

stress-strain curve like in tensile measurement, therefore it is difficult to define a point at which the elastic behaviour changes to the plastic deformation by using the 0.2% offset method. Therefore, the σ_y of the sample was taken at the point at which a linear part associated to the elasticity properties started to change to the plastic deformation, where the arc shape was being observed. A method of a linear fit in elastic region was applied to estimate the yield strength of the films. An example of one of a stress-strain curves obtained using a linear fit method of on how the yield strength was estimated is presented in Figure 7.18.

Figure 7.19 compares the yield strength, σ_y between the FeCo and FeCoCr samples. The error bars in the plot represents the standard error calculated from a series of indentation for each sample. It is shown that the FeCo film had a $\sigma_y = 828 \pm 75$ MPa. For the addition of Cr into FeCo, it is clearly seen that the yield strength, σ_y decreases initially from 821 ± 58 MPa (sample at.%2.6 Cr) to 770 ± 46 MPa as the concentrations increases to at.% 5.6 Cr. Then, the σ_y is considerably enhanced to the value of 1014 $\pm$

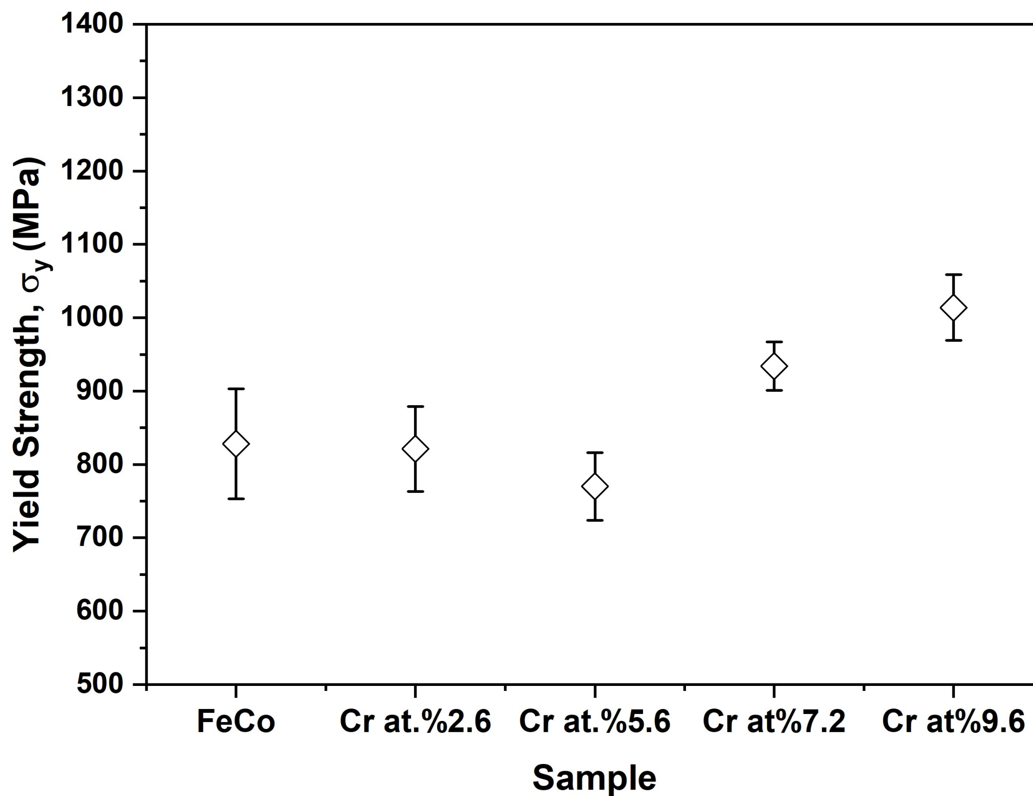

Figure 7.19: The graph of average yield strength, σ_y measured from strain-stress curves.

45 MPa for at.%9.6 Cr film. A maximum σ_y was observed at a concentration of at.%9.6 Cr indicated that there was an optimum Cr content can lead to the enhancement of σ_y. By comparing this value which was higher than the σ_y of FeCo sample it can therefore be suggested that incorporating the Cr atoms into FeCo can strengthen the FeCo sample. It is due to the fact that impurities atoms can hinder the movement of the dislocation. Additionally, the FeCoCr films have an amorphous structure with no grains, such that the atomic disorder causes discontinuity of any further dislocations motion. According to the Hall-Petch effect on grain-size strengthening, the yield strength increases with the reduction of the grain size [219].

A large σ_y of 1830 MPa has been reported previously on the FeCo films deposited on Si substrate [131]. The significant difference for the σ_y compared to our FeCo films grown also onto Si can be explained by the different sample thicknesses. In that published study, the thickness of FeCo films was 2000 nm, nearly three times larger than the film thickness in this current study. While in those reported study, they estimated the yield strength using the method developed by Giannakopoulos and Suresh [220] by utilizing

the hardness data obtained from the nanoindentation technique, instead of measuring them directly from the stress-strain plot.

7.10 Summary

The determination of mechanical properties of FeCo and FeCoCr thicker films has been successfully studied by the nanoindentation technique. Several important parameters have been determined including the hardness, reduced modulus, Young Modulus, elastic recovery, and the yield strength. Analysis of the hardness of FeCo films at different thickness have shown an increase in the hardness with the film thickness with the highest value of 15 GPa at thickness 758 nm. The Cr addition into FeCo, however, decreases the hardness to as low as 12 GPa for sample at.% 7.2 Cr. The Young's modulus of FeCo was also found to be higher $E_Y = 167$ GPa than the FeCoCr for sample at nearly the same thickness (≈ 600 nm). The E_Y of FeCoCr films were determined to be in the range of 144 GPa to 157 GPa. The load-displacement curves have also shown that the FeCoCr films tend to be more elastic compared to the FeCo as the calculated elastic recovery of FeCoCr sample was larger than the FeCo when the film thickness between them is comparable. Analysis of material effect from AFM and cross-sectional revealed the pile-up events occurred in the soft FeCoCr films, but those effect did not significantly occur for FeCo films. The pile-up effect may affect the calculation of the hardness and the modulus of the FeCoCr as it related to the determination of tip of contact area, which the value of hardness and the modulus of FeCoCr have been deviated from the expecting results. Interestingly, the yield strength obtained directly from the stress-strain curve found that Cr substitutions slightly enhanced the yield strength with the maximum σ_y achieved at 1014 MPa for sample at.%9.6 Cr compared to a σ_y of 828 MPa for the FeCo. This study then suggests that although the addition of Cr reduced the hardness and Young's modulus of the FeCo films, the yield strength of the FeCo films has been improved with adding a certain level of Cr concentrations, such that the Cr atoms are responsible to hamper the motion of dislocations in the soft amorphous FeCoCr films.

Chapter 8

Conclusion and Future Work

8.1 Conclusions

An investigation and characterization of the new soft amorphous material FeCoCr in thin films has been studied and demonstrated in this thesis. The FeCo thin films and FeCo doping with Cr have been successfully grown by RF Sputtering with different sputtering parameters including the sputtering power, thickness, and composition. The films' properties of structure, composition, magnetic response, magnetostriction, magnetic damping and mechanical response, have been investigated using various characterization techniques and the findings were described previously in three main result chapters (Chapter 5, Chapter 6 and Chapter 7). Summary of the thesis are drawn based on the following questions which have been addressed in Chapter 1:

a) Do the growth conditions, for instance, the application of a magnetic field during fabrication, sputtering power, film thickness, have a significant effect on the structural and magnetostriction constant of the FeCo and FeCoCr films?

b) Can Cr reduce the coercive and anisotropy fields, hence improve the soft magnetostrictive properties of the FeCo films?

c) How much percentages of Cr that can be added into FeCo to achieve the ideal soft magnetic properties; $H_c <$ 10 kAm^{-1}, $H_k <$ 15 kAm^{-1}, $\lambda_s >$ 20 ppm and magnetic damping constant $\alpha \leq$ 0.0100 of FeCoCr films?

d) Does the addition of Cr improve the mechanical properties such as the hardness, Young's Modulus and the yield strength, σ_y of the FeCo films?

Chapter 5 showed that the structure of FeCo films, was influenced by an applied magnetic field during fabrication using RF Sputtering. In the presence of an applied field, it can be seen a single diffraction peak represents the BCC (110) of FeCo ($2\theta \approx 45^0$). This peak is more intense for films compared to diffraction peak of the films fabricated without an applied field. For FeCoCr films sputtered at different sputtering power from 75 W to 150 W, it was determined for the sputtered films at higher power 125 W and 150 W, the structure of FeCoCr films significantly changed from amorphous to polycrystalline. Two diffraction angles were detected at $2\theta \approx 45^0$ and 81^0 for the films at these sputtering power. This was also confirmed by SAED images from TEM analysis, where an image of the film at the highest power (150 W) showed rings with small diffraction spots, while at lowest power 75 W only a diffuse ring was imaged. It was shown that by growing films at higher sputtering powers i.e in this study more than 100 W, the structure changed from amorphous to polycrystalline in the FeCoCr films. But changing the film thickness does not influence the structure of films for both FeCo and FeCoCr films, even though the FeCoCr films thickness was increased up to 165 nm. Study of the surface roughness of FeCoCr films by Atomic Force Microscopy demonstrated they were amorphous with no grains being observed regardless of film thickness. Neither film thickness nor sputtering power affected the surface roughness of FeCoCr films. Hence, the surface roughness was not the reason why the magnetisation changed in FeCoCr thin films despite other studies having reported the role of surface roughness effect on tuning the film's magnetisation.

Magnetic anisotropy was observed in the amorphous FeCoCr films, which was induced from the application of a magnetic field during deposition. Apart from that, the anisotropy for amorphous FeCoCr films can also have contributions from local random anisotropy as the local magnetocrystalline anisotropy is averaged out in most amorphous materials. The measured H_c and H_k of FeCoCr films using MOKE technique were found to be reduced with film thicknesses, in contrast to the FeCo films where their magnetic parameters increased with thickness. The coercive field of FeCoCr films, $H_c = 1.48$ kAm^{-1} was a factor of 6 lower than the H_c of FeCo, $H_c = 9.26$ kAm^{-1}. The lowest H_k of FeCoCr was found to be 12 kAm^{-1}. The purpose of adding Cr into the FeCo was to achieve an amorphous structure and to reduce the H_c and H_k since the FeCoCr thin film has not been studied comprehensively compared to the other amorphous

material (i.e FeCoB, FeGaB). Therefore, in this study, the FeCo films with different percentage of Cr were successfully grown with an optimized sputtering power 75 W and Argon pressure was 4.8 mTorr. It has been demonstrated that the FeCoCr films had an amorphous structure and is magnetically softer than FeCo films. Despite increasing the Cr compositions from at.2.6% Cr to at.9.6% Cr, the film structure does not change as the FeCoCr are still found to be amorphous. It was found that the anisotropy field H_k both measured along hard axes by MOKE and VNA-FMR techniques decreased with Cr compositions. Interestingly, both techniques demonstrated the lowest H_k for Cr at.9.6% films which were nearly the same $H_k \approx 2.7$ kAm^{-1}. The coercive field obtained also reduced with increasing Cr to at.5.6% before it remain constant $H_c \approx 0.14$ kAm^{-1} when Cr increased up to at.9.6%. The value of saturation magnetization, M_s as function of Cr concentrations measured from SQUID dropped from 1042 to 726 kAm^{-1}. The M_s was subsequently used to estimate the anisotropy constants K_U. It was implied that introducing Cr into FeCo decreased anisotropy energy from 3.930 to 1.269 kJm^{-3}, which is in an agreement with the reduction of H_c and H_k with Cr concentrations.

The damping parameters, α measured on the VNA-FMR were reproducible and well-fitted with the Kittle's equation. The lowest damping constants were obtained for films at.2.6% Cr $\alpha = 0.0065$. Nonetheless increasing the Cr concentrations increased the damping constant to a maximum 0.0100 for films at.7.2% Cr. The damping was associated with the sample inhomogeneity, also the presence of the uniaxial anisotropy was observed. Comparison between the FeCoCr films with other soft magnetic materials also has been presented in this thesis. The FeCoCr films in this study have demonstrated magnetically soft properties ($H_c < 200$ Am^{-1}) compared to some amorphous films reported in previous studies (i.e FeCoB, FeCoAlO, FeCoNi, FeCoCrN). The magnetic damping data of soft amorphous FeCoCr thin films presented in this thesis contributes to the fundamental study of the damping constants reported for other soft magnetic materials. From these finding this material may be the subject of interest in spintronic device application as the FeCoCr films have demonstrated not only soft properties but also lower magnetic damping.

For the magnetostriction study using the Villari technique it was found that increasing thickness of the FeCo film reduced the magnetostriction constant, while the magnetostriction constants of FeCoCr films were independent of film thickness. It was suggested that the interfacial magnetostriction constant does not strongly influence the

overall magnetostriction constant of the FeCoCr films. A comparison was also made between the λ_s of the FeCo and FeCoCr films at a similar thickness, 100 nm. It was shown that both films group have no significant difference in magnetostriction constant; λ_{FeCoCr} = 28 ppm and λ_{FeCo} = 26 ppm. However, the sputtering power had demonstrated a substantial effect on the magnetostriction constants, λ_s for films deposited at same thickness, 100 nm. The λ_s was considerably reduced with the increased sputtering power. For films sputtered at highest power, 150 W had the lowest constant, $\lambda_s = 6$ ppm which was six times lower than films sputtered at lowest power, 75 W (λ_s = 28 ppm). The structural difference between the FeCoCr films at the lowest power (disordered) and the highest power (polycrystalline) of FeCoCr thin films was identified as the factor that caused the reduction of magnetostriction constant upon increasing sputtering power.

The λ_s of films grown with varying Cr concentrations also have been described, as for an increase in Cr the λ_s dropped from 39 ppm (Cr at.2.6%) to 13 ppm (Cr at.9.6%). Therefore, from the investigation on the effect of Cr concentrations on magnetostriction constant, it can be inferred that to sustain the λ_s with the lowest magnetic damping a lower Cr concentration at.2.6% was sufficient to be added into FeCo. Although at this concentration the value of coercive field, H_c was found to be the highest, nonetheless the value was not too far from the H_c of other Cr concentrations and still magnetically soft (< 200 Am^{-1}).

The other most significant finding from this study is measuring the mechanical properties (hardness, Young's Modulus and Yield strength) of the FeCo films ($>$ 400 nm) and the FeCoCr films ($>$ 600 nm) by employing the nanoindentation technique. It has been shown that while the hardness of FeCo increased with thickness, the hardness of FeCoCr reduced upon increasing Cr compositions to at.7.2% (H = 12 GPa). The maximum hardness of FeCo was 15 GPa for sample of thickness 758 nm. The calculated Young's Modulus of FeCo films (E_Y = 167 GPa) was found to be higher than FeCoCr films (E_Y = 157 GPa) for the same thickness ($\approx$ 600 nm). The significant difference on the H and E_Y between the FeCo and FeCoCr films was described by an observation of different material effects that occurred within these samples. The AFM and cross-sectional studies revealed that the a pile-up event occurred in the FeCoCr films which suggested a lower hardness value determined compared to the FeCo films. It was interesting, however, the Yield strength, σ_y of FeCo films improved with Cr substitutions at.% 9.6 with the σ_y of FeCoCr was found to be 1014 MPa, compared to a σ_y of 828 MPa for the FeCo films.

From the mechanical studies, it has shown that even though the Cr substitutions into FeCo films do not have significant impact on improving the hardness and the Young's Modulus, nevertheless, the Cr did enhance the Yield strength of FeCo which it had reported issues with the brittleness of the FeCo materials. This study provide that at certain level of Cr concentrations into FeCo films causes the dislocations motion to be hindered in the soft amorphous magnetic materials.

Considering the fabrication parameters which employed in this research, it can be concluded that the optimised fabrication of the FeCoCr was the film deposited at the sputtering power of 75 W in the presence of a magnetic field. These conditions then result in the amorphous structure of the FeCoCr films with the lowest anisotropy and coercive fields. The highest magnetostriction constant was also determined at this lowest power. Although this optimum sputtering power condition improved the samples' magnetic properties by reducing the anisotropy and coercive fields, increasing the Cr concentrations from at.2.6% to at.9.6% at fixed power 75 W, however, did not significantly enhance both the magnetostriction constant and the magnetic damping of the FeCoCr films. The optimum Cr concentration which can be added into the FeCo to maintain the highest magnetostriction (39 ppm), was found to be 2.6 %, which at this concentration also gives the lowest magnetic damping ($\alpha = 0.0065$). Despite that, increasing the Cr concentration helps to strengthen the soft amorphous FeCoCr films' mechanical properties. Finally, controlling the sputtering power and adding a certain percentage of Cr was feasible to achieve the soft amorphous properties of the FeCoCr magnetostrictive thin films.

8.2 Future Works

Considerably more future work needs to be carried out to acquire a full understanding on the role of growth parameters and Cr substitutions on the soft magnetostrictive FeCoCr thin films. For example, other than effect of sputtering power and film thickness, one of the most significant impact of thin film properties is investigating the effect of sputtering pressure on the FeCoCr thin films. However, due to the limitation of the existing sputtering deposition system that has been used in this project, the effect of pressure on the structure, magnetic and magnetostrictive FeCoCr films were unable to be performed. The structural studies by XRD have demonstrated broader peaks of

amorphous FeCoCr was linked to an inhomogeneous strain within the films. Therefore, measurement of the film strains directly by using XRD technique is required for future works to obtain the level of strains within the FeCoCr films.

This work also can be extended to provide a comprehensive study on the role of Cr substitutions to the H_c, H_k and λ_s for wide ranges of Cr concentrations i.e until at.%30 Cr. Study the magnetic damping with wide range of thickness (5 nm $\leq t \leq$ 100 nm) would be interesting to explore the thickness dependence on mechanism of magnetic damping in FeCoCr films. As the data of mechanical properties; Young's Modulus and the Yield strength, particularly the FeCoCr thin films have not been published until to date, by investigating these parameters for wide range of thickness more than 2 μm in the future research would be useful to provide more understanding and information on the mechanical behaviour of this soft amorphous magnetic materials.

Bibliography

[1] H.H Wada, M.and Uchida, Y. Matsumura, H. Uchida, and H. Kaneko. Preparation of films of (Tb,Dy)Fe2 giant magnetostrictive alloy by ion beam sputtering process and their characterization. *Thin Solid Films*, 281-282:503–506, 1996.

[2] S. M. Na, S. J. Sun, and S. H. Lima. Fabrication condition effects on the magnetic and magnetostrictive properties of sputtered Tb-Fe thin films. *Journal of Applied Physics*, 93(10 3):8507–8509, 2003.

[3] L. Dai, J. Cullen, M. Wuttig, T. Lograsso, and E. Quandt. Magnetism, Elasticity, and Magnetostriction of FeCoGa alloys. *Journal of Applied Physics*, 93(10):8627, 2003.

[4] M. P. Hollingworth, M. R.J. Gibbs, and S. J. Murdoch. Magnetostriction and surface roughness of ultrathin NiFe films deposited on SiO2. *Journal of Applied Physics*, 94(11):7235–7239, 2003.

[5] A. Javed, N. A. Morley, and M. R. J. Gibbs. Structure, magnetic and magnetostrictive properties of as-deposited Fe-Ga thin films. *Journal of Magnetism and Magnetic Materials*, 321(18):2877–2882, 2009.

[6] Q.A. Abbas and N.A. Morley. Fabrication and characterization of magnetostrictive amorphous FeGaSiB thin films. *Journal of Magnetism and Magnetic Materials*, 439(1):353–357, 2017.

[7] E. Hristoforou and A. Ktena. Magnetostriction and magnetostrictive materials for sensing applications. *Journal of Magnetism and Magnetic Materials*, 316:372–378, 2007.

[8] Y. Torii, H. Wakiwaka, T. Kiyomiya, Y. Matsuo, Y. Yamada, and M. Makimura. Tb-Fe-Co giant magnetostrictive thin film and its application to force sensor. *Journal of Magnetism and Magnetic Materials*, 290-291 PA:861–864, 2005.

[9] A.G. Olabi and A. Grunwald. Design and application of magnetostrictive materials. *Materials & Design*, 29(2):469–483, 2008.

[10] J. Atulasimha and A.B Flatau. A review of magnetostrictive iron–gallium alloys. *Smart Materials and Structures*, 20(4):043001, 2011.

[11] R. Elhajjar, C.T. Law, and A. Pegoretti. Magnetostrictive polymer composites: Recent advances in materials, structures and properties. *Progress in Material Science*, 97(1):204–209, 2018.

[12] D. E. Parkes, L. R. Shelford, P. Wadley, V. Holý, M. Wang, A. T. Hindmarch, G. van der Laan, R. P. Campion, K. W. Edmonds, S. A Cavill, and A. W. Rushforth. Magnetostrictive thin films for microwave spintronics. *Scientific Reports*, 3: 2220, 2013.

[13] J. P. Joule. On a new class of magnetic forces. *Annals of Electricity, Magnetism, and Chemistry*, 8(1):219–224, 1842.

[14] A. E. Clark, B. F. DeSavage, and R. Bozorth. Anomalous thermal expansion and magnetostriction of single-crystal dysprosium. *Physical Review*, 138(1 A), 1965.

[15] R. Abbundi and A. E. Clark. Analogus thermal expansion and magnetostriction of single crystal $Tb_{0.27}Dy_{0.73}Fe_2$. *IEEE Transactions on Magnetics*, 13(5):1519–1520, 1977.

[16] A.E. Clark, J.B. Restorff, M. Wun-Fogle, T.A. Lograsso, and D.L. Schlagel. Magnetostrictive properties of body-centered cubic Fe-Ga and Fe-Ga-Al alloys. *IEEE Transactions on Magnetics*, 36(5 I):3238–3240, 2000.

[17] E. Yu, J. S. Shim, I. Kim, J. Kim, S. H. Han, H. J. Kim, K. H. Kim, and M. Yamaguchi. Development of FeCo-based thin films for gigahertz applications. *IEEE Transactions on Magnetics*, 41(10):3259–3261, 2005.

[18] G. Herzer. Grain Size Dependence of Coercivity and Permeability. *IEEE Transactions on Magnetics*, 26(5):1397–1402, 1990.

[19] R. S. Sundar and S. C. Deevi. *Soft magnetic FeCo alloys: alloy development, processing, and properties*, volume 50. 2005.

[20] D. L. Polla and L. F. Francis. Ferroelectric Thin Films in Micro- electromechanical Systems Applications. *MRS Bulletin*, 21(07):59–65, 1996.

[21] H. Steiner, M. Stifter, W. Hortschitz, and F. Keplinger. Planar magnetostrictive micromechanical actuator. *IEEE Transactions on Magnetics*, 51(1):2–5, 2015.

[22] V. Alexandrakis, W. Wallisch, S. Hamann, G. Varvaro, J. Fidler, and A. Ludwig. Combinatorial Development of Fe Co Nb Thin Film Magnetic Nanocomposites. 2015.

[23] R.M Bozorth. *Ferromagnetism*. D. Van Nostrand Co. Inc, 1951.

[24] S. I. Yamaura, T. Nakajima, T. Satoh, T. Ebata, and Y. Furuya. Magnetostriction of heavily deformed Fe-Co binary alloys prepared by forging and cold rolling. *Material Science and Engineering B*, 193(1):121–129, 2015.

[25] J.R. Hattrick-Simpers, D. Hunter, C. M. Craciunescu, K. S. Jang, M. Murakami, J. Cullen, M. Wuttig, I. Takeuchi, S.E. Lofland, L. Benderksy, N. Woo, R. B. Van Dover, T. Takahashi, and Y. Furuya. Combinatorial investigation of magnetostriction in Fe-Ga and Fe-Ga-Al. *Applied Physics Letters*, 93(10):10–13, 2008.

[26] E. Quandt. Giant magnetostrictive thin film materials and applications. *Journal of Alloys and Compounds*, 258(1-2):126–132, 1997.

[27] M. D. Cooke, L.C. Wang, R. Watts, R. Zuberek, G. Heydon, W. M. Rainforth, and G.A Gehring. The effect of thermal treatment, composition and substrate on the texture and magnetic properties of FeCo thin films. *Journal of Physics D: Applied Physics*, 33:1450–1459, 2000.

[28] W.R Jones. Magnetostriction of Fe-Cr-Co Alloys. *IEEE Transactions on Magnetics*, MAG-17(4):1459–1461, 1981.

[29] W. Wang, G. H. Yue, Y. Chen, W. B. Mi, H. L. Bai, and D. L. Peng. Structural, electrical and magnetic properties of Fe-Co-Cr and Fe-Co-Cr-N nanocrystalline alloy films. *Journal of Alloys and Compounds*, 475(1-2):440–445, 2009.

[30] V. A. Vas'Ko, V. R. Inturi, S. C. Riemer, A. Morrone, D. Schouweiler, R. D. Knox, and M. T. Kief. High saturation magnetization films of FeCoCr. *Journal of Applied Physics*, 91(10 I):6818–6820, 2002.

[31] D. Jiles. *Introduction to Magnetism and Magnetic Materials*. CRC Press, third edition edition, 2016.

[32] J.P. Jakubovics. *Magnetism and Magnetic Material*. The Institute of Material, 2nd edition, 1994.

[33] N. Spaldin. *Magnetic Materials. Fundamentals and applications*. Cambridge University Press, 2010.

[34] P. Weiss. L'hypothèse du champ moléculaire et la propriété ferromagnétique. *Journal de Physique et le Radium*, 6(1):661–690, 1907.

[35] R.C. O'Handley. *Modern Magnetics Materials : Principles and Application*. John Wiley & Sons, Inc, 2000.

[36] B.D. Cullity and C.D. Graham. *Introduction to Magnetic Materials*. Institute of Electrical and Electronics Engineers, Inc, second edition edition, 2009.

[37] S. Chikazumi. *Physics of Ferromagnetism*. Oxford University Press, 2nd edition, 1997.

[38] T.L. Gilbert. A phenomenological theory of damping in ferromagnetic materials. *IEEE Transaction on Magnetics*, 40(6):3443–3449, 2004.

[39] S. Azzawi, A.T. Hindmarch, and D. Atkinson. Magnetic damping phenomena in ferromagnetic thin films and multilayers. *Journal of Physics D: Applied Physics*, 50:473001, 2017.

[40] L.D Landau and E.M. Lifshitz. On the theory of the dispersion of magnetic permeability in ferromagnetic bodies. *Physikalische Zeitschrift der Sowjetunion*, 8(1): 153–169, 1935.

[41] B. Anjan and H. Arabinda. Time-Domain study of magnetization dynamics in magnetic thin films and Micro- and Nanostructures. *Solid State Physics*, 65(1): 1–108, 2014.

[42] A. Conca, J. Greser, T. Sebastian, S. Klingler, B. Obry, B. Leven, and B. Hillebrands. Low spin-wave damping in amorphous $Co_{40}Fe_{40}B_{20}$ thin films. *Journal of Applied Physics*, 113:213909, 2013.

[43] B. Heinrich and G Woltersdorf. Intrinsic Spin Relaxation Processes in Metallic Magnetic Multilayers. *Journal of Superconductivity and Novel Magnetism*, 20(2): 83–89, 2007.

[44] Kh. Zakeri, J. Lindner, I. Barsukov, R. Meckenstock, M. Farle, U. von Hörsten, H. Wende, W. Keune, J. Rocker, S. Kalarickal, K. Lenz, W. Kuch, K. Baberschke, and Z. Frait. Spin dynamics in ferromagnets: Gilbert damping and two-magnon scattering. *Physical Review B*, 76(2):104416, 2007.

[45] H. Kurebayashi, T. D. Skinner, K. Khazen, K. Olejník, and D. Fang. Tuning magnetic relaxation by oblique deposition. *Applied Physics Letter*, 102(1):062415, 2013.

[46] I. Barsukov, P. Landeros, R. Meckenstock, J. Lindner, D. Spoddig, Zi-An Li, B. Krumme, H. Wende, D. L. Mills, and M. Farle. Tuning magnetic relaxation by oblique deposition. *Physical Review B*, 85(1):014420, 2012.

[47] J.R. Fermin, A. Azevedo, F.M. De Aguiar, B. Li, and S.M. Rezende. Ferromagnetic resonance linewidth and anisotropy dispersions in thin Fe films. *Journal of Applied Physics*, 85(10):7316–7320, 1999.

[48] W. Platow, A. Anisimov, G. Dunifer, M. Farle, and K. Baberschke. Correlations between ferromagnetic-resonance linewidths and sample quality in the study of metallic ultrathin films. *Physical Review B - Condensed Matter and Materials Physics*, 58(9):5611–5621, 1999.

[49] R. Alben, J. J. Becker, and M. C. Chi. Random anisotropy in amorphous ferromagnets. *Journal of Applied Physics*, 49(3):1653–1658, 1978.

[50] G Herzer. Chapter 3 Nanocrystalline soft magnetic alloys. *Handbook of Magnetic Materials*, 10:415–462, 1997.

[51] G. Herzer. Modern soft magnets: Amorphous and nanocrystalline materials. *Acta Materialia.*, 61(3):718, 2013.

[52] S. Chikazumi. Ferromagnetic Properties and Superlattice Formation of Iron Nickel Alloys (I). *Journal of Physical Society of Japan*, 5(1):327–333, 1950.

[53] S. Chikazumi and T. Oomura. On the Origin of Magnetic Anisotropy Induced by Magnetic Annealing. *Journal of Physical Society of Japan*, 10(1):842–849, 1955.

[54] M. Ali and R. Watts. Measurement of saturation magnetostriction using novel strained substrate techniques and the control of the magnetic anisotropy. *Journal of Magnetism and Magnetic Materials*, 202(1):85–94, 1999.

[55] N.B. Ekreem, A.G. Olabi, T. Prescott, A. Rafferty, and M.S.J. Hashmi. An overview of magnetostriction, its use and methods to measure these properties. *Journal of Materials Processing Technology*, 191(1-3):96–101, 2007. ISSN 09240136.

[56] R.C. O'Handley and S.W. Sun. Surface Magnetostriction In: Hadjipanayis G.C., Prinz G.A. (eds) Science and Technology of Nanostructured Magnetic Materials. *NATO ASI Series (Series B: Physics)Springer*, 259(1):109–116, 1991.

[57] H. Szymczak and R. Zuberek. Surface Magnetostriction. *Acta Physica Polonica A*, 83(1):651–659, 1993.

[58] T.A. Lafford and M. R. J. Gibbs. Interpretation of saturation magnetostriction data in multilayer systems. *IEEE Transactions of Magnetics*, 31(6):4094–4096, 1995.

[59] T.A. Lafford, M. R. J. Gibbs, and R. Zuberek. Magnetic properties of $Co_{32}Pd_{68}$ / Ag multilayer. *Journal of Magnestism and Magnetic Materials*, 140-144(1):577–578, 1995.

[60] H.J. Hatton and M.R.J. Gibbs. Interface contributions to magnetostriction in transition metal based soft magnetic multilayers. *Journal of Magnetism and Magnetic Materials*, 156(1-3):67–68, 1996.

[61] I.N. Sneddon. *Fourier Transforms.* McGraw-Hill Inc, New York, 1951.

[62] M.F. Doerner and W.D. Nix. A method for interpreting data from depth-sensing indentation instruments. *Journal of Materials Research*, 4:601–609, 1986.

[63] W.C. Oliver and Pharr. G.M. Measurement of hardness and elastic modulus by instrumented indentation: Advances in understanding and refinements to methodology. *Journal of Materials Research*, 19:3–20, 2004.

[64] W.C. Oliver and Pharr. G.M. An improved technique for determining hardness and elastic modulus using load and displacement sensing indentation experiments. *Journal of Materials Research*, 7:1564–1583, 1992.

[65] L. Riester, T.J. Bell, and A.C. Fischer-Cripps. Analysis of depth-sensing indentation tests with a knoop indenter. *Journal of Materials Research*, 16:1660–1667, 2001.

[66] H. Uchida, Y. Matsumura, H. Uchida, and H. Kaneko. Progress in thin films of giant magnetostrictive alloys. *Journal Magnetism and Magnetic Materials*, 239 (1-3):540, 2002.

[67] S. R. Williams. The joule magnetostrictive effect in a group of cobalt-iron alloys. *Review of Scientific Instruments*, 3(11):675–683, 1932.

[68] R. C. Hall. Magnetic anisotropy and magnetostriction of ordered and disordered Cobalt-iron alloys. *Journal of Applied Physics*, 157(5):199–201, 1960.

[69] T. Yokoshima, K. Imai, T. Hiraiwa, and T. Osaka. Preparation of high-B/sub s/ Co-Fe soft magnetic thin films by electrodeposition. *Magnetics, IEEE Transactions on*, 40(4):2332–2334, 2004.

[70] C. H. Lin, W. H. Chen, J. S. Tsay, I. T. Hong, C. H. Chiu, and H. S. Huang. Structures and magnetic properties of Co and CoFe films prepared by magnetron sputtering. *Thin Solid Films*, 519(23):8379–8383, 2011.

[71] N. A. Morley, S. Rigby, and M. R. J. Gibbs. Anisotropy and magnetostriction constants of nanostructured $Fe_{50}Co_{50}$ films. 1(2):109–113, 2009.

[72] Y. Fu, X. Cheng, and Z. Yang. Magnetically soft and high-saturation-magnetization FeCo films fabricated by co-sputtering. *Physica Status Solidi (A) Applications and Materials Science*, 202(6):1150–1154, 2005.

[73] F. Yang, J. Min, J. Li, H. Chen, D. Liu, W. Li, X. Chen, and C. Yang. The influence of film composition and annealing temperature on the microstructure and

magnetic properties of FeCo thin film. *Journal of Materials Science: Materials in Electronics*, 28(1):11733–11737, 2017.

[74] M. Coïsson, F. Celegato, P. Tiberto, and F. Vinai. Magnetic properties of field-annealed FeCo thin films. *Journal of Magnetism and Magnetic Materials*, 320(20): 739–742, 2008.

[75] D. Hunter, W. Osborn, K. Wang, N. Kazantseva, J. Hattrick-Simpers, R. Suchoski, R. Takahashi, M.L. Young, A. Mehta, L. A. Bendersky, S.E. Lofland, M. Wuttig, and I. Takeuchi. Giant magnetostriction in annealed Co1xFex thin-films. *Nature Communications*, 2(May):518, 2011.

[76] T. Nakajima, T. Takeuchi, I. Yuito, K. Kato, M. Saito, K. Abe, T. Sasaki, T. Sekiguchi, and S. Yamaura. Effect of Annealing on Magnetostrictive Properties of Fe Co Alloy Thin Films. *Materials Transactions*, 55(3):556–560, 2014.

[77] G Varvaro, D. Peddis, G. Barucca, P. Mengucci, V. Rodionova, K. Chicay, Testa A.M, E. Agostinelli, and S. Laureti. Highly textured FeCo thin films deposited by low temperature pulsed laser deposition. *Applied Materials and Interfaces*, 7(1): 22341–22347, 2015.

[78] P. Gupta, K.J. Akhila, V. Srihari, P. Svec, S.R. Kane, S.K S.K. Rai, and T. Ganguli. On the origin of magnetic anisotropy of FeCo(Nb)B alloy thin films: A thermal annealing study. *Journal of Magnetism and Magnetic Materials*, 480: 64–72, 2019.

[79] H. Fukuzawa, Y. Kamiguchi, K. Koi, H. Iwasaki, and M. Sahashi. Saturation magnetostriction of an ultrathin CoFe free-layer on double-layered underlayers. *Journal of Applied Physics*, 91(5):3120–3124, 2002.

[80] S. Cakmaktepe, M.I. Coskun, and A. Yildiz. Underlayer effect on structural and magnetic properties of Co90Fe10 thin films. *Lithuanian Journal of Physics*, 53(2): 112–117, 2013.

[81] H. S. Jung, W. D. Doyle, and S. Matsunuma. Influence of underlayers on the soft properties of high magnetization FeCo films. *Journal of Applied Physics*, 93(10 2): 6462–6464, 2003.

[82] A. Caruana Finkel, N. Reeves-Mclaren, and N. A. Morley. Influence of soft magnetic underlayers on the magnetic properties of Co90Fe10 films. *Journal of Magnetism and Magnetic Materials*, 357:87–92, 2014.

[83] H. Katada, T. Shimatsu, I. Watanabe, H. Muraoka, and Y. Nakamura. Soft magnetic properties and microstructure in NiFe/FeCo/NiFe films with large saturation magnetization. *IEEE International Digest of Technical Papers on Magnetics Conference*, 38(5):2225–2227, 2002.

[84] N. Hayashi, Y. Miyamoto, K. MacHida, and T. Tamaki. Influence of underlayers on the soft magnetic properties of Fe-Co-Al-O films. *Journal of Magnetism and Magnetic Materials*, 287(SPEC. ISS.):387–391, 2005.

[85] N.A. Morley, F. Anastasia Caruana, Y Yang, Weigang, and N. Reeves-Mclaren. Magnetic and structural characterization of NiFe/Fe30Co70 Bilayers. *IEEE Transactions on Magnetics*, 50(11), 2014. ISSN 00189464.

[86] R. Gupta, A. Khandelwal, R. Ansari, A. Gupta, and K. G M Nair. Investigation of structural and magnetic properties of nanoscale Fe/Co bilayers. *Surface and Coatings Technology*, 203(17-18):2717–2720, 2009. ISSN 02578972.

[87] Y. Fu, T. Miyao, J. W. Cao, Z. Yang, M. Matsumoto, X. X. Liu, and A. Morisako. Effect of Co underlayer on soft magnetic properties and microstructure of FeCo thin films. *Journal of Magnetism and Magnetic Materials*, 308(1):165–169, 2007.

[88] B. Y. Yoo, S. C. Hernandez, D. Y. Park, and N. V. Myung. Electrodeposition of FeCoNi thin films for magnetic-MEMS devices. *Electrochimica Acta*, 51(28): 6346–6352, 2006.

[89] I. Kim, J. Kim, K.H. Kim, and M. Yamaguchi. Effects of boron contents on magnetic properties of Fe-Co-B thin films. *IEEE Transactions on Magnetics*, 40 (4 II):2706–2708, 2004.

[90] M. Munakata, S. I. Aoqui, and M. Yagi. B-concentration dependence on anisotropy field of CoFeB thin film for gigahertz frequency use. *IEEE Transactions on Magnetics*, 41(10):3262–3264, 2005.

[91] F. Zheng, F. Luo, Y. Lou, Y. Wang, Ji. Bai, D. Wei, X. Liu, and F. Wei. Magnetic properties and high-frequency characteristics of FeCoAlO gradient composition thin films. *Journal of Applied Physics*, 111(7):109–112, 2012.

[92] F. Zheng, X. Wang, X. Li, J. Bai, D. Wei, X. Liu, W. Xie, and F. Wei. High frequency characteristics of FeCoAlO thin films combined the effects of stress and magnetic field. *Journal of Applied Physics*, 109(7):31–34, 2011.

[93] T. Miyazaki, T. Saito, and Y. Fujino. Magnetostrictive properties of sputtered binary TbFe and pseudo-binary (TbDy)Fe alloy films. *Journal of Magnetism and Magnetic Materials*, 171(3):320–328, 1997.

[94] A. Speliotis, O. Kalogirou, and D. Niarchos. Magnetostrictive properties of amorphous and partially crystalline TbDyFe thin films. *Journal of Applied Physics*, 81: 5696–5698, 1997.

[95] N.H. Duc, K. Mackay, J. Betz, and D. Givord. Giant magnetostriction in amorphous $(Tb_{1-x}Dy_x)(Fe_{0.45}Co_{0.55})y$ films. *Journal of Applied Physics*, 79:973–977, 1996.

[96] R.R. Basantkumar, B.J. Hills Stadler, W.P. Robbins, and E. M. Summers. Integration of thin-film galfenol with MEMS cantilevers for magnetic actuation. *IEEE Transactions on Magnetics*, 42(10):3102–3104, 2006.

[97] B. W. Wang, S. Y. Li, Y. Zhou, W. M. Huang, and S. Y. Cao. Structure, magnetic properties and magnetostriction of Fe81Ga19 thin films. *Journal of Magnetism and Magnetic Materials*, 320(5):769–773, 2008.

[98] A. Javed, N.A. Morley, and M.R.J. Gibbs. Thickness dependence of magnetic and structural properties in Fe[sub 80]Ga[sub 20] thin films. *Journal of Applied Physics*, 107(9):09A944, 2010.

[99] A. Javed, N.A. Morley, T. Szumiata, and M.R.J. Gibbs. A comparative study of the microstructural and magnetic properties of textured thin polycrystalline Fe100xGax (10x35) films. *Applied Surface Science*, 257(14):5977–5983, 2011.

[100] E. W. Lee. Magnetostriction and Magnetomechanical Effects. *Reports on Progress in Physics*, 18(1):184–229, 1955.

[101] N. Tsuya and K. I. Arai. Magnetostriction Constants of Cubic Ferrites Containing Only Fe+3 as Magnetic Ions. *Journal of Applied Physics*, 42(1):1637–1638, 1971.

[102] Y. Masiyama. *The Science Reports of the Tohoku Imperial University, 1st series*, 21(1):394–410, 1932.

[103] R. C. Hall. Single crystal anisotropy and magnetostriction constants of several ferromagnetic materials including alloys of NiFe, SiFe, AlFe, CoNi, and CoFe. *Journal of Applied Physics*, 30(6):816–819, 1959.

[104] S. Kotapati, A. Javed, N. Reeves-McLaren, M.R.J. Gibbs, and N.A. Morley. Effect of the Ni81Fe19 thickness on the magnetic properties of Ni81Fe19/Fe50Co50 bilayers. *Journal of Magnetism and Magnetic Materials*, 331(1):67–71, 2013.

[105] M. D. Cooke, M. R J Gibbs, and R. F. Pettifer. Sputter deposition of compositional gradient magnetostrictive FeCo based thin films. *Journal of Magnetism and Magnetic Materials*, 237(2):175–180, 2001.

[106] A. E. Clark, K. B. Hathaway, M. Wun-Fogle, J. B. Restorff, T. A. Lograsso, V. M. Keppens, G. Petculescu, and R. A. Taylor. Extraordinary magnetoelasticity and lattice softening in bcc Fe-Ga alloys. *Journal of Applied Physics*, 93(10):8621, 2003.

[107] E. M. Summers, T. A. Lograsso, and M. Wun-Fogle. Magnetostriction of binary and ternary Fe-Ga alloys. *Journal of Materials Science*, 42(23):9582–9594, 2007.

[108] J.E. Goldman. Magnetostriction of annealed and cold worked nickel rods. *Physical Review*, 72(1):529, 1947.

[109] Du Trémolet De Lacheisserie, E. *Magnetostriction: Theory and Applications of Magnetoelasticity*. CRC Press, 1993.

[110] M.A Chaudhri. A microcomputer-controlled system for the measurement of magnetostriction with a 13 T superconducting solenoid. *Journal of Physics E: Scientific Instruments*, 17(1):287–290, 1984.

[111] N. Tsuya, A.K. Ichi, O. Kenji, and S. Yoshiaki. Magnetostriction Measurement by Three Terminal Capacitance Method. *Japanese Journal of Applied Physics*, 13 (11):1808–1810, 1974.

[112] M.S Boley, W.C Shin, D.K. Rigsbee, and D.A Franklin. Capacitance bridge measurements for magnetostriction. *Japanese Journal of Applied Physics*, 11(10): 8210–8212, 2002.

[113] D. Sanders. The correlations between mechanical stress and magnetic anisotropy in ultra thin film. *Reports on Progress in Physics*, 62(5):809–858, 1999.

[114] E. Klokholm. The measurement of magnetostriction in ferromagnetic thin films. *IEEE Transactions Magnetics*, 12(6):819–821, 1976.

[115] Du Trémolet De Lacheisserie, E., K. Mackay, J. Betz, and J. C. Peuzin. From bulk to film magnetostrictive actuators. *Journal of Alloys and Compounds*, 275-277: 685–691, 1998.

[116] A. B. Smith and R. V. Jones. Magnetostriction Constants from Ferromagnetic Resonance. *Journal of Applied Physics*, 34(1):1283–1284, 1963.

[117] J.C.M. Henning and J. den Boef. Magnetostriction measurement by means of strain modulated ferromagnetic resonance (SMFMR). *Journal of Applied Physics*, 16(1):353–357, 1978.

[118] S.E. Bushnell, W.B. Nowak, S.A. Oliver, and C. Vittoria. The measurement of magnetostriction constants of thin films using planar microwave devices and ferromagnetic resonance. *Review of Scientific Instruments*, 63(3):2021–2025, 1992.

[119] K. Nesteruk, R. Żuberek, S. Piechota, M.W. M W Gutowski, and H. Szymczak. Thin film's magnetostriction investigated by strain modulated ferromagnetic resonance at low temperature. *Measurement Science and Technology*, 25(7):075502, 2014.

[120] Z. Uberek, H. Szymczak, R. Krishnan, and M. Tessier. Influence of interdiffusion layer on magnetostriction of Fe/CoNbZr multilayers. *Journal of Magnetism and Magnetic Materials*, 133(1):490–492, 1994.

[121] M.A.W. Schoen, D. Thonig, M.L. Michael L. Schneider, T. J. Silva, H.T. Hans T. Nembach, O. Eriksson, O. Karis, and J.M. Shaw. Ultra-low magnetic damping of a metallic ferromagnet. *Nature Physics*, 12:839–842, 2016.

[122] R. Weber, D.S Han, I. Boventer, S. Jaiswal, R. Lebrun, G. Jakob, and M. Kläu. Gilbert damping of cofe-alloys. *Journal of Physics D: Applied Physics*, 52:325001, 2019.

[123] T. Devolder, P.H. Ducrot, J. P. Adam, I. Barisic, N. Vernier, J. B. Kim, B. Ockert, and D. D. Ravelosona. Damping of $Co_xFe_{80-x}B_{20}$ ultrathin films with perpendicular magnetic anisotropy . *Applied Physics Letters*, 102(1):1–4, 2015.

[124] M. Bi, X. Wang, H. Lu, L. Deng, K.J. Sunday, M. L. Taheri, and V. G. Vincent G. Harris. Magnetic and microwave properties of amorphous FeCoNbBCu thin films . *Journal of Applied Physics*, 119(1):1–7, 2016.

[125] X. Yang, J. Q. Wei, X. H. Li, L. Q. Gong, T. Wang, and F. S. Li. Thickness dependence of microwave magnetic properties in electrodeposited FeCo soft magnetic films with in-plane anisotropy. *Physica B: Condensed Matter*, 407(3):555–559, 2012.

[126] C. Bilzer, T. Devolder, J.V. Kim, G. Counil, C. Chappert, S. Cardoso, and P. P. Freitas. Study of the dynamic magnetic properties of soft CoFeB film . *Journal of Physics D: Applied Physics*, 100(1):1–4, 2006.

[127] X. Guo, L. Xi, Y. Li, X. Han, D. Li, Z. Wang, and Y. Zuo. Reduction of magnetic damping constant of feco films by rare-earth gd doping. *Applied Physics Letters*, 105:072411, 2014.

[128] X. Liang, C. Dong, S.J. Celestin, X. Wang, H. Chen, K.S. Ziemer, M. Page, M.E. McConney, B.M Jones, J.G Howe, and N.X. Sun. Soft Magnetism, Magnetostriction, and Microwave Properties of Fe-Ga-C Alloy Films. *IEEE Magnetics Letter*, 1:5500705, 2019.

[129] Th. Gerrits, M.L. Schneider, and T.J. Silva. Enhanced ferromagnetic damping in permalloy/cu bilayers. *Journal of Applied Physics*, 99:023901, 2006.

[130] J. Fassbender, J. Von Borany, A. Mücklich, K. Potzger, W. Möller, J. McCord, L. Schultz, and R. Mattheis. Structural and magnetic modifications of Cr-implanted Permalloy. *Physical Review B - Condensed Matter and Materials Physics*, 73(18):1–8, 2006. ISSN 10980121.

[131] K.S. Chan, H. Ji, X. Wang, S.J. Hudak Jr., and B.R. Lanning. Mechanical properties and interface toughness of FeCo thin films on Ti–6Al–4V. *Materials Science and Engineering*, A 422:298–308, 2006.

[132] S.U. Jen, T. L. Tsai, P. C. Kuo, W. L. Chi, and W. C. Cheng. Magnetostrictive and structural properties of FeCoGa films. *Journal of Applied Physics*, 107:013914, 2010.

[133] R. Ranjana Saha and W.D Nix. Effects of the substrate on the determination of thin film mechanical properties by nanoindentation. *Acta Materialia*, 50:23–38, 2002.

[134] C.T. Chuang, C.T. Chao, R.C. Chang, and K.Y. Chu. Effects of internal stresses on the mechanical properties of deposition thin films. *Journal of Materials Processing Technology*, 201:770–774, 2008.

[135] Q.A. Abbas. *Magnetic and Mechanical Properties of Magnetostrictive FeGaSiB Films: PhD Thesis*. The University of Sheffield, 2018.

[136] L.B. Freund and S. Suresh. *Thin Film Materials : Stress, Defect Formation and Surface Evolution*. Cambridge University Press, 2003.

[137] T.M. Adam and R. A. Layton. *Introductory MEMS : Fabrication and Applications*. Springer, 2010.

[138] D.M Mattox. *Handbook of Physical Vapor Deposition (PVD) Processing*. Elsevier, second edition edition, 2010.

[139] D. Depla, S. Mahieu, and J. Greene. Sputter deposition processes. *Handbook of deposition technologies for films and coatings*, 281:253–296, 1991.

[140] M. Ohring. *Materials Science of Thin Films: Depositions and Structure*. San Diego, Calif. ; London : Academic, second edition edition, 2002.

[141] H. Basumatary, J. Arout Chelvane, D. V. Sridhara Rao, S. V. Kamat, and R. Ranjan. Effect of sputtering parameters on the structure, microstructure and magnetic properties of Tb-Fe films. *Thin Solid Films*, 583(1):1–6, 2015.

[142] J.A. Thornton. High rate thick film growth. *Annual Review of Materials Science*, 7(1):239–260, 1977.

[143] N. Evcimen Duygulu, A. O. Kodolbas, and A. Ekerim. Influence of r.f power on structural properties of ZnO thin films. *Journal of Crystal Growth*, 381:51–56, 2013.

[144] R.K. Waits. *American Vacuum Society Monograph Series : Thin Film Deposition and Patterning*. American Vacuum Society, 1998.

[145] J.A. Venables. *Introduction to Surface and Thin Film Processes*. Cambridge University Press, 2000.

[146] B.A. Movchan and A.V. Demchishin. Study of the structure and properties of thick vacuum condensates of nickel, titanium, tungsten,aluminum oxide and zirconium oxide. *Physics of Metals and Metallography*, 28(1):83–91, 1969.

[147] M.F. Doerner and W.D. Nix. Stresses and deformation processes in thin films on substrates. *Critical Reviews in Solid State and Materials Sciences*, 14(3):225–268, 1988.

[148] R.W. Hoffman. Stresses in thin films: The relevance of grain boundaries and impurities. *Thin Solid Films*, 34(2):185–190, 1976.

[149] E. Chason, B.W. Sheldon, L.B. Freund, J.A. Floro, and S.J. Hearne. Origin of compressive residual stress in polycrystalline thin films. *Physical Review Letters*, 88(1):1–4, 2002.

[150] S. Swann. Magnetron sputtering. *Physics in Technology*, 19(1):67–75, 1988.

[151] G. F. Weston. Pumping system. *Vacuum*, 35(10–11):493–497, 1988.

[152] P.C. Braga and D. Ricci. *Atomic Force Microscopy : Biomedical Methods and Applications*. Humana Press, 2004.

[153] *Dimension 3100 Instruction Manual*. Digital Instruments, Inc., 1997.

[154] L. Reimer. *Scanning Electron Microscopy : Physics of Image Formation and Microanalysis*. Springer, 1998.

[155] P.J. Goodhew, J. Humphreys, and R. Beanland. *Electron Microscopy and Analysis*. CRC Press, 2000.

[156] P.K. Harold and E. A Leroy. *X-Ray Diffraction Procedures for Polyscrystalline and Amorphous Materials*. John Wiley Sons, 1974.

[157] B.B. He. *Two-Dimensional X-Ray Diffraction.* John Wiley Sons, 2009.

[158] J. Ron and L.S Robert. *Introduction to X-Ray Powder Diffractometry.* John Wiley Sons, 1996.

[159] H. Bubert and H. Jenett. *Surface and Thin Film Analysis : Principles, Instrumentation, Applications.* Wiley-VCH Verlag GmbH, 2002.

[160] B.A. van Brussel and J. Th. M. De Hosson. Glancing angle x-ray diffraction: A different approach . *Applied Physics Letters*, 1(64):1585–1587, 1994.

[161] C. Hudson. Origin of stresses in sputtered elemental and alloy thin films. *Journal of Vacuum Science & Technology A: Vacuum, Surfaces, and Films*, 14(4):2169, 1996.

[162] H. J. Kleebe, S. Lauterbach, and M. M. Mathis M. Muller. *Transmission Electron Microscopy in Methods in Physical Chemistry.* John Wiley Sons, 2012.

[163] R.F. Egerton. *Physical Principles of Electron Microscopy : An Introduction to TEM, SEM and AEM.* Springer, 2005.

[164] D.A. Allwood, G. Xiong, M. D. Cooke, and R. P. Cowburn. Magneto-optical Kerr effect analysis of magnetic nanostructures. *Journal of Physics D: Applied Physics*, 36(18):2175–2182, 2003. ISSN 0022-3727.

[165] N. A. Morley, M. R J Gibbs, E. Ahmad, I. Will, and Y. B. Xu. MOKE hysteresis loop method of determining the anisotropy constants of ferromagnetic thin films: Fe on GaAs(1 0 0) with overlayers of Au and Cr. *Journal of Magnetism and Magnetic Materials*, 300(2):436–444, 2006.

[166] P. Weinberger. John Kerr and his effects found in 1877 and 1878. *Philosophical Magazine Letters*, 88(12):897–907, 2008.

[167] R. Schäfer A. Hubert. *Magnetic Domains,The analysis of magnetic microstructures.* Springer-Verlag Berlin and Heidelberg GmbH Co., 1999.

[168] A. Stupakiewicz, A. Chizhik, M. Tekielak, A. Zhukov, J. Gonzalez, and A. Maziewski. Direct imaging of the magnetization reversal in microwires using all-MOKE microscopy. *Review of Scientific Instruments 85*, 85(1):103702, 2014.

[169] S. Yamamoto and I. Matsuda. Measurement of the resonant magneto-optical kerr effect using a free electron laser. *Applied Science*, 7(662):1–23, 2017.

[170] J. M. Florczak and E. Dan Dahlberg. Magnetization reversal in (100) Fe thin films. *Physical Review B*, 44(17):9338–9347, 1991. doi: 10.1103/PhysRevB.44.9338.

[171] N. A. Morley, A. Javed, and M. R.J. Gibbs. Effect of a forming field on the magnetic and structural properties of thin Fe-Ga films. *Journal of Applied Physics*, 105(7), 2009.

[172] D. Cao, X. Cheng, H. Feng, C. Jin, Z. Zhu, L. Pan, Z. Wang, J. Wang, and Q. Liu. Investigation on the structure and dynamic magnetic properties of FeCo films with different thicknesses by vector network analyzer and electron spin resonance spectroscopy. *Journal of Alloys and Compounds*, 688(1):917–922, 2016.

[173] C. Kittel. On the Theory of Ferromagnetic Resonance Absorption . *Physical Reviews*, 73(2):155–161, 1948.

[174] Quantum Design. *Magnetic property measurement system : MPMS 3 User's Manual 1500-100, Rev. F1.* Quantum Design, Inc, 2016.

[175] M. Abuín, L. Pérez, A. Mascaraque, and M. Maicas. Tuning the magnetic properties of FeCo by pulsed DC magnetron sputtering. *CrystEngComm*, 16(40):9528–9533, 2014. ISSN 1466-8033.

[176] A. Gayen, G.B. Prasad, S. Mallik, S. Bedanta, and A. Perumal. Effects of composition, thickness and temperature on the magnetic properties of amorphous CoFeB thin film. *Journal of Alloys and Compounds*, 694(1):823–832, 2017.

[177] W. Wang, Y. Chen, G. H. Yue, W. B. Mi, H. L. Bai, K. Sumiyama, and D. L. Peng. Dependence of soft-magnetic properties on film thickness and high frequency characteristics for Fe-Co-Cr-N alloy films. *Journal of Alloys and Compounds*, 476 (1-2):599–602, 2009.

[178] M. Li, Y.P. Zhao, G.C. Wang, and H.G. Min. Effect of surface roughness on magnetization reversal of Co films on plasma-etched Si(100) substrates. *Journal of Applied Physics*, 83(11):6287, 1998.

[179] K. Srinivas, M. Manivel Raja, D. V. Sridhara Rao, and S. V. Kamat. Effect of sputtering pressure and power on composition, surface roughness, microstructure

and magnetic properties of as-deposited Co2FeSi thin films. *Thin Solid Films*, 558: 349–355, 2014.

[180] C.L. Platt, A.E. Berkowitz, D.J. Smith, and M.R. McCartney. Correlation of coercivity and microstructure of thin CoFe films. *Journal of Applied Physics*, 88 (4):2058–2062, 2000.

[181] C. Das, S. Mohapatra, G.A. Vitthal, and P. Alagarsamy. Magnetic properties of single-layer and multilayer structured Co40Fe40B20 thin films. *Thin Solid Films*, 616:126–133, 2016.

[182] A. T. Hindmarch, A. W. Rushforth, R. P. Campion, C. H. Marrows, and B. L. Gallagher. Origin of in-plane uniaxial magnetic anisotropy in CoFeB amorphous ferromagnetic thin films. *Physical Review B*, 83(1):1–4, 2011.

[183] H. Szymczak, R. Zuberek, and J. Gonzalez. Mechanisms responsible for magnetostriction in heterogeneous magnetic systems. *Journal of Magnetism and Magnetic Materials*, 191(1):199–202, 1999.

[184] P. H. H. Duc and P.E. Bromer. Magnetoelasticity in nanoscale heterogeneous materials. *Handbook of Magnetic Material*, 14(1):275–423, 202.

[185] J. Lou, R.E. Insignares, Z. Cai, K.S. Ziemer, M. Liu, and Sun N. X. Soft magnetism, magnetostriction, and microwave properties of FeGaB thin film. *Applied Physics Letters*, 91:182504, 2007.

[186] X. Liu, W. Zhang, M.J. Matthew J. Carter, and G. Xiao. Ferromagnetic resonance and damping properties of CoFeB thin films as free layers in MgO-based magnetic tunnel junctions. *Journal of Applied Physics*, 11:033910, 2011.

[187] T. P. T. Prasanna Kumari, M.M. Manivel Raja, A. Kumar, S. Srinath, and S.V. Kamat. Effect of thickness on structure, microstructure, residual stress and soft magnetic properties of DC sputtered Fe65Co35 soft magnetic thin films. *Journal of Magnetism and Magnetic Materials*, 365:93–99, 2014.

[188] D. Kirk, A. Kohn, K.B. Borisenko, C. Lang, J. Schmalhorst, G. Reiss, and D. J. H. Cockayne. Structural study of amorphous CoFeB thin films exhibiting in-plane uniaxial magnetic anisotropy. *Physical Review B*, 79(1):1–8, 2009.

[189] L. Kipgen, H. Fulara, M. Raju, and S. Chaudhary. In-plane magnetic anisotropy and coercive field dependence upon thickness of CoFeB. *Journal of Magnetism and Magnetic Materials*, 324:3118–3121, 2012.

[190] M. Tamisari, G. Ausanio, V. Guidi, V. Iannotti, I. Neri, F. Spizzo, and P. Vavassori. Magnetic and structural investigation of growth induced magnetic anisotropies in Fe 50 Co 50 thin lms. *EPJ Web of Conferences*, 40:09002, 2013. ISSN 2100-014X.

[191] Z. Tanga, H. Ni, B. Lua, M. Zheng, Y.A. Huanga, S.G. Lua, M. Tang, and J. Gao. Thickness dependence of magnetic anisotropy and domains in amorphous $co_{40}fe_{40}b_{20}$ thin films grown on pet flexible substrates. *Journal of Magnetism and Magnetic Materials*, 426:444–449, 2017.

[192] V.A. Lukshina, N.V. Dmitrieva, M.A. Cerdeira, and A.P. Potapov. Stress-induced magnetic anisotropy in fe-based nanocrystalline alloy with addition of 1–5 at.% cr. *Journal of Alloys and Compounds*, 536s:s374–s376, 2012.

[193] A. E. Clark, M. Wun-Fogle, J. B. Restorff, T. A. Lograsso, and J. R. Cullen. Effect of quenching on the magnetostriction on $\mathrm{fe}_{1-x}\mathrm{ga}_x$ (0.13<x<0.21). *IEEE Transactions on Magnetics*, 37:2678–2680, 2001.

[194] S. V. Von Sovski. *Ferromagnetic Resonance: The Phenomenon of Resonant Absorption of a High-Frequency Magnetic Field in Ferromagnetic Substances.* Pergamon Press, 1966.

[195] M.C. Hickey and J.S. Moodera. Origin of intrinsic gilbert damping. *Physical Review Letters*, 102:137601, 2009.

[196] J.M. Beaujour, D. D. Ravelosona, I Tudosa, E. E. Fullerton, and A. D. Kent. Ferromagnetic resonance linewidth in ultrathin lms with perpendicular magnetic anisotropy. *Physical Review B*, 80:180415, 2009.

[197] K. Seemann, H. Leiste, and A. .Kovàcs. Damping and ferromagnetic resonance linewidth broadening in nanocrystalline soft ferromagnetic fe–co–hf–n films. *Journal of Magnetism and Magnetic Materials*, 320:1952–1957, 2008.

[198] M. Oogane, T. Wakitani, S. Yakata, R. Yilgin, Y. Ando, A. Sakuma, and T. Miyazaki. Magnetic damping in ferromagnetic thin films. *Japanese Journal of Applied Physics*, 45:3889–3891, 2006.

[199] W. Zhang, S. Jiang, P. K. J. Wong, L. Sun, Y.K. Wang, K. Wang, M. P. de Jong, W. G. van der Wiel, G. van der Laan, and Y. Zhai. Engineering gilbert damping by dilute gd doping in soft magnetic fe thin films. *Journal of Applied Physics*, 115 (17):17A308, 2014.

[200] A. Conca, E.Th. Papaioannou, S. Klingler, J. Greser, T. Sebastian, B. Leven, J. Lösch, and B. Hillebrands. Annealing influence on the gilbert damping parameter and the exchange constant of cofeb thin films. *Applied Physics Letters*, 104 (18):182407, 2014.

[201] S. Azzawi, A. Ganguly, R. M. Tokaç, M. Rowan-Robinson, J. Sinha, A. T. Hindmarch, A. Barman, and D. Atkinson. Evolution of damping in ferromagnetic/nonmagnetic thin film bilayers as a function of nonmagnetic layer thickness. *Physics Review B*, 93:054402, 2017.

[202] A Ruiz-Calaforra, T. Brächer, V. Lauer, P. Pirro, B. Heinz, M. Geilen, A. V. Chumak, A. Conca, B. Leven, and Hillebrands. B. The role of the non-magnetic material in spin pumping and magnetization dynamics in nife and cofeb multilayer systems. *Journal of Applied Physics*, 117:163901, 2015.

[203] T. Osaka, M. Takai, K. Hayashi, K. Ohashi, M. Saito, and K. Yamada. A soft magnetic conife film with high saturation magnetic flux density and low coercivity. *Nature*, 392:796–798, 1998.

[204] N. D. Ha, M. H. Phan, and C.O. Kim. Influences of rapid annealing and substrate temperature on the magnetic properties of Co-Fe-V films. *Journal of Applied Physics*, 99(8):10–13, 2006.

[205] S. Ohnuma, H. Fujimori, T. Masumoto, X. Y. Xiong, D. H. Ping, and K. Hono. FeCo-Zr-O nanogranular soft-magnetic thin films with a high magnetic flux density. *Applied Physics Letters*, 82(6):946–948, 2003.

[206] K.I Arai and K. Ishiyama. Recent developments of new soft magnetic materials. *Journal of Magnetism and Magnetic Materials*, 133:233–237, 1994.

[207] R.S. Sundar and S.C Deevi. Influence of alloying elements on the mechanical properties of FeCo–V alloys. *Intermetallics*, 12:921–927, 2004.

[208] S.M. Han, Shah. R., R. Banarjee, G.B. Viswanathan, B.M. Clement, and W.D. Nix. Combinatorial studies of mechanical properties of ti–al thin films using nanoindentation. *Acta Materialia*, 53(7):2059–2067, 2005.

[209] S. Hadjiyiannis G. Skordaris K.D. Bouzakis, N. Michailidis and G. Erkens. The effect of specimen roughness and indenter tip geometry on the determination accuracy of thin hard coatings stress–strain laws by nanoindentation. *Materials Characterization*, 49:149–156, 2003.

[210] D.Chicota, M.Yetna N'Jocka, E.S.Puchi-Cabrera, A. Iost, M.H.Staia, G.Louis, G.Bouscarrat, and R.Aumaitre. A contact area function for berkovich nanoindentation: Application to hardness determination of a tihfcn thin film. *Thin Solid Films*, 558:259–266, 2014.

[211] G.Feng, W.D. Nix, Y. Yoon, and C. J. Lee. A study of the mechanical properties of nanowires using nanoindentation. *Journal of Applied Physics*, 99:074304, 2006.

[212] R. Gaillac, P. Pullumbi, and F.X Coudert. Elate: an open-source online application for analysis and visualization of elastic tensors. *Journal of Physics: Condensed Matter*, 28(27):275201, 2016.

[213] Anthony C. Fischer-Cripps. *Nanoindentation [electronic resource] 3rd ed.* Mechanical engineering series (Berlin, Germany). Springer, 2011.

[214] A. Bolshakova and G. M. Pharr. Influences of pileup on the measurement of mechanical properties by load and depth sensing indentation techniques. *Journal of Material Research*, 13:1049–1058, 1998.

[215] N. Moharrami and S. J. Bull. A comparison of nanoindentation pile-up in bulk-materials and thin films. *Thin Solid Films*, 512:189–199, 2014.

[216] S.R. Kalidindi and S. Phatak. Determination of the effective zero-point and the extraction of spherical nanoindentation stress-strain curves. *Acta Materialia*, 56: 3523–3532, 2008.

[217] J.S. Field and M.V. Swain. Determining the mechanical properties of small volumes of material from submicrometer spherical indentation. *Journal of Material Research*, 10(19):101–112, 1995.

[218] M. Beghini, L. Bertini, and V. Fntanari. Evaluation of the stress–strain curve of metallic materials by spherical indentation. *International Journal of Solids and Structures*, 43(7):2441–2459, 2006.

[219] X.D. Liu, M. Nagumo, and M. Umemoto. The hall-petch relationship in nanocrystalline material. *Materials Transactions JIM*, 38:1033–1039, 1997.

[220] A. E. Giannakopoulos and S. Suresh. Determination of elastoplastic properties by instrumented sharp nanoindentation. *Scripta Materialia*, 40:1191–1198, 1999.